Annual Report 2011

Physik-Department E13

Lehrstuhl für Funktionelle Materialien

Technische Universität München

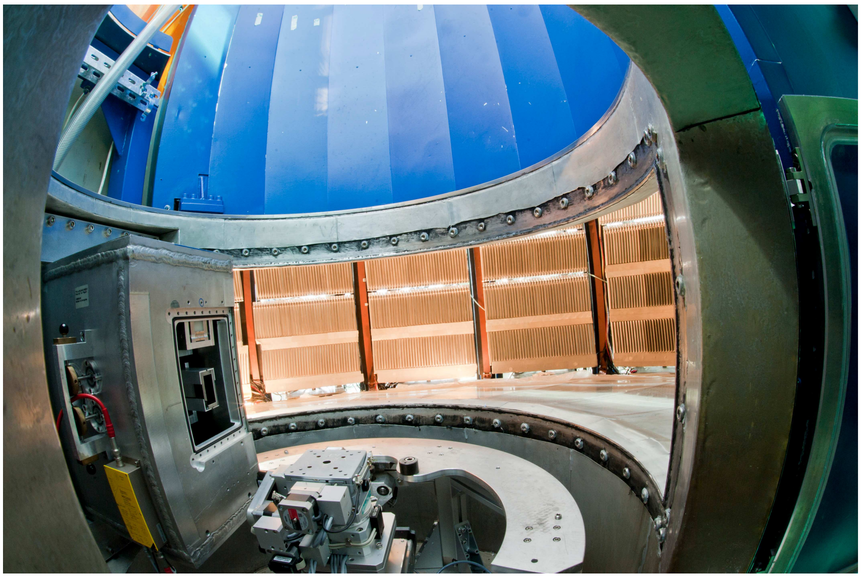

Prof. Dr. Winfried Petry
Chair of Functional Materials
Physik-Department

Deputy chairman for Prof. Dr. Petry:
Prof. Dr. Peter Müller-Buschbaum

Physik-Department E13
Technische Universität München
James-Franck-Straße 1
85748 Garching

Secretaries: Marion Waletzki
Susanna Fink

Tel.: +49(0)89 289 12452
Fax: +49(0)89 289 12473

Email: peter.mueller-buschbaum@ph.tum.de
marion.waletzki@ph.tum.de
http://www.functmat.ph.tum.de

Editor: Dr. Volker Körstgens

Cover-page picture:

View on the *treasure room* of TOFTOF. The new focusing neutron guide (left side) and the 1000 ^{3}He detector tubes (on the background) as seen from the sample chamber.

1 Preface

It is a great pleasure to present in the name of the staff of the Chair of Functional Materials the annual report for the year 2011. It provides an overview of our teaching, research, and development activities. Our research activities are focused on functional materials and cover a broad range from soft matter physics to developments in methods and instrumentation. We examine the fundamental physics of material properties using mainly scattering methods (neutrons-, x-ray and light scattering). The general goal of our research is to explain the functional characteristics of soft condensed matter from the knowledge of the microscopic dynamics and structure.

In 2011, the chair activities covered the specific areas of water-based polymer systems, thin polymer films, polymer films for application in photovoltaics, polymer-hybrid systems, dynamics, and methodological and instrumental developments. The activities in the fields of polymer films for application in photovoltaics and polymer-hybrid systems have increased significantly.

The in-house experiments available in the laboratories of the chair were supplemented by the lively activities at numerous large scale facilities, comprising synchrotron radiation and neutron scattering experiments. The upgrade of the instrument TOF-TOF at the research reactor FRM-II was one of the major activities concerning the developments in methods and instrumentation. With the new focusing neutron guide, the increased detector capacity and an improved signal-to-noise ratio, quasi-elastic measurements can be done four times faster after this upgrade. In addition to instrumentation at large scale facilities, with the renewing of our in-house x-ray scattering instrument dedicated to small angle x-ray scattering (SAXS) and wide angle x-ray scattering (WAXS) our experimental capabilities have improved significantly.

In 2011, the Chair of Functional Materials comprised 14 fellows, 35 PhD students, 12 diploma students, 6 master students, 14 bachelor students, 11 student assistants and 11 administrative and technical staff members. 6 PhD theses were accomplished, moreover, 5 diploma and 2 master theses as well as 12 bachelor theses were finished. As all the years before, we had the pleasure to host several guests from abroad which stimulated a lively scientific atmosphere.

In general, all members of the chair were very active at conferences and workshops, participating with both talks and posters. Moreover, important conferences were organized by members of the chair: two Edgar-Lüscher Seminars were again organized, this year on the subjects 'Biologisch inspirierte Syteme' and 'Nanophysik'. The 1st Colloquium of the Munich School of Engineering 'Sustainable Energy Supply of the Future' took place in Garching. Moreover, a Tutorial on 'Physics with Neutrons - From Proteins via Polymer Thin Films to Spin Waves' and Symposium on 'Elementary Processes in Organic Photovoltaics' was organized in the framework of the spring meeting of the Condensed Matter Division of the German Physical Society in Dresden. Moreover, the International workshop 'GISAXS 2011' was organized in Hamburg as well as a workshop on 'Hydrogel Analytics' in the framework of the SPP 'Intelligente Hydrogele' in Garching. The chair participated in the 5th FRM II Science Meeting at Burg Rothenfels with a number of oral and poster presentations.

Regarding teaching activities of the chair, we offered general physics lectures for students of mechanical engineering (Müller-Buschbaum) and in the new Bachelor of Engineering Science at the Munich School of Engineering (MSE) (Papadakis). Specialized lectures comprised

'Polymer physics' (Müller-Buschbaum/Papadakis), 'Nanostructured soft materials' (Müller-Buschbaum/Metwalli and Papadakis/Metwalli) and 'Neutron scattering and complementary methods' (Petry/Unruh). Prof. Papadakis acted again as a women's representative of the Physics Department. Moreover Prof. Müller-Buschbaum is heading the activities in the 'Network Renewable Energies (NRG)' in the MSE.

This annual report comprises a selection of the different research topics and projects carried out in the individual groups of the chair. It highlights the dedicated and successful research activities and collaborations with other groups and large scale facilities. We wish all chair members a fruitful continuation and a successful year 2012.

Peter Müller-Buschbaum and Christine Papadakis April 2012

Contents

2 Water based polymer systems

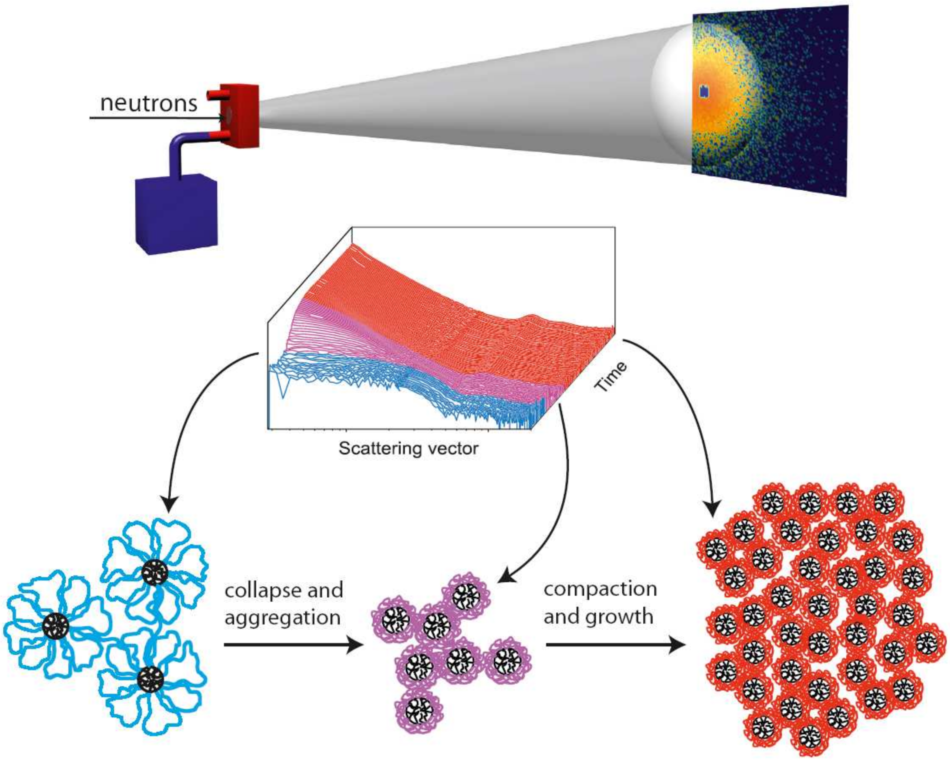

2.1 Switching behavior of thermoresponsive poly(2-oxazoline)s

S. Jaksch, C. M. Papadakis, S. Salzinger[1], S. Huber[1], R. Jordan[1,2], P. Busch[3]

[1] WACKER-Lehrstuhl für Makromolekulare Chemie, Department Chemie, TU München
[2] Professur für Makromolekulare Chemie, Department Chemie, TU Dresden
[3] Jülich Center for Neutron Science, Garching, Germany

Thermoresponsive polymers in aqueous solution exhibit a reversible strong change in solubility and conformation when heated above their cloud point. Especially interesting polymers of this class of materials are poly(2-oxazoline)s (POx) whose behavior can be tuned from hydrophilic over thermoresponsive to hydrophobic by a pendant 2-substitution. They have a very broad range of accessible architectures [1,2]. Moreover they are non-toxic and biocompatible [3]. By including hydrophobic moieties in a thermoresponsive copolymer, the cloud point can be tuned in a wide range. These properties make them ideal candidates for medical applications such as drug delivery [3].

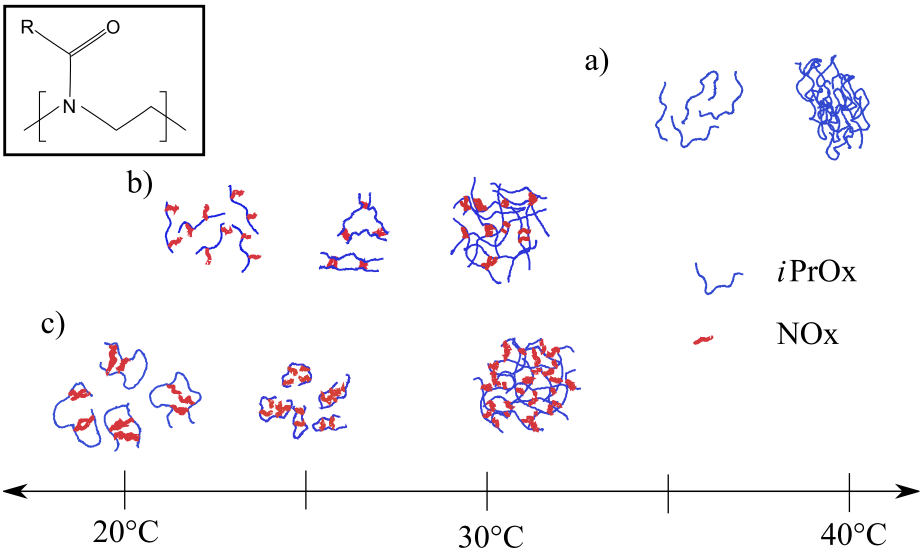

Figure 2.1:
Schematics of the aggregation behavior of a) P*i*PrOx$_{50}$, b) P[*i*PrOx$_{48}$NOx$_{2}$]$_{grad}$ and c) P[*i*PrOx$_{46}$NOx$_{4}$]$_{grad}$. Inset: Structure of a poly(2-oxazoline) monomer.

We have studied the aggregation behavior of poly(*iso*-propyl-2-oxazoline)$_{50}$ (P*i*PrOx$_{50}$) (inset of fig. 2.1) as a reference homopolymer as well as poly[(*iso*-propyl-2-oxazoline)-(*n*-nonyl-2-oxazoline)]$_{grad}$ gradient copolymers (P[*i*PrOx$_{48}$NOx$_{2}$]$_{grad}$ and P[*i*PrOx$_{46}$NOx$_{4}$]$_{grad}$) around their cloud points [4]. The inclusion of the NOx moieties changes the cloud point from 40.3°C for P*i*PrOx$_{50}$ to 25.2°C and 23.2°C for P[*i*PrOx$_{48}$NOx$_{2}$]$_{grad}$ and P[*i*PrOx$_{46}$NOx$_{4}$]$_{grad}$, respectively (fig. 2.1).

To elucidate the aggregation behavior around the cloud point, we performed small-angle neutron scattering (SANS) experiments of 20 mg/ml solutions in D_2O at the KWS-1 beamline at the FRM II. Representative scattering curves are shown in fig. 2.2. The curves feature both, single chain scattering above 0.2 nm^{-1} and forward scattering due to large aggregates. The single chain scattering is described by a Debye function for P*i*PrOx$_{50}$ and P[*i*PrOx$_{48}$NOx$_{2}$]$_{grad}$; i.e. Gaussian coils, whereas the aggregate scattering in the low q-region is described by a form factor for solid homogeneous spheres larger than $\approx$ 50 nm. For P[*i*PrOx$_{46}$NOx$_{4}$]$_{grad}$, in contrast, the single chains are more compact and are modelled by homogeneous spheres.

The temperature-dependent aggregation behavior of the different polymers is detailed in fig. 2.1. For P*i*PrOx$_{50}$, large aggregates form immediately at the cloud point (fig. 2.2b,c). The

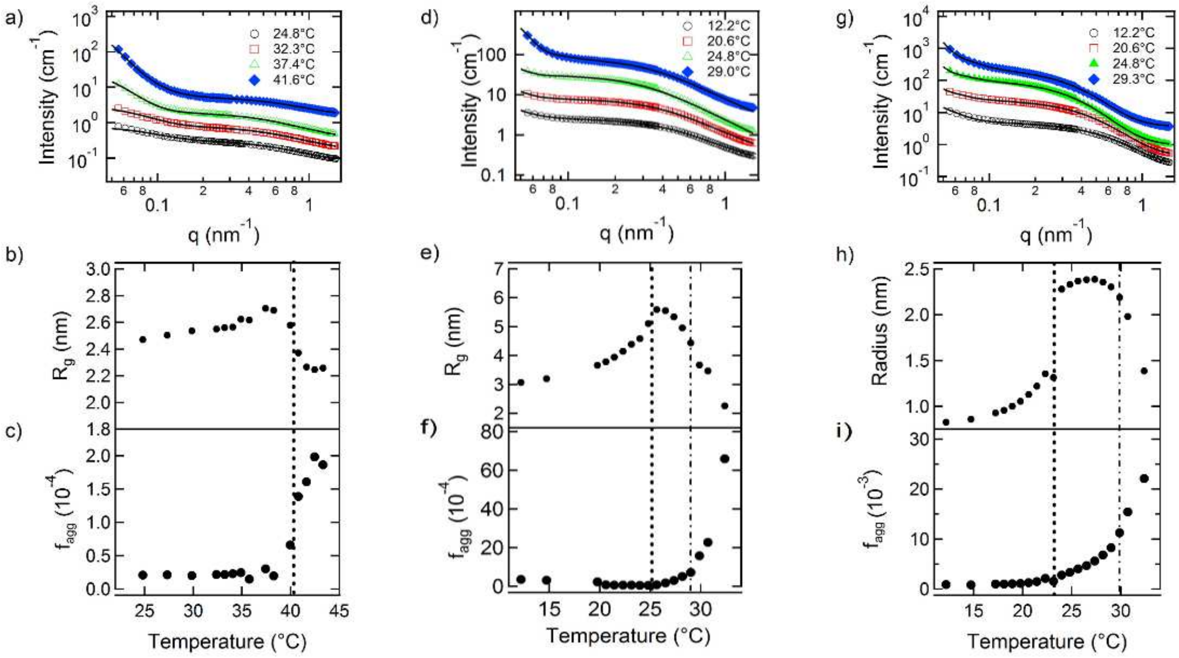

Figure 2.2: Representative SANS curves for P*i*PrOx$_{50}$ (a), P[*i*PrOx$_{48}$NOx$_2$]$_{grad}$ (d) and P[*i*PrOx$_{46}$NOx$_4$]$_{grad}$ (g). The intensities are shifted vertically. The full lines are fits. (b,e,h) Resulting chain radii. (c,f,i) Relative intensities of the aggregates. The dashed lines are the cloud points from turbidimetry and the dash-dotted lines the upper limits of the intermediate aggregation regime.

gradient copolymers behave differently: Aggregation of P[*i*PrOx$_{48}$NOx$_2$]$_{grad}$ sets in already at temperatures below the cloud point, and small precursor aggregates are formed. These aggregates consist of few chains, and the intermolecular interaction is mediated by the hydrophobic NOx groups which form bridges between the chains. Upon heating above the cloud point, these small aggregates remain stable and do not immediately form large aggregates. Only a few Kelvin above the cloud point, large aggregates form (fig. 2.2e, f). Thus, above the cloud point an intermediate regime is encountered. The behavior is very similar for P[*i*PrOx$_{46}$NOx$_4$]$_{grad}$, but here, the small aggregates are more stable which results in a more pronounced intermediate regime than for P[*i*PrOx$_{48}$NOx$_2$]$_{grad}$ (fig. 2.2h,i). This is due to higher amount of NOx moieties resulting in a higher probability for intramolecular bridging.

We conclude that the aggregation process for amphiphilic thermoresponsive POx gradient copolymers is a two-step process with an onset of aggregation already below the macroscopic cloud point. The small precursor aggregates remain stable above the cloud point, and only at higher temperatures, larger aggregates are formed.

This project is supported by the DFG within the project „Multicompartment systems based on poly(2-oxazolines)“(Pa771/6-2).

[1] T. B. Bonné, K. Lüdtke, R. Jordan,C. M. Papadakis, *Macromol. Chem. Phys.* **208**, 1402-1408 (2007)

[2] R. Ivanova, T. Komenda, T. B. Bonné, K. Lüdtke, K. Mortensen, P. K. Pranzas, R. Jordan, C. M. Papadakis, *Macromol. Chem. Phys.* **209**, 2248-2258 (2008)

[3] F. C. Gärtner, R. Luxenhofer, B. Blechert, R. Jordan, M. Essler, J. Contr. Release **119**, 291-300 (2007)

[4] S. Salzinger, S. Huber, S. Jaksch, R. Jordan, C. M. Papadakis, *Coll. Polym. Sci.*, DOI: 10.1007/s00396-011-2564-z

2.2 Kinetics of structural changes in thermoresponsive triblock copolymer solutions after a temperature jump

J. Adelsberger, A. Diethert, E. Metwalli, I. Grillo[1], A. M. Bivigou Koumba[2], A. Laschewsky[2], P. Müller-Buschbaum, C. M. Papadakis

[1] Institut Laue-Langevin, Grenoble, France

[2] Institut für Chemie, Universität Potsdam, Potsdam, Germany

Thermoresponsive polymers have received increasing attention because they respond with a strong volume change to a small variation of temperature across the lower critical solution temperature (LCST). A widely used LCST polymer is poly(N-isopropyl acrylamide) (PNIPAM) which has an LCST of 32 °C. We investigate triblock copolymers consisting of two short hydrophobic polystyrene (PS) endblocks and a longer hydrophilic PNIPAM middleblock. In aqueous solution, they form flower-like core-shell micelles or, above the critical gel concentration, micellar hydrogels. When heated above the LCST, the PNIPAM block becomes hydrophobic and releases water from the micellar shell, which consequently collapses. This volume change is reversible [1].

Time-resolved small-angle neutron scattering (SANS) experiments allow to investigate the kinetics of the collapse of the micellar shell and the cluster formation with an excellent time resolution (0.1 s) and give information on a wide range of length scales. At this, a stopped-flow apparatus was used at beamline D22 at ILL. The triblock copolymer solutions (PS-d_8-*b*-PNIPAM-*b*-PS-d_8 in D_2O) were kept in a reservoir at a temperature below the LCST. To realize a fast temperature jump above the LCST, the solution was injected into the preheated sample cell and the time-resolved measurement was started. The curves were fitted using a model for spherical core-shell micelles together with different form and structure factors for their clusters [2]. The resolution functions were taken into account.

In figure 2.4, four different regimes are observed: (i) Before the LCST is reached, the micellar structure is nearly unchanged and the form factor of core-shell micelles together with a hard-sphere structure factor [2] describe the data well. (ii) As soon as the micellar shell collapses and becomes hydrophobic, the micelles start to form fractal clusters. The fractal dimension, d_f, and the cluster size show, that, after an initial growth step, the fractal clusters rearrange and become more compact, thus d_f increases while the cluster size stays constant. (iii) After the fractal dimension $d_f = 3$ is reached, the compact clusters continue to grow to a size of ~60 nm. The evolution of cluster sizes r_{cl} in this second growth step follows the diffusion limited colloidal aggregation (DLCA) mechanism, i.e. the law $r_{\mathrm{cl}} = k \cdot r_{\mathrm{cl}}^{\beta}$. $\beta = 0.60 \pm 0.01$ matches the prediction of 0.57 well. However, the cluster growth in regime (ii) does not follow the DLCA because the intermicellar cross-links dominate the rate of aggregation [3]. In regime (iv), the clusters merge, and gelation sets in. Figure 2.3 summarizes the four regimes.

Thermoresponsive triblock copolymer solutions thus show a multistep cluster growth after the collapse of the micellar shell, when heated quickly above the LCST (Figure 2.3).

This work is funded by the DFG within the priority program SPP1259 "Intelligent Hydrogels".

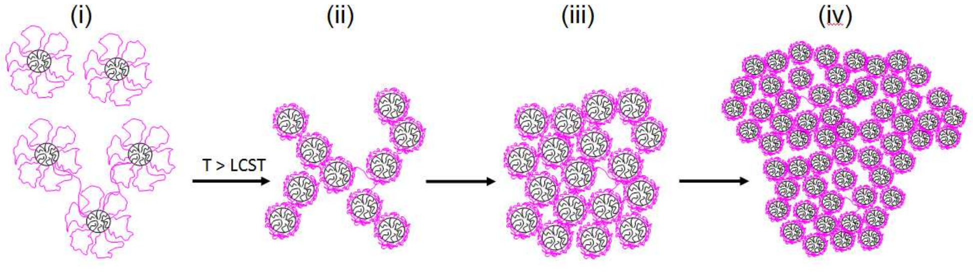

Figure 2.3: Scheme of cluster formation and growth for the four different regimes.

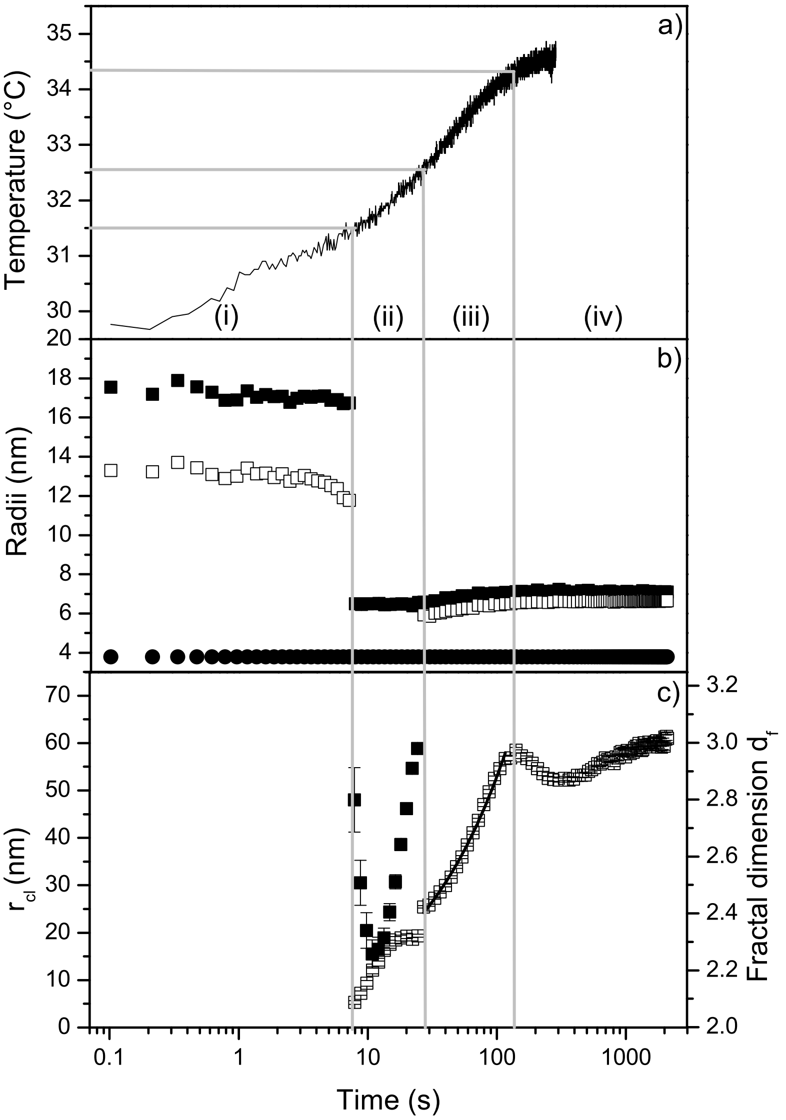

Figure 2.4:
(a) Temperature profile for a jump from 29.6 to 34.6 °C at a concentration of 50 mg/ml. (b) Core radius (filled circles), micellar radius (filled squares) and hard sphere radius (open squares). (c) Cluster size r_{cl} (open squares) and fractal dimension d_f (filled squares). The black line is a fit of $r_{\mathrm{cl}} = k \cdot r_{\mathrm{cl}}^{\beta}$. The grey lines separate the four different regimes.

[1] A. Jain, A. Kulkarni, A. M. Bivigou Koumba, W. Wang, P. Busch, A. Laschewsky, P. Müller-Buschbaum, C. M. Papadakis, *Macromol. Symp.* **291-292**, 221-229 (2010); J. Adelsberger, A. Kulkarni, A. Jain, W. Wang, A. M. Bivigou-Koumba, P. Busch, V. Pipich, O. Holderer, T. Hellweg, A. Laschewsky, P. Müller- Buschbaum, C. M. Papadakis, *Macromolecules* **43**, 2490-2501 (2010)

[2] J. Teixeira, *J. Appl. Cryst* **21**, 781-785 (1988); D. Posselt, J. S. Pedersen, K. Mortensen, *J. Non-Cryst. Solids* **145**, 128-132 (1992)

[3] J. Adelsberger, E. Metwalli, A. Diethert, I. Grillo, A. M. Bivigou-Koumba, A. Laschewsky, P. Müller-Buschbaum, C. M. Papadakis, *Macromol. Rapid Commun.*, in press, DOI: 10.1002/marc.201100631

2.3 Thermoresponsive hydrogels from symmetrical triblock copolymers poly(styrene-*b*-(methoxy diethylene glycol acrylate)-*b*-styrene)

G. De Paoli, A. Miasnikova[1], A. Laschewsky[1], P. Müller-Buschbaum, S. S. Funari[2], C. M. Papadakis

[1] Institut für Chemie, Universität Potsdam
[2] HASYLAB at DESY, Hamburg, Germany

Symmetrical amphiphilic block copolymers BAB with hydrophobic outer blocks B and a hydrophilic inner block A can form physical hydrogels under appropriate conditions. Above a critical concentration, a gel of bridged micelles is formed. The mechanical properties result mainly from the proportion of active bridges. In this study, we describe the temperature-dependent gelation behavior of a series of BAB symmetrical triblock copolymers, namely poly(styrene-*b*-methoxy diethylene glycol acrylate-*b*-styrene (PS-PMDEGA-PS) (Fig. 2.5). The inner PMDEGA block is thermo-responsive. The phase transition temperature of PMDEGA in aqueous solution is around 35-45°C, i.e. in the most interesting physiological window. Moreover, PMDEGA cannot form self-consistent inter- and intra-molecular H-bonds. This presumably leads to transitions with virtually no hysteresis between the cooling and the heating cycles. We were interested in the effects that PMDEGA inner block will exert on the hydrogel mechanical properties. In particular, we investigated the influence of the inner block length on the gel formation. Moreover, we wanted to correlate the changes of the mechanical properties to the structural changes with temperature. For this purpose, we carried out temperature-resolved small-angle x-ray scattering (SAXS) experiments.

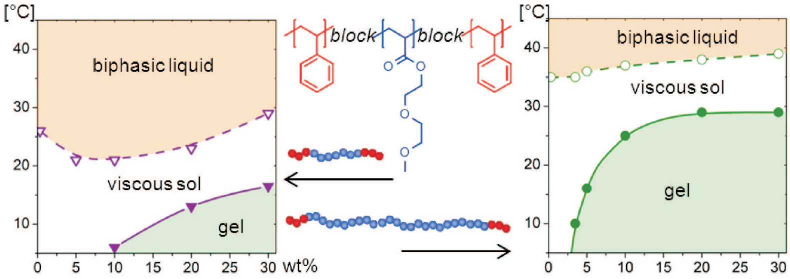

Figure 2.5:
Structure of PS-PMDEGA-PS and phase behavior as determined from turbidimetry and rheology.

Cloud points were determined by visual observation. Concentration dependent sol-gel transitions were evaluated by the tube inversion test. Rheological experiments were performed with an ARG2 rheometer (TA Instruments) in cone-plate geometry. SAXS experiments were performed at beamline A2 at HASYLAB/DESY. An X-ray beam with a wavelength $\lambda = 0.15$ nm was used. A 2D MarCCD detector was mounted at a distance of 3.24 m from the sample.

Representative scattering curves of PS_8-$PMDEGA_{452}$-PS_8 at 10 wt. % in water are displayed in Fig. 2.6. At low temperatures, a broad peak is present which is due to the correlation between the positions of the micelles. It becomes weaker upon heating to the cloud point, and, at the same time, the forward scattering increases. At high temperatures, the peak is shifted to higher q-values, indicating the collapse of the micellar network, and forward scattering becomes more intense. The decrease of the overall intensity above the cloud point is due to sedimentation of large clusters formed by collapsed micelles.

We attribute the peak to a liquid-like correlation between the PS cores with a close to hard-sphere interaction; thus a Percus-Yevick structure factor was used to model the correlation. The forward scattering was modeled using a Porod law describing large, homogeneous and smooth clusters formed by water-insoluble and bridged micelles. The X-ray scattering length density of PMDEGA differs strongly from the nearly equal ones of PS and H_2O, and the PS blocks

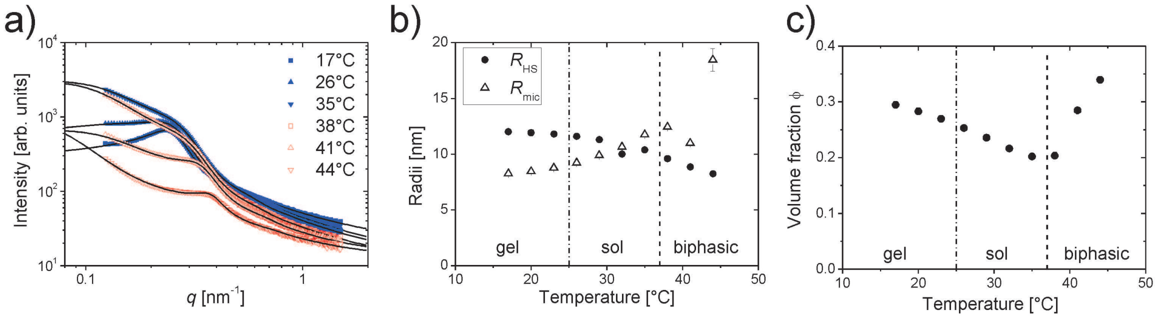

Figure 2.6:
(a) Temperature-resolved SAXS curves of PS_8-$PMDEGA_{452}$-PS_8 at 10 wt. % in water (symbols) together with model fits (lines). (b) Micellar radius, R_{mic}, and hard-sphere radius, R_{HS}. (c) Volume fraction of correlated micelles, ϕ.

are very short; thus, the scattering signal in PS-PMDEGA-PS is dominated by the scattering of the PMDEGA corona of the presumably formed core-shell micelles. We therefore modelled the micelles by homogeneous spheres. Fluctuations within the PMDEGA shells were taken into account by an Ornstein-Zernike structure factor.

Below the cloud point, R_{HS} decreases slightly as temperature is increased towards the cloud point, whereas the micellar radius, R_{mic} increases slightly (Fig. 2.6b), whereas the volume fraction of correlated micelles, ϕ, decreases slightly (Fig. 2.6c). The latter may be due to the fact that single micelles are released from loose aggregates of micelles. No change of the radii is observed at the gel point. Above the cloud point, R_{HS} continues decreasing, whereas R_{mic} slightly decreases and ϕ increases strongly.

We conclude that the SAXS curves of PS_8-$PMDEGA_{452}$-PS_8 can be described by a model including spherical micelles with liquid-like correlation and a loose corona consisting of a solvent-swollen polymer matrix. Interestingly, discontinuities are neither observed at the gel point nor at the cloud point. The distance between the micelles keeps decreasing smoothly. Only the correlation between micelles decreases slightly below the cloud point, while it increases above. This makes an important difference of the thermo-responsive BAB triblock copolymer systems containing PMDEGA as switchable inner A block compared to the analogous system based on PNIPAM, which is widely used as model for thermo-responsive systems.

In this series of new amphiphilic symmetrical triblock copolymers BAB, based on PMDEGA as block A and bearing two short hydrophobic PS outer blocks B, which still allow direct dissolution in water, the behavior of the triblock copolymers is found to be dominated by the length of the thermo-responsive inner block. Two thermal transitions are observed, namely from gel to liquid at temperatures well below the cloud point, and from sol to phase separated liquid at the cloud point. This makes a marked difference to the behavior of analogous triblock copolymers containing PNIPAM as thermo-responsive inner block, for which gelling can be induced by heating close to the phase transition temperature. This exemplifies the importance of the chemical nature of the thermo-responsive block for controlling not only the phase transition temperature, but also the polymer-polymer interactions in the amphiphilic copolymers. The unusual temperature dependence of the hydrogels seems to be due to a decreasing number of micelle-bridging polymers. Though polystyrene is commonly believed to build kinetically frozen glassy micelle cores, the short PS_8 blocks studied seem to represent a good compromise for already providing sufficient hydrophobicity while still maintaining a certain mobility in aqueous self-organization.

This work is funded by DFG within the priority program "Intelligente Hydrogele".

[1] A. Miasnikova, A. Laschewsky, G. De Paoli, C. M. Papadakis, P. Müller-Buschbaum, S. S. Funari, *Langmuir* **28**, 4479 - 4490 (2012)

2.4 Swelling behavior of novel thermo-responsive poly(styrene-*b*-monomethoxydiethylenglycol-acrylate-*b*-styrene) thin films probed by in-situ neutron reflectivity

Q. Zhong, E. Metwalli, M. Rawolle, C. M. Papadakis, A. M. Bivigou Koumba[1],
A. Laschewsky[1], R. Cubitt[2], P. Müller-Buschbaum

[1] Universität Potsdam, Potsdam-Golm, Germany
[2] ILL, Grenoble, France

Thermo-responsive hydrogels are three-dimensional networks of polymer chains that swell, but do not dissolve in water. Under an external thermal stimulus, these hydrogels can switch between an extended and a collapsed chain conformation, thereby exhibiting a strong change in volume.[1] In case of a thin film geometry, such a collapse transition with a lower critical solution temperature (LCST) behavior will induce a change in film thickness, which is interesting for applications as nano-switches or nano-sensors. A novel thermo-responsive poly(monomethoxy diethyleneglycol acrylate) (PMDEGA) exhibits a higher LCST (39 °C) when compared to the frequently investigated thermo-responsive polymer poly(N-isopropylacrylamide) (PNIPAM). Thus PMDEGA can be an interesting alternative to PNIPAM in tropical countries where the mean temperature is already above the LCST of PNIPAM (32 °C). In order to self-assemble thermo-responsive micelles in the solutions, both ends of PMDEGA are hydrophobically modified with polystyrene end-blocks giving rise to a triblock copolymer. In our investigation, P(S-*b*-MDEGA-*b*-S) is used to prepare thin films by spin-coating out of a 1,4-dioxane solution. The micellar structure in the solution is installed in the film, and forms interesting internal layer structures.

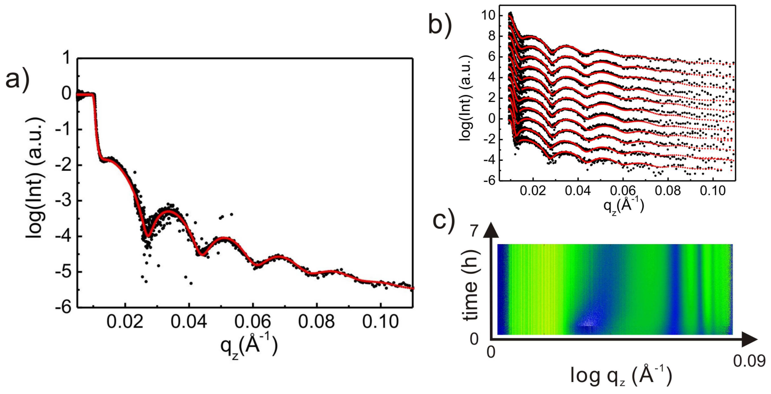

Figure 2.7:
(a) A neutron reflectivity curve (dots) together with the model fit (solid line) for the initially dry P(S-*b*-MDEGA-*b*-S)) film. (b) selection of eleven neutron reflectivity curves (dots) together with the model fit (solid lines). (c) two dimensional intensity presentation (mapping) of the neutron reflectivity as a function of time.

To investigate the swelling behavior of P(S-*b*-MDEGA-*b*-S) films in a vapor atmosphere, in-situ neutron reflectivity is performed at D17 (ILL Grenoble) in the time-of-flight (TOF) mode. Fig. 2.7a shows a neutron reflectivity curve (dots) together with the model fit (solid line) for a initially dry P(S-*b*-MDEGA-*b*-S)) film. A four-layer model is used for the fitting, resulting in a total film thickness of 39.4 nm. For a swelling experiment, 8 mL D_2O is injected into the cell and the hydrogel film starts to swell in a moderate vapor atmosphere.

The swelling behavior is followed with a time resolution of 20 s for a full neutron reflectivity curve. In order to determine the thickness and density profile during the film swelling, the individual neutron reflectivity curves are fitted with the model mentioned before. Fig. 2.7b shows a selection of eleven neutron reflectivity curves (dots) together with the model fit (solid lines). The intensity oscillations show no pronounced shift with respect to the scattering vector component q_z, revealing that the film thickness keeps constant. This is better seen in a two dimensional intensity presentation (mapping) as a function of time (Fig. 2.7c). In contrast to the maxima in the intensity modulation, the position of the critical edge shifts towards larger value of q_z and the overall scattering intensity increases with time in Fig. 2.7c. Both observations indicate that the film absorbs D_2O vapor.

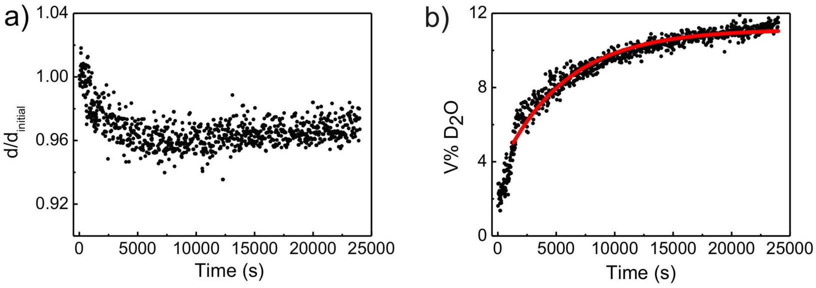

Figure 2.8:
(The relative film thickness d/d_{initial} (a) and D_2O volume fraction (V%D_2O) (b) as a function of time during swelling. The solid line is the fitting by the model mentioned in text.)

From the density profile obtained from fitting of the reflectivity data the D_2O volume fraction (V%D_2O) is calculated. Fig. 2.8 presents the relative film thickness d/d_{initial} and D_2O volume fraction (V%D_2O) as a function of time. The whole swelling process can be divided into two stages. In the first stage, from 0 s (D_2O is injected into the reservoir) to 2000 s, the film shrinks from 39.4 nm to 37.8 nm. During this shrinkage the value of V%D_2O increases dramatically from 0 to 6%. Obviously the P(S-*b*-MDEGA-*b*-S) film can absorb water while the film does not swell but reduces in total film thickness. When the thin film is exposed to the D_2O vapor atmosphere, vapor enters into the film immediately. As the film has been prepared with spin-coating, the polymer chains are in a non-equilibrium state after preparation. The absorbed vapor introduces a mobility of the chains. The chains can rearrange themselves, resulting in a total film thickness to decrease. In the second stage, from 2000 s to 24000 s, as PMDEGA is soluble in D_2O, the PMDEGA chains absorb water, both of the film thickness and water content increase with time. This second stage can be described by a model from Li and Tanaka.[2] The final film thickness is 38.2 nm, which is still 3% thinner than the initially dry film. This unusual behavior might be attributed to two reasons. First of all, the vapor atmosphere in the cell is undersaturated, which limits the amount of absorbed water. Second, the PMDEGA chains are hydrophobic modified by the PS blocks, which will hinder the swelling of the film.

In summary, in-situ neutron reflectivity is a very useful method to probe the swelling behavior of hydrogel films such as the investigated triblock copolymer P(S-*b*-MDEGA-*b*-S) film. In comparison with a PMDEGA homopolymer the observed water uptake is significantly different. In contrast to the expected film swelling, which implies an increase in film thickness, the total film thickness is reduced by the uptake of water.

[1] M. J. Snowden, M. J. Murray, B. Z. Chowdry, *Chem. Ind.* **15**, 531-534 (1996)

[2] Y. Li, T. J. Tanaka, *Chem. Phys.* **92**, 1365-1371 (1990)

2.5 Interface correlation in thin PNIPAM films

M. Philipp, D. Magerl, J. Perlich[1], P. Müller-Buschbaum

[1] HASYLAB at DESY, Hamburg

The miniaturization occurring e.g. in microelectronics provokes the need for increasingly thin protective coatings. The thinner the coatings are, the more relevant becomes their surface roughness as compared to the average layer thickness. This phenomenon is expected to be one reason for failure of thin dielectric polymeric films, which purpose is to act as insulating layers. Hence the understanding of the basic reasons leading to surface roughness of thin polymer films is not only of general scientific interest, but also of technological relevance.

Spin-coating is a widely used technique that can lead to films with very uniform thickness and small surface roughness (below one nanometer) deposited on solid substrates. The quality of the films depends amongst others on the used solvent, the angular velocity of the spinning disk, temperature and humidity conditions [1]. Typically films with thicknesses ranging from some nanometers up to a few microns can be realized by spin-coating.

For very smooth polymer films a roughness correlation between the silicon substrate and the polymer surface at the film/air interface may be observed. This effect has so far only be noticed for a few amorphous polymeric films, based e.g. on polystyrene [2] and for smectic films. In case of interface correlation, part of the roughness spectrum of the substrate is replicated by that of the upper surface of the polymer film. As a consequence, the resulting in-plane morphology of the polymer layer strongly depends on the underlying one. The smallest replicable in-plane length scale R_c, which is defined by the transition from a correlated to a statistically independent roughness spectrum of both film interfaces, permits to quantify the degree of interface correlation. Using grazing incidence small angle X-ray scattering (GISAXS), the smallest replicable in-plane length scale R_c was shown to depend on the polymer composition, on the film thickness d, and on thermal annealing (see [2] and ref. therein). The obtained scaling laws concerning $R_c(d)$ raised the question whether the state of interface correlation achieved after spin-coating consequences from a frozen morphology dominated by the capillary waves present in the liquid film during spin-coating. It was evidenced that the interface correlation vanishes during thermal annealing of a brominated polystyrene film above its glass transition temperature [2].

The aim of the present study is to investigate correlated roughness for poly(N-isopropyl acrylamide) (PNIPAM) homopolymer and P(S-b-NIPAM-b-S) block copolymer films produced by spin-coating. The focus of these studies lies on the dependence of the interface correlation on film thickness of the respective polymer layers and the underlying reasons responsible for correlated roughness. All films are deposited either on silicon wafers or on glass slides. During sample preparation first the substrates are treated in three chemical baths according to a basic cleaning protocol in order to achieve reproducible surface properties of the substrate. The PNIPAM homopolymer (M_n = 20.5 kg/mol and PDI = 1.23) was purchased from PSS, Mainz. As mentioned above, the solvent used for spin-coating codetermines the resulting morphology and homogeneity of the spun film. It could be shown that much more homogeneous and smooth PNIPAM films are produced while using a chloroform solution of PNIPAM as compared to ethanol, methanol or acetone solutions. For both type of polymers, films with seven different thicknesses ranging from 10 nm up to about 200 nm are prepared on silicon substrates. PNIPAM films with six different thicknesses between 15 and 200 nm are spin-coated on glass slides.

The GISAXS investigations of the interface correlation were performed at BW4, HASYLAB at DESY, Hamburg using an angle of incidence α_i = 0.5°, an X-ray wavelength λ = 0.138 nm and a sample-detector-distance of 2116 mm. In Fig. 2.9a) the GISAXS picture of a 55 nm thin PNIPAM homopolymer film deposited on glass is exemplarily shown. In case of partially or fully correlated roughness, intensity streaks of resonant diffuse scattering are expected that are oriented parallel to the q_x axis [2]. This is in fact responsible for the pronounced modulation of intensity in the detector scan of the PNIPAM film. The spacing of these fringes $\Delta q_z = \frac{2\pi}{d_{corr}}$ allows for estimating the distance between the correlated interfaces, which indeed coincides with the film thickness of 55 nm determined by X-ray reflectivity.

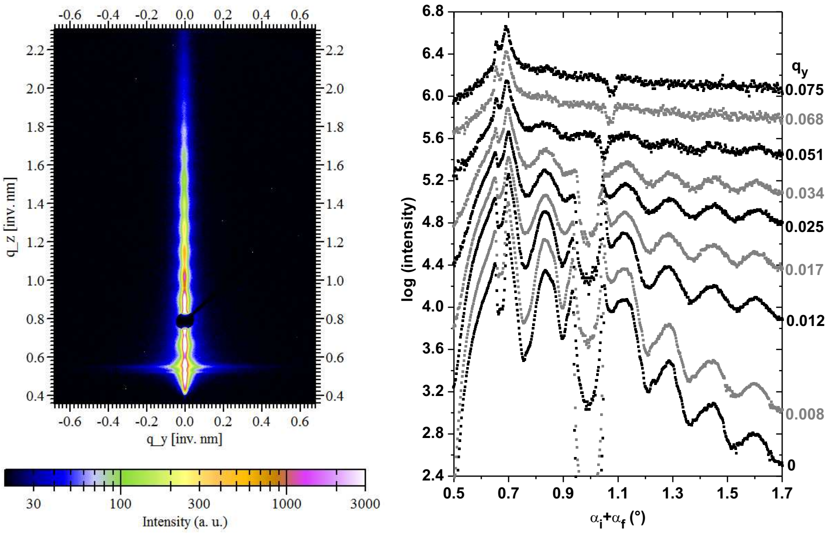

a) b)

Figure 2.9:
a) GISAXS image of a 55 nm thin PNIPAM film deposited on glass. b) Off-detector cuts determined for nine different q_y values (given in nm^{-1}).

In Fig. 2.9b) off-detector cuts are shown. These cuts are calculated from the GISAXS data by summing in q_y-direction over three pixels for each off-detector cut. The cuts permit to determine the smallest replicable in-plane length scale R_c, given by $R_c = \frac{2\pi}{q_{yc}}$. q_{yc} describes that wavenumber q_y for which in the corresponding off-detector cut the intensity modulation based on the resonant diffuse scattering fringes is totally lost. The upper curve of Fig. 2.9b) shows that in case of the 55 nm thin PNIPAM homopolymer q_c = 0.075 nm^{-1}. The information transfer concerning the roughness spectrum between both film interfaces over distances far larger than the intrinsic molecular distances, like the radius of gyration of the polymers (which is estimated to be smaller than 3 nm) is striking. It is speculated whether this information transfer is provoked by the eigenmodes of the spectrum of guided acoustic waves propagating within the still liquid film, as present during spin-coating. This could be the reason why the capillary waves, which are part of the eigenmodes of the liquid film, may contain information about the substrate roughness.

M.P. thanks the Fonds national de la Recherche (Luxembourg) for receiving a Marie Curie cofunded AFR Postdoc grant.

[1] C. J. Lawrence, *Phys. Fluids* **31**, 2786-2795 (1988)

[2] P. Müller-Buschbaum, J. S. Gutmann, C. Lorenz, T. Schmitt, M. Stamm, *Macromolecules* **31**, 9265-9272 (1998)

2.6 Interface correlation in cyclic poly(N-isopropylacrylamide) thin films

D. Magerl, M. Philipp, M. Rawolle, G. Herzog[1], X.-P. Qiu[2], F. M. Winnik[2], S. V. Roth[1], P. Müller-Buschbaum

[1] HASYLAB at DESY, Hamburg, Germany
[2] Université de Montréal, Faculty of Pharmacy and Depatment of Chemistry, Montréal, Canada

In recent years the investigation of thermoresponsive hydrogels has become increasingly popular. Hydrogels are chemically or physically cross-linked polymers that have the capability of attaching large amounts of water molecules to the polymer chain and therefore drastically increase their volume. The special class of thermoresponsive hydrogels gains/looses this capability upon heating/cooling. Poly(N-isopropylacrylamide) (PNIPAM) is a promising candidate in this field and widely studied. An even more specialized class of polymers is that of cyclic polymers, which do not consist of a linear chain but are closed to form a ring structure and therefore lack end-groups. So far studies focus on solutions of cyclic PNIPAM [1] whereas we are interested in its behavior in a thin film geometry. To achieve such thin films the spin coating technique is used. Because we work with initially dry films we are not dependent on water as our solvent. Therefore films are spin cast from chloroform solutions which results in very smooth films of film thickness from 20 nm to 300 nm, depending on the concentration used during spin coating.

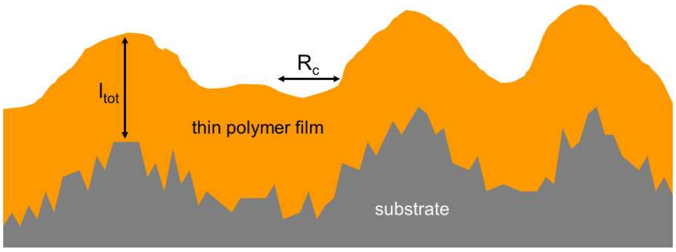

Figure 2.10:
Sketch of interface correlation: Roughness on large scale is replicated by the film of thickness l_{tot}. On small scales, below the critical length scale R_c, it is not replicated.

Typically thin films of PNIPAM can be analyzed for their thermal switching behavior in presence of a humid atmosphere [2]. In our case we are interested in a more fundamental understanding of the state of the film after spin coating without the presence of humid air. Thus we are investigating the interface correlation between the film surface and the interface substrate/polymer. On the one hand large length scales the roughness of the substrate is perfectly replicated by the thin film surface. On the other hand on small length scales the film cannot follow the roughness of the substrate as depicted in Fig. 2.10. Such behavior can be easily visualized in real life with snow covering a lawn. In this picture, the general shape of the ground like small hills are replicated by the snow, but the small structure like blades of grass are not replicated. Thus there is a critical length scale R_c at which the correlation starts. Above R_c the two interfaces are correlated, below they are not. R_c is a function of thickness and from the form of this relationship it information about the interaction between the thin film surface and the substrate can be deduced.

For the detection of such interface correlation grazing incidence small-angle X-ray scattering (GISAXS) has proven to be well suited. [3] In this set-up the film is illuminated under a very shallow angle (i.e. below 1°) and the scattered intensity is recorded in reflection geometry on a 2D-detector, typically in a distance of a few meters. The very shallow angle of incidence increases the probed volume drastically and gives access to structures parallel to the sample surface that would be hidden in conventional SAXS experiment. The GISAXS measurements are performed at the new MiNAXS beamline at the PETRAIII storage ring at HASYLAB, Hamburg. A typical 2D-detector image is shown in Fig. 2.11a. The horizontal and the vertical axis show the y-component and z-component of the scattering vector $\vec{q}$, respectively. Films with a thickness in the accessible range of the GISAXS set-up show a modulation of the intensity along the q_z-axis at $q_y = 0$ due to the presence of correlated roughness. These modulations extend to higher q_y values corresponding to the length scales that can be replicated by the film surface and can therefore be seen in cuts in q_z direction that are at $q_y > 0$. Correspondingly, the critical length scale R_c is determined from the cut along the q_z-axis that is not correlated to the cut next to it (the distance of the cuts is limited by the pixel size of the detector) and therefore the interface correlation is lost. A representation of multiple cuts shifted against each other is shown in Fig. 2.11b.

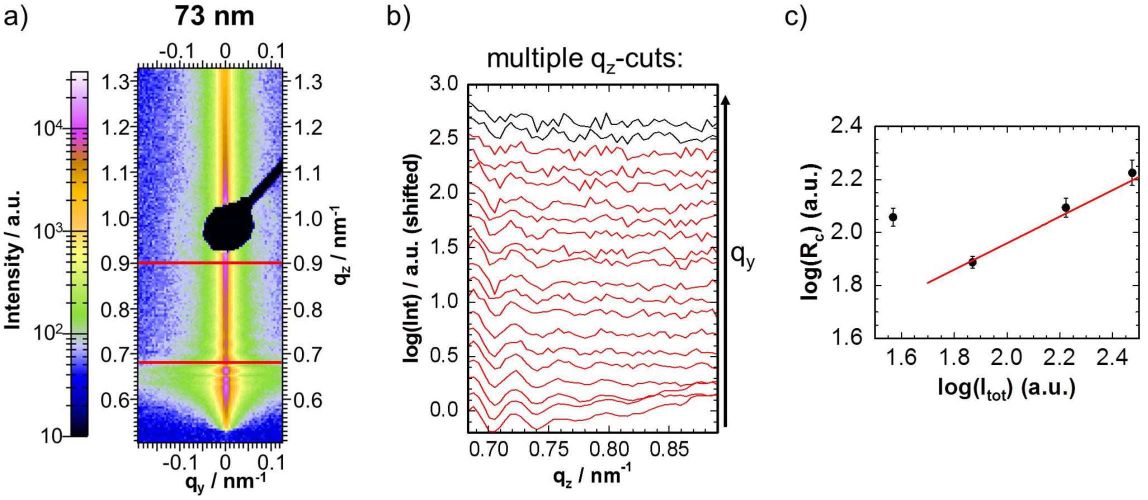

Figure 2.11:
a) Zoom-in of the 2D scattering image of a thin film of PNIPAM with 73 nm thickness. The marked area is the region that is investigated for interface correlation (see b). b) Multiple cuts along the q_z-axis at increasing q_y positions from bottom to top, the cuts that show correlation are marked. c) Plot of critical length scale R_c against the total film thickness l_{tot} on a double logarithmic scale. The shown linear fit excludes the left most point.

Previous studies have shown that depending on the underlying interaction the critical length R_c increases with the total film thickness l_{tot} following different power laws [3]. Thus R_c as function of l_{tot} is shown in a double logarithmic plot in Fig. 2.11c. Excluding the data point for the smallest film thickness, a line can be fitted to the data with a slope of 0.5. This power law corresponds to a frozen-in liquid morphology which shows that the hydrogel film is still in a state like shortly after spin coating and not dominated by the interaction of the molecules with the surface as it would be after annealing (e.g. due to water in the ambient air). The behavior of the sample with the smallest film thicknesses is unexpected and not yet explained. Earlier investigations on other polymers such as polystyrene had not shown such deviation from power laws. [3] For a more detailed examination more data are needed. Therefore the measurements will be extended towards more thicknesses to get a better understanding of complex behavior of cyclic PNIPAM films.

[1] X.-P. Qiu, F. Tanaka, F. M. Winnik, *Macromolecules* **40**, 7069-7071 (2007)

[2] W. Wang, E. Metwalli, J. Perlich, C. M. Papadakis, R. Cubitt, P. Müller-Buschbaum *Macromolecules* **42**, 9041-9051 (2009)

[3] P. Müller-Buschbaum, J. S. Gutmann, C. Lorenz, T. Schmitt, M. Stamm, *Macromolecules* **31**, 9265-9272 (1998)

2.7 In-situ thickness measurement of thermoresponsive hydrogel thin films with white light interferometry

E. Kopperger, D. Magerl, P. Müller-Buschbaum

Hydrogels are chemically or physically cross-linked polymers that build-up networks in which large amounts of water, i.e. more than the volume of the polymer, are stored. In thermoresponsive hydrogels this property is linked to the temperature in a way that the amount of stored water is controlled by the temperature. A promising and frequently investigated candidate of thermoresponsive hydrogels is poly(N-isopropylarylamide) (PNIPAM), which exhibits a lower critical solution temperature (LCST) at around 32° C. As a consequence, the polymer can store water below its transition temperature and precipitates from water at higher temperatures as shown in fig. 2.12a. In general, these thermoresponsive hydrogels with transition temperatures in the regime of the human body temperature are of particular interest because they are candidates for drug delivery systems and sensors. Studies on the thermoresponsive switching of hydrogels have been popular in recent years [1]. Those studies mostly concentrate on the behavior of the polymer when dissolved (diluted) in water.

In our work, we are interested in thin films of PNIPAM and the swelling of these films when exposed to humid air as also shown by W. Wang et al. [2,3]. As compared with volume samples, the thin film geometry reduces the degree of freedom to one dimension (see fig. 2.12b). To specify the swelling of such hydrogel films, accurate, fast and non-destructive measurements of the thickness are needed.

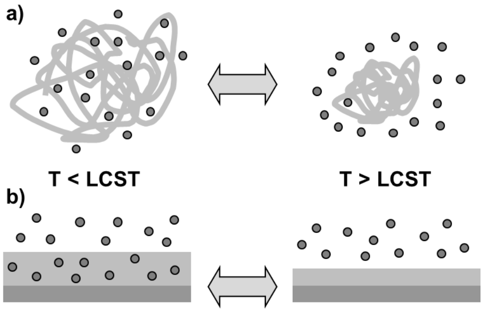

Figure 2.12:
Thermoresponsive switching from below to above the LCST. a) in dilute solutions polymer coils are separated and expand by attaching water to the chain. When the LCST is crossed the chain collapsed and releases the bound water. b) In thin films the expansion parallel the surface is hindered and expansion and contraction can only occur along the surface normal. This leads to pronounced changes in film thickness.

To fulfill all the experimental requirements a small sample chamber is used which is tightly sealed. A sketch of the whole set-up is shown in fig. 2.13. The sample is held on a small elevated platform surrounded by a channel that can be filled with liquid, e.g., water. Through evaporation of the water in the channel an under-saturated atmosphere is generated within the chamber in which the hydrogel film accordingly swells. The chamber is temperature controlled by a thermostated bath that pumps liquid through small channels in the upper and lower plate of the chamber. The measurement of the thickness is conducted by white light interferometry through a small window in the top cover of the chamber. The reflected light is captured at the same position as the light is emitted and then transferred to the detector, where the spectrum of the reflected light is recorded.

White light interferometry uses the interference of reflected light on the sample surface and the substrate to calculate the thickness and optical properties of the sample. Therefore, the sample is illuminated by light with a broad wavelength distribution (in our case 200-1100 nm) perpendicularly to the sample surface. The light is generated by a regulated deuterium and tungsten halogen lamp and is lead to the sample by a fiber optic cable. The reflection is also captured by such a cable and its intensity is then detected in a wavelength sensitive detector. The reflected light from the sample surface and the interface sample/substrate interfere with each other and increase or reduce the intensity for a certain wavelength. From this measurement a

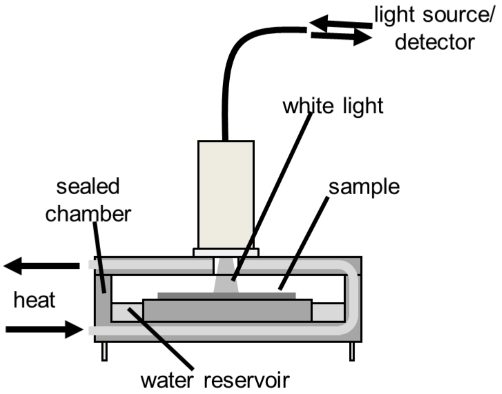

Figure 2.13:
Sketch of the experimental set-up used to measure swelling of hydrogel films. The sealed chamber is temperature controlled via small channels in the top and bottom part. Thickness measurement is conducted with white light interferometry through a glass window on the top side of the chamber.

reflectance spectrum as shown for example in fig. 2.14a is obtained. From a fit to the spectrum it is possible to get the film thickness as well as information about roughness and non-uniformity of the film.

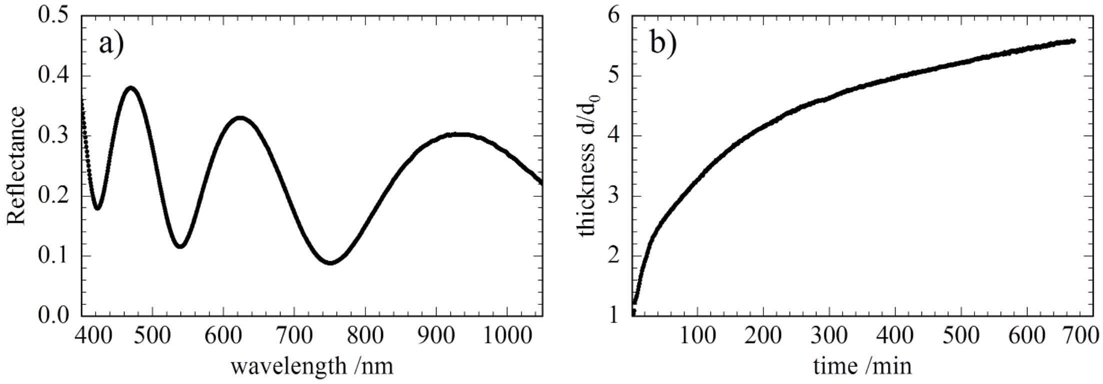

Figure 2.14:
a) Sample spectrum obtained from a white light interferometry measurement of a PNIPAM film swollen to about 680 nm in water vapor. b) Relative thickness change d/d_0 with time upon exposure to water vapor. Initial film thickness d_0 is about 140 nm.

The total optical pathlength in the thin film is $2nd$, where n and d denote the refractive index and film thickness, respectively. The factor 2 arises because the light traverses the film twice, due to the reflection off the substrate surface. The condition for constructive interference is fulfilled when the optical pathlength is equal to a multiple of the wavelength ($2nd = i\lambda$). From this equation the general distance between two maxima follows the equation $\lambda_1^{-1} - \lambda_2^{-1} = (2nd)^{-1}$ and from this the film thickness can be deduced.

An example of the swelling of an PNIPAM thin film with an initial thickness of around 140 nm is shown in fig. 2.14b. Shown is the relative thickness change with time. It is clearly seen that the film increases its thickness and therefore its volume by a factor of about 5. In our future investigations films of different film thicknesses will be investigated and for each film the swelling behavior at a given temperature as well as the change upon temperature variation will be studied.

[1] V. Aseyev, H. Tenhu, F. M. Winnik, *Adv. Polym. Sci.* **242**, 29-89 (2011)

[2] W. Wang, E. Metwalli, J. Perlich, C. M. Papadakis, R. Cubitt, P. Müller-Buschbaum, *Macromolecules* **42**, 9041-9051 (2009)

[3] W. Wang, G. Kaune, J. Perlich, C. M. Papadakis, A. M. Bivigou Koumba, A. Laschewsky, K. Schlage, R. Röhlsberger, S. V. Roth, R. Cubitt, P. Müller-Buschbaum *Macromolecules* **43**, 2444-2452 (2010)

2.8 Cononsolvency of P(S-*b*-NIPAM) diblock copolymers in aqueous solution

K. Kyriakos, M. Philipp, J. Adelsberger, S. Jaksch, A. Miasnikova[1], A. Laschewsky[1], I. Grillo[2], P. Müller-Buschbaum, C.M. Papadakis

[1] Institut für Chemie, Universität Potsdam
[2] ILL, Grenoble, France

Poly N-isopropylacrylamide (PNIPAM) and its thermoresponsive behavior in aqueous solutions have been widely studied. In water, this polymer exhibits lower critical solution temperature (LCST) behavior with T_c = 32 °C. When heated above T_c, the PNIPAM chains release the bound water and collapse, which results in a very sharp coil-to-globule transition. Interestingly, T_c is almost independent of the degree of polymerization and the polymer concentration (up to 20 wt.%). This behavior is attributed to the balance between hydration of the chains and aggregation of *iso*-propyl groups. Recently, strong interest has arisen in the PNIPAM chain conformation in water upon addition of a second, water-miscible solvent, e.g. methanol. Although both water and methanol are good solvents for PNIPAM, the addition of the latter induces a phase separation and decreases T_c. This enhanced phase separation is known as cononsolvency [1].

We investigate diblock copolymers having a long PNIPAM block and a short, hydrophobic polystyrene (PS) block. In aqueous solution, they form flower-like core-shell micelles and, when heated above T_c, the micellar PNIPAM shell undergoes a sharp and reversible collapse [2]. We investigated the conformational changes occurring upon addition of methanol. Fully deuterated methanol (*d*-MeOH) was added in various mixing ratios (90:10, 85:15 and 80:20 vol.% D2O/ *d* -MeOH) to a solution of P(S-*b*-NIPAM) in D_2O (20 mg/ml). T_c was found to decrease with increasing *d*-MeOH content. To elucidate the kinetics of the collapse of the micellar shell and the subsequent aggregation of the collapsed micelles, *d*-MeOH was added to solutions of P(S-*b*-NIPAM) in D_2O (20 mg/ml) using a stopped-flow cell (Biologic SFM-300, dead time 0.25 ms), and the changes were followed using time-resolved small-angle neutron scattering (SANS) at the high flux small-angle neutron scattering instrument D22 at the Institut Laue-Langevin in Grenoble, France. The selected neutron wavelength was λ = 8 Å and the sample-to-detector distances (SDD) 4 m and 14.4 m.

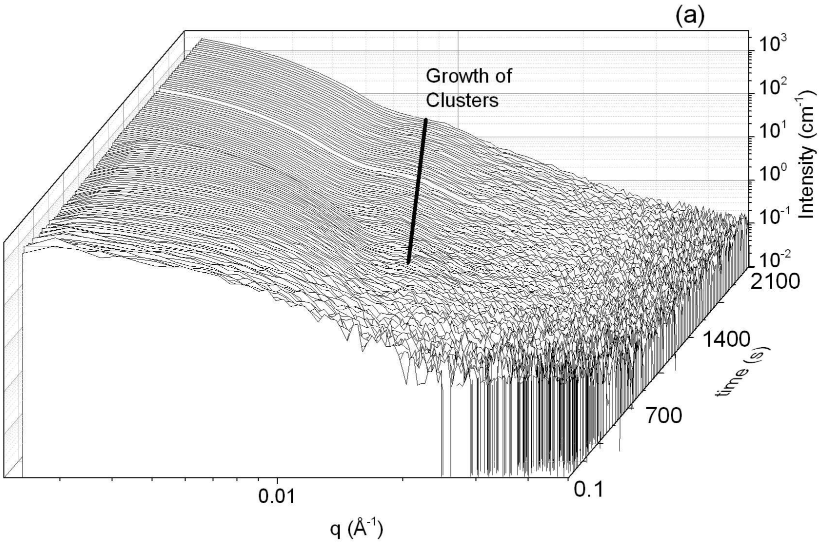

Figure 2.15: Time-series of SANS curves for a mixing ratio 80:20.

Figure 2.15 shows a series of SANS curves for the mixing ratio of 80:20. With time, the fringe of the form factor of the clusters moves to lower q values, i.e. the size of the spheres increases. The curves are well described by a form factor of polydisperse spheres with their radius having a Gaussian distribution (Fig. 2.16). The mean radii of the particles during the whole time range increase from 15 nm to 49 nm and keep growing (Fig. 2.17). This large size points to the fact that we observe aggregates of collapsed micelles. The aggregation process continues even 35 min after the addition of co-nonsolvent. Investigations of the earlier time range are underway.

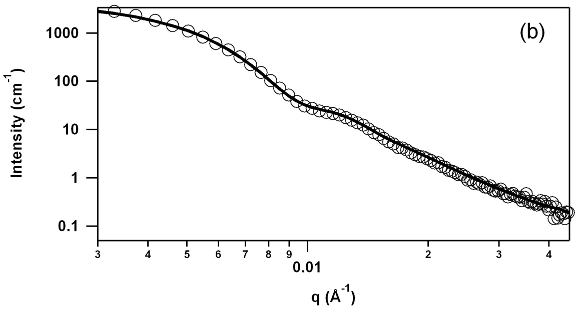

Figure 2.16:
Fit of the form factor of polydisperse spheres for a selected time (300 s). Circles: experimental data, line: fitting curve.

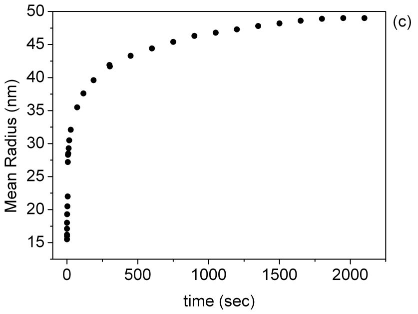

Figure 2.17:
Resulting mean cluster radius for selected time frames over the whole measure time range.

To summarize, the presented results of the behavior of the diblock P(S-*b*-NIPAM) in various mixing ratios of two competing solvents (D_2O and *d*-MeOH) show the presence of aggregates of collapsed micelles which form after the addition of the cononsolvent *d*-MeOH and their slow growth. The aggregation behavior follows a different pathway than the one observed by us previously in aqueous solutions of P(S-*b*-NIPAM-*b*-S) which is rapidly heated through T_c [4]. The project is supported by DFG within the priority program SPP1259 (Intelligente Hydrogele).

[1] F. Tanaka, T. Koga, H. Kojima, N. Xue, F. Winnik, *Macromolecules* **44**, 2978-2989 (2011)

[2] K. Troll, A. Kulkarni, W. Wang, C. Darko, A. M. Bivigou-Koumba, A. Laschewsky, P. Müller-Buschbaum C. M. Papadakis, *Colloid Polym. Sci.* **286**, 1079-1092 (2008)

[3] J. Adelsberger, A. Meier-Koll, A. M. Bivigou-Koumba, P. Busch, O. Holderer, T. Hellweg, A. Laschewsky, P. Müller-Buschbaum, C. M. Papadakis, *Colloid Polym. Sci.* **289**, 711-720 (2011)

[4] J. Adelsberger, E. Metwalli, A. Diethert, I. Grillo, A. M. Bivigou-Koumba, A. Laschewsky, P. Müller-Buschbaum, C.M. Papadakis, *Macromol. Rapid Commun.* **33**, 254-259 (2011)

2.9 Stimuli-responsive amphiphilic polyelectrolyte heptablock copolymer hydrogels: an unusual pH response

M.-T. Popescu[1,2], C. Tsitsilianis[1,2], C. M. Papadakis, J. Adelsberger, S. Balog[3], P. Busch[4], N. A. Hadjiantoniou[5], C. S. Patrickios[5]

[1] University of Patras, Greece
[2] Institute of Chemical Engineering and High Temperature Chemical Processes, Patras, Greece
[3] Paul-Scherrer-Institut, Villigen PSI, Switzerland
[4] Jülich Center for Neutron Science, Garching, Germany
[5] University of Cyprus, Nicosia

Amphiphilic block copolymers forming reversible hydrogels represent a very important class of polymeric materials with fascinating properties. At high concentration, a 3D transient network is formed, composed from hydrophobic nanodomains (physical crosslinks) interconnected by hydrophilic chains (elastic chains) imposing dramatic effects on the rheological properties of the solution. The considerable interest of these materials is due to their various applications as rheology modifiers, e.g. in cosmetics or as injectable hydrogels. One class of associative gelators is that of multiblock copolymers containing short hydrophobic and long polyelectrolyte blocks which may show remarkable rheo-thickening solution properties. We report here on a rheological and structural study of a heptablock copolymer $\mathrm{BuMA_5}$-*b*-$\mathrm{DMA_{25}}$-*b*-$\mathrm{BuMA_5}$-*b*-$\mathrm{DMA_{25}}$-*b*-$\mathrm{BuMA_5}$-*b*-$\mathrm{DMA_{25}}$-*b*-$\mathrm{BuMA_5}$ in aqueous media (Fig. 2.18a) where DMA is the ionisable poly[2-(dimethylamino)ethyl methacrylate] block and BuMA is the hydrophobic poly(*n*-butyl methacrylate) block [1]. A peculiar pH dependence of the rheological properties was observed, namely two soft gel – stiff gel – soft gel transitions around pH 4.5 and pH 6.5. Small-angle neutron scattering (SANS) was used to determine the microstructure of the gels at different pH.

The rheological measurements were carried out using stress controlled rheometers in cone and plate geometry (Rheometric Scientific SR 200 and AR-2000ex, TA Instruments). Solutions for small-angle neutron scattering (SANS) experiments were prepared in D_2O, and the pD was adjusted by adding deuterium chloride. The experiments were carried out using the SANS-II instrument at SINQ/PSI and the KWS 2 instrument of JCNS at FRM II.

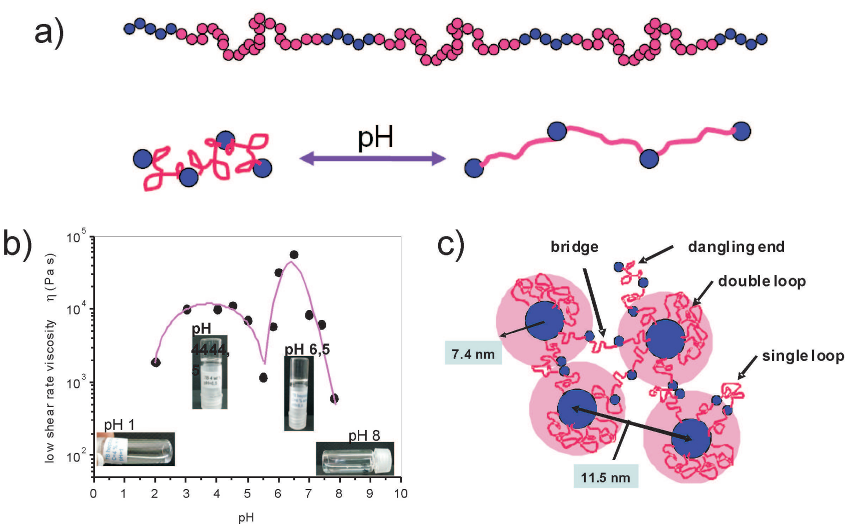

Figure 2.18:
(a) Schematic representation of the heptablock copolymer topology and its conformations in water at low (left) and high pH (right). (b) Low-shear viscosity as a function of pH of a 4 wt% solution at 25°C. (c) Structure resulting from SANS.

In concentration-dependent viscosity measurements as well as in tube inversion tests at pH 6 and 25°C, it was found that a gel is formed above 0.6 wt%, a remarkably low concentration.

Above, the viscosity rises steeply with concentration, and a free standing gel is formed above 3.5 wt%. As a function of pH, the low shear rate viscosity shows complex behavior with a sharp sol-gel transition around pH 1.5 and a gel-sol transition close to pH 8 (Fig. 2.18b). In the gel phase region, the viscosity exhibits two maxima at pH 4.5 and 6.5, revealing a stiff gel – soft gel – stiff gel transition.

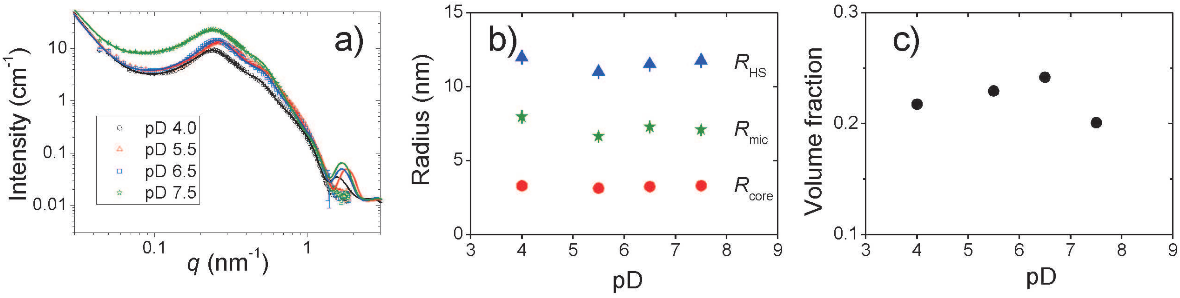

Figure 2.19:
(a) SANS curves of the heptablock copolymers at 4 wt% in D_2O at different pD values (symbols) together with model fits (lines). $T = 25°\mathrm{C}$. Resulting radii (b) and volume fractions of correlated micelles (c).

To understand the influence of pH on the viscoelastic properties of the hydrogels, SANS measurements were carried out at pD values between 4.0 and 7.5 in the gel-like region at 4 wt% (Fig. 2.19a). They reveal a correlation peak together with smeared oscillations at high q values and forward scattering at low q-values. We attribute the former to the liquid-like correlation between the bridged micelles and modelled the structure factor by a Percus-Yevick peak. The micelles were assumed to be spherical and of core-shell type. The forward scattering from large aggregates of bridged micelles was taken into account by a Porod term. Good fits were obtained. The resulting fitting parameters show that all radii display a minimum at pD 5.5 (Fig. 2.19b), implying that the aggregation number of the micelles and the distance between them exhibit a minimum which may be at the origin of the minimum in viscosity at this pH (Fig. 2.18b). The volume fraction of the correlated micelles is maximum at pD 6.5, thus the highest fraction of micelles is connected in aggregates at this pD which is at the origin of the relatively strong network. The network structure resulting from the SANS investigations is depicted in Fig. 2.18c. However, the SANS results do not reflect entirely the drastic changes of mechanical properties with pD. It seems that rearrangements of the number of bridges of the network and changes in their degree of stretching is the main reason for the pH dependent viscosity behavior. These rearrangements are not necessarily reflected in the SANS curves.

These studies provide insight into the factors governing the association towards a reversible hydrogel and its final properties, useful for the design of stimuli responsive hydrogelators. This kind of materials may find applications as injectable hydrogels since they exhibit a sol state at pH 8 and a gel state at physiological pH.

This work is funded by DFG within the priority program "Intelligente Hydrogele".

[1] M.-T. Popescu, C. Tsitsilianis, C. M. Papadakis, J. Adelsberger, S. Balog, P. Busch, N. A. Hadjiantoniou, C. S. Patrickios, *Macromolecules*, accepted

2.10 Influence of temperature on the film morphology of thin casein films

E. Metwalli, A. Diethert, J. Adelsberger, R. Cubitt[1], P. Müller-Buschbaum
[1] ILL, Grenoble, France

Casein, a family of phosphoproteins, is one of the major milk proteins. Four main types of proteins are involved: α_{1s}-casein (38 %), α_{2s}-casein (10 %), β-casein (36 %) and κ-casein (13%). The casein micelle is a nano-biocolloid. The hydrated casein micelles are about 100 nm in size [1]. Casein micelles efficiently transport calcium and phosphates from the mammary gland to the neonate. Due to their binding ability, casein micelles for non-food applications include coatings, adhesives, paints, textile fabrics and cosmetics. As an adhesive for modern labeling of glass containers, casein has proved a superior mechanical and thermal stability. Additionally, as we experience from daily-live, the casein-based bottle labels are stable and can sustain temperatures range as low as 2 °C up to 40 °C at different humidity. Various models are proposed for casein micelle structure including coat-core, sub-micelles, and the internal structure. The coat-core model describes the micelle as an aggregate of casein proteins with inner hydrophobic layer different from the outer layer. Casein micelles in a thin film geometry have been intensively investigated in our lab [2-4]. Using the GISANS technique and introducing D_2O vapor, we have recently [2] probed the kinetics of water uptake at 30 °C and detailed the structure of the protein film. We showed that two objects of spherical shape but different sizes, which were identified as mini-micelles ($R \leq 20$ nm) and micelles ($R \approx 80$ nm), coexist in the protein film.

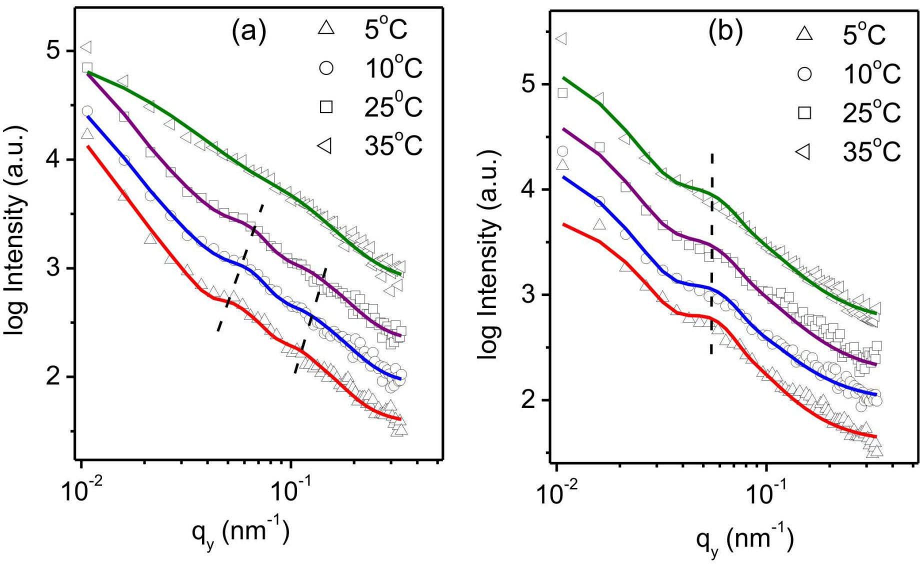

Figure 2.20:
The q_y line-cuts of the 2d GISANS pattern measured for samples prepared at different temperatures for both fresh (a) and 100 days aged (b) films. The lines are the best fits using the IsGISAXS program based on a model as explained in the text.

Here, we report on a GISANS investigation for films prepared out of casein solutions which are equilibrated at different temperatures from as low as 2 °C up to 35 °C. The same set of samples is prepared and aged for about 100 days at room temperature. The GISANS measurements aim to explore the aging effect on the morphology of the casein micelles. In this study, casein micelles were extracted from commercial-grade skim milk using the microfiltration/ultrafilteration diafiltration process. The dry casein powder was then dissolved in D_2O (10 wt %) and spin coated [3] on a pre-cleaned glass substrates. Both the casein solutions and the pre-cleaned glass substrates are equilibrated at different temperatures of 2, 5, 10, 25 and 35 °C before the coating step.

The second set of samples are aged (for 100 days in air at room temperature) prior to the GISANS measurements. The GISANS experiments were performed on D22 beamline at the high-flux reactor of the Institut Laue-Langevin, Grenoble, France. A dry casein film format together with the surface sensitive technique GISANS is an interesting approach to probe the casein protein structure when compared with solution-based techniques such as SAXS or NMR. The q_y profiles for both fresh and aged samples at different temperatures are shown in Fig. 2.20. The fitting of the GISANS data was performed using the IsGISAXS software (which can be applied to GISANS as well) based on χ^2-minimization. Using a model of two spherical objects of different sizes we are able to fit the measurement. For all samples, casein micelles of sizes between 110-140 nm and mini-micelle of sizes 30-50 nm are obtained from these fits (Fig. 2.21). The result of different average micelle sizes, with large size distribution, is due to an aggregation behavior of the proteins at different temperatures. For the freshly prepared samples the average micelle size is increasing from about 110 to 140 nm with decreasing the temperature of the casein film preparation. The latter behavior is attributed to the decrease of the hydrophobic interaction in proteins at low temperatures. Weak hydrophobic interaction within the micelle creates more porous micelles that swell water and hence their radii become larger.

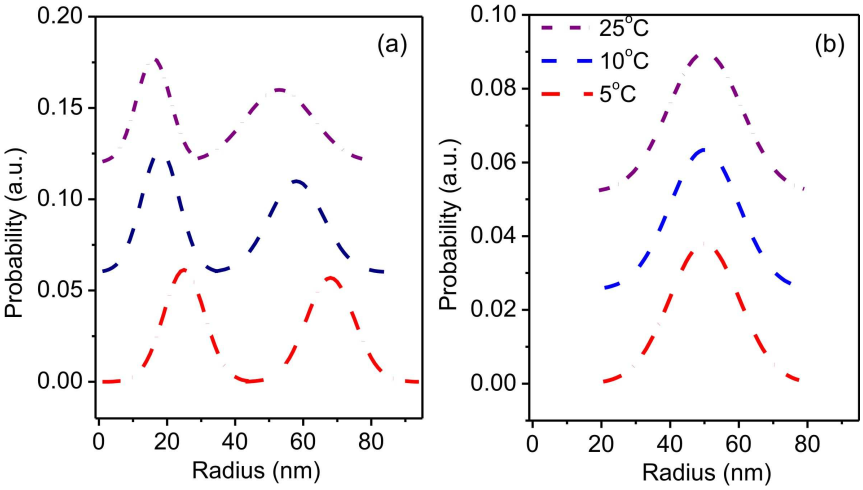

Figure 2.21:
Bimodal distribution of sizes for the fresh casein films (a), however unimodal size distribution for aged films (b) at all temperatures.

The samples aged in air at room temperature for 100 days, however, have introduced an interesting behavior that the micelles reorganize and equilibrate to a stable permanent film morphology expressed by the same film morphology of all samples that are prepared at temperatures lower than the room temperature (2, 5, 10 and 25 °C). The aged micellar films are fitted using a unimodal size distribution model. No bimodelsize distribution is needed. The continuous aggregation between hydrated micelles in the film to reach equilibrated structures (micelle size is about 100 nm) may explain high stability casein-based coatings and adhesive by the ability to adapt itself to varying external conditions.

[1] J.E. Kinsella , *CRC Crit. Rev. Food Sci.* **21**, 197 (1984)

[2] E. Metwalli, J.-F. Moulin, R. Gebhardt, A. Tolkach, U. Kulozik, P. Müller-Buschbaum, *Langmuir* **25**, 4142 (2009)

[3] P. Müller-Buschbaum, R. Gebhardt, S.V. Roth, E. Metwalli, W. Doster, *Biophys. J.* **93**, 960 (2007)

[4] R. Gebhardt, W. Holzmüller, Q. Zhong, P. Müller-Buschbaum, *J. Coll. Surf. B* **88**, 240 (2011)

3 Thin polymer films

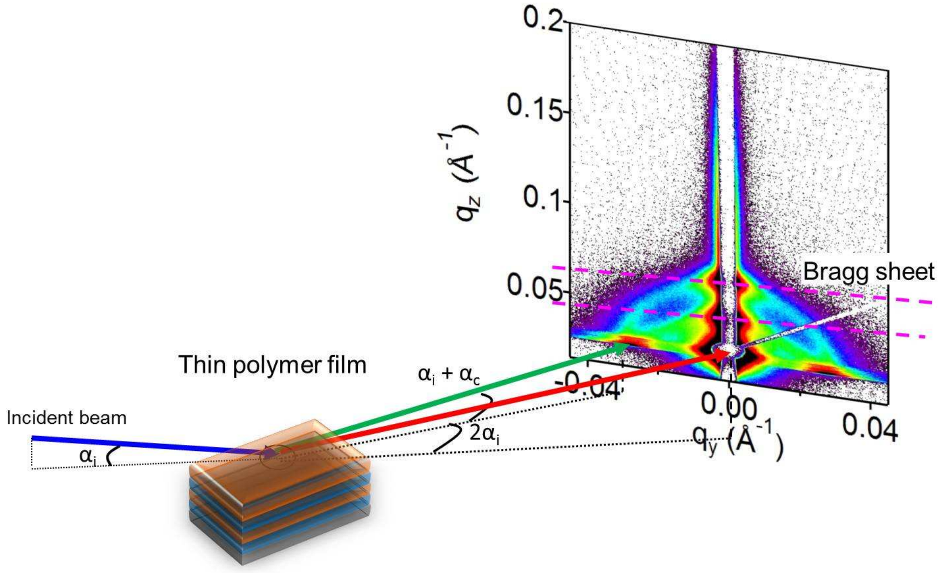

3.1 Structural evolution in diblock copolymer thin films with perpendicular lamellar structure during solvent vapor treatment

J. Zhang, A. Sepe, R. Steinacher, J. Perlich[1], D. Posselt[2], C.M. Papadakis

[1] HASYLAB at DESY, Hamburg, Germany
[2] Department of Science, Systems and Models, Roskilde University, Denmark

Well-ordered structures formed by self-assembly of diblock copolymer have attracted increasing interest due to their potential applications, such as the preparation of nanoporous films, nanostructured templates, ultrahigh-density data storage media, and biosensors [1]. However, the thin film preparation by solvent-casting or spin-coating does not necessarily lead to the equilibrium structure. Often, only short-ranged order is observed in the self-assembled structures, which hampers many applications. Methods to bring the samples into their equilibrium states and to reduce the number of defects are thus highly desirable. Vapor treatment with solvents is a commonly used technique to anneal defects in block copolymer thin films. The solvent vapor swells the film and effectively lowers the glass transition temperature (T_g) of blocks; meanwhile it affects the interactions between blocks (χ_{eff}) and the relative volume fractions. The mentioned parameters all depend on the selectivity of the solvent [2].
In the present work, thin films of lamellar poly(styrene-*b*-butadiene) (P(S-*b*-B)) diblock copolymers having a molar mass of 216 kg/mol were studied to elucidate the mechanisms of structural changes induced by solvent vapor treatment. As in our previous studies, the thin films feature perpendicular lamellae with respect to the substrate [3]. Cyclohexane (CHX) which is slightly selective for the PB block was used to treat films with three different initial thicknesses. In addition to ex-situ atomic force microscopy (AFM) to investigate the film surfaces, time-resolved in-situ grazing-incidence small-angle X-ray scattering (GISAXS) at beamline BW4, HASYLAB at DESY, together with VIS interferometry were used. The time resolutions of GISAXS and VIS interferometry are 30 s and 1 s, respectively. This way, changes of the inner film thickness structure as well as the degree of film swelling could be monitored. 120 s after the GISAXS and VIS measurements were started, solvent vapor was let into the cell via a bubbler. After 2500 s, the film was slowly dried by letting dry N_2 gas stream slowly into the cell.

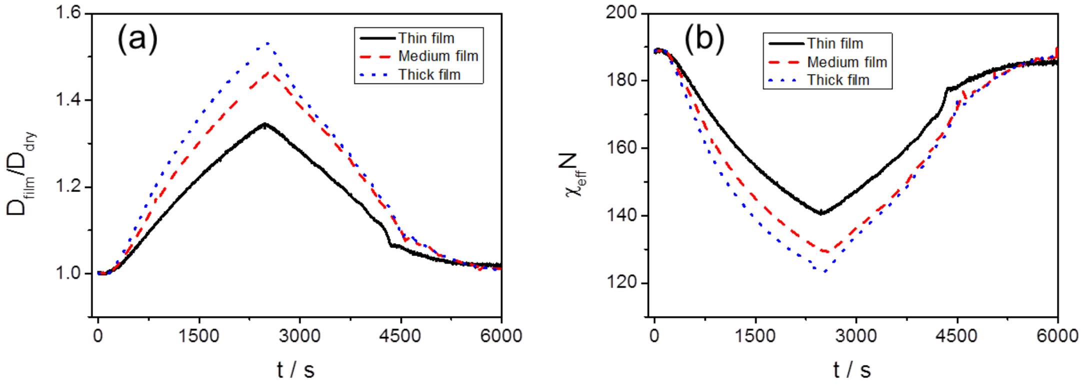

Figure 3.1:
Results obtained from VIS interferometry. (a) Swelling and drying behavior of three films having different initial film thicknesses. Full line: 1570 Å, dashed line: 4743 Å, dotted line: 9757 Å. (b) Resulting $\chi_{eff}N$ as a function of time during vapor treatment and drying.

Fig. 3.1a shows the film swelling behavior. Interestingly, the degree of swelling increases with the film thickness. The effective repulsion between the PS and the PB blocks, $\chi_{eff}N$, as a function of time is shown in fig. 3.1b. Here, χ_{eff} is the effective Flory-Huggins parameter between

PS and PB in the presence of CHX and N the degree of polymerization of P(S-*b*-B). χ_{eff} is calculated from $\phi\chi$ where ϕ is the volume fraction of polymer in the film, calculated from the swollen and the dry film thickness. $\chi_{eff}N$ decreases from 190 to values between 120 and 140; thus the P(S-*b*-B) thin film is in the strong segregation limit during the entire vapor treatment and drying process and far away from the order-to-disorder transition expected at $\chi_{eff}N \approx 10$.

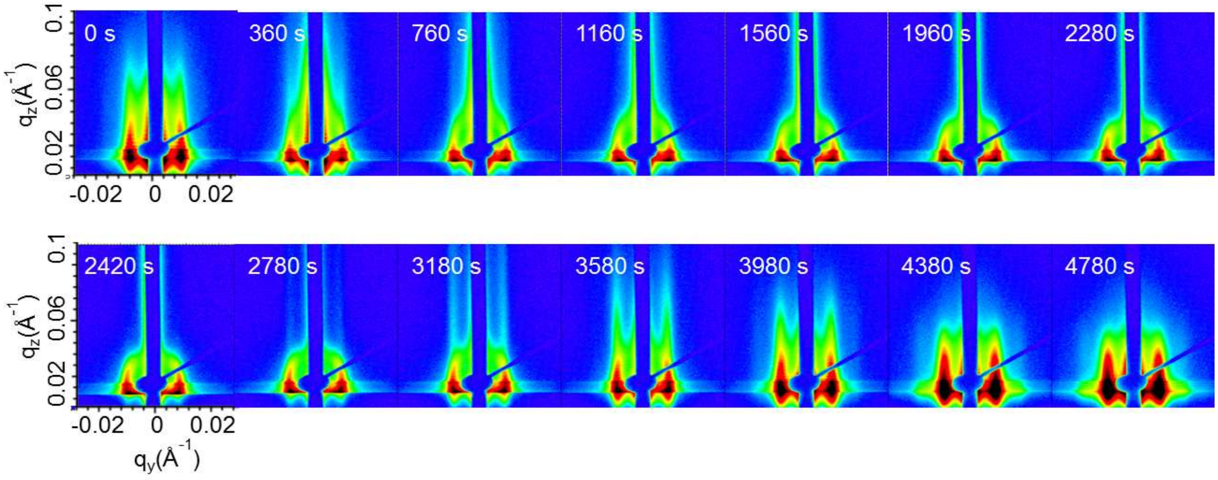

Figure 3.2:
Two-dimensional GISAXS images before and during vapor treatment (upper row) and during drying (lower row) of the thin P(S-*b*-B) film. The times after the start of the vapor treatment are indicated.

Fig. 3.2 shows representative two-dimensional GISAXS images of the as-prepared thin film as well as during vapor treatment and drying. For the medium and the thick film, the behavior is similar. For the as-prepared film, the image displays straight diffuse Bragg rods (DBRs) which indicate the perpendicular lamellar orientation. From their lateral positions, a lamellar thickness of 81 nm is determined using Bragg's law. There are many remarkable oscillations along the rod beamstop, indicating a very strong correlation between thin film surface and the substrate surface, i.e. the film surface is very smooth. During vapor treatment, the DBRs bend inwards which we attribute to tilting of a fraction of the lamellae away from the purely perpendicular orientation. Upon subsequent drying, the straight diffuse Bragg rods reappear, i.e. the perpendicular orientation is recovered. Moreover, second-order DBRs appear, indicating that a more ordered structure is formed after solvent vapor treatment and drying. Additional narrow and elongated DBRs appear during a certain time range in the drying process. This finding points to the formation of a thin near-surface layer having a well-defined perpendicular orientation. The main reason for this is that the swelling of the two blocks by the solvent is expected to result in a reduction of the block stretching and the interfacial tension and a reduction of the glass transition of PS, resulting in an increased copolymer mobility, which enables large-scale structural rearrangements. At the beginning of the drying process, the copolymer chains are still able to move at the film surface, resulting in a thin layer of well-defined perpendicular lamellae.
This project is funded by DFG.

[1] J. Albert, T. H. Epps III, *Mater. Today* **13**, 24-33 (2010)

[2] Z. Di, D. Posselt, D-M. Smigies, C. M. Papadakis, *Macromolecules* **43**, 418-427 (2010)

[3] P. Busch, D. Posselt, D-M. Smigies, B. Rheinländer, F. Kremer, C. M. Papadakis, *Macromolecules* **36**, 8717-8727 (2003)

3.2 In-situ study of structural changes in lamellar poly(styrene-*b*-butadiene) diblock copolymer thin films during heat treatment

A. Sepe, E. T. Hoppe, S. Jaksch, D. Posselt[1], D. Magerl, Q. Zhong, J. Perlich[2], D. M. Smilgies[3], C. M. Papadakis

[1] Department of Science, Systems and Models, Roskilde University, Denmark
[2] HASYLAB at DESY, Hamburg
[3] Cornell University, Ithaca, U.S.A.

Diblock copolymer thin films are prominent candidates for a range of applications requiring nanostructured surfaces, such as the creation of nanoporous films and of arrays of nanowires as well as their use as photonic crystals and biosensors [1]. Thermal annealing has frequently been applied to remove defects and to improve the long-range order [2]. Annealing temperature is a key parameter because it influences both, the interfacial tension between the two blocks and the polymer mobility. We wish to elucidate the mechanisms of structural changes induced by thermal treatment. In-situ grazing-incidence small-angle X-ray scattering (GISAXS) and VIS interferometry as well as ex-situ atomic force spectroscopy (AFM) and X-ray reflectivity (XR) were used. The poly(styrene-*b*-butadiene) (P(S-*b*-B)) system studied by us is well-suited to address this question because it has initially the perpendicular lamellar orientation [3].

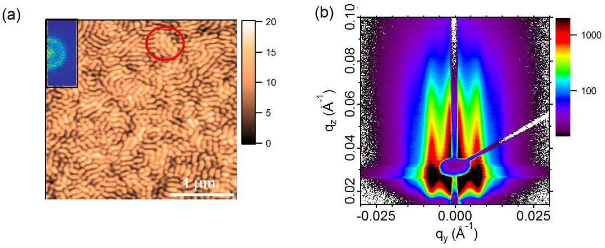

Figure 3.3:
(a) AFM height image, size 3 μm $\times$ 3 μm with the 2D Fourier transform in the inset. The circle marks a lamellar domain where the lamellae are composed of grains. The height scale is in nm. (b) 2D GISAXS image of the as-prepared film, both measured at RT. The intensity scale is logarithmic.

The AFM height image taken after spin-coating and drying at RT shows small and randomly oriented lamellar domains (Fig. 3.3a). The lamellae themselves are not continuous but consist of small round grains. The 2D GISAXS image displays straight and elongated Bragg rods (BRs) at $q_y = \pm\, 2\pi/\mathrm{D}_{lam}$ which indicate the perpendicular lamellar orientation (Fig. 3.3b). From the q_y-positions of the BRs the lamellar thickness is determined to be 861 ± 5 Å. In-situ GISAXS measurements elucidate the structural changes during heat treatment at temperatures between 60 and 130°C. Thermal treatment below 100°C does not destroy the perpendicular lamellar order, but the shape of the BRs changes (Fig. 3.4a,b) with respect to RT (Fig. 3.3b): In addition to the straight part extending to high values of q_z, a contribution which is slightly bent inwards is present as well. The higher the temperature, the shorter is the bent part. We attribute the bending to tilting of the lamellae away from the purely perpendicular orientation. In contrast, treatment between 105 and 120°C leads to a broad distribution of lamellar orientations which only partially recovers upon subsequent cooling (Fig. 3.4c,d, left picture), the elongated straight parts vanish, and the bent parts become shorter and broader with increasing temperature. Treatment at 130°C leads to severe changes of the film structure (Fig. 3.4e, left picture), no more BRs can be discerned. AFM images show that after thermal treatment between 60 and 100°C and subsequent cooling to RT, the order at the surface is locally slightly improved (Fig. 3.4a,b, right pictures). The grains have merged and form continuous lamellae. In contrast, after thermal treatment at 105-120°C, the surface order is lost. Larger structures are present at the surface which have no well-defined length scale (Fig. 3.4c,d, right pictures). We attribute these changes to a migration of PB to the surface. After thermal treatment at 130°C, even larger surface structures appear (Fig. 3.4e, right picture). This process which requires large-scale motion is enabled by the increased mobility of the block copolymers above T_g(PS). Our results indicate that the perpendicular lamellar orientation for high molar mass (216 kg/mol) samples is not stable under all conditions. The best correlated structure is obtained by treatment at 100°C. We attribute the change of behavior at 100°C to the onset of the glass transition of the polystyrene block and the related increase of long-range mobility. We have found that for annealing temperatures below the glass transition temperature of the PS block and subsequent cooling to room temperature (RT), the lateral order is improved, whereas above, a random lamellar orientation and subsequent severe changes of the film structure are observed [4].

This project is funded by the Graduate School 'Materials Science of Complex Interfaces'.

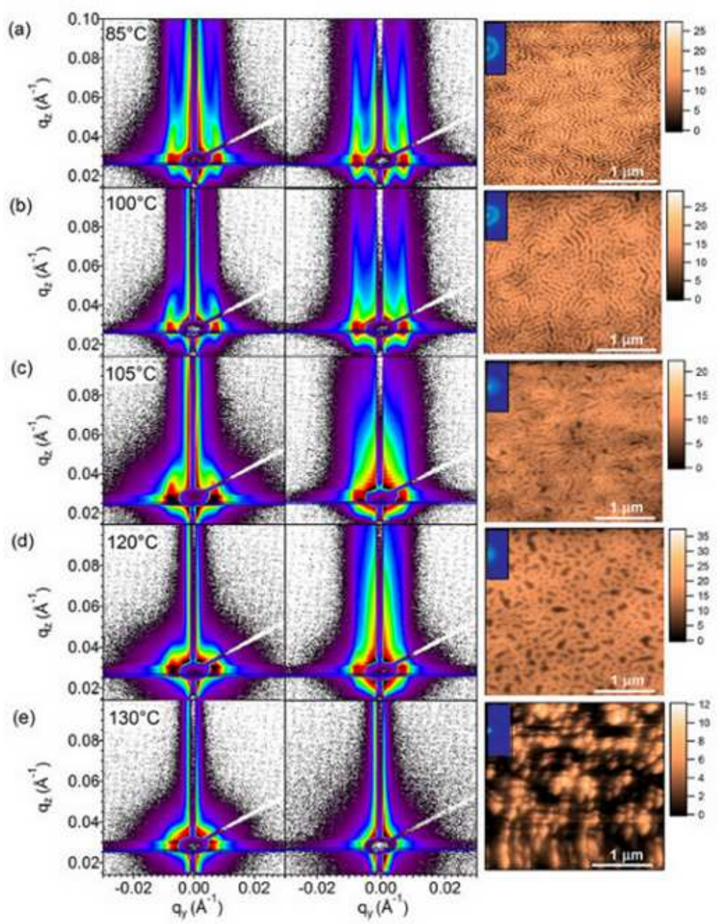

Figure 3.4:
In-situ results at the target temperature and after cooling down. For each annealing temperature, we show 3 images: GISAXS at the target temperature (left) and after cooling down to RT (middle) and ex-situ AFM image (right). The target temperatures are given in each row. The color scale for all GISAXS pictures is the same as in Fig. 1. The AFM height images have a size of 3 μ m × 3 μ m. The height scale is in nm. The insets show the corresponding 2D Fourier transforms.

[1] I. W. Hamley, *Prog. Polym. Sci.* **34**, 1161-1210 (2009)

[2] R. J. Albalak, E. L. Thomas, M. S. Capel, *Polymer* **38**, 3819-3825 (1997)

[3] P. Busch, D. Posselt, D.-M. Smilgies, M. Rauscher, C. M. Papadakis, *Macromolecules* **40**, 630-640 (2007)

[4] A. Sepe, E. T. Hoppe, S. Jaksch, D. Magerl, Q. Zhong, J. Perlich, D. Posselt, D.-M. Smilgies, C. M. Papadakis, *J. Phys.: Condens. Matter* **23**, 254213 (2011)

3.3 Stepwise swelling of a thin film of lamellae-forming poly(styrene-*b*-butadiene) in cyclohexane vapor

Z. Di, D. Posselt[1], D.-M. Smilgies[2], R. Li[2], M. Rauscher[3], I. I. Potemkin[4], C. M. Papadakis

[1] Department of Science, Systems and Models, Roskilde University, Denmark
[2] Cornell University, Ithaca, New York, U.S.A.
[3] MPI for Intelligent Systems, Stuttgart
[4] Moscow State University, Russia

Block copolymer thin films form nanostructures which are of interest for a number of nanotechnology applications, e.g. ultra-high density data storage media and dielectric reflectors. However, the thin film preparation by solvent-casting or spin-coating often results in defectuous structures. Post-preparation methods such as solvent vapor treatment have thus been used to heal these defects. We have previously carried out investigations of the structural changes in block copolymer thin films during solvent-induced swelling of lamellae-forming poly(styrene-*b*-butadiene) (P(S-*b*-B)) in saturated cyclohexane (CHX) vapor using in-situ, real-time grazing-incidence small-angle X-ray scattering (GISAXS) [1]. We found a sequence of processes: First, the glass transition of the PS domains is crossed. Then, the lamellar film rearranges by orienting the lamellae parallel to the film surface and by forming additional lamellae. Later, the order-to-disorder transition is crossed, and the film becomes disordered. To discriminate whether the structural changes are a result of kinetic effects during the fast swelling in saturated vapor, we chose a different strategy in the present work: The vapor pressure of CHX was increased step by step with a long waiting time in between steps [2].

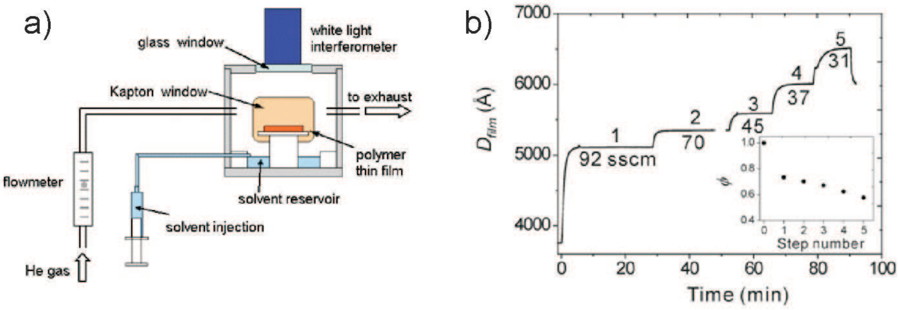

Figure 3.5:
(a) Sketch of the sample cell used for stepwise film swelling. (b) Film thickness during stepwise swelling and drying as a function of time. The numbers of the steps as well as the He gas flow are given above and below the curve, respectively. The inset shows the corresponding polymer volume fractions, ϕ, at the end of each step.

The P(S-*b*-B) diblock copolymer used has a molar mass of 28.0 kg/mol with a PB volume fraction of 0.51. A thin film was prepared by spin-coating from toluene solution on Si wafers. GISAXS experiments were performed at beamline D1 at CHESS, Cornell University. The wavelength was 1.23 Å and the incident angle 0.14°. A CCD camera was used as a detector at a distance of 1.76 m from the sample. The sample cell is shown in Fig. 3.5a. Liquid CHX was injected into a reservoir below the sample. The film swelling was adjusted by means of the helium gas flow through the cell: The higher the gas flow, the lower was the local vapor pressure at the sample. The film thickness was measured in-situ using a white light spectroscopic reflectometer. The time-dependent polymer volume fraction in the film, ϕ, is calculated from the ratio of the dry film thickness to the actual swollen film thickness (Fig. 3.5b).

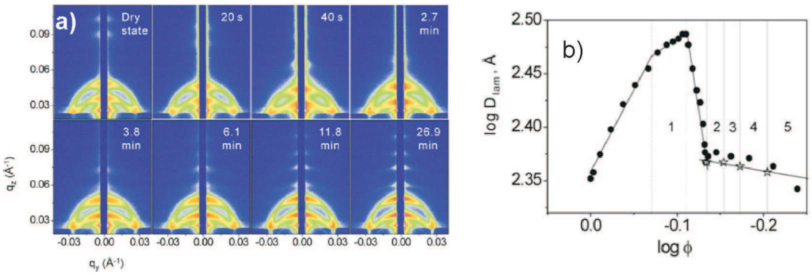

Figure 3.6:
(a) GISAXS images of the film during the first swelling step at the times given in the figures.
(b) D_{lam} as a function of ϕ for all five swelling steps. Closed circles: during swelling, open stars: at the end of each step. The full lines are linear fits. The vertical full lines mark the end of each swelling step.

The as-prepared film has a thickness of 3755 Å and a lamellar thickness of 225 Å (Fig. 3.6), i.e. 17 lamellae are stacked. The 2D GISAXS image features two pairs of diffuse Debye-Scherrer rings (DDSRs), the first- and third-order DDSRs from randomly oriented lamellae. Second-order DDSRs are absent, i.e. the PS and the PB layer are equally thick. The DDSRs are enhanced near $q_y = 0$, i.e. a significant fraction of the lamellae is parallel to the film surface. During the first swelling step, the film thickness increases within 3.9 min to 5114 Å, which corresponds to a decrease of ϕ from 1 to 0.734. The GISAXS images show drastic changes (Fig. 3.6): During the first 2 min, the first-order DDSRs move to significantly lower q-values, as expected for swelling lamellae. Later, they move again to higher values. The intensity distribution along the DDSR changes as well: Initially, the intensity near q_y = 0 is strongly enhanced, however, after 2.7 min and later, this maximum extends more and more towards higher q_y values and bends downwards along the DDSRs. These changes are accompanied by the transient broadening of the DDSRs along q_z after 0.8-2.4 min and the transient disappearance of the third-order DDSRs/DBSs during the time range 7 s - 6.1 min which indicate the break-up of the lamellar correlation and the formation of additional lamellae, in line with our previous observations in saturated CHX vapor [1]. Moreover, second-order DDSRs/DBSs appear after 6.1 min and persist. We attribute them to the stronger swelling of the PB domain and the resulting asymmetry of the lamellae. In the end of this swelling step, the lamellar thickness is with 233 Å only 3.6% higher than in the dry state, whereas the film has swollen by 36% , i.e. the number of lamellae has increased to 22. All these changes in the GISAXS maps are finished after 10 min, i.e. a stable state is reached at this time. The lamellar thickness as a function of ϕ reveals a pronounced maximum (Fig. 3.6b) which reflects the initial swelling and the subsequent creation of additional lamellae. At the end of the subsequent swelling steps, it is observed that the lamellar thickness only decays weakly from step to step. The block conformations thus become slightly more coiled, as the vapor pressure increases, because increasing amount of the solvent weakens incompatibility of the different blocks (Fig. 3.6b). A power law $D_{lam} \propto \phi^{0.14}$ is found for these stable states. This is very similar to the power law $D_{lam} \propto \phi^{1/6}$ which results from a consideration of the elastic and interfacial contributions to the free energy and the mean-field calculation of the interfacial tension between the two blocks on solvent content. We conclude that the structural changes during step-wise swelling of a lamellar diblock copolymer film are complex, especially in the first swelling step.

This work is funded by the Graduate School of Excellence ”CompInt”.

[1] Z. Di, D. Posselt, D.-M. Smilgies, C. M. Papadakis, *Macromolecules* **43**, 418-427 (2010)

[2] Z. Di, D. Posselt, D.-M. Smilgies, R. Li, M. Rauscher, I. I. Potemkin, C. M. Papadakis, submitted

3.4 Linear and cyclic siloxane containing mesogens: smectic structures in bulk and thin films

P. Heinz[1], K. Hindelang[1], B. Rieger[1], A. Golosova, S. S. Funari[2], J. Perlich[2], C. M. Papadakis

[1] Department Chemie, TU München
[2] HASYLAB at DESY, Hamburg, Germany

Liquid crystals (LCs) show anisotropic optical properties and are therefore used in displays, electronic or optoelectronic technologies. In low-molecular-weight systems (LMW-LCs), a typical structural motif for molecules which form mesophases is the combination of rigid and flexible parts. The rigid part may be a disc-like organic molecule and the flexible (coil-like) part usually consists of a long alkyl-chain. Mesophase formation is not only restricted to carbon based systems; numerous studies describe integration of silicon based compounds into the mesogen structures. Incorporation of Si atoms affects in most cases the overall packing of the molecules and alters important features, such as melting points or mesophase morphologies.

The present work focuses on novel low-molecular-weight bi- and tetramesogens with linear disiloxane and cyclic tetrasiloxane linkers in combination with long-chain mono and trialkoxy mesogens. The synthesis proceeded via hydrosilylation of mono- and trialkoxy substituted phenyl acetylenes with varying alkyl chain lengths, which were derived from gallic acid and p-hydroxy aldehyde. The formation of mesophases was demonstrated by polarized optical microscopy and thermal analysis. Layer distances and domain dimensions of smectic mesophases were determined using transmision small-angle x-ray scattering (SAXS) on bulk materials and grazing incidence small-angle x-ray scattering (GISAXS) on thin films [1].

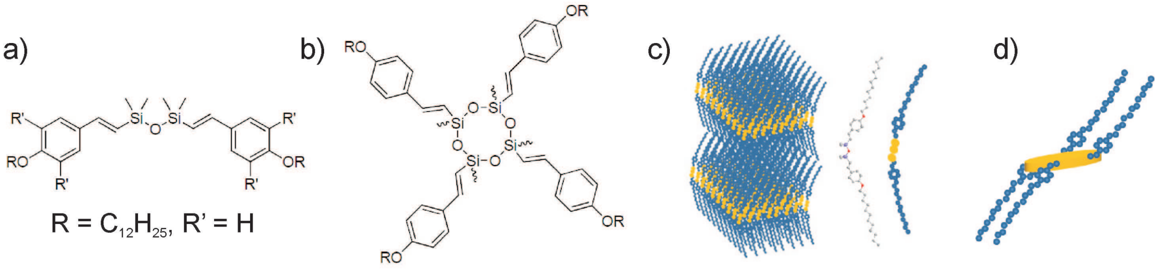

Figure 3.7:
Structures of the two LCs studied: (a) linear, (b) cyclic, and corresponding structures from SAXS (c,d).

SAXS experiments were carried out at beamline A2 at HASYLAB/DESY using an X-ray beam with a wavelength $\lambda = 1.50$ Å, a MarCCD camera mounted in $\sim 1 - 1.30$ m distance from the sample. Thin films were prepared by spin-coating Si wafers, vacuum drying and annealing above the corresponding melting temperatures. GISAXS experiments were carried out at beamline BW4 at HASYLAB/DESY, using a microbeam with $\lambda = 1.381$ Å. A MarCCD camera was used as a detector with a sample-detector distance of 1.9 m.

The SAXS images show strong Debye-Scherrer rings at ratios 1:2 which indicates layered structures typical for a smectic arrangement. The corresponding layer spacings amount to 46 Å and 41 Å for for the linear and the cyclic compounds, respectively. In the case of the linear compound, the observed spacing corresponds very well with the values of 47 Å calculated from a molecular model for a completely stretched molecule. As result thereof, we propose densely packed and stacked domain structures of fully stretched bimesogens (Fig. 3.7c). From the smaller value of the spacing for the cyclic compound, we conclude that only the stretched isomer with ’2up-2down’ conformation (Fig. 3.7c) was obtained. One possible reason for lower spacing values than in the case of the linear compounds with the same substitution is the angulated core of the tetramesogens. Another reason may be the stacked arrangement, which leads to a tilting of the mesogens in the stacks and thus to a lower spacing compared to the non-tilted arrangement.

AFM revealed that, even though the stacking in the films is not perfect, both compounds form smectic domains (Fig. 3.8a,b). The domains formed by the linear compound are more extended and much better defined than the ones formed by the cyclic compound.

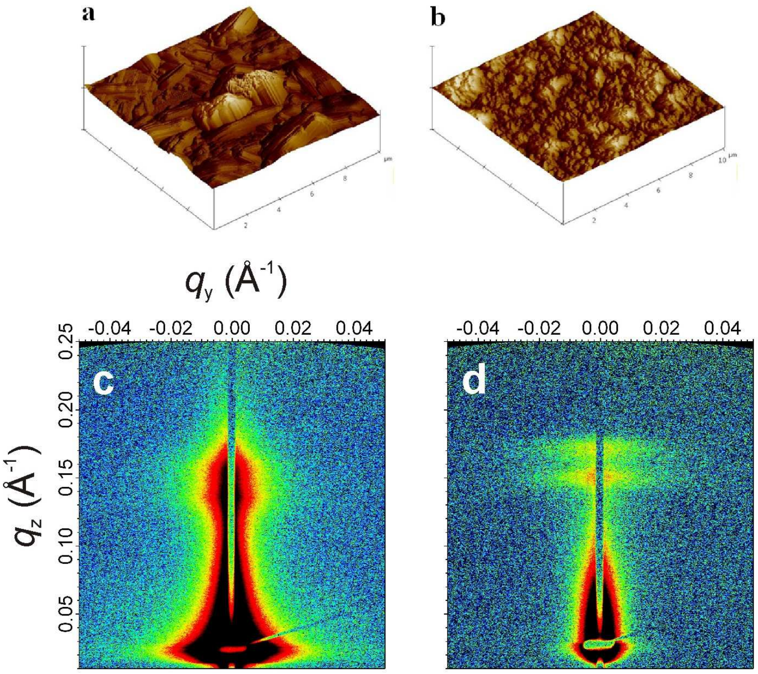

Figure 3.8:
AFM (a,b) and GISAXS images (c,d) of the linear (a,c) and the cyclic compound (b,c).

The GISAXS image of the film from the linear compound shows two diffuse Bragg sheets (DBS, Fig. 3.8c), which are the first-order reflections of the layered structure having a layer spacing of 48 Å, i.e. unchanged from the bulk. For this film, the DBSs are relatively broad along the film normal (in q_z direction). From the width, we calculate that only $\sim$ 6 out of the 18 layers stacked in the film are correlated. In contrast, the DBSs do not extend far in the film plane (along q_y); i.e. the layer thickness remains correlated over a large distance.

The GISAXS image from the cyclic compound is given in Fig. 3.8c. It resembles the one of the linear compound; thus a layered structured is formed as well, and the layer spacing is found at 43 Å, which is also similar to the bulk value. However, the DBSs are much wider along q_y and much narrower along q_z than the ones of the linear compound. The number of correlated lamellae is with $\sim$ 9 comparable to the number of layers stacked in the film.

In conclusion, different mesogenic systems, containing mesogens made from long-chain substituted gallic acid derivatives and linear and cyclic oligo(siloxane) linkers have been synthesized and characterized. SAXS revealed smectic layered assemblies in the bulk. In thin films on substrates, layers parallel to the substrate surface are formed both for linear and the cyclic compounds. They differ in the quality of layer stacking and in the lateral roughness.

This work was supported by WACKER Chemie AG.

[1] P. Heinz, K. Hindelang, A. Golosova, C. M. Papadakis, B. Rieger, *ChemPhysChem* **12**, 3591-3603 (2011)

3.5 Reorganization of the near-surface composition in pressure sensitive adhesive films stored under nitrogen atmosphere

M. Schindler, A. Kriele[1], P. Müller-Buschbaum

[1] FRM II, Garching, Germany

Pressure-sensitive adhesives (PSAs) are widely applied for their fast and permanent tack, the low force needed for bonding compared to the energy needed for the release and many other advantages like the nearly residual free removal from the adherent. Also very different classes of materials such as paper, glass, polymers and metal can not only be joint by common adhesives like epoxies, but also using PSAs. PSAs also play a big role in medicine for the removable attachment of patches and sensors to the human skin. These features are all of macroscopic nature while the origin of the tackiness is found in the structure and the properties of the nanoscopic polymer chains of the adhesive.

Adhesion of PSAs is based on van der Waals interactions, which are in theory strongest for molecules at the very top surface. In practice the adherent penetrates the adhesive due to its rough surface. As a consequence, not only the PSA surface is important for proper adhesion but the near surface region of the PSA film contributes as well. Recently, this surface near region was investigated by Diethert et al. using X-ray reflectometry (XRR)[1]. They addressed the near-surface composition profile of a PSA and investigated the influence of aging under ambient conditions as well as the use of different solvents during sample preparation. Moreover, Diethert et al. showed that an additional treatment of the PSA film with various different relative humidities not only alters the near-surface composition but also the tack performance [2].

In this project the reorganization of the near-surface composition of a PSA film upon exposure to apolar nitrogen atmosphere is investigated. PSA films are prepared via solution casting onto pre-cleaned glass substrates. As model PSA system we use the statistical copolymer P(EHA-stat-20MMA) which consists of 80% ethylhexylacrylate as the sticky majority component and 20% methylmethacrylate as the glassy minority component. The freshly cast films are exposed to a nitrogen atmosphere representing an apolar and inert gas. This treatment causes a reorganization of the inner morphology in the PSA film. Using XRR it is shown that the freshly prepared films show a solubility driven enrichment of the PMMA component at the very surface. Due to the interaction with the apolar nitrogen atmosphere the less polar component of the copolymer, PEHA, enriches on top with time. The timescale of this internal rearrangement is of major importance for predictions of the durability and long time performance of adhesives in storage as well as of bonds established with PSA.

Fig. 3.9a and b show the XRR measurement of a freshly prepared sample in two representations. The first shows the classical logarithmic reflectivity versus the momentum transfer with very small modulations superposed to the inherent decay of reflected intensity. To better emphasize these small oscillations the Fresnel representation is chosen for proper fitting of the data (Fig. 3.9b). The inset in (Fig. 3.9a) shows the refractive index profile which is derived from the fit. Clearly an enrichment layer of the glassy PMMA on the very surface is visible. The reason for this layer lies in the slightly better solubility of this component in the used solvent toluene compared to the soft component PEHA. Upon solvent evaporation, the better soluble parts of the copolymer get dragged to the surface.

During the exposure of the sample to nitrogen the inner structure changes due to the interactions with the apolar nitrogen at the upper interface of the adhesive film. Fig. 3.9c shows the final measurement with the respective fit and the refractive index profile. It can be seen that after 12days a PEHA enrichment has been established, followed by an PMMA-rich layer. PEHA is not only less polar than PMMA and therefore prefers to enrich on top but also has a lower surface energy which also adds to this effect. To better see the evolution inside the film color coded

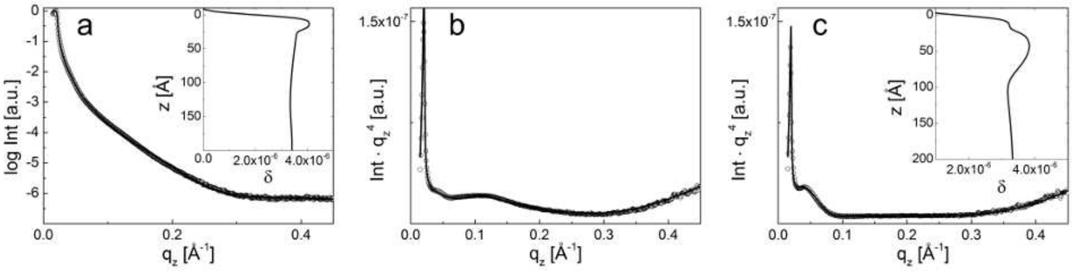

Figure 3.9:
Reflectivity curve of a freshly cast film of P(EHA-stat-80MMA) with its refractive index profile shown in the inset. An enrichment layer of PMMA at the very surface is clearly visible. For more careful fitting of the data and to emphasize also very small modulations in the general slope the Fresnel representation is used (b) where the reflectivity is multiplied by q_z^4 to correct for the inherent steep slope. (c) XXR measurement of a sample which was stored under nitrogen for 12 days. The inset shows the corresponding refractive index profile and reveals an enrichment layer of the soft component, PEHA, at the surface.

compositional maps are shown in Fig. 3.10 for all different investigated time steps. Pure PEHA is resembled by white color while black color represents pure PMMA. A smooth transition and diffusive reorganization of the near-surface composition can be seen.

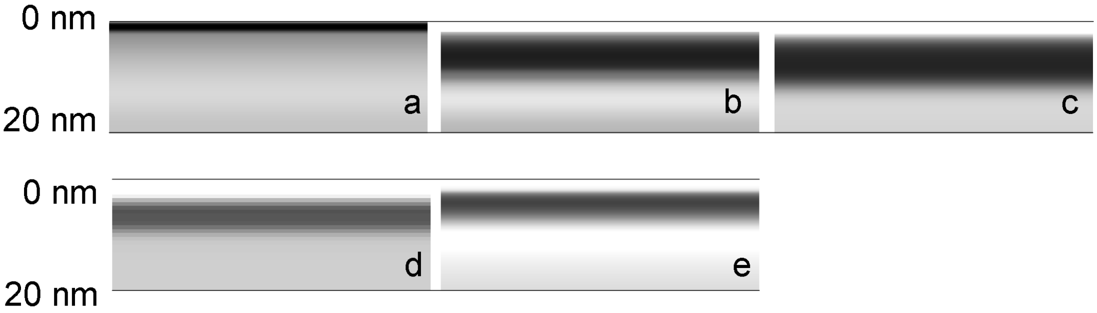

Figure 3.10:
Color coded compositional maps of samples that have been exposed to nitrogen for different times. PEHA is represented by white, PMMA is shown in black.

Thus it is shown that the exposure of P(EHA-stat-20MMA) to nitrogen atmosphere leads to a reorganization in the near-surface region. The solubility driven PMMA enrichment layer shows a thickness of about 2.5 nm in the freshly cast sample. This composition changes gradually to an enrichment of PEHA with a thickness of 2 nm after 12 days. As a consequence, 12 days storage are already sufficient to achieve such reversal of the two component statistical copolymer with respect to the component being enriched at the surface. AFM measurements proof the presence of smooth surfaces directly after casting and a slight increase in surface roughness and the presence of small defects after nitrogen storage.

[1] A. Diethert, P. Müller-Buschbaum, *J. Adhes.* **87**, 1067-1090 (2011)

[2] A. Diethert, K. Ecker, Y. Peykova, N. Willenbacher, P. Müller-Buschbaum, *ACS Appl. Mater. Interfaces* **3**, 2012-2021 (2011)

3.6 Creation of lateral structures in diblock copolymer thin films during vapor treatment

A. Sepe, P. Černoch[1], P. Štěpánek[1], E. T. Hoppe, A. Timmann[2], C. M. Papadakis

[1] Institute of Macromolecular Chemistry, Academy of Sciences of the Czech Republic, Prague
[2] HASYLAB at DESY, Hamburg

Thin block copolymer films are promising candidates for a variety of applications, such as the preparation of nanoporous films, nanostructured templates, photonic crystals and biosensors [1]. Lateral structures are of special interest, e.g. for the structuring of inorganic substrates [2] and for the preparation of nanoporous membranes [3]. Solvent annealing offers a simple and flexible method with a potentially high degree of controllability through careful choice of solvent [4]. We have studied the structure formation in lamellar poly(4-octylstyrene-b-butylmethacrylate) (P(OS-b-BMA)) films during exposure to saturated vapor of n-hexane (HX) and subsequent drying using real-time, in-situ grazing-incidence small-angle X-ray scattering (GISAXS). Previous surface studies on hexane treated samples revealed a lateral surface structure [5]. Combining in-situ, real-time GISAXS with atomic force microscopy (AFM) and X-ray reflectometry (XR), detailed information on the processes during vapor treatment and drying can be gained giving information on their molecular origin. We report on the structural changes during vapor treatment of spin-coated films having different film thicknesses (D_f).

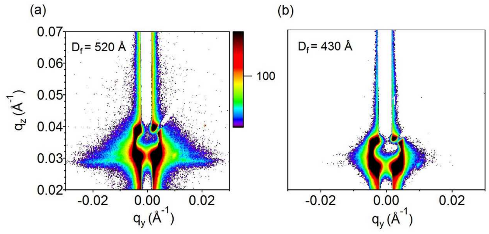

Figure 3.11:
2D GISAXS images of as-prepared films. The color scale for all GISAXS pictures is the same as in Fig. 3.11a.

AFM images (not shown) were taken of the as-prepared films, i.e. after spin-coating and drying at room temperature. They do not show any evidence of surface order for both thick (D_f = 520 Å) and thin (D_f = 430 Å) film. The RMS surface roughnesses are 30 Å and 20 Å, for the thick and the thin film, respectively. GISAXS maps of both as-prepared films (Fig. 3.11a,b) do not show any features apart from the specularly reflected beam and diffuse scattering, which is presumably due to surface roughness and to weak internal structuring.

During treatment with saturated HX vapor, in the thick film, we observe a tendency to a formation of the lamellar structure (Fig. 3.12). This structure is most ordered after 5 min. Further vapor treatment results in a partial deterioration of the structure. Moreover, upon drying, the structure is only partially stable which explains why the surface texture is only weak (Fig. 3.11c). The lateral repeat distance shows relatively fast kinetics with the changes being finished within $\sim$ 20 min upon vapor treatment and $\sim$ 5 min upon drying.

Intensity profiles along q_y of the thin film shows qualitatively the same behavior as the thick film (Fig. 3.13). However, the changes are slightly faster. Out-of-plane peaks become more intense during the vapor treatment, i.e. the fraction of the film displaying a lateral structure increases with time. In contrast to the thick film, the growth of the peak intensity stops already after $\sim$ 20 min. When drying is started, the peaks weaken immediately.

Our study shows that lateral structures can be obtained most rapidly for the thin film. In the thick film, the same behavior with an undershoot of lamellar thickness is observed, however, on a longer time scale. Complex, non-monotonous behavior is observed for both films. Upon drying, the lateral structure is stable only for the thick film, not for the thin film. We conclude that, to achieve lateral structures, both blocks need to have certain mobility.

This project is funded by the Graduate School 'Materials Science of Complex Interfaces'.

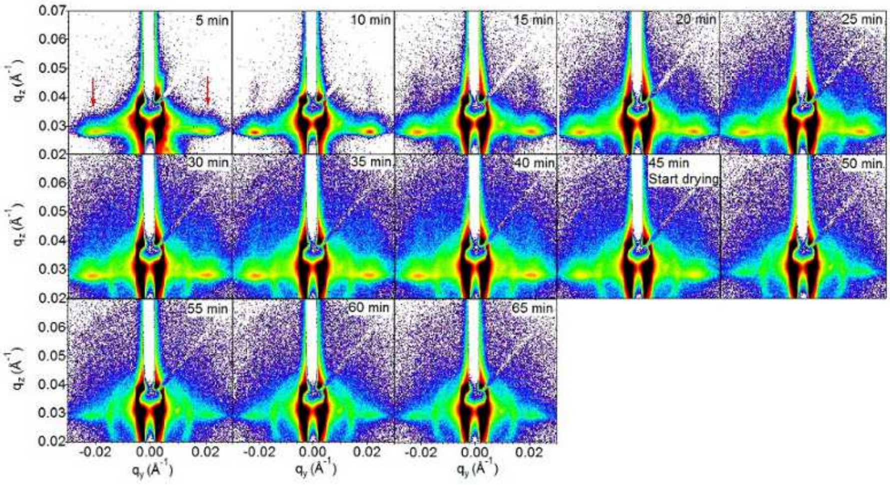

Figure 3.12:
Representative GISAXS images of the thick film during treatment with HX vapor and subsequent drying. The times after injection of HX into the cell are given in each image. Drying starts after 45 min. The arrows mark the out-of-plane peaks. For all images, the color scale is the same as in Fig. 3.11a.

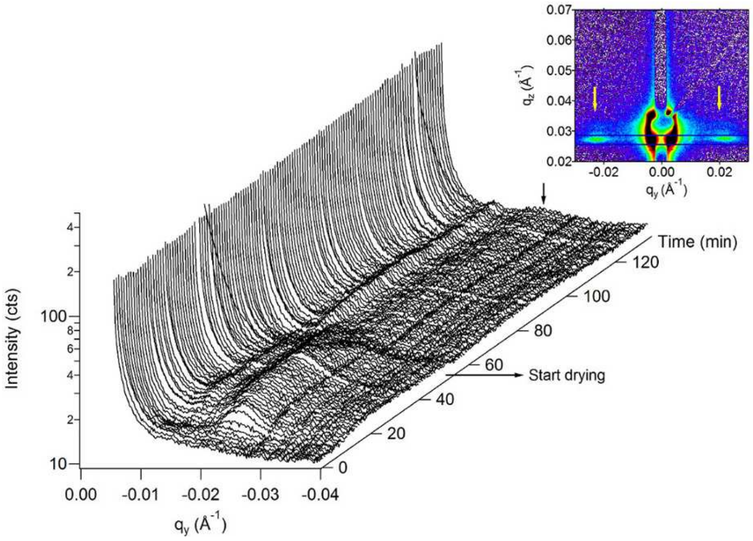

Figure 3.13:
Intensity profiles along q_y of the thin film as a function of HX vapor treatment time and subsequent drying. The drying starts at the marked position. The inset shows the region of the GISAXS images used to construct the intensity profiles (blue horizontal lines). The vertical arrows indicate the position of the out-of-plane peaks.

[1] I. W. Hamley, *Nanotechnology* **14**, R39-R54 (2003)

[2] M. Park, C. Harrison, P. M. Chaikin, R. A. Register, D. H. Adamson, *Science* **276**, 1401-1404 (1997)

[3] S. Y. Yang, J. Park, J. Yoon, M. Ree, S. K. Jang, J. K. Kim, *Adv. Funct. Mater.* **18**, 1371-1377 (2008)

[4] R. J. Albalak, M. S. Capel, E. L. Thomas, *Polymer* **39**, 1647-1656 (1998)

[5] P. Černoch, P. Štěpánek, J. Pleštil, M. Šlouf, A. Sidorenko, M. Stamm, *Eur. Polym. J.* **43**, 1144-1153 (2007)

3.7 Optical properties of polybutadiene in the bulk and near a gold interface

E. T. Hoppe, I. Hopp[1], M. Port[1], B. Menges[1], C. M. Papadakis

[1] MPI für Polymerforschung, Mainz

The properties of polymers near a solid interface are of importance for lubricants or polymer nanocomposites. Basic research has focused on the question whether and in which way the polymer properties change near a solid interface, e.g. the chain conformation, the mass density and the chain mobility. Experimentally, the polymer/solid interface is not easily accessible, unlike the polymer surface. A vast number of studies have therefore made use of the thin film geometry where the properties of the polymer film have been expected to be significantly determined by the presence of the solid substrate. However, in thin films, the film surface may have an influence on the results. Interface-sensitive methods specific to the polymer/solid interface are thus highly desired.

In the present work, we have used surface plasmon resonance / leaky optical waveguide spectroscopy (SPR/OWS) to investigate the optical properties of a polybutadiene (PB) melt near a solid surface. Measurements on thick films comprise both the optical waveguide modes as well as the surface plasmon resonance, thus giving simultaneous information on the bulk properties and the interface-near region, respectively. We have covered a wide range in PB molar masses and have focused on the changes of the refractive index in the polymer film. Moreover, from the position of the surface plasmon resonance in comparison to the ones of the waveguide modes, we have detected an interphase which has properties different from the bulk. We discuss these changes in terms of chain alignment.

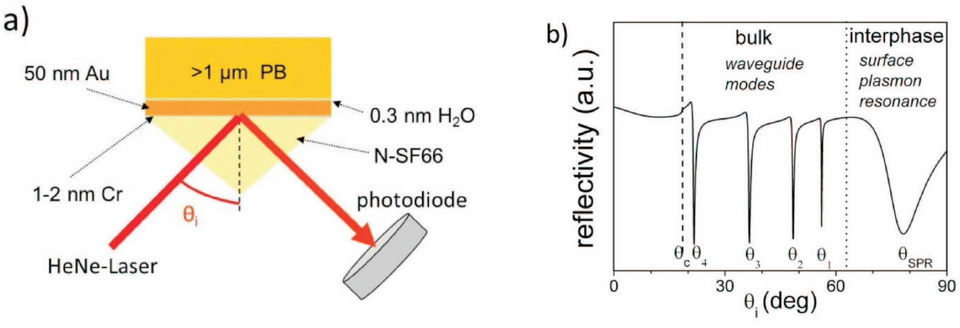

Figure 3.14:
(a) Schematic sample configuration. (b) Calculated reflectivity curve of the layer sequence in (a) as a function of the incident angle θ_i. Deep minima due to waveguide modes are present and a broader one due to the surface plasmon resonance.

For SPR/OWS in Kretschmann configuration, rectangular prisms were custom-made from N-SF66 glass, having a refractive index of 1.914 at 632.8 nm. A 632 nm laser (HeNe) was used for excitation. The base was coated by 50 nm of gold. Solutions of PB in toluene (2.2-17 wt%, depending on molar mass) were spin-coated onto the gold coated prism, resulting in films with thicknesses of $\sim 1-3\ \mu$m. The films were vacuum dried at room temperature. Nine PB samples having molar masses between 0.7 and 2200 kg/mol were investigated. The SPR/OWS feature the waveguide modes which are sensitive to the bulk properties of the polymer film: The number and positions of modes observed increase with the optical thickness of the polymer film. The more homogeneous and flat is the polymer film, the deeper are the minima. At the surface plasmon resonance angle, θ_{SPR}, another, broader minimum is observed, which is due to the excitation of a surface plasmon at the gold/polymer interface. The value of θ_{SPR} increases with the index of refraction of the near-gold layer of the polymer film, it is thus sensitive to a possible interphase with properties different from the bulk. The extinction length of the plasmon amounts to approx. 160 nm, the surface plasmon thus contains information about a near-gold layer of approximately this thickness. For the thick films used in the present work, the waveguide modes and the surface plasmon depend nearly exclusively on the bulk properties and the ones of the near-gold layer, respectively.

Measurements on vacuum-dried PB films revealed a bulk refractive index which increases from 1.512 ± 0.003 at 9.5 kg/mol to 1.517 ± 0.003 at 2200 kg/mol. The molar mass dependence was confirmed by Abbé refractometry. When fitting the waveguide modes properly, the surface plasmon resonance could not be recovered, neither the position nor the shape (Fig. 3.15a). This was the case for all molar masses investigated and indicates a lower average refractive index of the interphase in the plane of incidence for all molar masses. While this is a qualitative but model-free consideration of the interphase, it proves the presence of a layer close to the gold interface with a lower refractive index for p-polarized light.

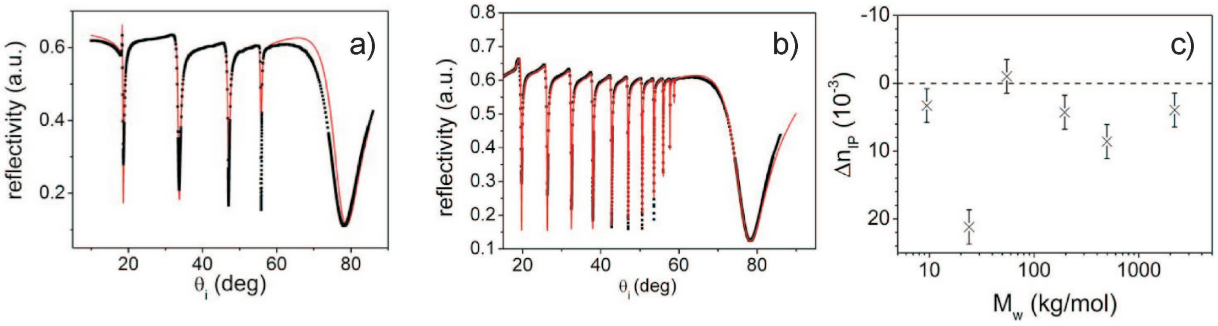

Figure 3.15:
a) SPR/OWS reflectivity curves of a film from PB having 55 kg/mol (black circles) and fit of a single layer model (red line). (b) Curves of PB having 196 kg/mol (black circles) and fit of the two-layer model (red line). (c) Resulting differences of the refractive indices of the interphase (crosses) from the bulk (dashed line) after vacuum treatment in dependence on molar mass.

To derive the origin of this deviation, a model including an interphase in the PB film near the gold interface was used. This way, the measured reflectivity curves are described well (Fig. 3.15b). For all molar masses, the refractive indices of the interphase (in the plane of incidence) are slightly lower (0.4%) than the ones of the bulk part of the film as expressed by the difference between bulk refractive index and interphase refractive index (Fig. 3.15c). To elucidate the role of the solvent for the interphase, a film was prepared from n-hexane, a solvent with a much lower vapor pressure and a lower refractive index than toluene. Similar results as from toluene were found; thus, the solvent does not seem to play a role for the interface properties. Additional measurements with s-polarized light revealed that PB chain segments seem to be aligned parallel to the gold inrface.

To summarize, an interphase has been detected in PB melts in a wide molar mass range near a gold interface where the refractive index is lower than in the bulk which seems to be due to segment alignment along the gold interface.

This work was supported by the DFG priority program SPP 1369 'Polymer-Surface Contacts: Interfaces and Interphases'.

[1] E. T. Hoppe, I. Hopp, M. Port, B. Menges, C. M. Papadakis, submitted

3.8 In-situ GISAXS study of gold electrode growth on spiro-OMeTAD films

M. A. Niedermeier, E. Metwalli, V. Körstgens, J. Perlich[1], A. Buffet[1], M. M. Abul Kashem[1], K. Schlage[1], R. Röhlsberger[1], S. V. Roth[1] and P. Müller-Buschbaum

[1] HASYLAB at DESY, Hamburg, Germany

In the fast developing field of organic electronics thin metal films play a huge role as they are commonly applied as electrode materials. A well defined organic/metal interface is crucial for a good overall device performance. For a deeper understanding of this interface, information about the morphology and the incorporation of the electrode material into the organic film is essential. However, so far still only little fundamental knowledge on this topic is available and only a few systems have been investigated [1].

Solid state dye sensitized solar cells (ssDSSC) are among the most promising candidates for organic photovoltaics. The solid hole conductor spiro-OMeTAD is a standard mediator for ssDSSC and gold is typically used as an electrode material in these solar cells. In the present investigation, a thin gold layer is sputter deposited with a nominal sputter rate of 3.2 nm/s on top of a 100 nm thick spiro-OMeTAD film and monitored in-situ with grazing incidence small angle x-ray scattering (GISAXS), using an incidence angle of 0.41° and a sample detector distance of 2.02 m. The experiment has been performed in a start-stop-sputtering mode, i.e. each deposition step is followed by a subsequent GISAXS measurement.

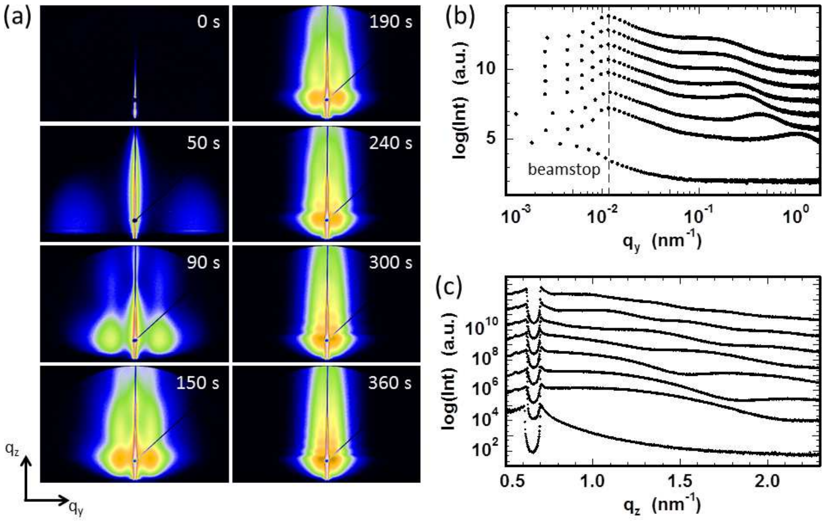

Figure 3.16:
2D GISAXS images taken after 0, 50, 90, 150, 190, 240, 300 and 360 s of gold sputter deposition (a). Out of plane cuts of the respective 2D GISAXS images, taken at the critical angle of gold (b). Detector cuts of the respective 2D GISAXS images (c). The line cuts are shifted along the y-axis with increasing sputtering time, starting from the bottom in each case.

Figure 3.16 (a) shows a series of 2D scattering images after 0, 50, 90, 150, 190, 240, 300 and 360 s of gold sputter deposition. The most prominent feature, especially in the first four GISAXS patterns, is a side peak emerging at larger scattering angles and, with proceeding sputtering time, shifting towards smaller values. This indicates a cluster formation of the gold which is anticipated, since gold is not expected to show a wetting of the spiro-OMeTAD surface but to exhibit a Volmer-Weber 3D cluster growth. The peak is related to a maximum in the interference function describing the cluster correlation distance and, therefore, represents a change in the relative cluster position, i.e. an increasing center-to-center distance. In the last four GISAXS images change of the intensity related to lateral structures is observable, indicating that the growth of the gold cluster stopped in lateral direction, and hence, that the surface is completely covered by gold islands. From that time on, the gold film only grows vertically. Figure 3.16 (b) shows the out of plane cuts of the various GISAXS images, taken at the critical angle of gold. The fast cluster growth in the early stages of the sputtering process is visible, along with the stagnation of the lateral peak position after 200 s. By fitting the respective curves, the center-to-center distance is accessible. That way, we observe a quick growth of the gold clusters until a center-to-center distance of roughly 40 nm is reached within the first 200 s. However, from that time on, only an increase to 60 nm is observed for the remainder of the sputter deposition. That change, as already mentioned, is explained by the fact that after about 200 s, a complete surface coverage is reached, so there is no more space left on the surface for further lateral growth of individual gold cluster. The increase of the center-to-center distance which is observed for longer sputtering times results from a coalescence of the cluster, a process also known as grain growth.

While the out of plane cuts are useful to obtain lateral information, the detector cuts provide information about the vertical growth of the gold layer. Figure 3.16 (c) shows detector cuts of the various GISAXS images. With proceeding time, fringes become visible in the detector cuts. Evaluation of the fringe distances reveal that the film thickness increases slower than the nominal thickness until roughly 200 s of sputtering time. For the remainder of the sputtering time, the thickness increment of the gold film follows the nominal growth rate. This time correlates very well with the observations from the lateral investigation where we found a complete surface coverage after 200 s, as well. As a consequence, the condensation coefficient is smaller than 1 if the spiro-OMeTAD surface is not completely covered yet, meaning the gold atoms are not guaranteed to stay adsorbed to the surface, but also desorbing again with a certain probability. However, once a full coverage is reached, the condensation coefficient is equal to 1, i.e. every incoming gold atom is adsorbed on the surface and, hence, resulting in a thickness increase equal to the nominal growth rate.

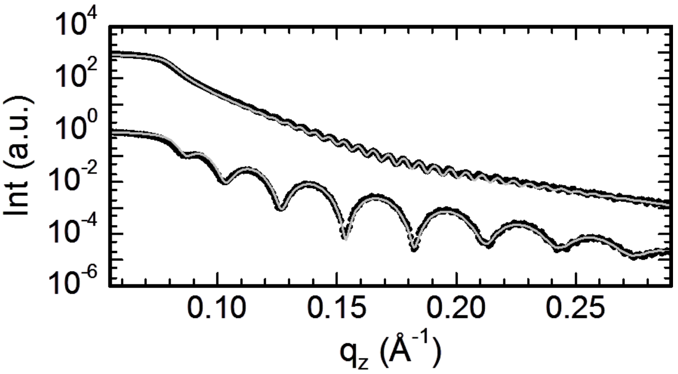

Figure 3.17:
XRR measurements after 480 s (bottom curve) and after 1800 s (top curve) of gold sputtering on a spiro-OMeTAD film. The grey solid lines show the fits to the respective curves, obtained using the Parrat algorithm. The curves are shifted along the y-axis for clarity.

Additionally, investigations about enrichment layers of the electrode material into the organic thin film are done using x-ray reflectometry (XRR). Figure 3.17 show XRR measurements performed on the gold sputtered film on spiro-OMeTAD, once after 480 s of sputtering time and once after 1800 s of sputtering time to investigate possible influences of thicker gold films on the enrichment layer formation. The large difference in the scattering length densities of gold and spiro-OMeTAD makes this method sensitive to small amounts of metal incorporated in the spiro-OMeTAD layer. The XRR measurements revealed the formation of a gold enrichment layer in the spiro-OMeTAD film with a thickness of 3.5 nm for both sputtering times. It is of importance that the penetration of gold into the spiro-OMeTAD film under the chosen deposition conditions is present. The XRR results suggest that the depth of the penetration layer is not affected by the total thickness of the gold electrode, at least as soon as the spiro-OMeTAD surface is completely covered. Thus, doping of the spiro-OMeTAD with gold occurs most likely during the early stages of the deposition.

[1] G. Kaune, M. A. Ruderer, E. Metwalli, W. Wang, S. Couet, K. Schlage, R. Röhlsberger, S. V. Roth, P. Müller-Buschbaum, *ACS Appl. Mater. Interfaces* **1**, 353 (2009)

3.9 Film thickness controllable wet-imprinting of nanoscale channels made of conducting polymers

R. Meier, F. Markl, C. Birkenstock, P. Müller-Buschbaum

In general, conducting polymers are promising candidates for a future mass production of organic electronics at low-costs. The key advantages result from the chemical variety of the materials and the easy solution-based processability. Recently, also the structuring properties of photoactive polymers started to attract more and more interest for the fabrication of structured organic solar cells (OSCs) or other electronic devices.

Different methods have been established to texture polymer films. The two most common techniques are MIMIC (micromolding in cappilaries)[1] and NIL (nanoimprint lithography)[2]. However, both methods have the disadvantages of missing a homogeneous substrate coverage or requiring annealing steps at elevated temperatures. In consequence, we came up with an inverted MIMIC approach which allows the fabrication of polymeric nanostructures on top of a homogeneous polymer support based on simple wet embossing principles.[3]

In Figure 3.18 the imprinting routine is illustrated applying a novel semi-flexible polycarbonate (PC) structure mold. Therefore, the master mold has to be leveled (step 1) and the desired amount of polymer solution is spread on the master structure (step 2). Following, the substrate is gently put on top of the solution (step 3) and an external pressure is applied during solvent evaporation to control the thickness of the homogeneous polymer layer (step 4). For the lift off the PC mold can be easily bend (step 5) and a perfectly structured polymer film remains on the substrate (step 6).

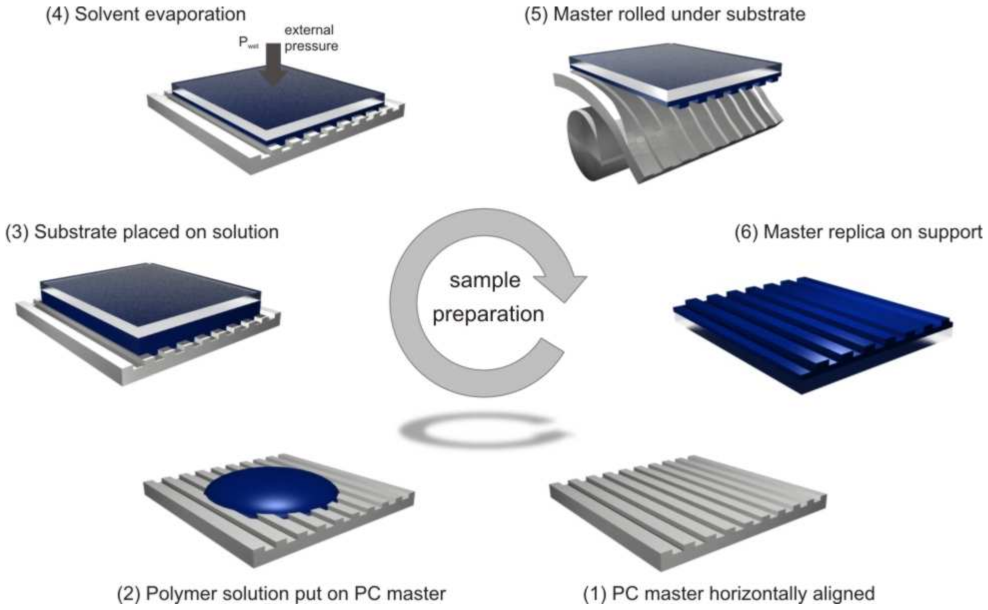

Figure 3.18:
Schematic procedure for the formation of patterned polymer films based on semiflexible polycarbonate master molds.

We have applied this method to fabricate structured polymer films made of poly(3,4-ethylenedioxy-thiophene):poly(styrene sulfonate) (PEDOT:PSS) as it is commonly used as electron blocking layer in OSCs. In such devices a complete substrate coverage with PEDOT:PSS is crucial in order to fully utilize the properties of the interfacial layer. Figure 3.19a shows the total final film thickness d_{wet}^{tot} of the fabricated structured PEDOT:PSS film in dependence on the applied external pressure P_{wet}. The film thickness is adjustable between 100 and 250 nm by varying the applied pressure. However, it was observed that for film thicknesses below the actual structure height of the applied master molds (in the present investigation: h_{struct} = 175 nm) the fabricated textured films are defective and the substrate is not fully covered (see Fig. 3.19c), whereas in case of thicker films perfect polymer structures are formed (Fig. 3.19b). Substrates with a size of up to 20 x 30 mm^2 are coated homogeneously.

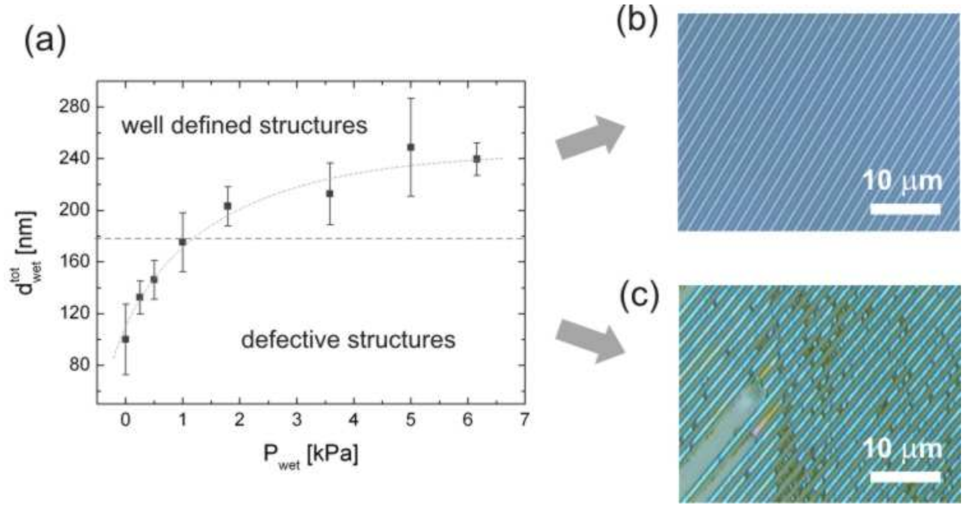

Figure 3.19:
(a) The overall film thickness is plotted with respect to the applied pressure during imprinting. The optical micrographs show (b) perfect imprints for films with a thickness above 175 nm and (c) incomplete structures for thinner films.

In order to prove the presence of a homogeneous PEDOT:PSS layer underneath the polymer structures in figure 3.20 a scanning electron microscopy (SEM) image of such a channel structure with an overall film thickness of 250 nm is shown taken at an incident angle of 50°. Since the imprinted channels have a height of 175 nm the homogeneous layer thickness is around 75 nm. Explicitly also the area between the fabricated structures shows a smooth PEDOT:PSS film.

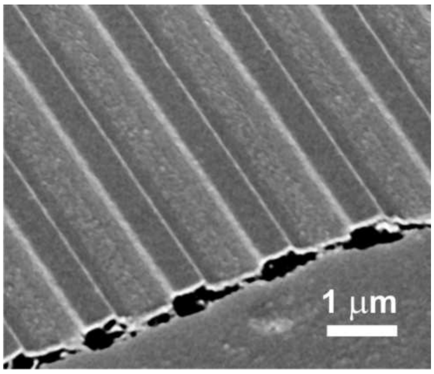

Figure 3.20:
The side view SEM image of the channel structures reveals a homogeneous polymer layer underneath.

In summary, we developed an easy structuring routine which allows for the fabrication of polymer structures on top of a homogeneous polymer layer. The key advantage of this approach is that it does not require any high temperature or other cost intensive fabrication steps. In order to prove the wide application possibilities of the structuring routine also gratings made of thermoresponsive polymer have been fabricated.[3]

[1] E. Kim, Y. Xia and G. M. Whitesides, *Nature* **376**, 581-584 (1995).

[2] S. Y. Chou, P. R. Krauss and P. J. Renstrom, *Science* **272**, 85-87 (1996).

[3] R. Meier, F. Markl, C. Birkenstock and P. Müller-Buschbaum, *J. Mater. Chem.* **22**, 192-198 (2012).

4 Polymer films for applications in photovoltaics

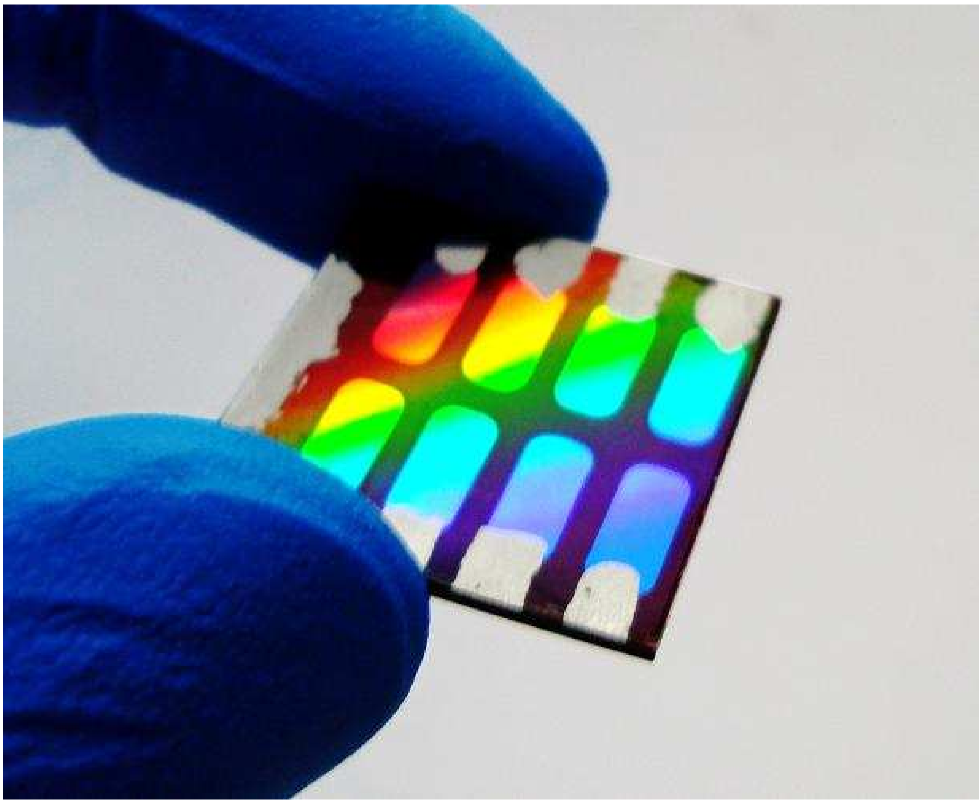

4.1 X-ray reflectivity measurements on ternary blend thin films for photovoltaic applications

E. M. Herzig, P. Müller-Buschbaum

Organic solar cells have established themselves as a promising candidate for future energy supply. Features like simple, cost effective production methods and shape versatility give this technology additional attractiveness compared to existing Si-based photovoltaic systems. However, analogous to other energy converting devices, one of the key properties for potential users are cost and efficiency. In recent years it has been shown that the efficiency is very much dependent on the morphology of the active layer of the solar cell [1].

In the present investigation we aim to gain understanding on the relationship between the morphology of the active layer and photovoltaic performance. So far mostly binary systems were under investigation, however, to tune the morphology in binary systems, there is only a limited set of parameters that can be varied. By adding a third component, a much wider range of parameters becomes accessible extending possibilities for altering the morphology of the active layer. So far there are several different approaches ranging from the aim to increase the absorption range with respect to wavelength to improving the efficiency of individual steps in the chain of charge processing. In most cases these properties are tightly knit, resulting in the fact that the exact working and the influence of various properties on an organic solar cell are not straight forward to understand.

Recently, it has been shown by Kim et al. [2] that the addition of an amorphous, non-photoactive polymer but charged electrolyte, PSS (polystyrene-sulfonate) to the standard and well-examined binary system P3HT:PC$_{60}$BM has a positive influence on efficiency. For a certain composition the efficiency of the ternary system is increased compared to the binary one. However, a morphology based understanding is still missing. Therefore we examine a similar system to connect performance with the internal structure of the active layer.

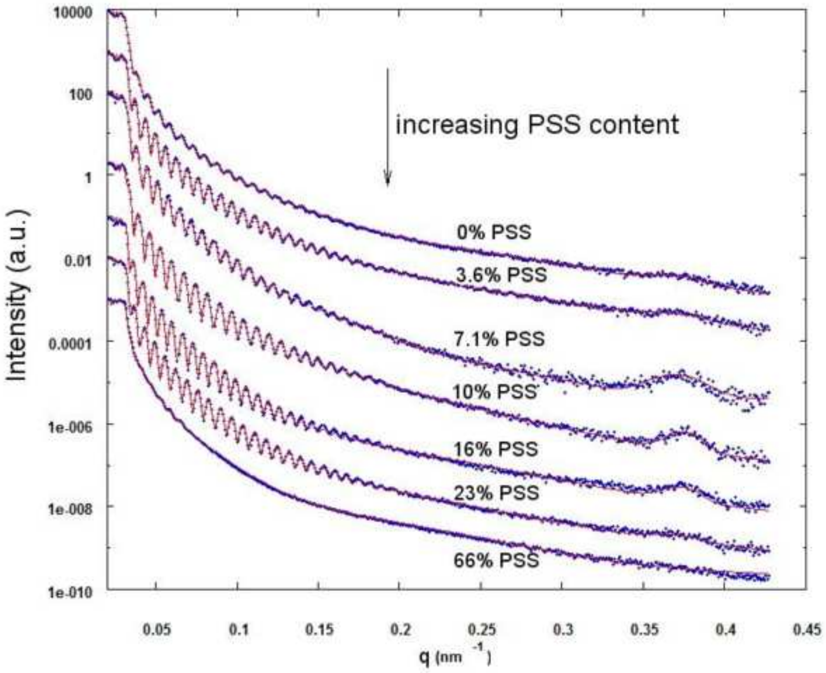

Figure 4.1:
X-ray reflectivity curves on thin film ternary blend samples containing different amounts of PSS given in % volume fraction. The P3HT:PCBM ratio is 50:50 for all samples. Data are shown in blue, fits obtained with the Parrat algorithm are shown in red. The thickness of samples extracted from the fits is 85 ±4 nm.

X-ray reflectivity is used to examine the vertical composition of the ternary system. The sample is probed at small incident angles θ up to 3° while the reflection is recorded at 2θ. Below the critical angle of the material total external reflection occurs, while above the critical angle the sample starts refracting the x-ray beam. In the latter regime the x-rays penetrate the sample and reflection can occur at refractive index variations within the film. The detected x-ray reflectivity curves are shown in figure 4.1. Using the Parrat algorithm it is possible to compute such reflectivity data and - by varying the assumed model - to fit the curves which is a powerful method because vertical refractive index profiles of the investigated films are obtained. This way even very complex, layered structures can be analyzed. While refractive index variations in binary films with sufficient contrast between the two materials can incontrovertibly be attributed to the one or other component this no longer holds for three component systems.

The investigated films have a thickness of 85 ±4 nm. The fits depicted in figure 4.1 are based on profiles of the real part of the refractive index with a low value enrichment layer near the substrate surface. This enrichment layer has a value that is not low enough for a pure layer but clear evidence for enrichment of either P3HT or PSS or both.

Additionally the reflectivity curves show the development of a pronounced peak at 0.38 nm^{-1}. This peak is weakly present in the binary blend and is most pronounced for the sample containing 10% PSS. The location of the peak coincides with the 100-separation distance of crystalline P3HT [3], indicating that P3HT in the binary blend orders differently in the presence of PSS. Namely, there is an increase in the amount of P3HT aligned in the edge-on orientation. Other orientations cannot be probed with this technique.

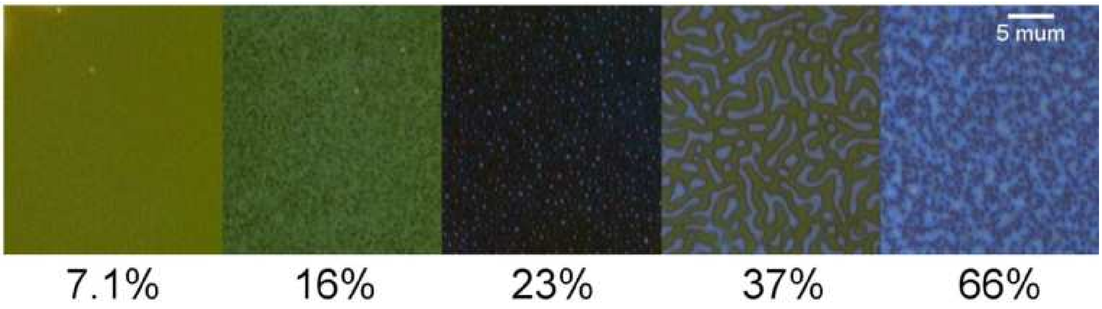

Figure 4.2:
Reflected light microscopy for ternary blend thin films containing different amounts of PSS. The magnification is 100x and the scale bar shown depicts 5μm.

While the reflectivity measurements provide laterally averaged information on the nanoscale, reflected light microscopy can resolve micron sized structures in the plane of the film. Reflected light microscopy images are shown in figure 4.2 and show domains of 300 nm for films with high 100-peak intensity. Increasing the volume fraction of PSS leads to larger domains, eventually turning into a large-scale bi-continuous pattern followed by a phase inversion. The light color of the continuous phase for high PSS content suggests that islands of the photoactive material are created in this regime resulting in the bad photovoltaic performances for high PSS content as shown by Kim et al. [2]. While for the binary blend film no features can be discerned in reflected light microscopy, the PSS induced phase separation for lower PSS concentrations might be connected to the increased crystallinity observed in the reflectivity measurements.

Additional experiments currently on the way will clarify the situation further.

[1] M. A. Ruderer, P. Müller-Buschbaum, *Soft Matter* **7**, 5482-5493 (2011)

[2] K. C. Kim, J. H. Park, O. O. Park, *Sol. Energy Mater. Sol. Cells* **92**, 1188-1191 (2008)

[3] S. Lilliu, T. Agostinelli, E. Pires, M. Hampton, J. Nelson, J. E. Macdonald, *Macromolecules*, **44**, 2725-2734 (2011)

4.2 Polymer blends in applications for organic photovoltaics

K. Wagenbauer, E. M. Herzig, P. Müller-Buschbaum

Organic photovoltaic is a hot topic of worldwide research. This is mainly due to the great potential of conjugated polymers to fabricate solar cells on a mass production scale at low-costs. Nevertheless a lot of challenges have to be overcome before final commercialization. Compared to the conventional competitive solar cells made of silicon, organic devices still provide low efficiencies. Recent investigations are therefore focusing on the improvement of organic solar cells. A well-known and strongly investigated system for organic solar cells is the combination of poly(3-hexylthiophene-2,5-diyl)(P3HT) and phenyl-C61-butyric-acid-methyl-ester (PCBM). Many approaches have been made to improve this system. One approach focuses on the improvement of the morphology by adding a third component. For example, Kim et. al improved the efficiency by adding a third component to the well known P3HT:PCBM system. The ternary system consisted of P3HT, PCBM and A-Lithium-polystyrenesulfonate better known as PSS. In a certain ratio of the three components the performance of the solar cells increased about 30 percent compared to the reference binary P3HT:PCBM cell. [1] A detailed understanding of such improvement is still missing. Thus in the present investigation, we are investigating in which way PSS takes influence on the morphology of the P3HT:PCBM system.

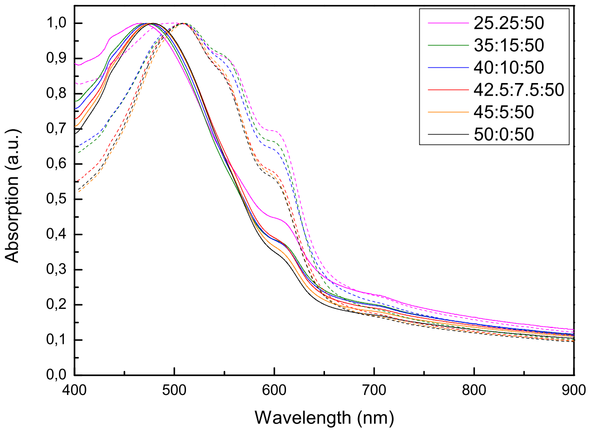

Figure 4.3:
Absorption spectrum of P3HT:PSS:PCBM films in different blending ratios normalized to the main peak caused by P3HT: not annealed (line) and annealed (dashed line)

In a first step of our investigation the layer thickness of PSS films depending on the PSS concentration used for spin-coating is investigated. The film thickness is determined with XRR. We observe a linear correlation between concentration and film thickness. The corresponding PSS concentration is calculated for an aspired film thickness of 85 nm. This is necessary to compared sample with one fixed film thickness and thereby to avoid thickness dependent effects. In a next step the films are investigated with optical microscopy, UV-Vis measurement and photoluminescence measurement. These measurements are performed in order to get information about surface structure as well as morphology. Optical microscopy provides information about homogeneity and defects of the films. The way the films are produced guarantees defect-free and reproducible films. UV-Vis measurements provide information about the morphology of the films. Figure 4.3 shows the respective curves of the ternary system. The curves are normalized to the main peak of P3HT to point out the changes due to changed composition. A significant peak at 500 nm and two vibronic shoulders at 550 nm and 600 nm are observed. After annealing (dashed line) a red-shift is seen. This overall red-shift as well as the increasing shoulders are both typical for higher order within the P3HT. Such increased order can be caused by increasing interchain interaction among P3HT chains. A red-shift also indicates an increase of the conjugation length. Due to this, more delocalized conjugated π-electrons are lowering the band gap between HOMO and LUMO and increasing the optical π-π^*-transition causing the observed red-shift. [2]

A selection of four blend samples is investigated with grazing incidence wide angle x-ray scattering (GIWAXS). GIWAXS provides detailed information about the molecular morphology and the crystallinty of the blend films. Figure 4.4 shows the GIWAXS data of the samples. All displayed GIWAXS data show evidence of crystalline structures from scattering as rings and Bragg peaks. Cake integration in horizontal and vertical direction provides information about the morphology of the crystalline component, e.g. P3HT. By focusing on the cake integration in vertical direction the [100] peak of P3HT has the highest intensity. The 40:10:50 sample has the highest intensity. Cake integration in horizontal direction provides information whether P3HT is ordered in edge or face-on direction. In can be seen that the [100] peak vanishes with increasing amount of PSS. Almost no face-on orientation is detected for the 40:10:50 sample. Additionally the increasing [100] peak in vertical direction is a further evidence for higher order in edge-on orientation.

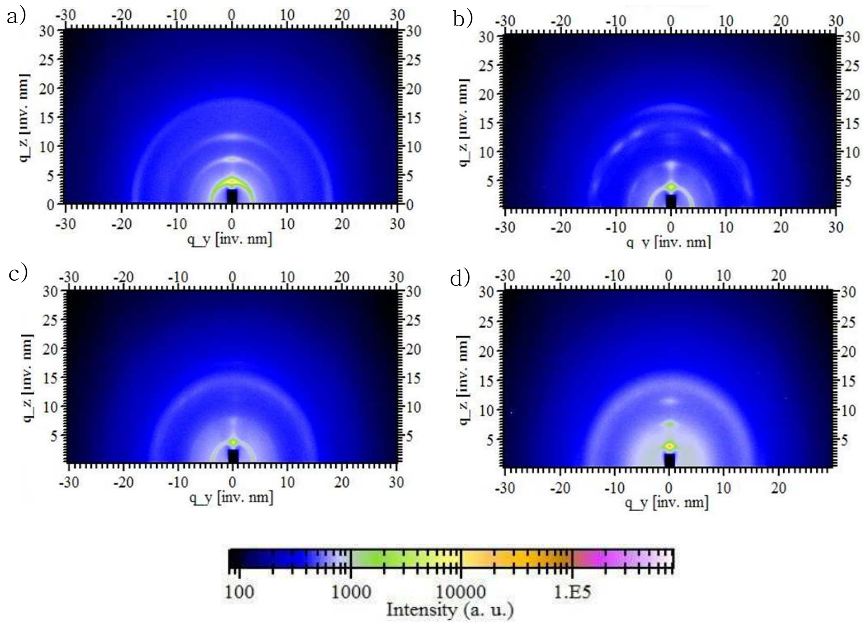

Figure 4.4:
GIWAXS scattering images for different samples: a) Pure P3HT, b) P3HT:PCBM, c) P3HT:PSS:PCBM (42.5:7.5:50) and d) P3HT:PSS:PCBM (40:10:50).

In addition to the structural characterization, the P3HT:PSS:PCBM samples are investigated with an electrical characterization. The above mentioned improvements in structure and morphology cannot be displayed within the efficiency of the solar cells. With increasing PSS content we observe an increasing series resistance which could be caused by higher contact resistance. Although the performance of the solar cells could not be improved we observe positive effects of PSS-addition on the crystal order of P3HT.

[1] K. C. Kim, J. H. Park, *Sol. Energ. Mat. Sol. Cells* **92**, 1188-1191 (2008)

[2] G. Li, V. Shrotriya, Y. Yao, Y. Yang, *J. Appl. Phys.*, **98**, 43704 (2005)

4.3 Nanostructured interfaces and degradation in PCBM:HBC(CuPc) solar cells

C. M. Palumbiny, S. Lindner[1], L. Schmidt-Mende[1], P. Müller-Buschbaum

[1] Hybrid Nanostructures, LMU München

One of the keys for the improvement of organic photovoltaic (OPV) devices is the precise control of the heterojunction morphology. A promising alternative approach (Fig.4.5 a) to augmenting of the blend morphology of a two component active layer system is introduced in the present investigation. The interdigitated interface of the organic components on the nanometer length scale allow for comprehensive exciton harvesting in the active layer and provide ideal charge extraction pathways for separated charge carriers towards the electrodes. Thus increased current generation and reduced bimolecular recombination can be expected in these OPV devices compared to a bilayer structure. Experience in fabrication techniques including solution processing and vacuum sublimation techniques [1] as well as different device geometries [2] enables us to study the device physics of these novel architectures in OPV devices.
Using anodized aluminum oxide (AAO) hard templates as stamps, the nanostructured organic layers on ITO support can be realized [1]. Precise control of the anodization process facilitates the control of the template dimensions including pore length, inter pore distance and pore diameter. As shown recently, a direct replica of the template structure can then be transferred to a layer of organic compound [1,3]. To provide a well-defined interface between the two active materials it is necessary to use solution processing in combination with vacuum sublimation. This guarantees that the first layer remains rather than being dissolved by the solvent of a second spin cast solution. A spin cast film of PCBM is used as the electron acceptor in combination with the evaporated small molecules HBC or CuPc as the electron donor material.

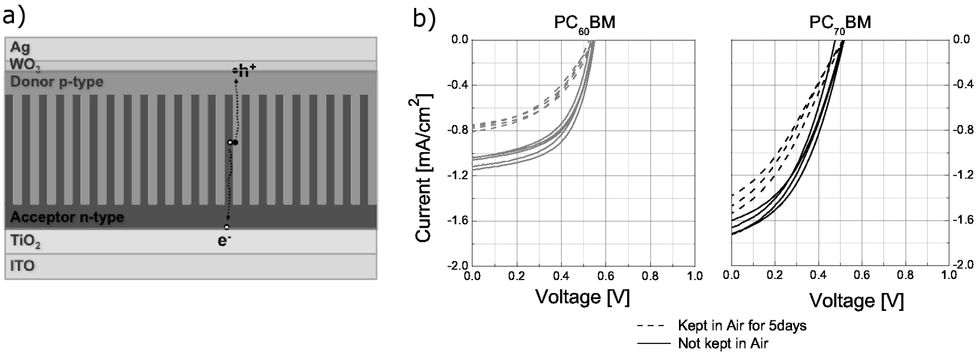

Figure 4.5:
a) Schematic of an interdigitated solar cell in inverted device geometry. **b)** Degradation of PCBM solar cells: storage of the PCBM layer for 5 days in ambient air is compared to storage in nitrogen atmosphere.

The fullerne C60 is known to degrade quickly if exposed to ambient air due to oxidization of the molecule. For air stable devices C60 molecules can be modified with side groups, as for example in the derivative PCBM. PCBM in OPV is commonly used in the polymer-fullerene blends P3HT:PCBM where it shows reasonable air stability. However, as we will show here, when used in a bilayer or nanostructure, PCBM shows a strong degradation when processed, heated or simply kept in ambient air. We could prove this effect for several layer combinations, PC60BM with HBC or CuPc. For PC70BM with HBC the same trend was observed, however with less strong effect (Fig.4.5 b). The observed degradation becomes even more distinct for structured PCBM which is referred to the larger surface area.

In order to study the influence of the nanostructured interface a reproducible aspect ratio of 0.5 is used in an inverted device geometry (Fig.4.6 a). For optimized comparison to the bilayer structure all cells are prepared in the same set and according to the experimental structure routine for the nanostructured devices. Fig.4.6 b shows the resulting current voltage (I-V) characteristics for varied HBC thickness and for both interface geometries. The inset shows the flat layer characteristics with a strong dependence on the upper layer thickness. Increased thickness leads here to a loss in short current density (I_{sc}) and a loss in fill factor (FF). This is due to lower exciton separation at the interface and higher recombination rates, respectively. For thick HBC layers excitons which are generated far away from the interface cannot reach the interface and recombine. As aconsequence, the FF decreases. Additionally, due to the overall very thin layers, the incident light is not completely absorbed during the first transit and therefore reflected at the top electrode. The intensity of the reflected transit near the PCBM/HBC interface for thick HBC layers is lower than for thin HBC layers due to the additional absorption. Thus for the thick layers an overall less charge carrier separation, extraction and therefore lower I_{sc} is observed. For thin HBC layers, all excitons can theoretically reach the interface during the incident and the reflected transit independent from the location of excitation which leads to the higher I_{sc}. In Fig.4.6 b the nanostructures cells are shown for comparison. Weaker thickness dependence is observed for the nanostructured interface introduced to the system. The pillar height of 20-30 nm lowers the resulting upper layer thickness due to material distribution into the pores and therefore decreases the thickness dependence. Therefore, the performance depends less in the total HBC thickness. However, the device performance of the nanostructured devices is lower than for the bilayer structures. We attribute this to a stronger degradation of the nanostructured PCBM layer in ambient air due to the increased surface area and possible higher recombination. As mentioned, the temperature of 120° C which is needed for the imprint routine even speeds up the degradation process.

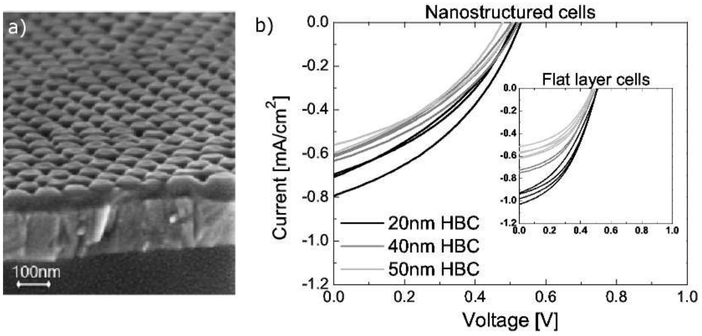

Figure 4.6:
a) SEM image of nanostructured PCBM. **b)** Bilayer cells compared to nanostructured cell (inset) for three HBC layer thicknesses.

The devices introduced here, especially the nanostructured devices are limited in their performance due to the degradation of the PCBM layer and the low aspect ratio of the nanostructure. Improving the imprinting process and transferring the process routine to nitrogen atmosphere, e. g. to a glove box, would not only increase the overall performance but also show the effect of the nanostructure more clearly. With the process routine introduced in this investigation we like to introduce the possibility of controlling the interface of the active layer on the length scale suitable for exciton diffusion and separation. Although the principle idea could be realized and is very promising, the process needs optimization to show better device performance.

[1] H. C. Hesse, D. Lembke, L. Dössel, X. Feng, K. Müllen, L. Schmidt-Mende, *Nanotechnology* **22**, 055303 (2011)

[2] J. Weickert, H. Sun, C. Palumbiny, H. C. Hesse, L. Schmidt-Mende, *Sol. Energy Mat. Sol. Cells* **94**, 2371-2374 (2010)

[3] W. Wiedemann, L. Sims, A. Abdellah, A. Exner, R. Meier, K. P. Musselman, J. L. MacManus-Discoll, P. Müller-Buschbaum, *Appl. Phys. Lett.* **96**, 263109 (2010)

4.4 Resonant soft X-ray scattering on conducting polymer films

M. A. Ruderer, C. Wang[1], A. Hexemer[1], P. Müller-Buschbaum

[1] ALS at LBNL, Berkeley, USA

In organic electronics typically a blend of two conducting polymers is used as the functional layer. This blended layer is mainly prepared by solution-based methods and the internal structure formation is controlled by a self-assembly process.[1] As the inner morphology of the functional layer is highly important for the device properties also the exact knowledge on the morphology as well as the structure formation are crucial. Scattering techniques are suited to probe the morphology in such systems without destroying them. However, for some material combinations the scattering contrast is rather limited. Therefore, resonant scattering is used to improve the contrast.

Scattering at the X-ray absorption edge of matter is called anomalous and resonant scattering for hard and soft X-rays, respectively. The absorption edge of polymers which are mainly consisting of carbon atoms is about 290 eV and therefore in the soft X-ray regime. In the region of the absorption edge of a material the refractive index is changing dramatically with the X-ray energy. In addition, the chemical structure of the molecule influences the shape and position of the absorption edge. Consequently, the material sensitivity of soft X-rays can be tuned easily by changing the energy.

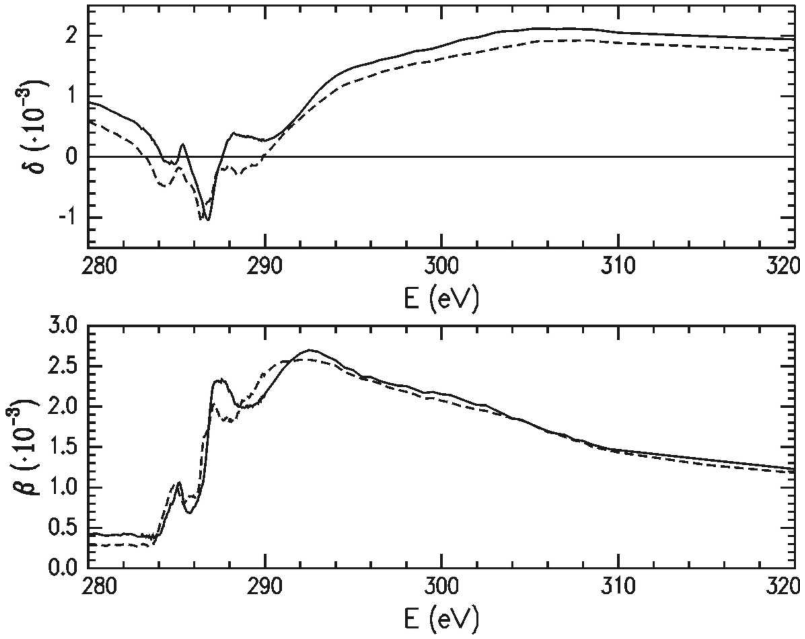

Figure 4.7:
The dispersion δ and the absorption β of P3HT (solid line) and MEH-CN-PPV (dashed line) for soft X-rays with an energy from 280 eV to 320 eV. The dispersion δ is calculated from the measured absorption β via the Kramers-Kronig integral relation.

The calculation of the exact energy-dependent refractive index $n = 1 - \delta + i\beta$ of an organic molecule at the absorption edge is almost impossible. Therefore, the absorption spectra β are measured using near edge X-ray absorption fine spectra (NEXAFS) measurements. The dispersion δ can be calculated by applying the Kramers-Kronig integral relation to the absorption spectrum which has to be extended to lower and higher energies using tabled values. In Fig. 4.7 the dispersion δ and the absorption β of the two conjugated polymers poly(3-hexyl-thiophene-2,5-diyl) (P3HT) and poly(5-(2-ethylhexyloxy)-2-methoxy-cyanoterephthalylidene) (MEH-CN-

PPV) are shown. The dispersion δ can be, in contrast to hard X-rays, for energies at the absorption edge negative. Moreover, the absorption β is in the order of 10^{-3} and therefore the penetration depth is in the range of the polymer film thickness of about $80\ nm$. By changing the X-ray energy the scattering contrast between P3HT and MEH-CN-PPV as well as the penetration depth can be tuned. In general, the scattering strength for soft X-rays is much higher than for hard X-rays when performing an experiment with soft matter.
We investigate the all-polymer blend of MEH-CN-PPV and P3HT with different blending ratios using resonant soft X-ray scattering in grazing incidence geometry (GISoXS) at the beamline 11.0.1.2 (ALS at LBNL). From the scattering experiment information on vertical material composition as well as lateral structure is extracted. Due to changing the X-ray energy the surface sensitivity can be altered. In Fig. 4.8 the 2d scattering patterns for different blending ratios at two different X-ray energies are shown. For 282 eV the penetration depth is larger than the film thickness and therefore the full film is probed. This is also visible from the oscillations, called correlated roughness, in vertical direction which reveals the polymer film thickness. To probe the surface structure only, the energy is changed to 288 eV with a penetration depth of several nanometers only. Consequently, the correlated roughness vanishes and only surface structures are resolved. From the scattering intensity in horizontal direction lateral length scales are extracted. The thin films of MEH-CN-PPV:P3HT blends reveal mixing ratio dependent structure sizes which are very similar for both energies. Thus, the surface structures dominate the overall morphology. Lateral length scales from 1 μm to 3 μm are probed. A maximum in lateral structure size is obtained at a blending ratio of 44 wt%.

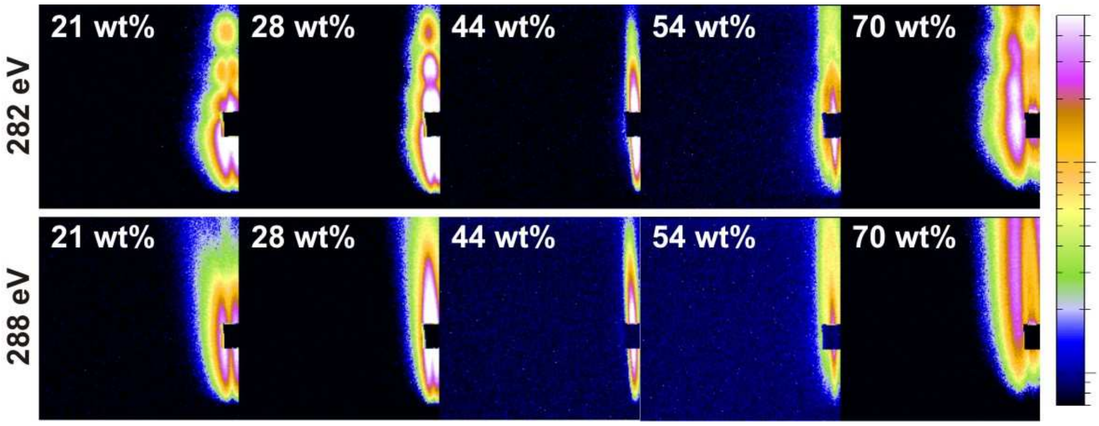

Figure 4.8:
2d scattering pattern of MEH-CN-PPV:P3HT blend with different blending ratios as depicted in the images. The data are measured at X-ray energies of 282 eV (top row) and 288 eV(bottom row).

In summary, resonant soft X-ray scattering in grazing incidence geometry (GISoXS) is used for the first time to probe the morphology in thin films and blending ratio dependent structural length scales are found. Tuning the penetration depth offers the possibility to change the surface or rather bulk sensitivity. However, for a more detailed structural information including structural length scales, object sizes and distributions the scattering data have to be modeled. The found morphologies will be compared with topography measurements and spectral characterizations.[2]

[1] M. A. Ruderer, P. Müller-Buschbaum, *Soft Matter* **7**, 5482-5493 (2011).

[2] M. A. Ruderer, C. Wang, A. Hexemer, P. Müller-Buschbaum, in preparation.

4.5 Modified surface of CNT electrodes for flexible all polymer solar cells

W. Wang, M. A. Ruderer, P. Müller-Buschbaum

Recently, organic solar cells attracted great attentions due to their unique features, such as light weight, easy processibility, potential low costs and flexibility [1]. Presently, indium tin oxide (ITO) electrodes are the typically used electrodes in organic solar cells. Although these ITO electrodes have high transmission and high conductivity, their mechanical rigidity limits an application in flexible and large area solar cells. Moreover, the worldwide known amount of indium is extremely limited and will make a mass production cost-intensive. So a replacement of ITO electrodes is of interest. Among the most promising alternatives to ITO electrodes are carbon nanotube (CNT) films due to their higher flexibility, similar transmission and lower costs as compared to ITO electrodes. However, the disadvantages of CNT films, such as high surface roughness and low surface energy, still limit its application as electrodes in solar cells. Therefore, modifications of CNT electrodes are needed to improve the performance of the solar cells.
In our investigation, CNT films on poly(ethylene terephthalate) (PET) are chosen as flexible electrode. Poly(3,4-ethylenedioxythiophene):poly(styrenesulfonate) (PEDOT:PSS) is spin coated on top of the CNT film to modify the surface morphology. The contact between PEDOT:PSS and CNT layers is improved by adding methanol in PEDOT:PSS solution. The resulting surface structure is investigated with atomic force microscopy (AFM). The thickness, surface roughness and sheet resistance of the PEDOT:PSS layer with different amounts of methanol are probed by X-ray reflectivity (XRR) and four point probe measurements.

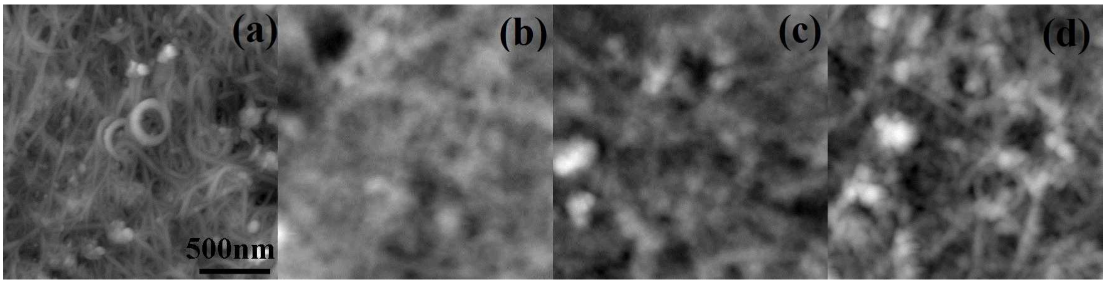

Figure 4.9:
AFM images of a) CNT film on PET foil, b) pure PEDOT:PSS film on CNT/PET, c) PEDOT:PSS film with 33% volume fraction methanol on CNT/PET and d) PEDOT:PSS film with 75% volume fraction methanol on CNT/PET with 2×2 μm^2 scan size.

Fig 4.9a presents AFM image of CNT/PET film. It is obvious that the CNTs are cross linked and bundled together which attributes to the high conductivity of CNT film. The roughness of the CNT film is approximately 13 nm. Considering such high roughness, some CNTs could penetrate the active layer placed on top of the CNT film, which would result in a short cut of the solar cells. To address this problem, the PEDOT:PSS layer is coated on top of the CNT layer. The contact between the PEDOT:PSS and the CNT layers is critical for the solar cell performance. The better contact introduces lower parallel resistance, which gives rise to high short circuit current and high efficiency. Usually, O_2 plasma is selected to improve the surface energy of electrodes, which contributes to the good contact between PEDOT:PSS layer and electrodes. But for CNT film, the O_2 plasma degenerates the CNTs, which makes the CNT electrodes insulating. Therefore methanol is added to the PEDOT:PSS solution to replace the O_2 plasma treatment. During the PEDOT:PSS deposition process, it is found that with more fraction of methanol, the wetting property of PEDOT:PSS solution on CNT/PET film is improved. It is inferred that adding methanol is an effective way to improve the wetting of the CNT layer with PEDOT:PSS.

For further investigation, PEDOT:PSS layers with different volume fractions of methanol are prepared. The thickness of the pure PEDOT:PSS layer is 90 nm. In order to keep the film thickness of the layer made of PEDOT:PSS with methanol constant, the rotational speed in the spin coating process is altered. The resulting film thickness is controlled by XRR. The corresponding XRR curves are shown in Fig 4.10. The PEDOT:PSS films with a volume fraction of 33%, 50% and 75% methanol have a similar film thickness as the pure PEDOT:PSS film. The determined film thickness is 85 nm. For the PEDOT:PSS film with a volume fraction of 75% methanol a smaller thickness of 65 nm is found. Moreover, some holes on the surface of the PEDOT:PSS layer are present due to a too dilute PEDOT:PSS solution with 75% methanol. From the fitting of the XRR curves, not only the film thickness, but also the roughness is obtained (Fig 4.10a). It is obvious that with the higher volume fraction of methanol, the roughness increases. Furthermore, the sheet resistance of all the films is also probed and the results are shown in Fig 4.10b. Adding methanol increases the sheet resistance, and the higher volume of methanol induces larger deviations, indicating that the film becomes less homogeneous.

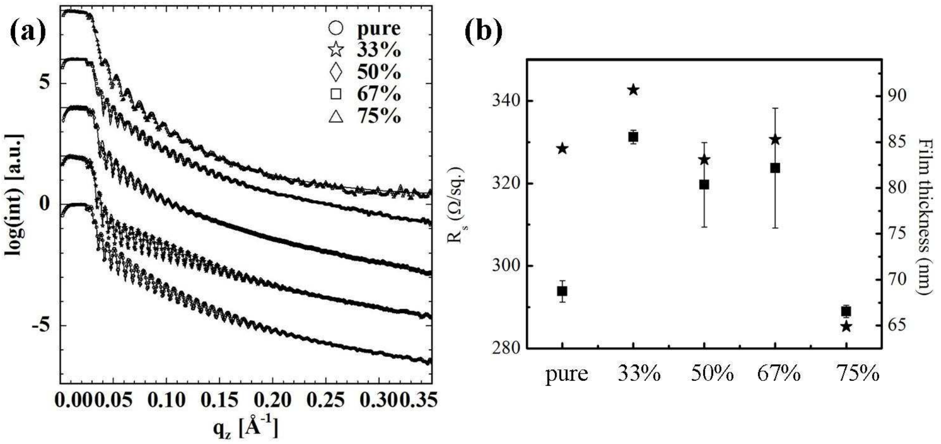

Figure 4.10:
a) XRR data (dots) with model fits (lines) of PEDOT:PSS film with 0, 33%, 50%, 67% and 75% volume fraction of methanol (as indicated). b) Film thickness and sheet resistance as function of volume fraction of methanol.

To detect the effect of methanol addition to the PEDOT:PSS solution on the surface topography, AFM measurements are performed. Fig 4.9b, c, d show the AFM images of pure PEDOT:PSS, PEDOT:PSS with 33% and 75% volume fraction methanol coated on CNT/PET films, respectively. It is found that the PEDOT:PSS layers follow the surface morphology of the underlying CNT substrate. At low methanol content the CNT structure is fully covered with PEDOT:PSS but with increasing methanol content it is becoming more pronounced again which is evidence for the better wetting of the CNT film. Due to the deposition of PEDOT:PSS the surface roughness is decreased by nearly 50% when compared to the initial CNT films. In conclusion, the methanol addition in PEDOT:PSS solution can improve the contact between PEDOT:PSS and the CNT substrate as well as decrease the surface roughness without changing the surface morphology of the pure PEDOT:PSS layer.

In summary, adding methanol in PEDOT:PSS improves the wetting of PEDOT:PSS on CNT substrates which is beneficial for a good electric contact. However, a too high amount of methanol causes a higher surface roughness and heterogeneities in the PEDOT:PSS films. Therefore, the volume fraction of 33% methanol is the optimum condition in our investigation.

[1] A. Pandey, J. Nunyi, *Appl. Phys. Lett.* **89**, 213506 (2006)

4.6 Influence of poly(4-vinylpyridine) on the binary blend system P3HT:PCBM

S. Ramirez, E. M. Herzig, P. Müller-Buschbaum

Due to potentially low cost production and its high flexibility, organic semiconductor systems have attracted increasing interest over the last years. In organic photovoltaic a widely-studied standard system is the well-known blend of P3HT and PCBM. [2] However, it is necessary to get a better handle on the structural assembly of the above-mentioned system, since the structural arrangement determines its performance. Latest investigations concentrate on the improvement of the morphology and the efficiency by adding a third component. In the present investigation the ternary system consists of poly(4-vinylpyridine) (P4VP), P3HT and PCBM. The core question is to identify in which way this system is influenced by P4VP. This third component, is known to build strong interactions with PCBM, as P4VP forms non-covalent bonds with PCBM. [1]
The first step in the production of thin and conductive polymer blend films is to find a common solvent for all three components. However, neither chlorobenzene nor 1,2-dichlorobenzene sufficiently dissolve this polymer, but chloroform successfully does. After this step, we proceed to determine the thickness-concentration relation for P4VP, this way the required concentration for a favorable layer thickness can be calculated, in our case the desired layer thickness is about 100 nm. The thickness of P4VP films is determined with white light interferometry.

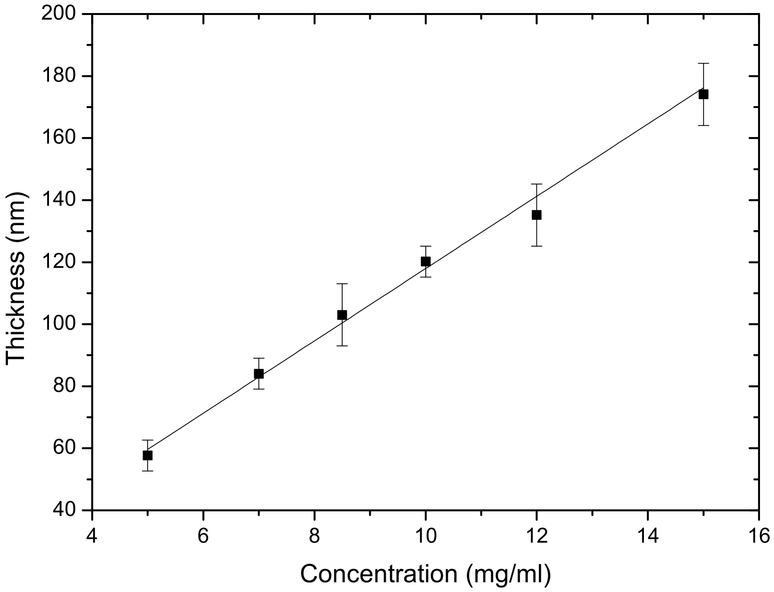

Figure 4.11:
Thickness of P4VP film as a function of concentration in the solution taken for spin-coating shown together with a linear fit.

According to the linear fit shown in figure 4.11 a concentration of 8.5 mg/ml is required for achieving 100 nm film thickness. Once this is established, we proceed to the preparation of polymer blend films with the same thickness. The blend films are made via spin coating onto silicon substrates which are pre-cleaned with a certain procedure. Different series of P3HT:P4VP:PCBM blends, based on different P4VP contents are investigated. To follow a procedure that is reproducible, the polymer blend films must have a uniform and equal layer thickness. Furthermore other aspects in absorption and emission spectrum that depend on the thickness can be eliminated and this way we can concentrate only on the morphology inside the blend films. The absorption and emission of the blend films are investigated using spectroscopic and microscopic methods. Apart from examining the as prepared films, the films are subsequently annealed for 10 min. Then we repeat the measurement with the above-mentioned techniques. By thermal annealing of the samples, the structure of the polymer film can also be influenced, since crystallinity increases and therefore the performance in organic cells can be improved.

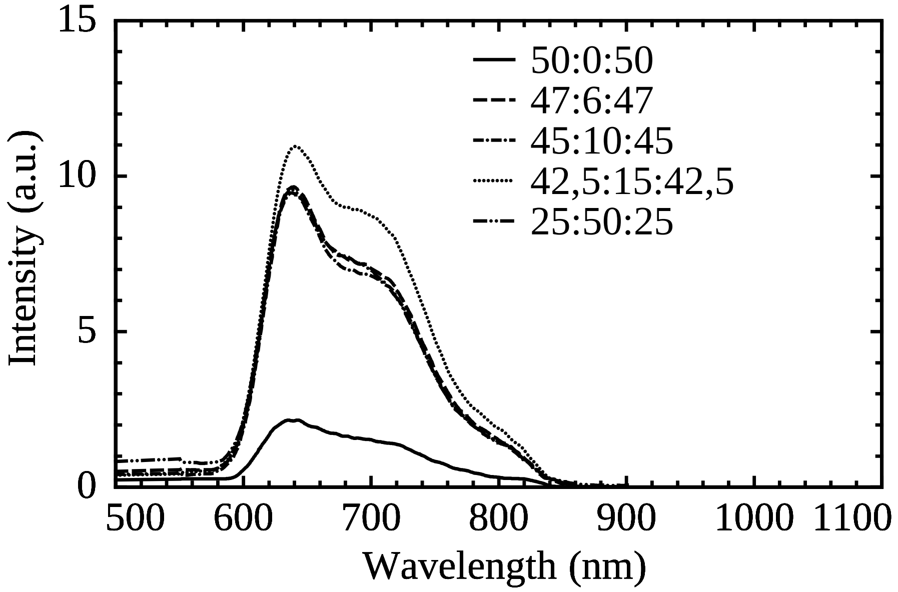

Figure 4.12:
Emission spectrum of P3HT:P4VP:PCBM blend films for different blending ratios after annealed.

The emission spectra of the P3HT:P4VP:PCBM blend films are determined with photoluminescence spectroscopy. Figure 4.12 shows these spectra of annealed films. For all compositions containing P4VP, independent of concentration, similar intensities are observed. In contrast, the intensity of the pure P3HT:PCBM system is reduced and thus photoluminescence is strongly quenched. Thus allover the efficiency in separating charges is reduced by the addition of P4VP. Interestingly, the addition of PSS gives a simple dependence in increasing photoluminescence with increasing amount of PSS. The reason for this different observation for P4VP might indicate a more complex interaction of the added P4VP to the binary blend PCBM:P3HT than expected. However, additional measurements concerning the photophysical behavior as well concerning the film morphology will be needed to gain a better understanding of this observation.
Moreover, the films will be measured with X-ray reflectivity, in order to characterize the roughness of surfaces, the thickness and the scattering length density profile of thin films. In conclusion the aim of this research is to influence and examine the effects on the internal structure induced by a third component and therefore gain understanding on how to improve solar cell performance.

[1] N. Sary, F. Richard, C. Brochon, N. Leclerc, P. Leveque, J. N. Audinot, S. Berson, T. Heiser, G. Hadziioannou, R. Mezzenga, *Adv. Mat.* **22**, 763-768 (2010)

[2] E. S. Shaheen, J. C. Brabec, S. N. Sariciftci, F. Padinger, T. Fromherz, C. J. Hummelen, *Appl. Phys. Lett.* **78**, 841-843 (2001)

4.7 Evolution of lateral structures during the functional stack build-up of P3HT:PCBM based bulk heterojunction solar cells

S. Guo, M. A. Ruderer, M. Rawolle, V. Körstgens, J. Perlich[1], S. V. Roth[1], P. Müller-Buschbaum

[1] HASYLAB at DESY, Hamburg, Germany

Relatively high performance polymer bulk heterojunction (BHJ) solar cells, based on a self-assembly phase separation of an electron-donating conjugated polymer P3HT (region-regular poly(3-hexythiophene)) and an electron-accepting fullerene PCBM(phenyl-C61-butyric acid methyl ester), have become of great interests over the past years. These systems offer a low-cost, flexible, light renewable energy source. Although the efficiency of this kind of polymer-based solar cells has been improving continuously and reached 7-8 % [1], the in-depth knowledge about the inner morphology of these solar cells is still limited. Therefore we investigate the inner morphology with GISAXS (grazing incidence small angle x-ray scattering) as a function of a multilayer stack build-up.

From GISAXS measurements, the buried structure inside the thin films or multilayer systems are obtained with mesoscopic resolution and without damaging the sample. As seen from the two-dimensional GISAXS images shown in figure 4.13a, strong intensity oscillations are observed for all the probed samples. These intensity oscillations are due to resonant diffuse scattering caused by rough and laterally disordered ITO surface, which roughness spectrum is replicated by the following thin films. To have a better understanding of the roughness correlation, as well as the lateral structure information, the analysis of detector cuts and out-of-plane cuts is required.

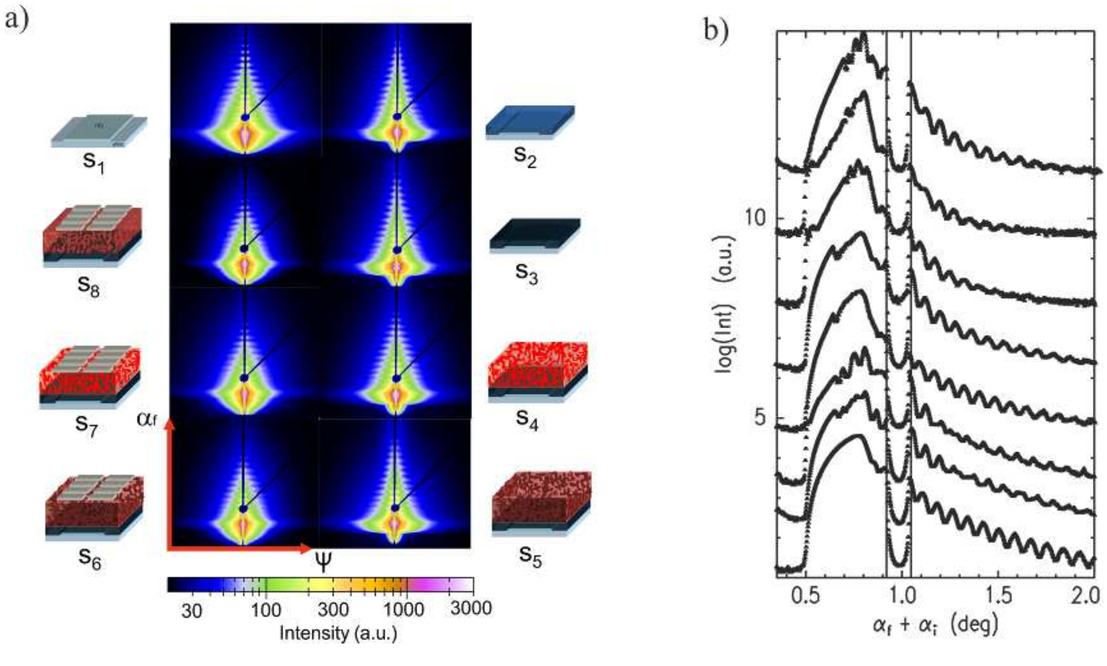

Figure 4.13:
(a) Composition of 2D GISAXS data as the function of the device built-up. In each image, exit angle of the X-ray beam α_f is plotted out versus the out-of-plane angle ψ. The intensity is shown in logarithmic scale. (b) Vertical cuts of the 2D GISAXS data shown as a function of the detector angle $\alpha_f + \alpha_i$ for the different steps of the functional stack build-up (S1 to S8 from bottom to top).

In the detector cuts shown in figure 4.13b, the specular reflected x-ray beam is shielded by a beamstop to protect the detector (at $\alpha_f + \alpha_i \approx 1.00^\circ$). The peaks at lower angles are the Yoneda peaks, which are material dependent features. Strong oscillations are observed at larger angles for all probed samples due to roughness correlation originated from the ITO substrate. In addition, a beat frequency type of modulation of the intensity osciallaitions is established for the samples S2 and S3, indicating a similar thickness between ITO and PEDOT:PSS layer, which is around 80 nm given by x-ray reflectivity measurement.

Lateral structural information is gained from the out-of-plane cuts (see figure 4.14). Fitting of the data is performed within the model of the effective surface approximation. As a result, the lateral structure size of ITO stay constant (105 nm) during the additional layers built-up on top, so is the lateral structure of the aluminum electrode (95 nm). However, the size of P3HT domains varies from sample to sample, which is directly related to the performance of the solar cells. The I_{sc}, U_{oc}, FF, and η of differently prepared solar cells are present in table 1. I_{sc} varies dramatically depending on the preparation route and post treatment. U_{oc}, however, rather remains constant for all the solar cells as it is expected (0.55±0.4 V), because it is determined by the difference between the HOMO of the donor and the LUMO of the acceptor. Further investigation with IsGISAXS is needed to fully address the correlation between vertical structural size of P3HT and solar cell performance.

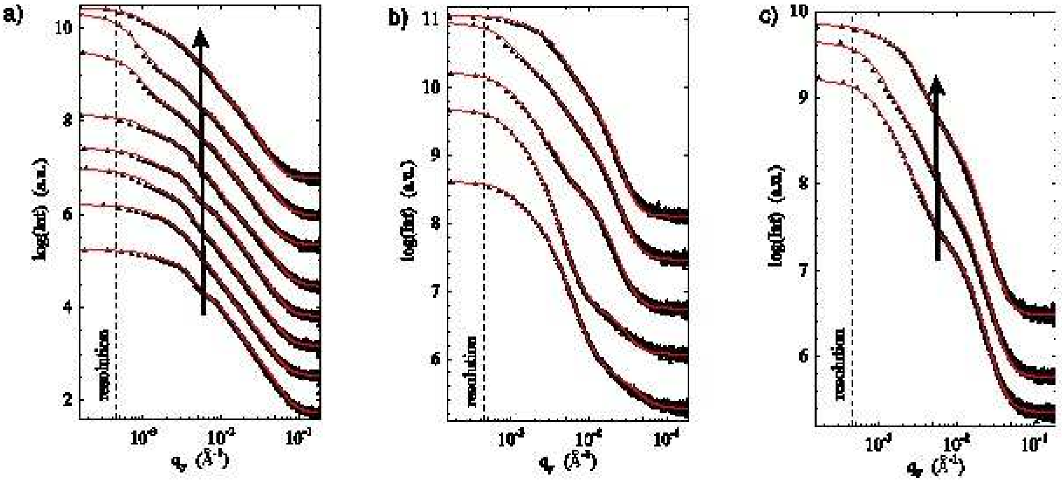

Figure 4.14:
Double-logarithmic plots of the out-of-plane cuts at the critical angles for a) ITO (from S1 to S8), b) P3HT (from S4 to S8), and c) aluminum (from S6 to S8). Solid lines are the fits with the so-called effective surface approximation to determine the prominent in-plane length scales.

sample	I_{sc} (mA/cm^2)	U_{oc} (V)	FF (%)	η (%)
S6	7.59	0.59	42.37	1.65
S7	5.60	0.56	47.21	1.52
S8	11.37	0.59	53.71	3.61

Table 1: I_{sc}, U_{oc}, FF, and η of solar cells annealed before deposition of aluminum, as-spun, and annealed afterwards.

In summary, the functional stack build up is followed via GISAXS, which is well suited to determine the mesoscopic lateral structures. The roughness correlation and the inner structure information are correlated with the device performance.

[1] Y. Liang, Z. Xu, J. Xia, S.T. Xia, Y. Wu, G. Li, C. Ray, L. Yu, *Adv. Mater.* **22**, E135 (2010)

4.8 The influence of PEDOT:PSS layer thickness on ternary bulk heterojunction based organic photovoltaic cells

B. H. Stafford, E. M. Herzig, P. Müller-Buschbaum

Tin-doped indium oxide (ITO) has long been a favorite transparent conducting oxide for the purposes of hole extraction in organic photovoltaic devices with its relatively high work function of 4.3-4.8 eV [1]. However, poly(3,4-ethylenedioxythiophene):poly(styrenesulfonate) (PEDOT:PSS), with the molecular structure as seen in figure 4.15, has shown an even lower hole extraction barrier of 5.2 eV [2]. This coupled with its mechanical flexibility as a polymer, its high transparency and its comparatively easy deposition compared to ITO has made PEDOT:PSS a forerunner in research into increasing performance in modern organic photovoltaics. In particular, it has been extensively studied in conjunction with the highly successful binary P3HT:PCBM system.

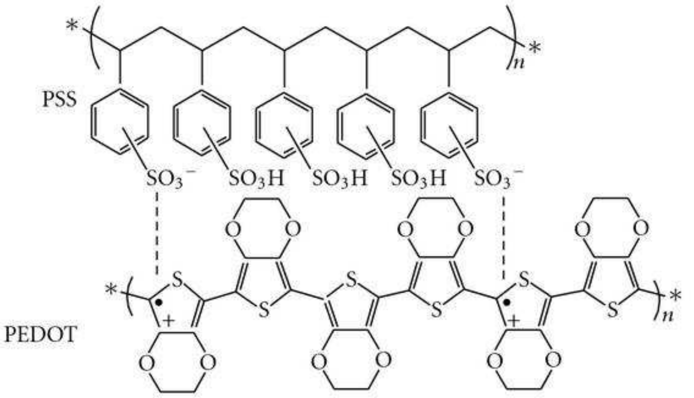

Figure 4.15:
The chemical structure of (a) PSS and (b) PEDOT. The dashed line indicates the conjugation path through the PEDOT. [5]

The inclusion of a PEDOT:PSS layer has shown to be influential on the power efficiency of bulk heterojunction active layer solar cells containing just two components (for example P3HT:PCBM, PFB:PDI, F8TBT:P3HT). Kim et al. have shown, that the thickness of the PEDOT:PSS layer does not strongly effect device performance [3], however Friedel et al. showed that the surface roughness, which is dependent on layer thickness, does effect the dark current density and the open-circuit voltage [4]. No measurements on the other hand have as of yet been made on ternary polymer bulk heterojunction systems. For this reason the effect of PEDOT:PSS layer thickness upon the power conversion efficiency of a solar cell based on a P3HT:PSS:PCBM bulk heterojunction will be carried out.

Firstly, an investigation will be made into the limit of deposition thickness via spin coating of PEDOT:PSS onto glass substrates. Experiments will then be carried out to determine the effect of PEDOT:PSS layer thickness on cell performance via construction of a cell of the structure depicted in figure 4.16.

For the former experiments, white light interferometry is the characterization method of choice for determining the polymer layer thickness and morphology. This often is a favored technique for nanomaterial characterization as it is non-destructive, can more easily measure larger areas compared to AFM and can measure to a vertical (i.e. height) resolution of as little as 0.01 nm. Being an optical technique, however limits lateral resolution to around 0.35 μm. The basic working technique firstly relies on light from a single source being split. One beam follows a known

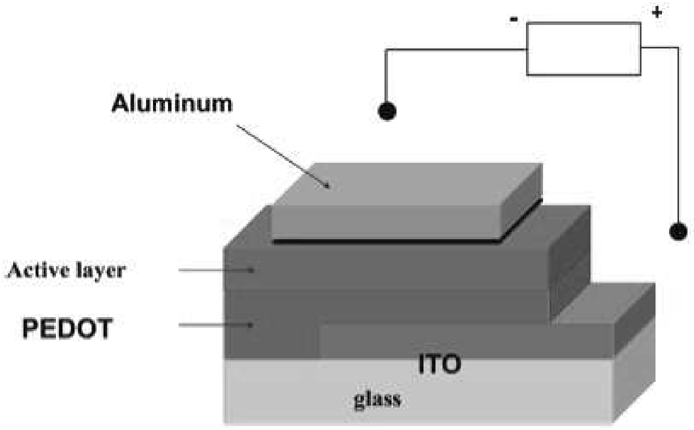

Figure 4.16: Schematic for the device structure of a conventional bulk heterojunction solar cell [6]

and constant path to a reference while the other is reflected from a sample surface. The two reflections are then combined, creating an interference pattern. Vertical movement of the objective lens allows for determination of the point at which maximum constructive interference occurs. Following this a 3D map of the sample surface can be constructed. Simultaneously using light of multiple wavelengths (i.e. white light) eliminates the possibility of there being multiple points at which the maximum constructive interference occurs from the same surface features.

For the preparation of samples for thickness measurement, glass substrates of 28x28 mm were cut and cleaned in an acidic solution of a 4:1 ratio of 96% sulphuric acid to 30% hydrogen peroxide in deionized water. The purpose of this was to remove organic matter from the glass surface and to make the glass more hydrophilic.

PEDOT:PSS (Sigma-Aldrich, 1.3 wt% dispersion in H2O) was then allowed to redisperse in a sonication bath for 15 minutes before spin-coating on the surface of the glass. Spin speeds ranging from 2000 - 6000 rpm were used with a duration of 60 seconds each. Following this, the thickness and morphology of the deposited films are to be measured via white light interferometry.

Sample roughness is expected to depend on the length of time spent by the PEDOT:PSS dispersion in the sonication bath. This parameter will therefore initially be kept constant. It could however be taken as a factor for optimization of performance once the stage of cell construction has been reached. Results are expected to be in agreement with Friedel et al., i.e. there being a variation in dark current density and open circuit voltage. However this is not yet certain for ternary systems such as P3HT:PSS:PCBM. If there is a variation in these parameters and therefore cell performance, more consideration must be given to PEDOT:PSS layer thickness than previously believed, especially when constructing cells of this type.

[1] C. C. Wu, C. I. Wu, J. C. Sturm, A. Kahn, *Appl. Phys. Lett.* **70**, 1348-1350 (1997)

[2] N. Koch, A. Kahn, J. Ghijsen, J. J. Pireaux, J. Schwartz, R. L. Johnson, A. Elschner, *Appl. Phys. Lett.* **82**, 70-72 (2003)

[3] Y. Kim, A. M. Ballantyne, J. Nelson, D. D. C. Bradley, *Org. Electron.* **10**, 205-209 (2009)

[4] B. Friedel, P. E. Keivanidis, T. J. K. Brenner, A. Abrusci, C. R. McNeill, R. H. Friend, N. C. Greenham, *Macromolecules* **42**, 6741-6747 (2009)

[5] J. Hwang, F. Amy, A. Kahn, *Org. Electron.* **7**, 387-396 (2006)

[6] J. S. Günes, H. Neugebauer, N. S. Sariciftci, *Chem. Rev.* **107**, 1324-1338 (2007)

4.9 Polyethylene induced structural modification of ternary polymer blends used in photovoltaic cells

A. Akhtar, E. M. Herzig, P. Müller-Buschbaum

Over the last decades, there has been an increased interest of research groups and industry in organic photovoltaics. Photovoltaic devices based on organic semiconductor systems such as poly(3-hexylthiophene) (P3HT): fullerene blends have been investigated by different research groups, because of their potential towards cheap and broad applicability. The tunability, processibility and flexibility of organic photovoltaics provide a broad range of applications. Furthermore the possibility of combining different polymer units to semiconducting polymers, enables it to adapt the absorption as well as the electrical behavior. Investigations have shown that the morphology of the active layer in such systems is a very important issue to gain reasonable device performance [1]. However, the achievement of mechanical stability under flexing or heating is one of the big difficulties [2].

In order to improve the morphology of organic materials in the solar cell, one approach is to add a third component, such as a commodity polymer, to the binary blends. It is reported that among different commodity polymers, high density polyethylene (HDPE) is a promising material for organic solar cells, because of the improvement in the photocurrent generation efficiency of such a system [3]. Furthermore, it is also expected that the use of HDPE instead of low density polyethylene (LDPE) provides a better control to the microstructure in the final photovoltaic cell, because of its highly crystalline nature [3]. In this work we investigate a ternary heterojunction system containing the conjugated polymer P3HT, the electron conductor PCBM and the commodity polymer HDPE. The system P3HT and PCBM was chosen because it is probably the best investigated polymer based system for photovoltaic applications.

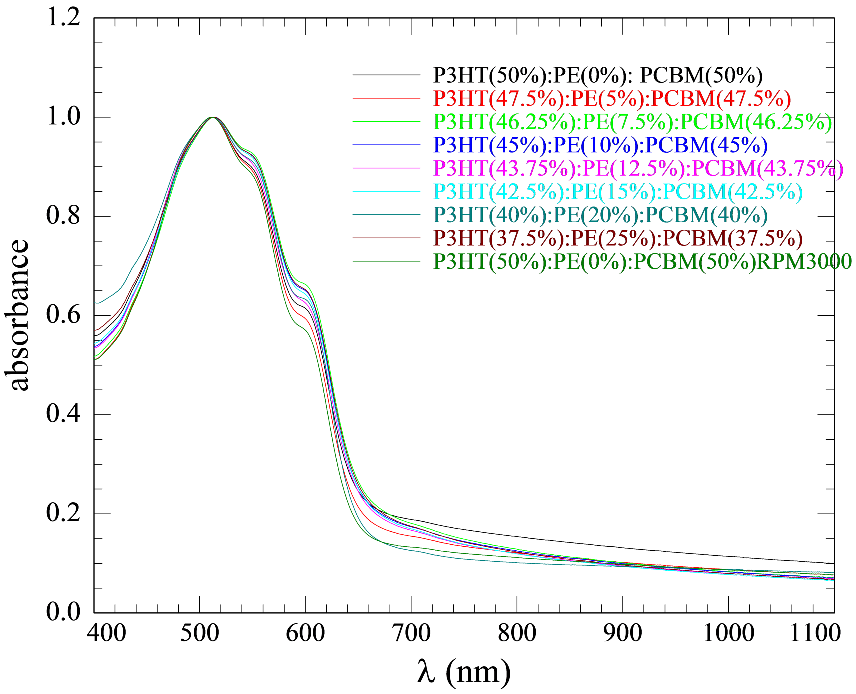

Figure 4.17: UV/Vis spectra normalized to maximum counts, after annealing at 140° C

An important step is the choice of a common solvent for the ternary system. Due to the high crystallinity of HDPE high temperatures are needed to dissolve the polymer. Therefore it was not possible to use chlorobenzene (boiling point 130°C) as in the standard system P3HT:PCBM. This leads to the selection of solvent which has a high boiling point. In this investigation trichlorobenzene is used which has a boiling point at 180°C. Furthermore, the spin coating at normal temperature leads to a crystallization process which in turn leads to an inhomogeneous film. Therefore all necessary equipment and substrates (silicon and glass) are preheated to 120°C and spin coating is also carried out at the same temperature (120°C).

In addition it is of importance, to have films of equal thickness to ruleout film thickness effects. The film thickness depends on several parameters, such as concentration, amount of solvent, spin coater speed etc. Due to the difficulty of producing smooth, pure HDPE films, the necessary HDPE concentration is obtained by varying the HDPE concentration in the ternary blend system at a fixed mass ratio of the three components. The film thickness has been measured with ellipsometry. In a first sample series the weight percentage of P3HT and HDPE (keeping HDPE concentration constant) is varied keeping PCBM constant at 50%. In a second sample series the HDPE content is varied, keeping P3HT and PCBM weight percentage constant. The optical absorption spectra of both sample series show a clear change. Shoulders increase as visible in the figure 4.17. In order to get more direct information about structural changes these two series are analyzed with grazing incidence small angle X-ray scattering (GISAXS). Lateral structural correlations and the vertical structure such as a domain geometry, size distributions and spatial correlations are probed with GISAXS. The 2D GISAXS data (see figure 4.18) indicate that the structure is changed as well. The detailed analysis of the GISAXS data is in progress.

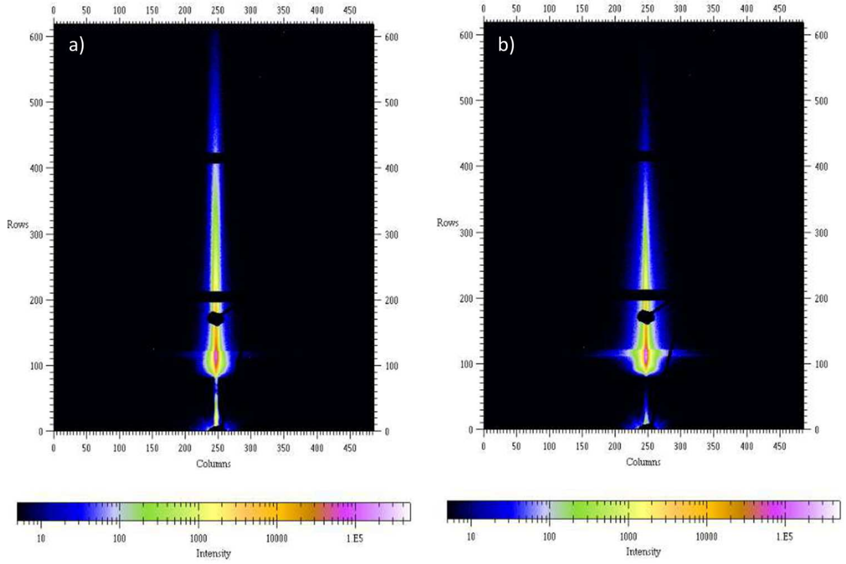

Figure 4.18:
2D GISAXS patterns of reference P3HT:PCBM (50:50) that is no HDPE (a) and maximum HDPE weight percentage P3HT:HDPE:PCBM (25:25:50)(b)

[1] M. A. Ruderer and P. Müller-Buschbaum, *Soft Matter* **7**, 5482-5493 (2011)

[2] T. A. M. Ferenczi, C. Müller, D. C. Bardly, P. Smith, J. Nelson, N. Stingelin, *Adv. Mater.* **23**, 4093-4097 (2011)

[3] S. Goffri, C. Müller, N. Stingelin-Stutzmann, D. W. Beriby, C. P. Radano, J. W. Andreasen, R. Thompson, R. A. J. Janssen, M. M. Nielsen, P. Smith, H. Sirringhaus, *Nat. Mater.* **5**, 950-956 (2006)

4.10 Influence of PSS on the morphology of P3HT:PCBM solar cells

A. Naumann, E. M. Herzig, P. Müller-Buschbaum

Polymer-based organic photovoltaics have attracted the worldwide interest over the last decades. Though still having low efficiencies and short lifetimes compared to their inorganic counterparts the advantages are more and more convincing. Some examples are the light weight property, the mechanical flexibility and the feasibility to fabricate organic solar cells on a mass production scale at low costs. At present, especially the exhaustless possibilities to vary the polymeric structure and thus the electronic characteristics attract the most attention for research. A very well investigated system for the active layer of organic solar cells is the combination of the fullerene-derivative PCBM as the n-type material and poly(3-hexylthiophene) (P3HT) as the p-type material. Mainly two topics are of great interest for such active layers. The first one is the tailoring of the blend morphology to the needs introduced by the two components. Due to the low absorption of the polymer, it is necessary to have an adequate thickness, which is in conflict with the exciton diffusion length (about 10 nm [1]), so that the blend should feature nanoscale interpenetrating networks. The second issue is the molecular arrangement of the thiophene polymer chains relative to each other. P3HT consists of a rigid backbone of conducting conjugated thiophene rings with non-conducting alkyl side groups, that are necessary for solubility reasons. Furthermore, particularly after annealing, the P3HT polymer chains tend to form stacked, two-dimensional crystallites, consisting of the backbones facing each other and hence forming a lamellar structure as shown in fig. 4.19 [2]. For such a lamellar structure the π -orbitals of the thiophene rings overlap and allow conduction from one lamella to the next. Thus there is only conductivity in two dimensions. Therefore it is of interest to manipulate the interactions within the active layer to gain control over the arrangement of the crystallites. In the present investigation we try to achieve this by adding a third component, which is polystyrenesulfonate (PSS). PSS is not conducting but it is an ionomer, i.e. it has a non-ionic part, which is well miscible with P3HT, and an ionic part, which may be miscible with PCBM [3]. Kim et al. postulate that it should interact with the P3HT and PCBM by reducing their interfacial energy, so that they form an interpenetrating network with a favorable structure size.

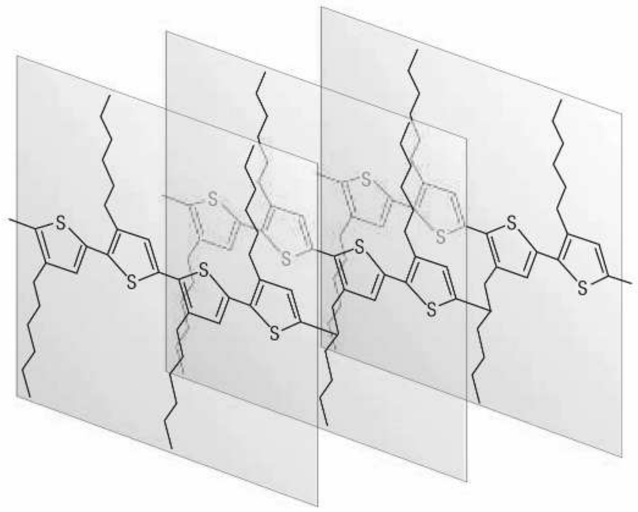

Figure 4.19: Illustration of the stacking of polythiophenes into an ordered lamellae (taken from reference [2])

First of all the best mixing ratio of the three components P3HT, PCBM and PSS has to be established. The first step in making films with different blending ratios is to make sure that they all have the same thickness, since samples with different film thicknesses cannot be compared in their structure due to various interactions between the two interfaces film-substrate and film-air. Typically, spin coated films have a linear dependence between concentration and film thickness at moderate concentrations of polymer solutions. Hence, a nearly similar thickness of polymer blends can be achieved with the following procedure [4]. First the thicknesses as a function of the concentration of the three polymers have to be determined. This is done by making films of one polymer with different concentrations, but otherwise completely similar conditions, e.g. the polymer molecular weight or the rotational speed. Then the thickness of each film has to be measured. For the PSS film this was done with white light interferometry, and then the measuring points can be fitted linearly, as it is shown for PSS in fig. 4.20. Finally, after doing this for all three components, the concentrations consistent with the same thickness for each polymer can be mixed in different ratios to blends, which will all have approximately the same thickness after spin coating.

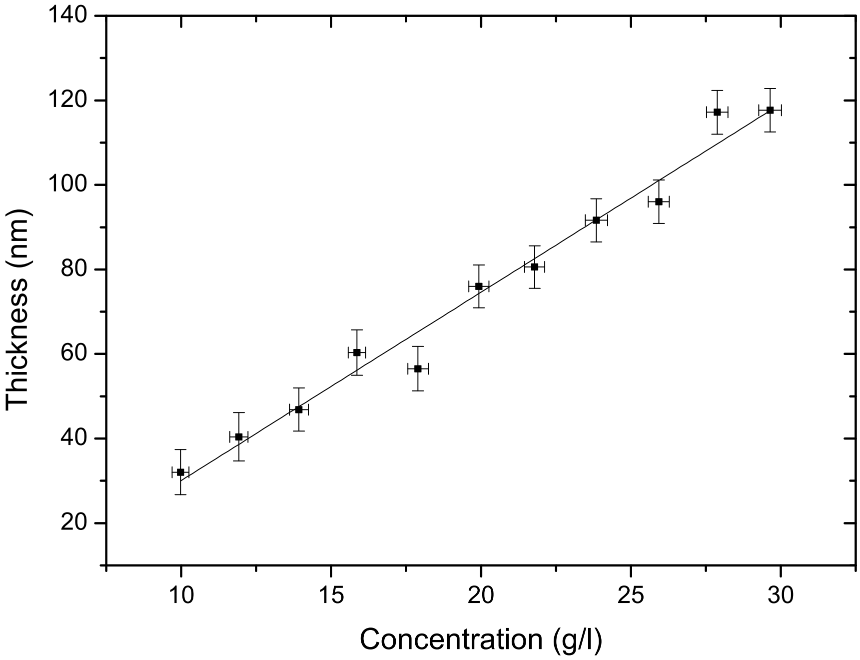

Figure 4.20:
PSS film thickness as a function of the PSS concentration of the solution used for spin coating

The next step in our research is the investigation of the films with different blending ratios regarding absorption, film surface and morphology or crystallization behavior respectively. Furthermore the influence of the substrate surface will be investigated, as it is our intention to improve the device performance. And last but not least solar cells with the researched ternary blend have to be measured regarding efficiency and degradation.

[1] X. Yang, J. Loos, S. C. Veenstra, W. J. H. Verhees, M. M. Wienk, J. M. Kroon, M. A. J. Michels, R. A. J. Janssen, *Nano Lett.* **5**, 579-583 (2005)

[2] R. A. Street, *Nat. Mater.* **5**, 171-172 (2006)

[3] K. C. Kim, J. H. Park, O. O. Park, *Sol. Energy Mater. Sol. Cells* **92**, 1188-1191 (2008)

[4] M. A. Ruderer, E. Metwalli, W. Wang, G. Kaune, S. V. Roth, P. Müller-Buschbaum, *ChemPhysChem* **10**, 664-671 (2009)

5 Polymer-hybrid systems

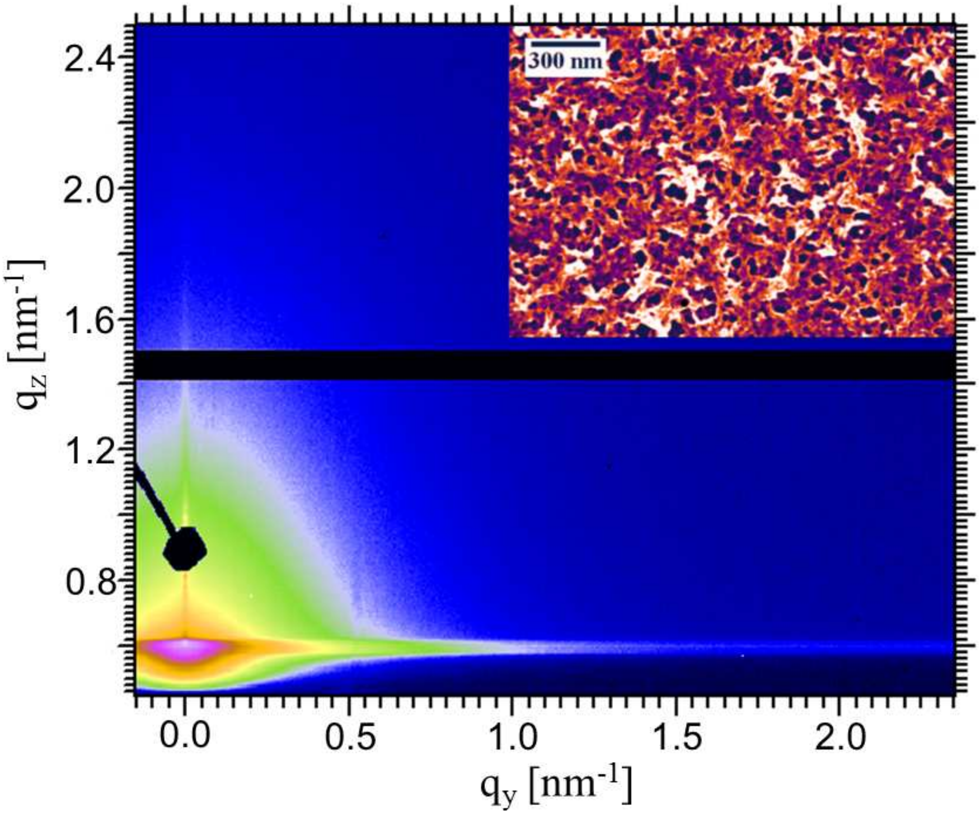

5.1 Inner morphology of titania-ceramic composites for photovoltaic applications

M. Rawolle, K. Sarkar, M. A. Niedermeier, P. Lellig[1], J. S. Gutmann[2], P. Busch[3], P. Müller-Buschbaum

[1] MPI-P, Mainz, Germany
[2] Deutsches Textilforschungsinstitut, Universität Duisburg-Essen, Krefeld, Germany
[3] JCNS, FRM II, Garching, Germany

Titanium dioxide, also known as titania, is an extensively studied material because of its photoelectronic properties [1]. Many applications in photocatalysis, gas sensing and photovoltaics have been explored because, in addition to the photoelectronic properties, titania is cheap and easily producible. For application in photovoltaics, for example in dye-sensitized solar cells (DSSCs), the structure of the titania has to be controlled on several length scales: On the one hand, a high surface-to-volume ratio is necessary for an effective charge separation, as this only takes place at the interface. On the other hand, larger structures are necessary to have good charge percolation paths and also to enhance the light scattering properties.

One successful route for the preparation of titania nanostructures is the combination of sol-gel synthesis with a structure templating by block copolymer micro-phase separation. Recently, it was shown that a poly(dimethyl siloxane) (PDMS) containing amphiphilic diblock copolymer, namely poly(ethylene oxide)-*block*-methyl methacrylate poly(dimethyl siloxane) (PEO-MA(PDMS)), can be used to create a hole blocking layer in a one-step process [2]. By plasma etching of the titania-polymer nanocomposite film, the titania is partially uncovered. During a calcination step at 450 °C in an inert gas, the PDMS block is converted to an SiOC type ceramic. Embedded in the ceramic matrix, the amorphous titania is converted to crystalline titania. This ceramic-titania nanocomposite allows for electron conductance in solid-state DSSCs, while preventing the direct contact of the hole-conducting material with the bottom electrode.

In the present investigation, the novel PDMS-containing block copolymer poly(dimethyl siloxane)-*block*-methyl methacrylate(poly ethylene oxide) (PDMS-MA(PEO)) is used as structure directing agent. This amphiphilic diblock copolymer is dissolved in a good-poor solvent pair, containing hydrochloric acid (HCl) as poor solvent for the PDMS block, to induce microphase separation. With the addition of the titania precursor, titanium tetra isopropoxide (TTIP), the sol-gel process is started, and the resulting titania coordinates to the PEO block. The titania-polymer nanocomposite solution is transferred to a substrate via spin-coating.

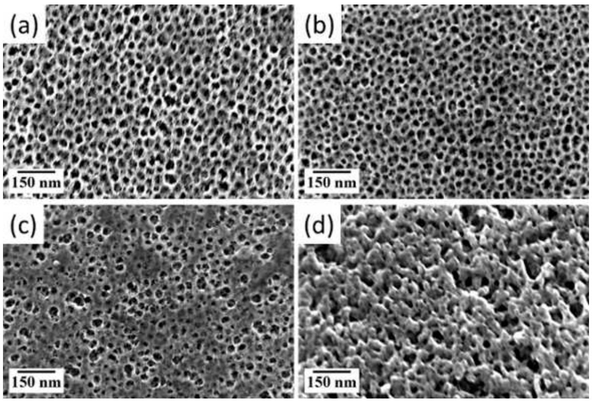

Figure 5.1:
SEM images of titania-ceramic composites as prepared by calcination with different parameters: at 400 °C in nitrogen atmosphere (a), at 600 °C in air (b), at 600 °C in nitrogen atmosphere (c) and at 1100 °C in nitrogen atmosphere (d).

In general, the sol-gel process can be further improved by the combination with micro-fluidics [3]. The fast reaction kinetics in the sol-gel process are controlled by mixing of the block copolymer solution with the selective solvent HCl and the titania precursor in a micro-fluidic channel. It was shown that this controlled mixing leads to the formation of titania-ceramic nanocomposite films with highly ordered nanostructures and less defects [3]. Moreover, the titania films

prepared by micro-fluidics, with more highly ordered structure, show a better light scattering performance as compared to the titania films prepared by the conventional sol-gel synthesis.
In this report, the effect of different calcination settings on the morphology of the titania-ceramic nanocomposite is shown. Calcination in air and in an inert gas atmosphere and at different calcination temperatures are compared. As can be seen in the scanning electron microscopy (SEM) measurements in figure 5.1, the surface morphology is affected by the calcination protocol. However, not only the surface structure but also the inner film morphology is of importance. To probe the inner morphologies of the titania films, grazing incidence small angle neutron scattering (GISANS) experiments are performed at the beamline KWS 2 of JCNS at FRM 2, Garching, Germany. A fixed incident angle of 0.54 °, a wavelength of 0.48 nm and a sample-to-detector distance of 6.7 m have been used. To enhance the scattering contrast, the measurements have been performed in an aluminum chamber filled with D_2O vapor at a temperature of 50 °C with a measurement time of only 3 h. The contrast between air, with a scattering length density (SLD) of approximately zero, and the porous titania, with an SLD of the bulk material of $2.61 \cdot 10^{-6}$ Å^{-2}, is quite small. When the pores of the titania sponge-like structure are filled with the D_2O vapor, with an SLD of $6.366 \cdot 10^{-6}$ Å^{-2}, the contrast is significantly increased.

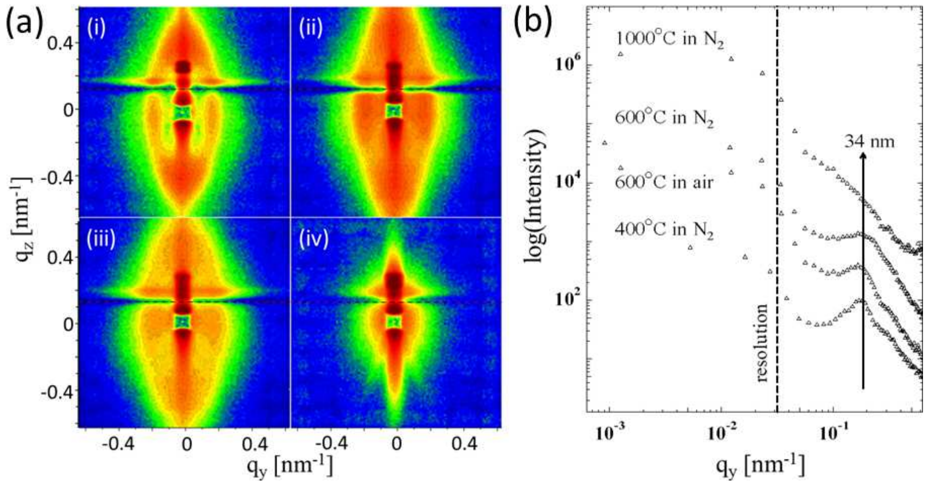

Figure 5.2:
GISANS data as measured at KWS 2 for the same samples as in figure 5.1: 2d scattering images (a) for calcination at 400 °C in nitrogen atmosphere (i), at 600 °C in air (ii), at 600 °C in nitrogen atmosphere (iii) and at 1100 °C in nitrogen atmosphere (iv). The horizontal cuts (b) for the different samples are showing the intensity profile at a constant q_z corresponding to the critical angle of titania. The cuts are shifted along the intensity axis for illustrative purposes.

The GISANS data are shown in figure 5.2. The same trend that is observed for the surface structures also holds for the inner morphology: the structures stay more defined after calcination in air as compared to calcination in an inert gas atmosphere at the same temperature. For calcination at increased temperatures, the structures collapse. Lower calcination temperatures lead to more defined well-ordered nanostructures in the volume of the thin films. However, the corresponding degrees of crystallinity differ for the different preparation protocols as well.

[1] X. Chen, S. S. Mao, *Chem. Rev.* **107**, 2891-2959 (2007)

[2] P. Lellig, M. A. Niedermeier, M. Rawolle, M. Meister, F. Laquai, P. Müller-Buschbaum, J. S. Gutmann, *Phys. Chem. Chem. Phys.* **14**, 1607-1613 (2012)

[3] M. Rawolle, M. A. Ruderer, S. M. Prams, Q. Zhong, D. Magerl, J. Perlich, S. V. Roth, P. Lellig, J. S. Gutmann, P. Müller-Buschbaum, *Small* **7**, 884-891 (2011)

5.2 Nanostructured titania thin films for hybrid photovoltaic applications derived from block copolymer based sol gel templating

G. Tainter, M. A. Niedermeier, P. Müller-Buschbaum

Metal oxide thin films are the subject of numerous studies due to their potential use as photoactive layers, particularly in photovoltaics. In dye-sensitized solar cells these layers are applied to transparent conducting oxide (TCO) substrates and coated with a monolayer of photoactive dye (e.g. Ruthenium-complexes). Between this dye and an applied back electrode (e.g. gold or platinum) either a p-type semiconductor or a liquid electrolyte is placed to transfer charge.
Increasing the surface area of the applied metal oxide film improves the absorption, and thus charge generation, by several orders of magnitude. In our research, the attainable morphologies of titania films are investigated using diblock copolymer scaffolds. This process results from a good-poor solvent pair induced micro-phase separation, and is capitalized upon by spin coating sol gels composed of a titania precursor and polymer solution onto a substrate. Ordering is strongly dependent on the respective chain lengths of the diblock copolymers and is on the nanoscale[1]. Calcination combusts the polymer matrix and titania is transformed from amorphous to anatase, resulting in freestanding crystalline nanostructured anatase thin films.
Two commercially available (Polymer Source Inc) diblock copolymers were used, each composed of poly(styrene-block-ethylene oxide) (P(S-b-EO)), one with a molecular weight of 21000 g/mol, and one with a molecular weight of 30000 g/mol. The molecular weights of the polystyrene and polyethylene oxide blocks were PS: 16000 g/mol, PEO: 5000 g/mol and PS: 23000 g/mol, PEO: 7000 g/mol respectively. 1,4-dioxane was used as a good solvent for both polymer blocks and 37% HCl was used as a bad solvent for the PS block. Titanium tetraisopropoxide (TTIP) was used as the titania precursor. From here on the two diblock copolymers will be referred to as P(S-b-EO)-(21000) and P(S-b-EO)-(30000). The results of spin coating these two polymers of different weights have been investigated with scanning electron microscopy (SEM) and white-light interferometry (WLI) measurements.
The effect of varying the size of the polymer chains used on film properties was studied by maintaining the same procedure and weight fractions of the liquid components throughout the study. The weight fractions of liquid components used are as follows: 0.92 weight fraction 1,4-dioxane, 0.005 weight fraction HCl and 0.075 weight fraction TTIP. This weight ratio has been shown to produce a foam-like structure which is suited for application in photovoltaics.[2]

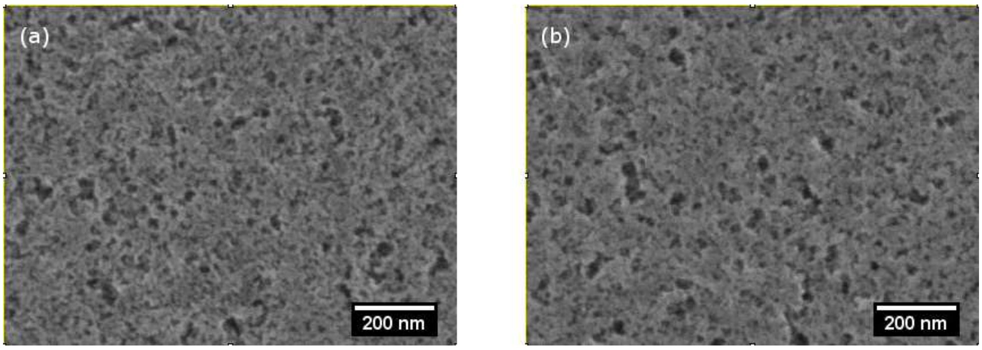

Figure 5.3:
SEM images of the structures obtained after sol gel processing and aging for 15 minutes using (a) the P(S-b-EO)-(21000) and (b) the P(S-b-EO)-(30000).

Figure 5.3 (a) and (b) reveal that despite the difference in molecular weight between the two polymer components the same weight ratios lead to very similar film morphologies. In both cases a porous foam-like titania structure is visible. Therefore, we can conclude that the chosen weight ratio yields quite stable results despite the changes in the respective polymer chain lengths. However, the film created using P(S-b-EO)-(21000) in Figure 5.3 (a) appears to possess slightly smaller pore sizes than the film obtained using the longer polymer P(S-b-EO)-(30000). WLI is used to more fully examine the changes in layer morphology. The optical properties of these composite films are heavily influenced by the varying densities of their components. The refractive indices of polystyrene and poly(ethylene oxide) are below 1.6, and thus lower than that of titania, which has a refractive index of over 2, depending on its crystalline phase. Therefore, films showing a lower refractive index contain less titania which was incorporated into the poly(ethylene oxide) block and, consequently, more polystyrene. This then suggests that the final films after calcination would be more porous.

Diblock Copolymer Used	**Thickness (nm)**	**Refractive Index**
P(S-b-EO)-(21000)	172 (± 4)	1.665 (± 0.009)
P(S-b-EO)-(30000)	186 (± 2)	1.495 (± 0.002)

Table: Thickness and refractive indices of composite films obtained from WLI.

The results in the table above show a clear decrease in refractive index with the use of the larger diblock copolymer, and thus indicate that the films obtained are more porous. This supports SEM observations. In addition, the increased thickness of the films shows that increasing the weight of the polymer in the solution has an influence on the thickness of the film obtained.

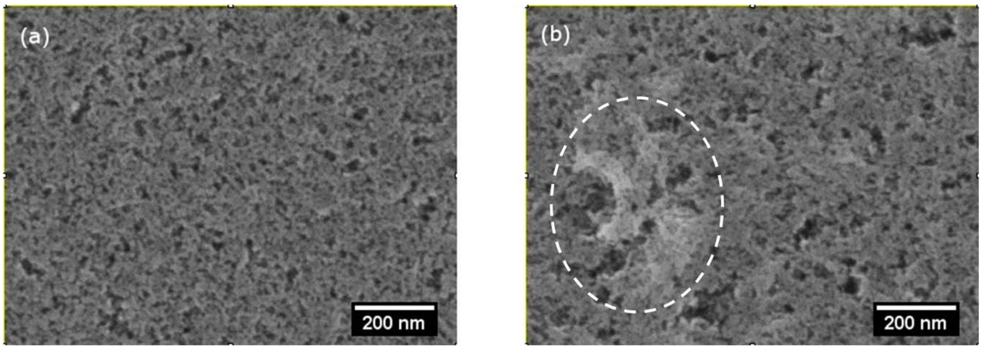

Figure 5.4:
SEM images of the structures obtained after sol gel processing and aging for 60 minutes using (a) the P(S-b-EO)-(21000) and (b) the P(S-b-EO)-(30000).

To better understand the properties and stabilities of these sol gels, the influence of aging time of the sol gel was also investigated. The solutions were allowed to age while under constant stirring from 15 to 90 minutes before being spin coated on to a silicon substrate. Figure 5.3 shows results of spin coating after 15 minutes, while Figure 5.4 displays the results of spin coating after 60 minutes. Figure 5.4 (b) shows that the solution containing P(S-b-EO)-(30000) contains agglomerates which are circled in white on the left of the image for display. Areas of porous material free of agglomerates are still clearly present but the SEM results reveal that starting at one hour of aging the sol gel forms agglomerates. SEM measurements of films obtained after an aging time of 90 minutes (not shown here) further confirm this observation, as agglomerates become larger and more numerous. This shows that changing the diblock copolymer weight requires adapting the sol gel recipe to account for altered dynamics during the aging process.

[1] P. D. Topham, A. J. Parnell, R. C. Hiorns, *J. Polym. Sci. Part B: Polym. Phys.* **49**, 1131-1156, (2011)

[2] Y. Cheng, J. S. Gutmann, *J. Am. Chem. Soc.* **128**, 4658-4674 (2006)

5.3 Titania nanostructures tailored by a sol-gel process in combination with a block copolymer template using micro-fluidics

W. Liu, M. Rawolle, T. Fröschl[1], N. Hüsing[1], P. Müller-Buschbaum
[1] FB Materialforschung und Physik, Universität Salzburg, Austria

Dye-sensitized solar cells (DSSC) have been studied extensively as an optional substitution or supplementation for silicon solar cells due to its potential low production costs [1]. However, the solar cells of DSSC type require sophisticated sealing in order to prevent the evaporation of the liquid electrolyte which is utilized as the hole conductor in conventional DSSCs. The solid state DSSC, in which the liquid electrolyte is replaced by a solid conducting polymer, has been coming up recently and is considered to be essential for commercialization. The synthesis of titania nanostructured thin films is of great importance to ensure a large surface area of the titania, which is essential for DSSC solar cell applications as the charge separation only takes place at the interface of titania and the dye. In addition, a high filling ratio of the organic hole conductor is also important, therefore larger structures are desired in addition to the nanostructures.

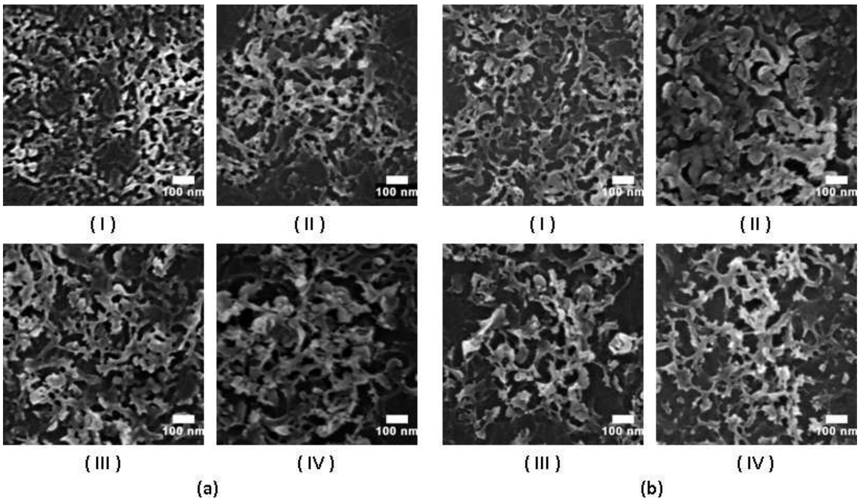

Figure 5.5:
(a) SEM images of samples prepared from sol-gel solutions mixed in one pot with a constant EGMT concentration and an increasing HCl concentration from 0.98 wt% (I) via 1.46 wt% (II) and 1.94 wt% (III) to 2.42 wt% (IV). (b) SEM images of samples prepared from sol-gel solutions mixed in a micro-fluidic channel with the same final concentrations as in (a)(IV). An improved morphological order can be seen, where the nanoparticle size varies roughly from 65 nm to 100 nm as the amount of HCl in the channel with the block copolymer solution is increased from equal portions in both channel in (b)(I) to 4:1 in (b)(IV).

In the present investigation, we use the amphiphilic diblock copolymer poly(styrene-*block*-ethylene oxide) (P(S-*b*-EO)) as template and an ethylene glycole modified titanate (EGMT) [2] as the titania precursor. P(S-*b*-EO) is dissolved in N,N-dimethylformamide (DMF), which is a good solvent for both polymer blocks. With the addition of a low amount of HCl, the interfacial energy between the PS block and the solvent is increased, as HCl constitutes a good solvent for the PEO block but a bad solvent for the PS block. To minimize the surface free energy, a micro-phase separation sets in. Subsequently, the titania precursor, EGMT, is added to the sol-gel solution, where EGMT reacts with the HCl and transforms to titania. The resulting titania coordinates to the PEO block in the micro-phase separated sol-gel solution. This coordination leads to a nanocomposition in solution. The nanocomposite titania-block copolymer solution is transferred to thin films via spin coating or solution casting. The final step is calcination. During this step, both blocks of the block copolymer are combusted, and the titania nanostructures are left behind on the substrate. Nanowire-, network- and granule-like structures are obtained as shown in the SEM graphs in figure 5.5(a). The morphology that forms is depending on the relative weight fractions of the sol-gel components. By keeping the weight fraction of EGMT relatively constant, the solutions containing up to 2.42 wt% of concentrated HCl are clear and the resulting film morphologies vary from nanoparticles via nanowires to granules. For higher concentrations of HCl, the solution turns turbid, indicating aggregates with diameters larger than 1 mirometer in the solution, and as a result, homogeneous thin films cannot be obtained by spin coating. The effect of an increasing weight fraction of EGMT is examined while keeping the weight fraction of HCl constant. A clear sol-gel solution can be obtained with a weight fraction of EGMT of up to 1.9 wt%. With a weight fraction in the range of 0.36 wt% to 0.96 wt%, the thin films become less homogeneous as the EGMT is increased in the sol-gel solution. For weight factions of EGMT higher than 0.96 wt%, the nanostructures collapse. The different morphologies that form for the different weight ratios of the sol-gel components are summarized in the phase diagram in figure 5.6.

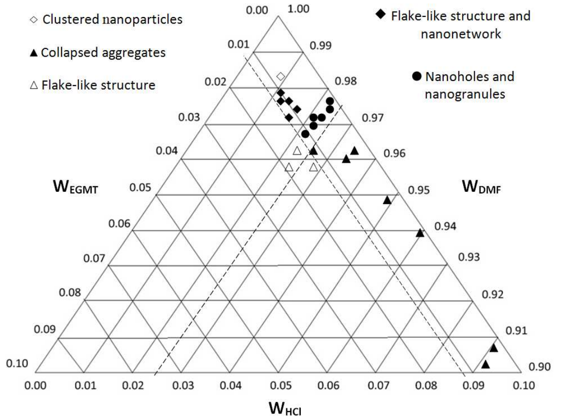

Figure 5.6:
Phase diagram of titania thin film morphologies as obtained by sol-gel synthesis with block copolymer templating. Various morphologies are obtained for different compositions in the sol-gel solution. The dashed lines describe the limiting weight fractions of EGMT and HCl in the sol-gel solution. Beyond the dashed lines, either collapsed aggregates or inhomogeneous flake coverage are observed. Inside the cross region, the titania morphology varies from nanoparticles via nanowires to granules.

Furthermore, the sol-gel synthesis in combination with a block copolymer template can be refined by the usage of micro-fluidics [3]. The mixing of the sol-gel components with the block copolymer template in a micro-fluidic channel leads to a higher control over the structure formation. The fast reaction kinetics can be controlled in the channel by the application of defined mixing speeds. As a result, titania nanostructures with less defects can be obtained.

The most promising sol-gel composition of the phase diagram is selected for further improvement with the usage of micro-fluidics. The micro-phase separation and the titania production in the sol-gel process are separately done in two solutions, these two solutions are then mixed in a micro-fluidic channel where lamellar flow dominates. The morphologies of samples prepared by this micro-fluidic method are dependent on several parameters, i.e. geometrical features, acid concentration and infuse rate. As shown in figure 5.5(b), titania thin films prepared by sol-gel solutions mixed in the micro-fluidic channel undergo an obvious improvement in terms of morphology order. The same final weight ratios are used for all the samples, but the amount of HCl in the channel with the block copolymer solution and in the channel with the EGMT solution is varied. The different ratios of HCl in both solutions are accountable for the final morphology, as well as the nanostructure size. As seen in figure 5.5(b) (I), with the same amount of HCl in both solutions, the titania film is most pronounced and shows least defects.

[1] B. O'Regan, M. Grätzel, *Nature* **353**, 737 (1991)

[2] Y. Denkwitz, M. Makosch, J. Geserick, U. Hörmann, S. Selve, U. Kaiser, N. Hüsing, R. J. Behm, *Appl. Catal. B: Environ* **91**, 470 (2009)

[3] M. Rawolle, M. A. Ruderer, S. M. Prams, Q. Zhong, D. Magerl, J. Perlich, S. V. Roth, P. Lellig, J. S. Gutmann, P. Müller-Buschbaum, *Small* **7**, 884-891 (2011)

5.4 Deposition of polymer-grafted metal nanoparticles on polymer nanotemplates: Effect of surface topography

E. Metwalli, I. Krisch, I. Markovits[1], S. Wyrzgol[1], A. Jentys[1], J. Perlich[2], P. Müller-Buschbaum

[1] TU München, Department Chemie, Garching
[2] HASYLAB at DESY, Hamburg

Incorporation of metal nanoparticles in polymer films would make hybrid films with catalytic, magnetic, optical, or sensing properties depending on both the type of the nanoparticles and the dispersability of the particles within the polymer matrix [1-3]. Here, we have deposited polymer-grafted metal nanoparticles on etched and non-etched nanostructured polymer films with the aim to emphasis the effect of surface topography on the deposition behavior of metal nanoparticles. After the spin coating of the symmetric P(S-*b*-MMA) diblock copolymer solution onto the pre-cleaned silicon substrate, different annealing temperatures were tested and the optimum annealing conditions with 120 °C for 3 days is used for all samples. At this temperature the P(S-*b*-MMA) diblock copolymer thin film builds lamella structure with a periodic distance of 40.5 nm as indicated from both AFM and GISAXS data. A topographically structured polymer film is obtained via a chemical etching process. The chemical etching process based on UV light exposure (5 min) and the chemical acetic acid (70% v/v) treatment was used and optimized to partially remove the PMMA domains without ruining the early established lamellar polymer film structure.

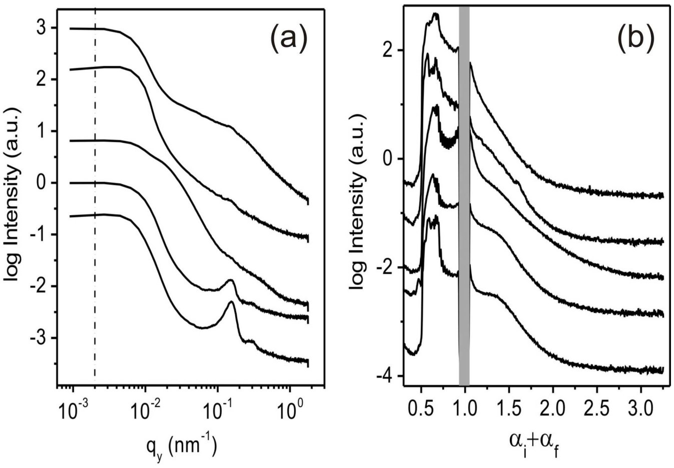

Figure 5.7:
The q_y (a) and α_i + α_f (b) GISAXS profiles of etched P(S-*b*-MMA) diblock copolymer thin films. From bottom to top: particles free, PSS-grafted PtCo nanoparticles, PVP-grafted PtCo nanoparticles with sizes 3.6, 4.6 and 4.9 nm, respectively.

In a following experiment, either PSS-grafted PtCo (2 nm) or PVP-grafted PtCo (sizes 3.6, 4.6, or 4.9 nm) nanoparticles were deposited on the polymer films after the chemical etching step via dip coating process. The GISAXS measurements were carried out at beamline BW4 at HASYLAB in Hamburg. Figure 5.7 shows the q_y profiles of the etched polymer film before and after the deposition of polymer-grafted nanoparticles. From the GISAXS data, less intense first order (q_y = 0.155 nm^{-1}) and the second order peak in the q_y profile of the metal-etched polymer hybrid film (second q_y profile from bottom in Fig. 5.7a) compared with the etched polymer film (first q_y profile from bottom) are observed. Examining the X-ray scattering length densities (SLDs) differences between the PtCo nanoparticles and the PS domains, one can predict where the nanoparticles are preferentially absorbed on the etched polymer film (either in the space between the PS domains or on the PS domains themselves). Due to the high SLD difference between the PtCo (assumed 0.5 Pt and 0.5 Co) and PS domains (90 x 10^{-4} nm^{-2}), comparable to that between PS and air (54 x 10^{-4} nm^{-2}), an improved contrast would result in an increased intensity of structural features in the q_y profiles (Fig. 5.7a). Contrarily, the intensity of the prominent first and second order peaks in the q_y profiles are diminished. Thus, the nanoparticles are preferentially deposited on the PS domains rather than in the space between the domains. For the PVP-grafted nanoparticles, particles sizes are larger than initially assumed as revealed by dynamic light scattering measurements. Broad scattering q_y profiles for hybrid films of the latter particles indicate that the particles are not deposited in registry with the film morphology.

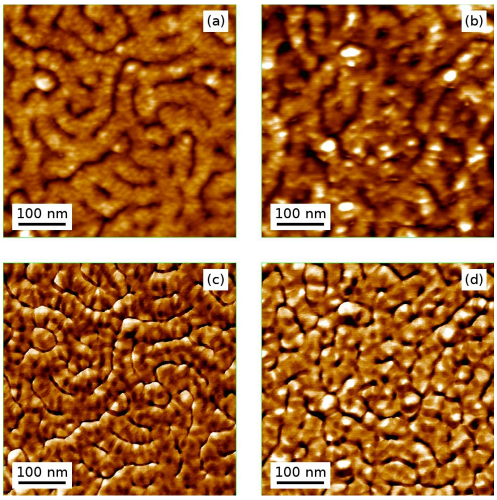

Figure 5.8:
AFM topography (a, b) and phase (c, d) images of etched P(S-*b*-MMA) diblock copolymer thin film before (left) and after (right) dip coating in a solution containing PSS-grafted PtCo nanoparticles

The real space structure is probed with atomic force microscopy (AFM) in air under ambient conditions. For hybrid film with PSS-grafted nanoparticles, both the AFM topography (a, b) and phase (c, d) images shows nanoparticles (brighter) on the PS (grey) domains (Fig. 5.8). These AFM images are collected after the DI washing step which means that the nanoparticles are strongly adhered to the polystyrene domains. Before the washing step there were bigger aggregated particles on the surface which prevented the clear observation of the deposition of small nanoparticles aligning along the lamella structure. Therefore, a washing step is needed. In conclusion, this study reveals that the preferential interaction between the nanoparticles and the PS domains is dominating over the topographical effect of the polymer surface. Due to preferable wetting of the metal nanoparticles on the PS domains, the alignment of the nanoparticles on the lamella structure is possible. Therefore metal nanopatterns can be obtained with structures independent of the film topography. Nanoscale arrays of these magnetic nanoparticles have been suggested as recording media to achieve higher recording densities as well as for sensor-related applications.

[1] G. Kaune, E. Metwalli, R. Meier, V. Körstgens, K. Schlage, S. Couet, R. Röhlsberger, S.V. Roth, P. Müller-Buschbaum, *ACS Appl. Mater. Interfaces* **3**, 1055 (2011)

[2] E. Metwalli, J.-F. Moulin, J. Perlich, W. Wang, A. Diethert, S.V. Roth, P. Müller-Buschbaum, *Langmuir* **25**, 11815 (2009)

[3] E. Metwalli, S. Couet, K. Schlage, R. Röhlsberger, V. Körstgens, M. Ruderer, W. Wang, G. Kaune, S.V. Roth, P. Müller-Buschbaum, *Langmuir* **24**, 4265 (2008)

5.5 Fabrication of titania nanostructures with different post-preparation treatments

C. Gebbe, M. Rawolle, T. Fröschl[1], N. Hüsing[1], P. Müller-Buschbaum

[1] FB Materialforschung und Physik, Universität Salzburg, Austria

In the field of solar cells, one popular concept is the dye-sensitized solar cell (DSSC). Its structure consists of a porous TiO_2 (titania) layer with an adsorbed dye and a liquid electrolyte. This liquid electrolyte may cause problems such as temperature instability, leakage and difficult sample preparation. Thus, there is a certain advantage to replace the electrolyte with a hole-conducting polymer, which does not show these shortcomings. The resulting device is then called a solid-state dye-sensitized solar cell (ssDSSC).

The porous titania structure is created by combining the two techniques sol-gel synthesis and micro-phase separation of a diblock copolymer [1]. The diblock copolymer poly(styrene-*block*-ethylene oxide), denoted P(S-*b*-EO), is dissolved in the good-poor solvent pair N,N-dimethylfomamide (DMF) and hydrochloric acid (HCl), which leads to the formation of micelles. An ethylene glycol modified titanate (EGMT) [2] is used as the titania precursor and poured into the dissolved P(S-*b*-EO). Upon contact with HCl, the sol-gel process is started. Titania coordinates to the PEO domains. This coordination, together with the micro-phase separation, eventually yields the desired porous titania structure. The sol-gel can then be deposited on a substrate via spin coating, solution casting or blade coating. A reproducible thin film of porous TiO_2 and PEO mixed with PS is obtained. Finally, the remaining P(S-*b*-EO) polymer has to be removed in order to have a pure TiO_2 structure. For this removal step, a high temperature calcination has been successfully applied in previous experiments.

In this report, we focus on two different post-treatments to remove the remaining polymer. The first method is a short ($\approx$5 min) soak in 1,4-dioxane, which represents a good solvent for both polymer blocks. This soak is followed by a brief rinse with acetone. The second method is a treatment with UV light. Nilsson *et al.* reported that a 24 h UV light treatment can be used to achieve similar results as a calcination treatment at high temperatures [3]. We are using a self-built UV light furnace, in which the sample temperatures stay just below 90 °C.

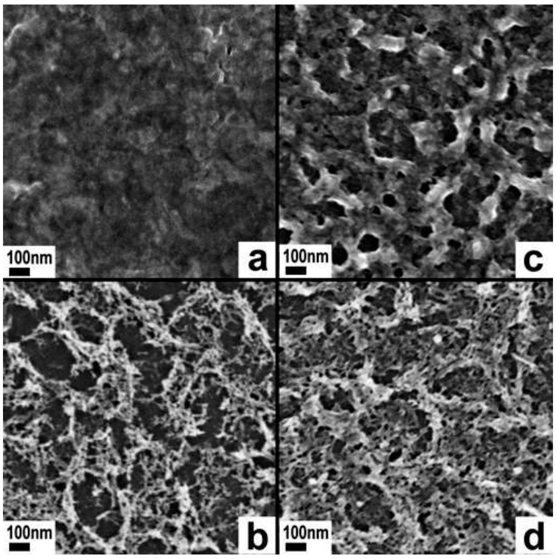

Figure 5.9:
SEM images of samples prepared by spin-coating for three subsequent times of the titania-block copolymer sol-gel. (a) shows the titania-polymer nanocomposite film with no post-treatment, (b) shows the titania film after removal of the polymer by calcination at 450 °C, (c) shows the titania film after removal of the polymer by soaking in 1,4-dioxane for 5 min 30 s and (d) shows the titania film where the polymer was removed by UV light treatment for 24 h.

Figure 5.9 shows scanning electron microscopy (SEM) images of four samples, on which the sol-gel was deposited by three times subsequent spin coating. With no further treatment after spin coating, as seen in figure 5.9(a), a rather homogeneous titania-polymer nanocomposite film without pores is obtained. After soaking in 1,4 dioxane for 5 min 30 s, on the other hand, a porous structure with a pore diameter in the range of 80 nm to 300 nm is observed, see figure

5.9(c). Compared to treatment with UV light (figure 5.9(d)), the porosity seems to be limited to the topmost layers. Furthermore, UV light treatment leads to pronounced frayed edges and additional smaller pores with diameters in the range of 10 nm to 30 nm. Both features are beneficial since they enlarge the interface area. With respect to the frayed edges and smaller pores, after calcination the titania structures as seen in figure 5.9(b) look very similar to the structures obtained after UV light treatment. After calcination, the titania structure also features the bigger pore structures of the order 80 nm to 300 nm, which are visible after 1,4-dioxane soaking as well as after UV light treatment, too.

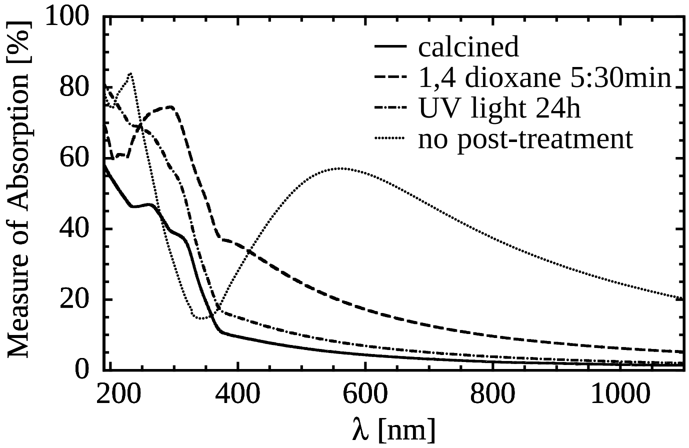

Figure 5.10:
Absorption as determined by UV/Vis spectroscopy: The dotted curve refers to a three times spin-coated film without further treatment. The solid curve represents the titania film after calcination, the dash-dotted curve titania after 24 h UV light treatment and the dashed curve titania after soaking in 1,4-dioxane for 5 min 30 s. The peaks at larger wavelengths are due to layer interference effects.

In figure 5.10, the absorption of titania films after different post-treatments is compared. All three curves with post-treatment show a sharp absorption edge at λ =370 nm, which indicates a band gap of E_g =3.35 eV. Crystalline TiO_2 has a band gap of 3.0 eV to 3.2 eV, depending on its phase, thus, considering the porous structure, crystalline titania is observed. The absolute absorption value in the UV region after one of the three post-treatments correlates well with the film thickness, as determined by white light interferometry. The as spin-coated film has a thickness of d ≈80 nm, post-treatment with dioxane for 5 min 30 s results in a thickness of d =40 nm, after UV-light treatment for 24 h the thickness is d =30 nm and after calcination d =26 nm. Due to the smaller film thicknesses, the absorption in the UV region is lower for these samples.

In conclusion, the investigated different treatments of the sol-gel synthesized titania nanocomposites all result in nanostructured titania thin films. Thus, the applied EGMT precursor works well in preparation routes which do not require high temperatures, which will be of interest for flexible substrates (polymer foils).

[1] M. Rawolle, M. A. Ruderer, S. M. Prams, Q. Zhong, D. Magerl, J. Perlich, S. V. Roth, P. Lellig, J. S. Gutmann, P. Müller-Buschbaum, *Small* **7**, 884-891 (2011)

[2] Y. Denkwitz, M. Makosch, J. Geserick, U. Hörmann, S. Selve, U. Kaiser, N. Hüsing, R. J. Behm, *Appl. Catal. B: Environ.* **479**, 91 (2009)

[3] E. Nilsson, Y. Sakamoto, A. E. C. Palmqvist, *Chem. Mater.* **23**, 2781 (2011)

5.6 Magnetic nanoparticles in thin block copolymer films

Y. Yao, E. Metwalli, H. Choe, S. V. Roth[1], M. Opel[2],P. Müller-Buschbaum

[1] HASYLAB at DESY, Hamburg, Germany
[2] Walther-Meissner-Institute, Garching, Germany

Block copolymers with embedded magnetic nanoparticles have attracted strong interest as a method to fabricate hybrid nanocomposites. Furthermore, the control over the alignment of the nanoparticles within the polymer matrix is essential for producing well-aligned, highly-oriented metal-polymer nanopatterns. It can be achieved by using a guiding polymer matrix [1-2]. In this work, we have investigated the alignment of maghemite nanoparticles within poly(styrene-*b*-methylmethacrylate) diblock copolymer films. Metal-polymer hybrid films are prepared by solution casting under an external magnetic field. We have studied the emerged morphologies as function of the nanoparticle concentration of the metal-polymer hybrid film by using optical microscopy (OM), atomic force microscopy (AFM), scanning electron microscope (SEM) and grazing incidence small-angle x-ray scattering (GISAXS). The magnetic behavior of the films is measured at different temperatures for two orthogonal directions (with the line-shaped particle aggregates parallel and perpendicular to the magnetic field) using a magnetic property measurement system (MPMS).

Hybrid films of the diblock copolymer containing the maghemite nanoparticles are prepared by solution casting on the Si substrates while the external magnetic field (173 G) is parallel to the sample surface. As Fig. 5.11 a) shows, the width of the metal stripes is monotonically increasing with increasing of the nanoparticles concentration. At concentration higher than 3%, the magnetic nanoparticles aggregate together and create larger metal wires. Metal wire length also increases with increasing nanoparticles concentration.

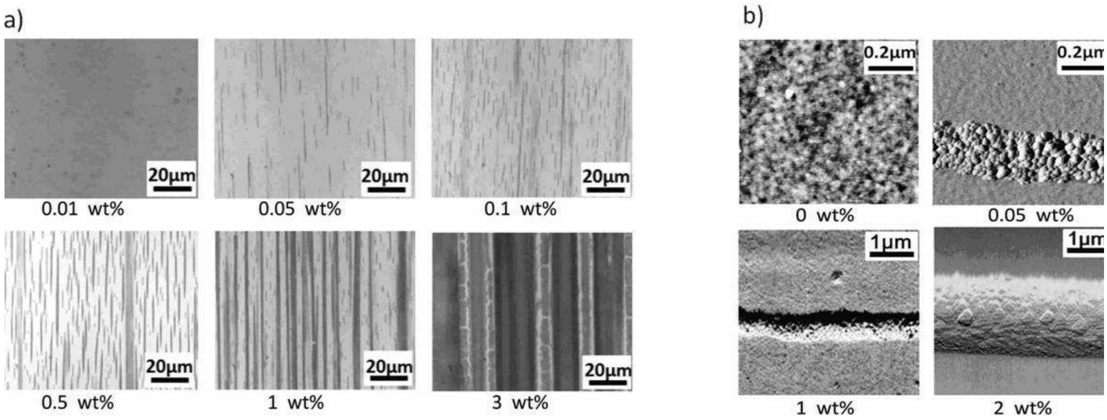

Figure 5.11:
a) Optical microscopy images and b) AFM images of the diblock copolymer films with different nanoparticles concentration as indicated.

As shown in the Fig. 5.11 b), the pure polymer film micro-phase separates and creates nanostructures. For the film with embedded nanoparticles, the nanoparticles are mainly driven by the external magnetic field to form metal line shape aggregates following the direction of the magnetic field. The formation of submicron metal wires is involving a limited modification of the polymer morphology.

In the Fig. 5.12 a) GISAXS data with distinct structure peaks are shown. Peak II is clearly visible for low nanoparticle concentrations and vanishes for the film with 3% wt nanoparticles. The inter-domain distance increases from 112 nm to 120 nm, due to the swelling of the PS domains

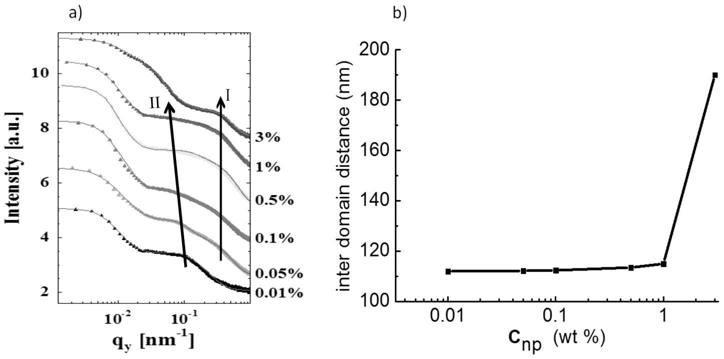

Figure 5.12:
a) Out-of-plane cuts (symbols) of the 2d GISAXS data as a function of the q_y component of the scattering vector. b) Inter-domain distance as a function of nanoparticles concentration.

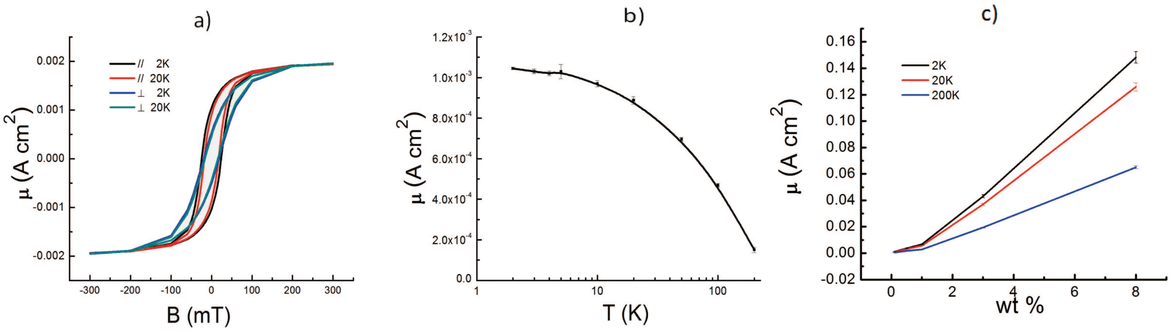

Figure 5.13:
a) Magnetic moment curves measured as a function of external field B at different temperatures. b) Temperature dependence of the measured remanence of the diblock polymer film with 0.1 wt% nanoparticles. c) Magnetic saturation measured as a function of the nanoparticles concentration at 2K, 20K and 200K.

with the nanoparticles. At concentrations higher than 3 wt%, the scattering is dominated by the form factor of the nanoparticles at 25 nm (peak I).

As visible in Fig. 5.13 a), the magnetic hysteresis loops interestingly show that the remanence is depending on the orientation of the sample. Magnetic anisotropy is imparted due to the formation of nanoparticles assemblies. Fig. 5.13 b) shows that the remanence keeps constant at lower temperatures and decays at higher temperatures indicating a typical feature of anisotropic superpara-magnetism [1]. As seen from Fig. 5.13 c), the remanence depends strongly on the temperature due to the thermal fluctuation and is also influenced by the nanoparticles concentration and temperature.

In summary, highly oriented wire-shaped metal patterns of magnetic nanoparticles can be achieved by using external magnetic fields, and the different metal stripe width of nanoparticle wires aligned parallel to the magnetic fields are due to the different nanoparticle concentrations. The polymer PS domain will be expanded by embedded high concentration of nanoparticles. The magnetic properties are highly dependent on the particles concentration.

[1] L. Schulz, W. Schirmacher, A. Omran, V. R. Shah, P. Böni, P. Müller-Buschbaum, *J. Phys. Condens. Matter* **22**, 346008 (2010)

[2] E. Metwalli, J. F. Moulin, J. Perlich, W. Wang, A. Diethert, S. V. Roth, P. Müller-Buschbaum, *Langmuir* **25**, 11815-11821 (2009)

5.7 Improvement of carbon nanotube dispersability by chemical modification

A. A. Golosova, J. Adelsberger, A. Sepe, P. Lindner[2], R. Jordan[1,3], C. M. Papadakis

[1] TU München, Department Chemie, Garching, Germany
[2] ILL, Grenoble, France
[3] TU Dresden, Department Chemie, Dresden, Germany

Nanocomposites from carbon nanotubes (CNTs) display interesting mechanical properties. However, mixing of CNTs with polymers requires strong mechanical forces and, in many cases, agglomeration is observed at later times [1]. Chemical modification of CNTs with polymers has been found to improve the dispersibility of CNTs in polymers [2].

We have used self-initiated photografting and photopolymerization [3] to form stable polystyrene (PS) grafts on CNTs. Both single- (SW) and multi-walled (MW) CNTs were modified this way. The effect of modification on the structure and aggregation behavior of the CNTs in solution was studied using small-angle neutron scattering (SANS). The focus was on the influence of the polymerization time, i.e. the amount of grafted PS on both SW and MW CNTs.

Dispersions of SW and MW CNTs modified with PS grafts for 1 or 3 days and of native SW and MW CNTs were prepared by ultrasonication in toluene. Immediately, SANS measurements were started at D22, ILL. The experiments were carried out at sample-to-detector distances of 1.2 m, 8 m and 20 m and a neutron wavelength of 8 Å. SANS images were taken with accumulation times between 300 and 7200 s. Using deuterated toluene (C_7D_8, D-toluene) or the mixture C_7D_8/C_7H_8 =11/89 vol.% (HD-toluene) as a solvent, the polymer shell or the bare CNTs were highlighted. Representative curves are shown in Fig. 5.14.

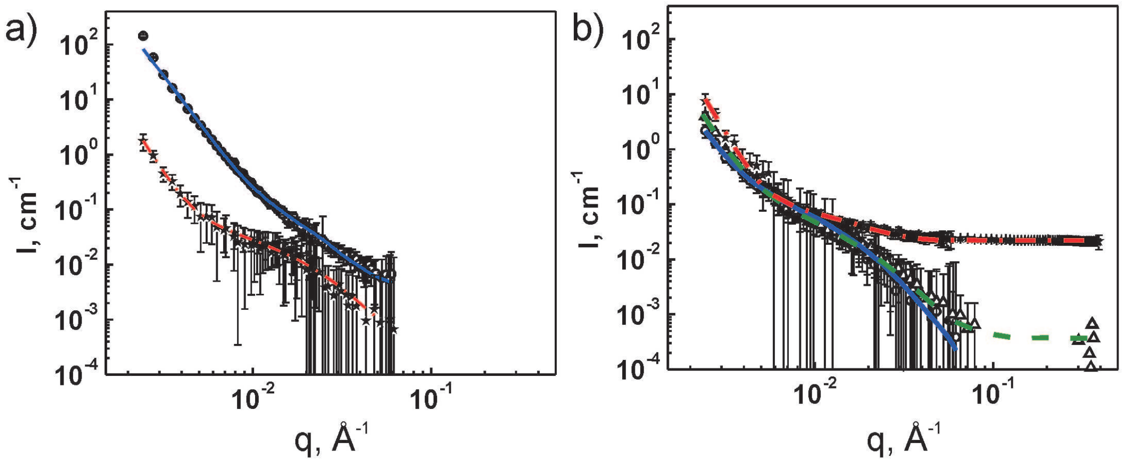

Figure 5.14:
Experimental SANS curves of the dispersions of (a) SW and (b) MW CNTs in D-toluene. Open circles: native CNTs, open triangles up: SW or MW CNT-PS polymerized for 1 day, filled stars: SW or MW CNT-PS polymerized for 3 days. Lines: model fits; full blue lines: native CNTs, green dashed lines: SW(MW)CNT-PS-1d, red dash-dotted lines: SW(MW)CNT-PS-3d.

The SANS curves were fitted by fractal aggregates of homogeneous cylinders (SW CNTs) or hollow cylinders (MW CNTs) (Figs. 5.15,5.16). As an example, we present here the analysis of the SANS data for MW CNTs with different amounts of grafted PS. The model fits the experimental curves well (Fig. 5.14a) with parameters compatible with the results of thermo gravimetric analysis (TGA).

Figure 5.15: Schematics of native and PS-modified aggregates as a function of polymerization time.

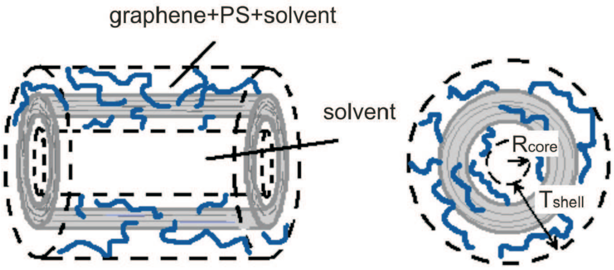

Figure 5.16: Core-shell cylinder model for modified MW CNTs.

In all SANS curves, forward scattering from aggregates is present. The fractal dimension turns out to be 3 in all cases, and the aggregate size remained at ca. $10^4 - 10^5$ Å. The effect of PS modification is evident on smaller length scales: The length of the cylindrical segments increases significantly for all samples (from ca. 700-900 Å to ca. 7000-9000 Å) upon modification, i.e. the mesh size in the fractal aggregate increases significantly. The aggregates are thus much more loosely packed for the PS-modified CNTs than in the native ones.

Moreover, in D-toluene, changes in the core and shell radii of the modified MW CNTs are observed compared to the native ones. For MW CNTs modified for 3 days, the shell thickness is with 58 Å larger than for the native MWCNTs (43 Å) due to the PS grafts. The core radius of the MW CNTs is 18.0-19.5 Å. From these values together with the known number of graphene layers in the MW CNT, we conclude that the thickness of the PS shell increases to 10-20 Å upon modification.

To conclude, SANS experiments gave detailed insight into the structures of PS-modified and native SW and MW CNTs in toluene. We found that the modification of the CNTs with PS grafts results in thicker PS shells along with a significant increase of the mesh size of the aggregates.

The project has been funded by the International Graduate School of Science and Engineering (IGSSE).

[1] D. W. Schaefer, J. Zhao, J. M. Brown, D. P. Anderson, D. W. Tomlin, *Chem. Phys. Lett.* **375**, 369-375 (2003)

[2] K. Balasubramanian, M. Burghard, *Small* **1**, 180-192 (2005)

[3] J. P. Deng, W. T. Yang, B. Ranby, *Macromol. Rapid Commun.* **22**, 535-538 (2001); M. Steenackers, S. Q. Lud, M. Niedermeier, P. Bruno, D. M. Gruen, P. Feulner, M. Stutzmann, J. A. Garrido, R. Jordan, *J. Am. Chem. Soc.* **129**, 15655-15661 (2007)

5.8 Foam-like ZnO nanostructured morphology synthesized via sol-gel technique for applications in photovoltaics

K. Sarkar, M. Rawolle, E. M. Herzig, W. Wang, A. Buffet[1], S. V. Roth[1], P. Müller-Buschbaum

[1] HASYLAB at DESY, Hamburg, Germany

Foam-like structures of inorganic semiconductors such as titania have been widely studied due to their promising capability of acting as a charge carrier for photovoltaic applications such as in hybrid solar cells. In general, a foam-like morphology is beneficial to the need of large surface-to-volume ratio in order to enhance light harvesting. Moreover, the interconnected network reduces probabilities for electron-hole recombination. [1]

In the present study, zinc oxide (ZnO) is used in replacement of titania as the inorganic material for hybrid solar cells. ZnO has a wide band gap of 3.37 eV, large exciton binding energy of 60 meV at room temperature, optical transparency, electrical conductivity, piezoelectricity and many more unique properties which make it a potential candidate for photovoltaic applications.[2] ZnO nanostructures are synthesized on silicon substrates using a sol-gel mechanism coupled with an amphiphilic diblock copolymer polystyrene-block-polyethyleneoxide, abbreviated as P(S-*b*-EO), acting as a template. The ZnO precursor Zinc acetate dihydrate (ZAD) is incorporated in the PEO block. The different morphologies are obtained by adjusting the weight fractions of the solvents and ZAD. Thin film samples with ZnO nanostructures are prepared via spin coating followed by a calcination step in air at 400 °C for 30 minutes. The predominant morphology observed after calcination corresponds to foam-like network structures. Varying the weight fractions of the good-poor solvent pair and the precursor, foam-like structures of different densities are obtained. Four different kinds of foams are studied by scanning electron microscopy (SEM) in order to probe the surface morphology as shown in Fig.5.17.

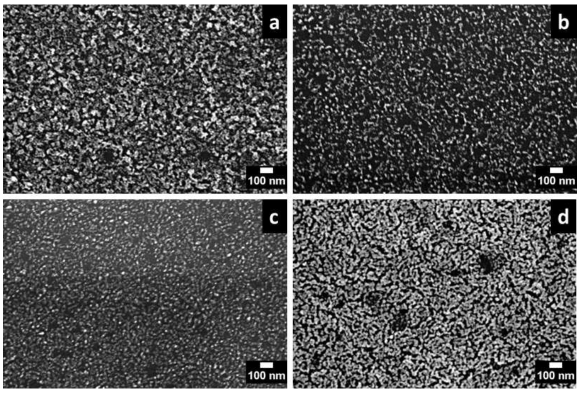

Figure 5.17:
SEM images of ZnO morphologies resembling foam-like structures obtained after calcination for the means of practical applications. (a) W_{DMF}:W_{H2O}:W_{ZAD} = 0.94:0.03:0.03 (b) W_{DMF}:W_{H2O}:W_{ZAD} = 0.98:0.01:0.01 (c) W_{DMF}:W_{H2O}:W_{ZAD} = 0.92:0.07:0.05 (d) W_{DMF}:W_{H2O}:W_{ZAD} = 0.925:0.01:0.065.

In order to explore the bulk morphologies, grazing incidence small angle X-ray scattering (GISAXS) was performed at the P03 Micro- and Nanofocus X-ray Scattering (MiNaXS) beamline of the PETRA III storage ring at HASYLAB, Hamburg. GISAXS is a highly sensitive tool to extract the structures buried several hundreds of nanometers underneath the surface of the samples. The 2D GISAXS data are shown in Fig. 5.18 for the calcined samples. Although, the SEM images of the samples appear very similar in their surface morphology, apart from the density of the foam, the 2D GISAXS data are quite distinct from one another. This exposes the diversity of buried structures in the volume of the films, which are not accessed with SEM. Despite the sample with W_{DMF}:W_{H2O}:W_{ZAD} = 0.92:0.07:0.05 all samples show a strong scattering signal at the Yoneda region (Fig.5.18) which is attributed by the dense ZnO network as also observed from the SEM images (Fig.5.17). The sample 0.98:0.01:0.01 has the lowest ZAD weight fraction of only 0.01 indicating a very thin layer. Hence, the intensity at the Yoneda is enhanced by the contribution from the underlying silicon (100) substrate, which is visible as a dark background in Fig.5.18b. Sample 0.92:0.07:0.05 (Fig.5.18c) shows the lowest intensity at the Yoneda position but in contrast very prominent lateral intensity peaks indicating the presence of mesopores in the volume of the film. Mesopores of several tens of nanometers are also observed in the calcined sample 0.925:0.01:0.065 (see Fig.5.17d). But the corresponding prominent lateral structure peaks are shielded by the strong intensity at the Yoneda position.

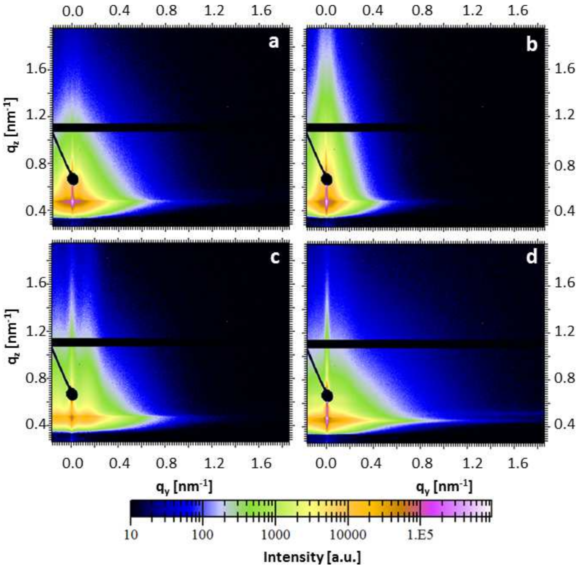

Figure 5.18:
2D GISAXS data of the calcined samples with ZnO morphologies as shown in Fig.5.17. All the images are summed up over 1 second acquisition time. The circular beamstop is installed to shield the specular peak. The intensity scale bar for all the images is the same as shown at the bottom.

In order to quantify the information about the structures installed in the sample plane, horizontal cuts of the 2D GISAXS data are performed at the characteristic q_z value of 0.47 nm^{-1}, corresponding to the observed Yoneda peak position. The horizontal cuts for all samples are shown in Fig.5.19. The horizontal cuts for the calcined samples show a prominent structure factor peak. Thus ordered structures are present in the calcined samples. However, the broadness of the peaks signifies a distribution over different length scales of the structures in the films. All horizontal cuts are analyzed with a model fit following the effective surface approximation of the distorted wave born approximation (DWBA). As obtained from the fits, the predominant length scales in the calcined samples are 20 nm, 38 nm, 60 nm and 56 nm, respectively. As evident from the SEM images of the samples (Fig.5.17), the values from the fit do not provide the exact size of the crystallites or the clusters, it rather resembles the distances between the clusters.

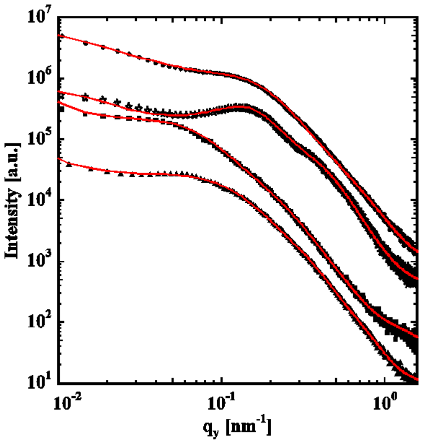

Figure 5.19:
Horizontal cuts of the 2D GISAXS data at the q_z-value of the Yoneda peak of the spin coated ZnO films after calcination for different combinations of weight fractions of DMF, water and ZAD. W_{DMF}:W_{H2O}:W_{ZAD} from top to bottom varies as 0.925:0.01:0.065, 0.92:0.07:0.05, 0.98:0.01:0.01 and 0.94:0.03:0.03. Solid lines are the fits to the data points shown as symbols. All the data are shifted along the intensity axis for clarity.

[1] G. Kaune, M. Memesa, R. Meier, M. A. Ruderer, A. Diethert, S. V. Roth, M. D'Acunzi, J. S. Gutmann, P. Müller-Buschbaum, *ACS Appl. Mater. Interfaces* **1**, 2862-2869 (2009)

[2] H. Yu, Z. Zhang, M. Han, X. Hao, F. Zhu, *J. Am. Chem. Soc.* **127**, 2378-2379 (2005)

5.9 Nanocomposite lithium-containing diblock copolymer thin films for solid-state batteries

W. Hefter, E. Metwalli, P. Müller-Buschbaum

Semi-crystalline polyethylene oxide (PEO) has been the focus of solid polymer electrolyte research due to its ability to solvate lithium ions, creating an ion-conductive membrane for lithium polymer batteries. The amorphous phase of PEO is generally believed to be responsible for the ionic conductivity through the segmental motion of low glass transition temperature PEO chains. However, for polymer electrolytes, good mechanical and thermal properties are also necessary. Therefore, various types of PEO based composites have been investigated to sustain high ionic conductivity along with an improved mechanical stability.

In this report we have empolyed diblock copolymers (DBC) electrolyte thin films as a solid-state membrane. A DBC polymer chain is composed of two large polymer blocks of distinctly different monomer units, such as PEO and polystyrene (PS). After a micro-phase separation process, nanostructured polymer with a conductive PEO matrix containing non-conductive, rigid and glassy PS domains can be obtained. The glassy PS domains may enhance the mechanical stability of the electrolyte membrane, they are, however, not conductive and therefore would decrease the overall membrane conductivity. Additionally inorganic nanoparticles (such as Al_2O_3, TiO_2 and SiO_2) have been previously incorporated into polymer electrolyte to improve the mechanical stability and to reduce PEO chain crystallization [1]. At elevated temperatures near the melting temperature of PEO (ca. 60 °C), these nanoparticles would prevent reorganization of the PEO chains and hence the crystallization.

We have previously studied the morphology of ultra-thin lithium-containing P(S-*b*-EO) films [2]. Our present work focuses on the study of DBC electrolyte thin films containing both lithium salt and inorganic nanoparticles for solid-state batteries. The diblock copolymer was chosen to have PEO as a major component to sustain high conductivity, and PS as a minor component to improve the film stability. Our main goal was to investigate the conductivity of thin films of nanocomposite lithium-containing DBC. Additionally, the structures of the hybrid electolyte films prepared in different solvents as well as the influence of humidity were studied using optical microscopy and scanning electron microscopy (SEM).

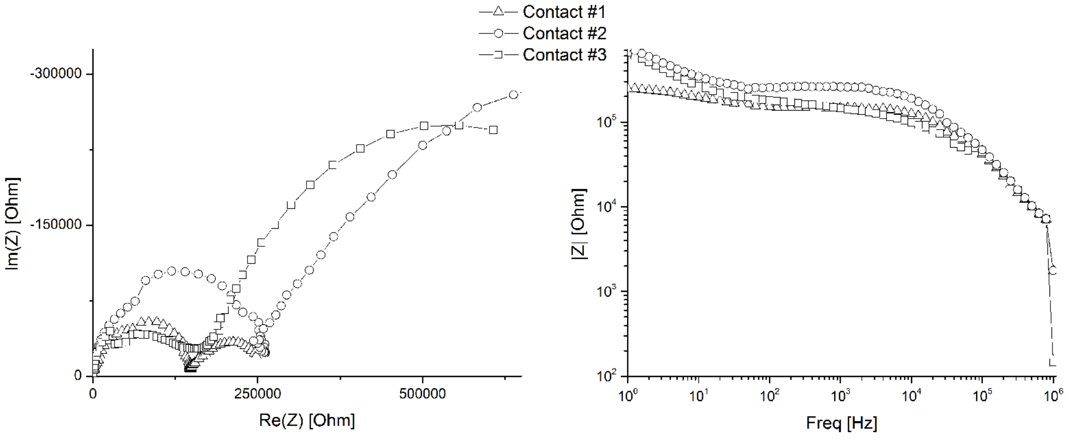

Figure 5.20:
Impedance spectroscopy plots of a nanocomposite P(S-*b*-EO)-film in the frequency range 1 MHz - 1 Hz.

To obtain ionic conductivity data, an assembly of metal electrodes (Au/Al) and the nanocomposite membrane was prepared. The hybrid polymer electrolyte was spin coated on the gold-

coated (100 nm) silicon substrates. Then an aluminum electrode was coated on top of the polymer hybrid film using thermal evaporation. The devices were sealed in a glove box with oxygen and water level below 3 ppm. The conductivity measurements were performed using a Solartron 1260 impedance/gain-phase analyzer combined with a Solartron 1287 electrochemical interface. Figure 5.20 shows the impedance spectroscopy measurement data of three different contacts on one cell. While the curves present the typical Nyquist plot half-circle behavior expected from an ionic conductor system, at the present state the overall data is not fully consitent. The discrepancies between data within different contacts on the same film or for duplicate samples may be explained using surface characterization methods.
Figs. 5.21 a-d) show the surface morphology of such a nanocomposite thin film after the spin coating step on a precleaned silicon substrate as obtained using both optical microscopy (a) and SEM (b-d). Fig. 5.21 a) shows a smooth homogeneous surface with few remaining impurities from the as-prepared coating solution. Figs. 5.21 a-d) show the surface morphology on a nanoscale. Here the polymer is seen to form agglomerates around 1 μm in diameter (fig. 5.21 b)) and a net-like structure with pores between a few 10 and around 200 nm in diameter (fig. 5.21 c)). Additionally, the Al_2O_3-nanoparticles aggregate to form clusters, which are seen as white dots in figs. 5.21 c) and d).
The microscale agglomerates in fig. 5.21 b) can be attributed to the humidity uptake by the lithium salt on the sample surface caused by the brief exposure to air prior to the sample being placed in the SEM vacuum chamber.

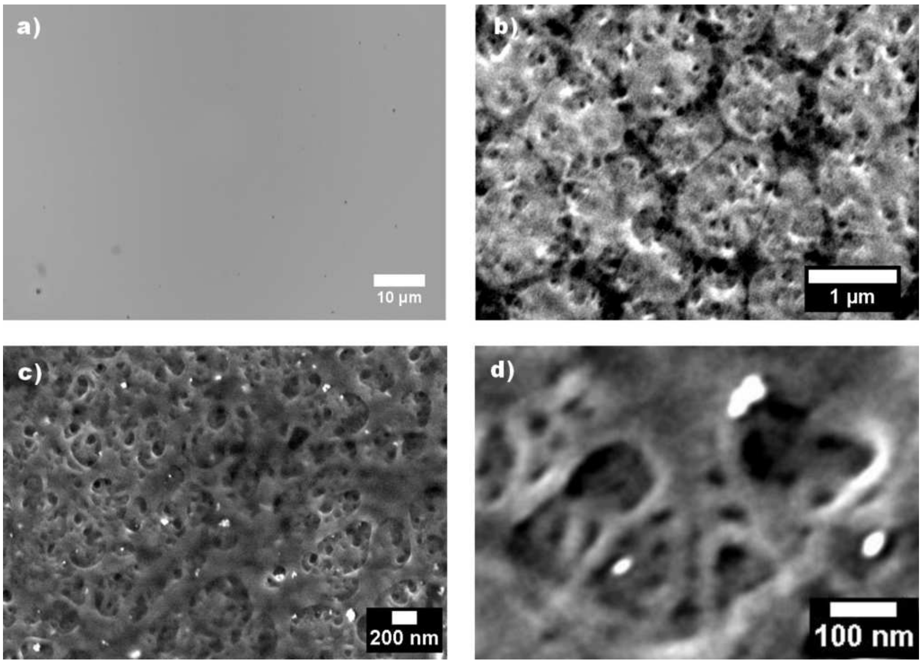

Figure 5.21:
a) Optical microscopy images and **b-d)** SEM images of the nanocomposite P(S-*b*-EO) films.

In conclusion, the morphology investigations of our thin nanocomposite lithium-polymer films show heterogeneities on the film surface in the form of agglomerates and residual impurities. These may be the source of the difficulties in obtaining valid, fully reproducible impedance measurements of these films for conductivity evaluation.

[1] B. Scrosati, F. Croce, S. Panero, *Journal of Power Sources* **100**, 93-100 (2001)

[2] E. Metwalli, M. Nie, V. Körstgens, J. Perlich, S. V. Roth, P. Müller-Buschbaum, *Macromol. Chem. and Phys.* **212**, 1742-1750 (2011)

5.10 Gold nanoparticle deposition onto doped polyaniline thin films – an in situ investigation with a combination of μGISAXS and imaging ellipsometry

V. Körstgens, M. Rawolle, A. Buffet[1], M. Abul Kashem[1], M. Schwartzkopf[1], S. V. Roth[1], P. Müller-Buschbaum

[1] HASYLAB at DESY, Hamburg, Germany

Conducting composite materials based on polyaniline and gold have a broad range of possible applications in the fields of electronics, optics and biology. In this work the deposition of gold nanoparticles as a droplet in aqueous dispersion onto a thin film consisting of poly(styrene-*b*-ethylene oxide) and doped polyaniline is used to obtain a composite. A dopant is necessary to transform polyaniline into an electric conducting state. The block copolymer together with polyaniline and the dopant campher sulfonic acid (CSA) is spin-coated out of chloroform solution on pre-cleaned silicon wafer. A composite with 20 nm spherical gold nanoparticles is established by solution casting of a drop of gold nanoparticle dispersion. The combination of μGISAXS (grazing incidence small angle x-ray scattering with a micro-focused x-ray beam) and imaging ellipsometry has been developed at HASYLAB, Hamburg and the instrument went into user operation at the beamline P03 of the third generation synchrotron source PETRA III at HASYLAB, Hamburg in 2011 [1, 2].

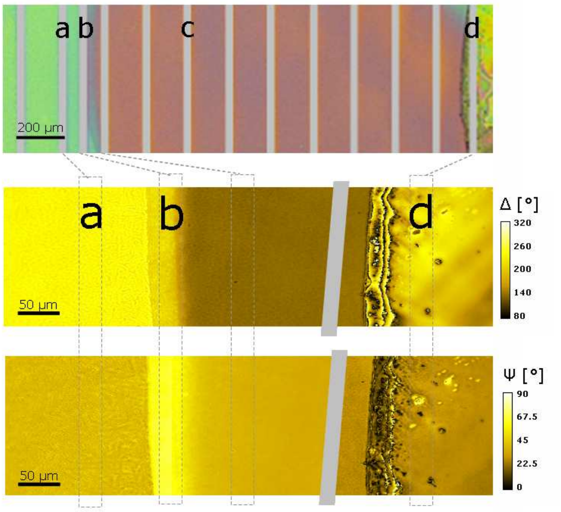

Figure 5.22:
Optical characterization of composite film: top row shows the real color optical microscopy image from the outside of the droplet (a) towards the center of the droplet (d). The thin film of doped polyaniline appears green, the outer range of the dried droplet of gold nanoparticles appears pink and the gray lines mark the positions where the sample is probed with the x-ray beam. Second and third row show the 2d maps of the ellipsometric values delta and psi. These maps are combined of several discrete maps recorded just before the x-ray experiment. In the images a, b, c and d refer to distinct positions on the sample where the scattering experiment has been performed.

One of the key features of the combined instrument is that after an initial alignment the x-ray beam and the laser beam of the imaging ellipsometer cross on one spot on the sample. This allows for a scanning GISAXS experiments in a chosen region of interest. For the composite structure evolved with a drying droplet this scan starts from the inside towards the center of the droplet in 200 μm steps as shown in Fig. 5.22.

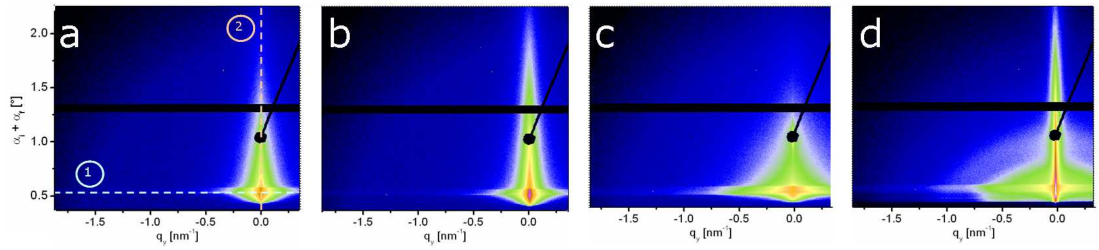

Figure 5.23: 2d GISAXS patterns of representative positions a, b, c and d as marked in Fig. 5.22.

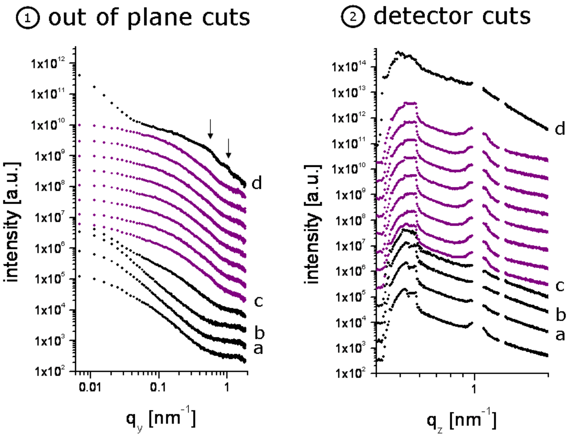

Figure 5.24:
Out of plane cuts and detector cuts from GISAXS pattern as marked (1) and (2) in Fig. 5.23. Scan from outside the droplet (bottom curve) to center of droplet (top curve). Intensity is shifted for clarity. Arrows indicate peaks originated by gold nanoparticles.

In the region outside the droplet (position a) the crystallized dopant CSA is enriched at the surface as visible with the imaging ellipsometer. Next to the first boundary of the dried droplet (position b) with increased surface roughness there is a larger rather homogeneous region (position c) with minor gold nanoparticle coverage. A rough top layer of gold nanoparticles is only built up in the center of the droplet with distinctive scattering (position d). As the combined instrument with GISAXS and imaging ellipsometry is particularly suited for the investigation of kinetic processes also the development of the composite structure during the drying process was followed. For this experiment a small droplet of nanoparticle dispersion was put on a certain chosen position on the sample and the drying was followed in-situ by recording the ellipsometric data and the scattering patterns.

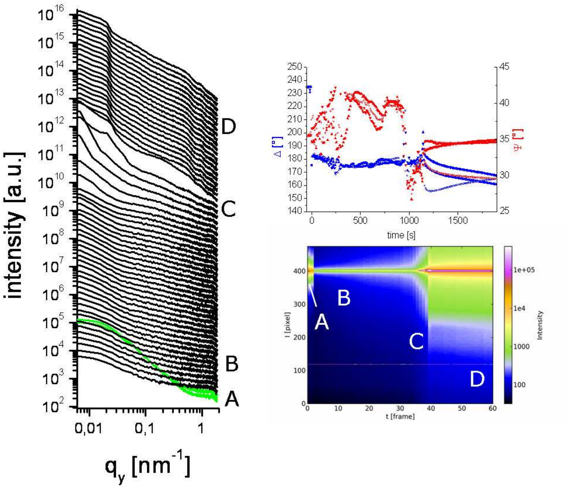

Figure 5.25:
On the left side the out of plane cuts shifted along y axis with time up to 3600 s are shown. The bottom green curve (A) represents the doped polyaniline film before application of the droplet. On the right side the course of ellipsometric values delta and psi with time is shown above a composite image of detector cuts on the same time axis.

The structure formation of the composite of doped polyaniline and gold nanoparticles is followed as pictured in Fig. 5.25. In the initial stage after droplet application (B) the detected intensity is low due to absorption of the water droplet. Drying and layering of gold nanoparticles can be followed in stage (C) until a stable structure is built up (D).

[1] V. Körstgens, J. Wiedersich, R. Meier, J. Perlich, S.V. Roth, R. Gehrke, P. Müller-Buschbaum, *Anal. Bioanal. Chem.* **396**, 139-149 (2010)

[2] S. V. Roth, G. Herzog, V. Körstgens, A. Buffet, M. Schwartzkopf , J. Perlich, M.M. Abul Kashem, R. Döhrmann, R. Gehrke, A. Rothkirch, K. Stassig, W. Wurth, G. Benecke, C. Li, P. Fratzl, M. Rawolle, P. Müller-Buschbaum, *J. Phys. Condens. Matter* **23**, 254208 (2011)

6 Dynamics

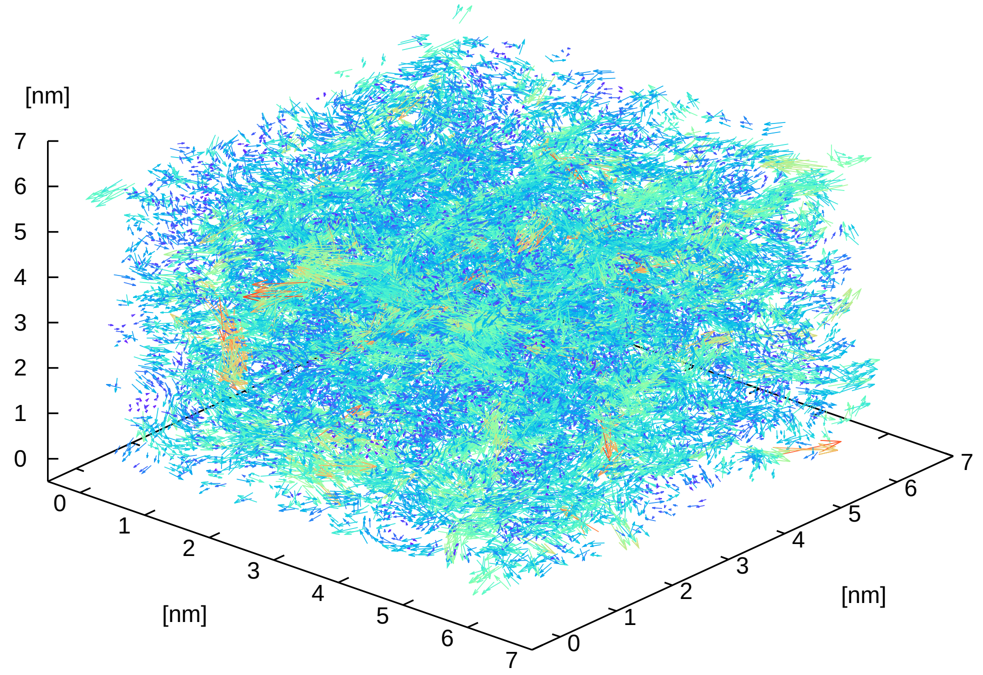

6.1 On the pico- to nanosecond time dynamics in a hexadecane melt

H. Morhenn, S. Busch, T. Unruh[1]

[1] LS für Kristallographie und Strukturphysik, FAU Erlangen-Nürnberg, Germany

In order to describe the mechanisms of molecular self-diffusion in liquids of organic medium-chain molecules, detailed knowledge about the short time dynamics of the molecules is required. At very short times the single atoms of the molecules move ballistically until they feel the force due to the bonds to their neighbors. This confinement of the atoms gives rise to a characteristic subdiffusive behaviour of the atoms. At much longer times the motion of the atoms relative to the cenver-of-mass motion of the entire molecule becomes vanishingly low, and the freely diffusive regime of the molecules is reached.

This intermediate subdiffusive time range depends on many factors, among others on temperature and the structure/dimensions of the molecules. With time-of-flight quasielastic neutron scattering (TOF-QENS), it is possible to probe the atomic motions on a molecular length scale in the pico- to nanosecond time regime. Smuda et al. performed TOF-QENS experiments on several *n*-alkanes [1]. The apparent diffusion coefficient they extracted for the observed dynamics is illustrated in figure 6.1, together with the long-time diffusion coefficients determined by pulsed-field gradient nuclear magnetic resonance (PFG-NMR) [2]. It can cleary be seen that with increasing chain length of the molecules, the observed dynamics are faster than the long-time long-range dynamics.

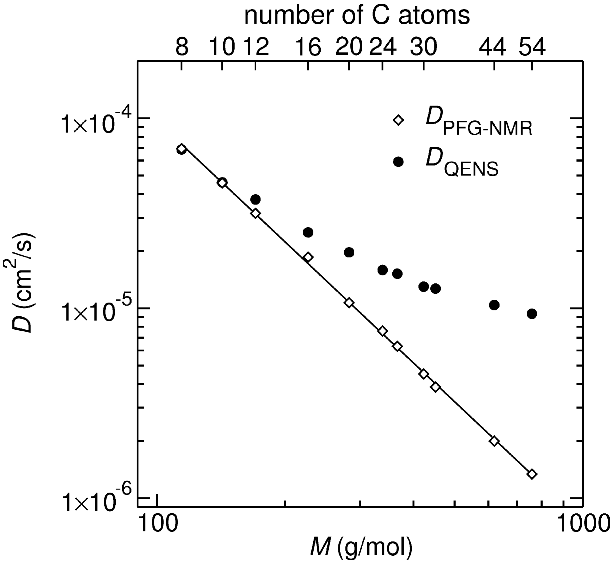

Figure 6.1:
Diffusion coefficients extracted from TOF-QENS [1] and measured by PFG-NMR [2] for 9 *n*-alkanes: The values differ with increasing chain length and decreasing temperature (not shown).

The aim of this work is to investigate the short-time dynamics observed by TOF-QENS. Therefore, as a first step, the motions in a hexadecane ($C_{16}H_{34}$) melt was analysed. The measured intermediate scattering functions can be described in terms of stretched exponential functions (see figure 6.2). The resulting fit parameters indicate that the dynamics of the atoms are different at seperate places along the molecule. Hence the observed dynamics arise from local chain dynamics and are not due to long-range diffusion alone. It can be imagined that with increasing chain length and/or decreasing temperature, these intrachain dynamics contribute more and more to the measured signal.

The idea that different dynamics are observed for different positions along the molecule, suggests the assumption that e. g some kind of rotational motion of the entire molecule is one of the prevailling dynamics in this short time regime. To what extend these motions are the fundamental steps of molecular self-diffusion is still under research.

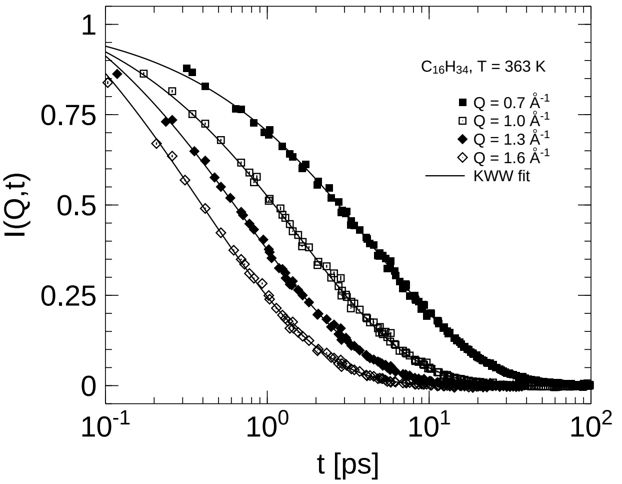

Figure 6.2:
Intermediate scattering function of a hexadecane melt at T = 363 K (symbols) together with a stretched exponential fit (solid lines) for several values of momentum transfer Q.

Additional information on the chain dynamics occuring in the picosecond time regime was obtained by performing detailed molecular dynamics (MD) simulations. The simulated trajectories can be verified by a comparison with the neutron scattering data and allow for an analysis of the dynamics of any atoms in real space. In order to quantify the local chain dynamics, the orientation autocorrelation function of the vector connecting two neighboring carbon atoms (C-C) along one molecule was calculated (see figure 6.3).

It can clearly be seen that the decorrelation of the C-C orientation follows a two-step behaviour. The first, short-time decay depends on the position along the molecule: The orientation between two carbon atoms at the end of the molecule changes faster than at the center of the molecule. The second decay, present at much longer time scales of around 100 to 1000 ps, is rather independent of the position along the chain. As a consequence, the dynamics giving rise to this long-time decay, is affecting the motion of the entire molecule, imaginable as a rotational motion of the molecule around its center.

These two dynamical processes take place on the pico- to nanosecond time regime and thus mainly contribute to the TOF-QENS signal. This shows that the combination of neutron scattering experiments and MD simulations is a suited tool, proving that with decreasing temperature local reorientations along the molecule or of the molecule itself are observed. Further analysis will focus on the dependency of chain length, in order to obtain an overall picture of the short-time dynamics of *n*-alkane melts.

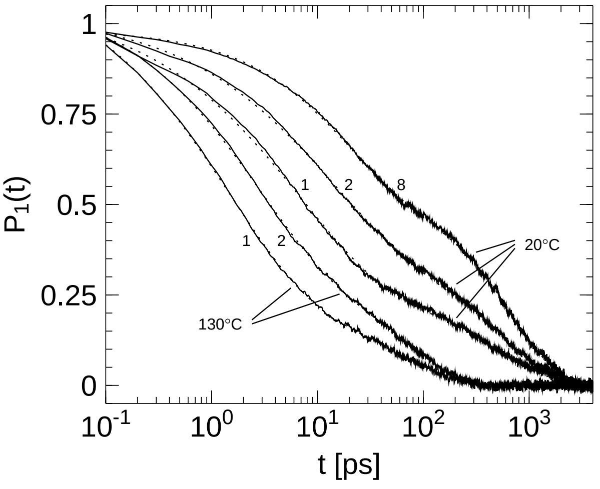

Figure 6.3:
Solid lines: Orientation autocorrelation function of the vector connecting two neighboring carbon atoms for several positions along one molecule. Position 1 is at the end of the molecule, while position 8 refers to the carbon atoms at the center of the molecules. Dashed line: Double exponential fit function.

[1] C. Smuda, S. Busch, G. Gemmecker, T. Unruh, *J. Chem. Phys.* **129**, 14513 (2008)

[2] E. v. Meerwall, S. Beckmann, J. Jang, W. Mattice, *J. Chem. Phys.* **108**, 4299 (1998)

6.2 Vibrational properties of austenite Ni_2MnGa Heusler alloy

S. Ener, J. Neuhaus, D. Lamago[1], W. Petry

[1] KIT, Institut für Festkörperphysik, Karlsruhe, Germany

After the discovery of the ferromagnetic Heusler structure in the beginning of the 20th Century, the X_2YZ composition became popular for different investigation fields. Discovery of giant magneto-resistance (GMR), magnetic cooling properties and magnetic shape memory effect on Ni_2MnGa makes this composition unique in its field. Among these properties the shape memory effect is the most investigated feature because of the unique magnetic field induces structural transition (MIT) and magnetic field induced variant reorientation (MIR) property of Ni-Mn-Ga alloy.

The aim of this work is to investigate the shape memory properties of stoichiometric Ni_2MnGa in the austenite phase by using the neutron scattering methods. To understand the vibrational properties we performed elastic and inelastic neutron scattering experiments on the Ni_2MnGa in the face centered cubic ($L2_1$) Heusler structure. The neutron scattering experiment were carried out on the thermal three axis spectrometer PUMA at the FRM II.

Figure 6.4 shows the results of the inelastic neutron scattering (INS) measurements in the high symmetry directions of the $L2_1$ structure. Scatters show the phonon results of the INS experiments. The solid lines are the Born-von Kármán (BvK) model fit to the experimental data by taking the 9th nearest neighbor interaction into account.

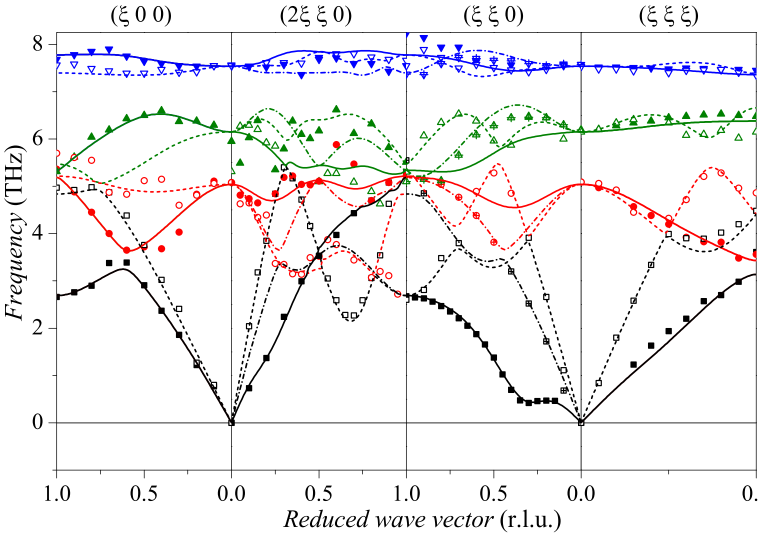

Figure 6.4: The phonon dispersion of the stoichiometric Ni_2MnGa in the austenite phase. Scatters indicate the experimental results. The lines incate the BvK fit. Each color represent different branch groups - acoustic(black), 1st optic(red), 2nd optic(green), 3rd optic(blue). Different line types represent different polarizations - solid (T_2), dashed (L) and dashed-dotted (T_1)

As shown in the figure (fig.6.4) the agreement between the experimental results and the BvK model is quite good. The inelastic structure factors calculated from the BvK model also fits quite well with the experimental intensities (not shown here). The calculated phonon dispersion agrees well with the first principle calculations which are already represented in our previous annual report [1].

By using the BvK model it is possible to calculate the phonon density of states (DOS) for each phonon measurements. Figure 6.5 shows the calculated DOSs for different temperatures. For each temperature we use the corresponding $TA_2[\xi\xi0]$ phonon measurements. The dramatic change in the temperature dependence of the $TA_2[\xi\xi0]$ branch does not effect the overall DOS properties. As shown in the inset the softening feature has only a small contribution to the phonon DOS.

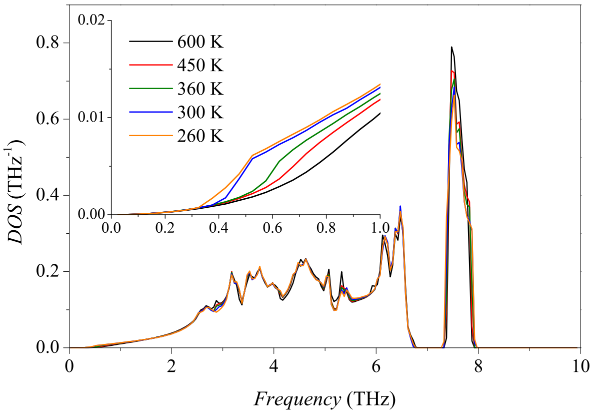

Figure 6.5:
The calculated phonon density of states (DOS) from the Born-von Kármán model. Inset figure shows the zoomed in version of the low frequency region up to 1 THz.

After the calculation of the phonon DOS one can calculate the macroscopic properties like vibrational entropy (S_{vib}), lattice specific heat (C_L), etc... Here we calculated the vibrational entropies for different temperatures by using:

$$S_{vib} = -3k_B \int_0^{\infty} g(\nu)\{n(\nu) \cdot ln[n(\nu)] - [1 + n(\nu)] \cdot ln[1 + n(\nu)]\}d\nu \tag{6.1}$$

where,

$$n(\nu) = \frac{1}{exp(\frac{h\nu}{k_B T}) - 1} \tag{6.2}$$

where k_B and h are the Boltzmann and Planck's constants, respectively, $g(\nu)$ is the phonon density of states and ν is the phonon frequency in THz.
Figure 6.6 shows the calculated vibrational entropies for Ni_2MnGa. The scatters are the calculated S_{vib} values directly from the corresponding phonon DOS results and the red line is the extrapolation of the vibrational entropy from 300K value with the harmonic approximation. One can see that the difference between the harmonic model and the experimental values are overlapping in the region of the error bars. From this result we can conclude that the softening on the $TA_2[\xi\xi\ 0]$ phonon branch does not have an effect on the vibrational entropies which is different from the group-IV metals like titanium [2].

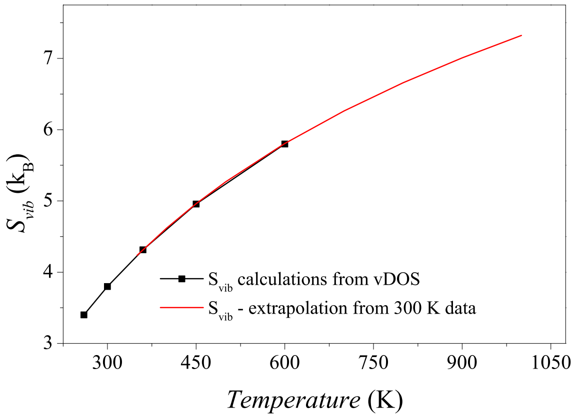

Figure 6.6:
Calculated vibrational entropies (S_{vib}) as a function of temperature. Black scatters are the calculated S_{vib} values directly from the phonon density of states (DOS) values. Red line is the extrapolation of the S_{vib} by using the harmonic approximation.

[1] S. Ener, J.Neuhaus, R. Mole, K. Hradil, M. Sievert1, B. Pedersen, I. Titov, and W. Petry *LS Funktionelle Materialien, Annual Report*, 90-91 (2010)

[2] W. Petry, A. Heiming, J. Trampenau, M. Alba, C. Herzig, H. R. Schober, G.Vogl, *Phys. Rev. B* **43**, 10933-10947 (1991)

6.3 Evolution of elastic properties at the collapse transition of aqueous PNIPAM solutions

M. Philipp, U. Müller[1], J. K. Krüger[1], P. Müller-Buschbaum

[1] University of Luxembourg, Luxembourg

Stimuli-responsive polymers, which undergo reversible volume phase transitions when subjected to external stimuli, like changes of temperature, pH or ionic strength have great potential in various fields of application, such as biomedicine and biotechnology. Among the stimuli-responsive polymers, poly(N-isopropyl acrylamide) (PNIPAM) has attracted attention because of its sharp and reversible molecular collapse transition in aqueous media at about 32 °C. On a microscopic level, while heating the aqueous PNIPAM solution above its lower critical solution temperature (LCST), the conformation of the flexible linear PNIPAM chain changes from a swollen coil to a collapsed globule as the solvent quality passes from good to poor. The related discontinuous phase transition interestingly also shows critical behavior (e.g. [1]).

Basic research has focused on different aspects of this complex coil-to-globule transition, like the critical fluctuations arising in the low temperature phase while approaching the LCST or the laws governing the growth of PNIPAM-rich aggregates in the high temperature phase. On the other hand, a more thorough study of macroscopic susceptibilities, which are especially sensitive to the collapse transition, may lead to a big step forward in understanding this phase transition. In case of chemically cross-linked PNIPAM hydrogels, Hirotsu et al. demonstrated that the mass density or the longitudinal elastic modulus could be considered as order parameter susceptibilities of the related volume phase transition [1]. By means of Brillouin spectroscopy, discontinuities in the longitudinal elastic modulus versus temperature, as well as soft mode behavior could be resolved [2].

In consequence, we studied the thermal evolution of the longitudinal elastic modulus at the collapse transition of nine aqueous PNIPAM solutions with PNIPAM concentrations between 0 mass% and 20 mass%. The Brillouin spectroscopic investigations are performed on a modified six-pass tandem Brillouin spectrometer of the Sandercock type. The vacuum laser wavelength of the frequency-doubled Nd-YAG laser equals to λ_0 = 532 nm, leading in the used backscattering geometry to an acoustic wavelength of $\Lambda^{180} = \frac{\lambda_0}{2n} \approx 200$ nm, where n represents the refractive index of the scattering volume. A self-built aluminum thermostat allowed for achieving an average heating rate of 5 °C/h at the sample position. The PNIPAM homopolymer (M_n = 20.5 kg/mol, PDI = 1.23) was purchased from PSS, Mainz.

For illustration, a representative selection of the Brillouin spectra recorded during the heating run of the 6 mass% PNIPAM solution is given in Fig. 6.7. At 24.8 °C one acoustic phonon doublet is recorded, which is related to a longitudinally polarized sound wave propagating within the acoustically homogeneous low temperature phase. While heating the PNIPAM solution towards the demixing temperature, the most significant change in the Brillouin spectra consists in the decrease of the intensity of the acoustic phonon doublet. The strongly increasing opacity of the PNIPAM solution during heating from about 30 °C to 32 °C is made responsible for the latter observation. Note that at about 34 °C a second longitudinally polarized acoustic phonon doublet with a hypersonic frequency of about 14 GHz appears. This phonon doublet gains in intensity upon further heating the heterogeneous PNIPAM solution. This is indicative for the increasing heterogeneity of the sample on the length scale of the acoustic wavelength, i.e. about 200 nm. Hence the qualitative changes of the Brillouin spectra at about 34 °C reflect the formation of macroscopic, compact PNIPAM-rich agglomerates embedded in the PNIPAM-poor phase.

In Fig. 6.8 the hypersonic frequency, as deduced from the position of the Brillouin lines given in the spectra, is represented versus temperature for the 6 mass% solution. For comparison the

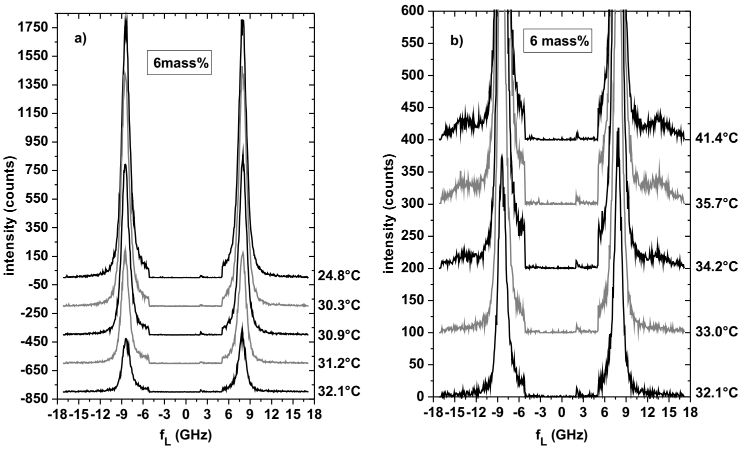

Figure 6.7:
Brillouin spectra of an aqueous 6 mass% PNIPAM solution in the vicinity of the collapse transition. For clarity the Brillouin spectra are vertically shifted, the Rayleigh line is suppressed because of technical reasons. a) Spectra measured from 24.8 °C to 32.1 °C. b) Spectra measured from 32.1 °C to 41.4 °C.

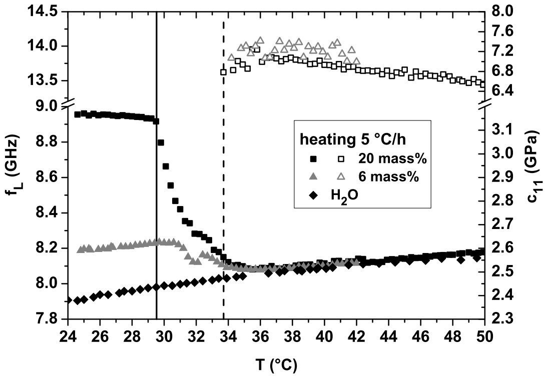

Figure 6.8:
Evolution of the hypersonic frequency f_L and the longitudinal elastic modulus c_{11} versus temperature for pure water, the 6 mass% and the 20 mass% PNIPAM solution.

corresponding data are added for pure water and the 20 mass% PNIPAM solution. The right axis gives approximate values of the longitudinal elastic modulus as determined at GHz frequencies c_{11}. Note that the behavior of the 20 mass% solution is consistent with that of the 6 mass% solution: for both systems a transitional zone with an extension of 3 to 4 °C is observed between the homogeneous low temperature phase and the acoustically heterogeneous high temperature phase, i.e. above 34 °C.

M.P. thanks the Fonds national de la Recherche (Luxembourg) for receiving a Marie Curie co-funded AFR Postdoc grant.

[1] S. Hirotsu, *Phase Transitions* **47**, 183-240 (1994)

[2] S. Hirotsu, I. Yamamoto, A. Matsuo, T. Okajima, H. Furukawa, T. Yamamoto, *J. Phys. Soc. Japan* **64**, 2898-2907 (1995)

7 Methodological and instrumental developments

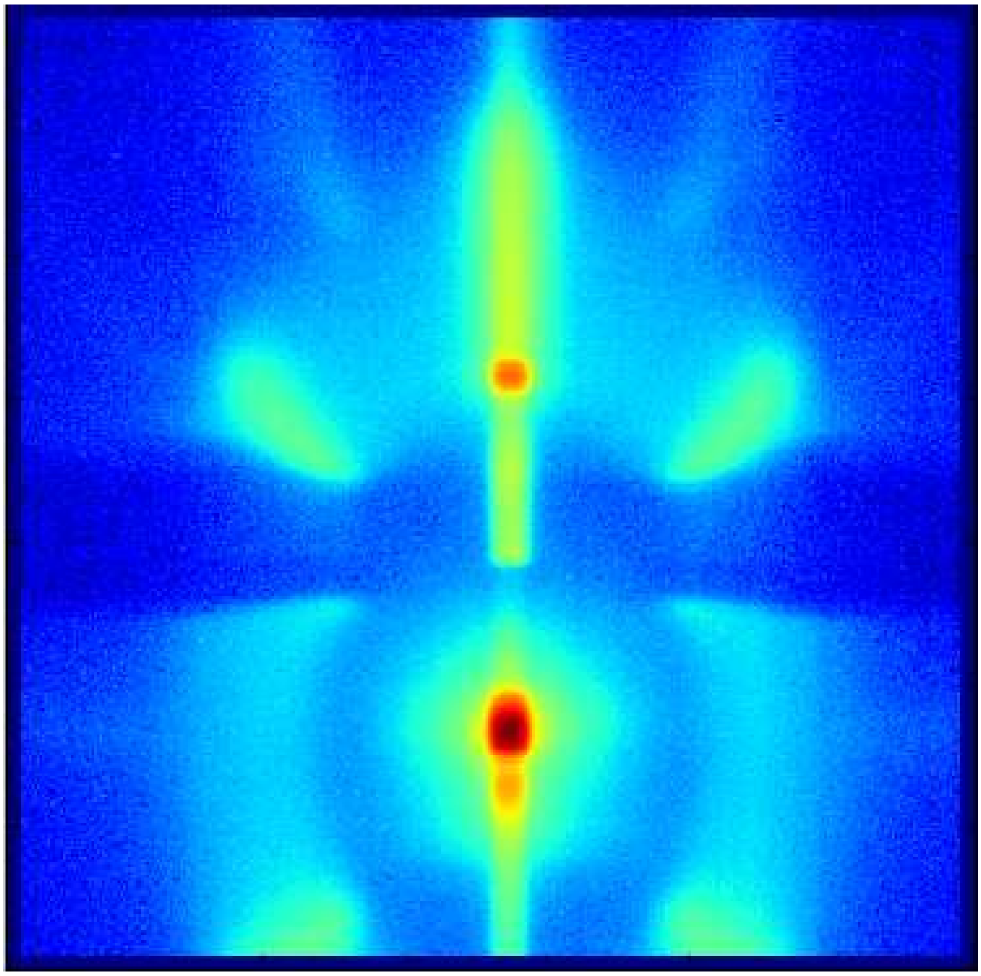

7.1 After the long upgrade: new scientific perspectives at the spectrometer TOFTOF

G. G. Simeoni, W. Lohstroh, R. Valicu, G. Borchert, K. Zeitelhack, J. Neuhaus,
W. Petry

TOFTOF is a cold neutrons time-of-flight spectrometer installed at the FRM II, suitable for both inelastic and quasi-elastic neutron scattering. It represents a quite versatile instrument, known for its excellent signal-to-background ratio as well as high energy resolution and high neutron flux (also at short wavelengths, down to 1.4 $\mathring{A}$). It allows the investigation of a great variety of scientific topics, ranging from the dynamics of disordered systems (liquids, glasses, colloids, proteins and biological samples) to the properties of new hydrogen storage materials and low-energy magnetic excitations in multiferroics or molecular magnets.

During the last long shut-down of the neutron source the instrument experienced an overall technical maintenance and a considerable upgrade of both the primary and the secondary spectrometers.

Figure 7.1: the 1000 He_3 detectors, during the big upgrade of the TOFTOF.

The detector capacity of the flight-chamber has been increased from 605 to 1000 detectors. Thanks to the almost doubled number of detectors, the active area has been enhanced from 7.26 m^2 up to 12 m^2, thus covering a solid angle of 0.75 sr (round 6% of the total scattering angle). Thanks to the higher neutron luminosity and statistics, the acquisition time (40% shorter) as well as the statistical error have been significantly reduced, thus allowing the investigation of weaker signals. In order to further improve the signal-to-noise ratio, a completely new electrical grounding concept for the whole flight-chamber has been developed, thus minimizing the electronic noise.

Its next-future technological development has been planned bearing in mind the improvement

in the study of magnetic systems as well as small samples. This is the case of pioneering and avant-garde experiments employing extreme conditions sample environment, like high pressure cells or electromagnetic (EML) and electrostatic (ESL) levitator devices. For all these kinds of investigations an increased neutron flux, squeezed over a small sample area, is required. The prototype of a new focusing neutron guide, elliptically shaped, has been recently installed at TOFTOF, replacing the final stage of the preexisting neutron guide. Its design combines the advantages of a supermirror coating with the leading-edge ”Adaptive Optics” technology.
It has been recently realized and is able to shrink the cross section of the cold neutrons beam over a surface of a squared centimeter, with an intensity gain up to about a factor 2.3. This is aimed at satisfying the crescent demand of studying quite small samples (limited availability or extreme environmental conditions).

7.2 Pattern formation of colloidal suspensions by dip-coating: An in situ grazing incidence X-ray scattering study

J. Perlich[1], M. Schwartzkopf[1], V. Körstgens, P. Müller-Buschbaum, S. V. Roth[1], R. Gehrke[1]

[1] HASYLAB at DESY, Hamburg, Germany

The dip-coating technique is one of the commonly applied methods for the preparation of thin films or the patterning of templates from polymer solutions and particle suspensions [1]. The coating principle is based on the withdrawal of a solid substrate out of a liquid solution. The withdrawal and supposed deposition of a specific material are mainly governed by the withdrawal speed and the physical as well as chemical sample surface properties [1]. Hence these parameters determine whether the deposition yields the desired patterning result. In this regard, Ghosh et al. prepared stripe-like pattern and demonstrated the dependence of the deposition as a function of particle diameter, withdrawal speed and entrained film thickness to come up with different deposition modes [2]. In general, the pattern formation takes place at the triple phase contact line (TPCL) of air, solution and substrate. Roth et al. investigated recently the air-water-substrate boundary of a drying droplet of colloidal solution obtaining a quantitative view of the nanostructuring during solution casting [3]. However, in contrast to the dip-coating process, the structuring process in solution casting is mainly evaporation driven.

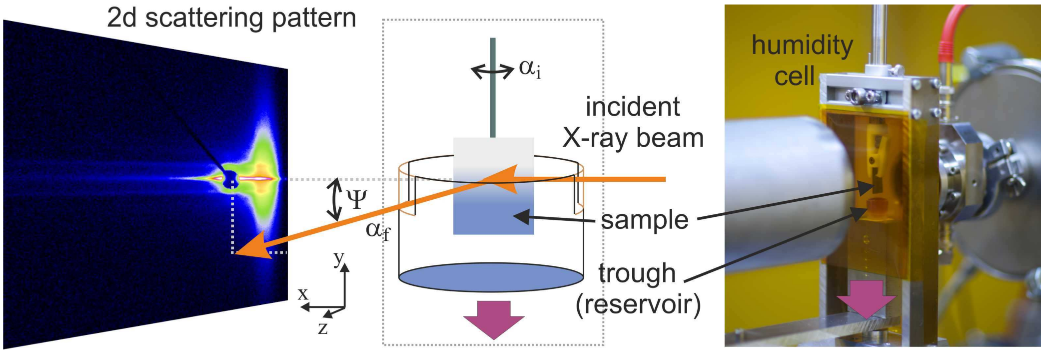

Figure 7.2:
Experimental GISAXS geometry and setup photograph. In contrast to conventional GISAXS experiments, the sample surface is positioned vertically in order to perform the dipping of the sample into the solution-containing trough. The X-ray beam impinges on the sample surface with a fixed angle of incidence α_i. The scattered beam is described by the exit angle α_f and the vertical scattering angle Ψ. The area detector shows the q_y dependence along the vertical axis and the q_z dependence along the horizontal axis. The detected 2d scattering pattern shows the diffuse scattering with a broad Yoneda peak and the specular peak (shielded by a beam stop). During the in situ dip-coating study the trough moves vertically, whereas the sample exhibits a stationary position.

We present preliminary results of an in situ investigation of the dip-coating process of colloidal suspensions and nanoparticles by the advanced scattering technique grazing incidence small angle X-ray scattering (GISAXS) as shown in the scheme in Fig. 7.2. The selected GISAXS method is predestined for this in situ investigation, because it is a non-destructive structural probe, surface sensitive, material selective and requires no special sample preparation. Nevertheless, for a detailed analysis of the scattering data, the usage of complementary characterization techniques is inevitable. After the in situ GISAXS experiments, the as-prepared samples are analyzed by optical microscopy for an overall homogeneity check of the dip-coated thin film. Furthermore, the surface structures are investigated by atomic force microscopy or electron microscopy, yielding real space information about the characteristic structure heights and widths.

Here, the focus is on the real-time monitoring of the vertical dip-coating process to deliver an insight of the structural changes during pattern formation. With the selected measurement configuration, a fixed spot on the sample surface is probed and the structural information at the time the contact line passes through the beam-illuminated area is obtained, hence revealing the structure at the vicinity of the flowing meniscus [4]. First experiments have been performed at beamline BW4 of the DORIS III storage ring of HASYLAB using a moderately micro-focused beam ($\lambda = 0.138$ nm) with a size 36 × 23 μm^2 (h × v) enabling the required lateral resolution. The distance between the sample and detector was set to $D_{SD} = 2015$ mm. Fig. 7.3 presents the results of the simultaneous GISAXS measurements of the dip-coating process of a model system of pure silica nanoparticles ($2R$ = 30 nm) with a low drawing speed of 200 μm/min at 10 s exposure time per frame. The final scattering pattern at time $t = \tau$ clearly indicates the successful deposition of the thin colloidal film. The evolution ($t_0 \rightarrow \tau$) to the final particle arrangement is described by the most evident change of the diffuse scattering intensity in the Yoneda-region within the first 100 s of the drying process.

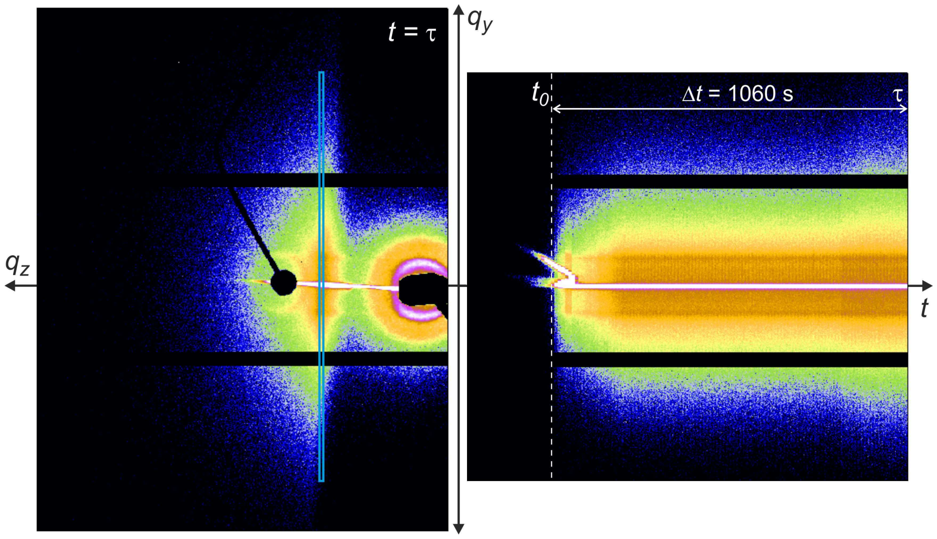

Figure 7.3:
(left) 2d GISAXS data of the dip-coated thin film of silica nanoparticles as the last frame recorded during the in situ measurement. (right) Intensity map representing the change in the Yoneda-region (blue box) as a function of time during the dip-coating process.

These successful experiments at beamline BW4 using GISAXS experiments on the pattern formation of drying colloidal suspensions illustrate strikingly the very high potential of advanced scattering experiments in grazing incidence. Nevertheless, these experiments show clearly, that the biggest changes occur during a rather narrow range of time. Hence, the general aim will be to investigate the structure formation process with a drastically increase in time resolution. This will be accomplished by the usage of the MiNaXS-instrument at PETRAIII. Furthermore a more detailed investigation of the process key parameters will be performed with purely colloidal suspensions as well as the successive patterning of these prepared colloidal templates with different species of nanoparticles.

[1] L. E. Scriven, *Mater. Res. Soc. Symp. Proc.* **121**, 717-729 (1988)

[2] M. Ghosh, F. Fan, K. J. Stebe, *Langmuir* **23**, 2180-2183 (2007)

[3] S. V. Roth, A. Rothkirch, T. Authenrieth, R. Gehrke, T. Wroblewski, M. Burghammer, C. Riekel, L. Schulz, R. Hengstler, P. Müller-Buschbaum, *Appl. Phys. Lett.* **91**, 091915 (2007)

[4] J. Perlich, M. Schwartzkopf, V. Körstgens, P. Müller-Buschbaum S. V. Roth, R. Gehrke, *submitted*

7.3 Micro-fluidics and microGISAXS – in situ characterization of nanostructures at the solid-liquid interface

V. Körstgens, M. Rawolle, M. Trebbin[1], J. Thiele[1], S. With[1], G. Benecke[2], G. Herzog[2], M. Schwartzkopf[2], A. Buffet[2], J. Perlich[2], S. V. Roth[2], S. Förster[1], P. Müller-Buschbaum

[1] Physikalische Chemie I, Universität Bayreuth, Germany
[2] HASYLAB at DESY, Hamburg, Germany

The ongoing general trend in miniaturization lead to the development of numerous micro-fluidic systems in which fluids in nanoliter volumes are transported, mixed and brought to reaction. The big advantage of micro-fluidic systems is the highly defined flow conditions which allow for the controlled mixing of reactants and dissipation of heat of reaction. More and more micro-fluidic systems are not only used in analytics, research and development, but also for commercial synthesis with high-throughput achieved by numbering-up of individual micro-fluidic cells. To get more insight in micro-fluidic systems however it remains of great importance to follow the processes directly in the micro-fluidic channel. Advances in x-ray optics also following the trend of miniaturization now allow for the application of x-ray scattering methods. Micro-focused x-ray beams in transmission geometry (SAXS, small angle x-ray scattering) became one option for the investigation of micro-fluidics in situ [1]. In our approach reflection geometry using GISAXS (grazing incidence small angle x-ray scattering) is combined with a special designed micro-fluidic cell where the nanostructures at the solid-liquid interface are investigated [2, 3]. With the micro-focusing of a highly brillant x-ray beam of a third generation synchrotron source the kinetics of growth and attachment processes of nanostructures are envisaged.

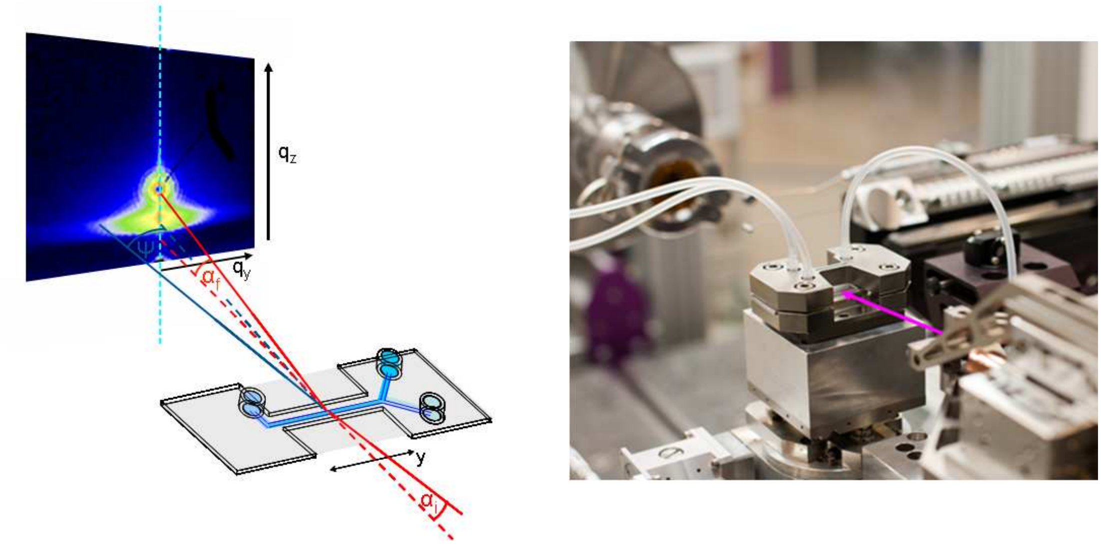

Figure 7.4:
Left: Design of the micro-fluidic cell and basic geometry of GISAXS; Right: Flow cell installed at beamline P03 at HASYLAB, Hamburg; the arrow marks the x-ray beam from the source toward the detector.

In figure 7.4 the design of the micro-fluidic cell and the basic geometry of GISAXS are sketched and juxtaposed to a photograph of the installation at the micro- and nanofocus x-ray scattering beamline (MiNaXS/P03) of the synchrotron source PETRA III at DESY in Hamburg. The x-rays can be focused down to a microbeam of 23 μm x 13 μm (H x V) by beryllium compound refractive lenses [4]. With the elongated footprint of the micro-focused beam the full width of the fluidic channel is probed. The micro-focused beam allows for scanning along the y-direction of the channel. The micro-fluidic cell for GISAXS investigations comprises a top part made of a copolymer based on cyclic olefines. The material is transparent to visible light and has a relative low absorption in the x-ray range used in the experiments. The top part is connected to the surface to be investigated by a clamp without the use of any kind of adhesive. The channel geometry enables the study of the solid-liquid interface during the continuous flow stream of a solution with a broad range of flow rates. The two inlets allow for mixing experiments and chemical reactions. Flow experiments are carried out with subsequent scans of the micro-fluidic channel in the x-ray beam along y-direction in figure 7.4. This procedure offers a time resolved as well as a position resolved investigation in one measurement.

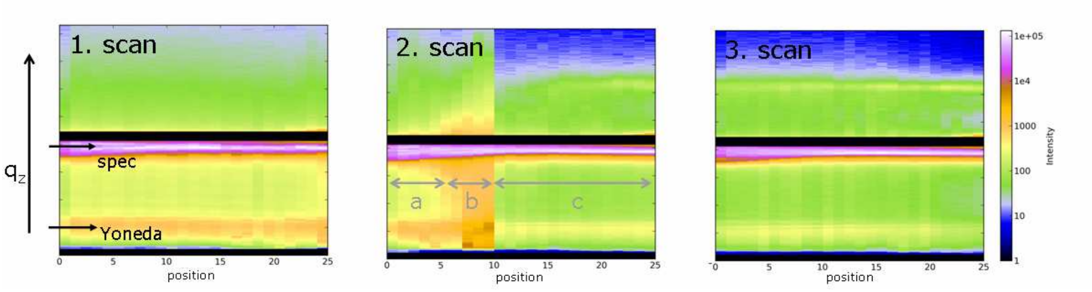

Figure 7.5: Micro-fluidic experiment with the attachment process of gold nanorods.

In figure 7.5 an example flow experiment showing the attachment of nanoparticles out of aqueous dispersion onto a thin polymer film is shown. Composite images of the detector cuts (at q_y = 0) are built up in real time and displayed during the measurement. The first scan shows the situation before the liquid approaches the channel. The q_z-positions of the specualar reflection and the Yoneda peak are constant along the channel indicating stable starting conditions for the experiment. During the second scan the liquid fills the channel. In the region marked with ″a″ the polymer film is still dry, whereas in region ″b″ a pre-cursor of liquid wets the surface clearly changing the scattering signal. The complete filling of the channel with liquid in region ″c″ is evident by the decrease of intensity due to absorption. The Bragg-peak assigned with a white arrow in the second scan indicates the surface coverage starting a few seconds after contact with nanoparticle dispersion. The third scan shown in figure 7.5 shows further coverage of the polymer substrate.

With this experimental micro-fluidic technique versatile structural investigations at the solid-liquid interface with high time resolution is possible. Applications are the investigation of attachment processes as in the layer formation of nanoparticles as well as in detachment processes of unwanted detrimental films. Further applications are based on using the two inlets of the micro-fluidic cell for mixing experiments with the formation of micellar structures and its subsequent attachment to surfaces.

This work has been financially supported by the BMBF (grant number 05K10WOA).

[1] M. E. Brennich, J. F. Nolting, C. Dammann, B. Nöding, S. Bauch, H. Herrmann, T. Pfohl, S. Köster, *Lab Chip* **11**, 708-716 (2011)

[2] J.-F. Moulin, S. V. Roth, P. Müller-Buschbaum, *Rev. Sci. Instrum.* **79**, 015109 (2008)

[3] E. Metwalli, J.-F. Moulin, J. Perlich, W. Wang, A. Diethert, S. V. Roth, P. Müller-Buschbaum, *Langmuir* **25**, 11815-11821 (2009)

[4] S. V. Roth, G. Herzog, V. Körstgens, A. Buffet, M. Schwartzkopf, J. Perlich, M. M. Abul Kashem, R. Döhrmann, R. Gehrke, A. Rothkirch, K. Stassig, W. Wurth, G. Benecke, C. Li, P. Fratzl, M. Rawolle, P. Müller-Buschbaum, *J. Phys. Condens. Matt.* **23**, 254208 (2011)

7.4 RF sputter depostion of Au on Si

S. V. Roth[1], R. Döhrmann[1], G. Herzog[1], G. Benecke[1,2], S. Bommel[1], S. Botta[1], A. Buffet[1], B. Heidmann[1], R. Gehrke[1], M. Schwartzkopf[1], E. Metwalli, and P. Müller-Buschbaum

[1] DESY, Hamburg, Germany
[2] MPIKG Golm, Potsdam, Germany

Sputter deposition is one of the most widely used methods to deposit nanostructured thin films in science and technology [1]. It is used for polymer-metal-nanocomposite production, to introduce contacts in photovoltaic devices using magnetron sputter deposition [2] or to tailor ultra-high density magnetic structures using radio-frequency (RF) sputter deposition [3].
Fig. 7.6 shows a first evaluation of the μGISAXS data using the software package DPDAK [7]. In Fig. 7.6a), the evolution of the intensity near the Au Yoneda peak is presented as a function of deposited Au. Clearly, the leveling off - when maximum coverage is reached - is around d=6nm, i.e. at the nominal percolation threshold of Au on flat surfaces. In Fig. 7.6b), we present the evolution of the lateral nanostructuring as a function of deposited Au. D denotes the most-prominent in-plane length, i.e. the distance of the cluster formed by self-assembly on the Si surface at RT. While around d=6nm no profound change is visible, a first cross-over point is already seen around d=0.6nm: The slope of the curve clearly changes. In previous studies, we introduced the so-called stop-sputter deposition method in combination with grazing incidence small-angle X-ray scattering (GISAXS) at DESY [2,5,6]. This method enables to follow

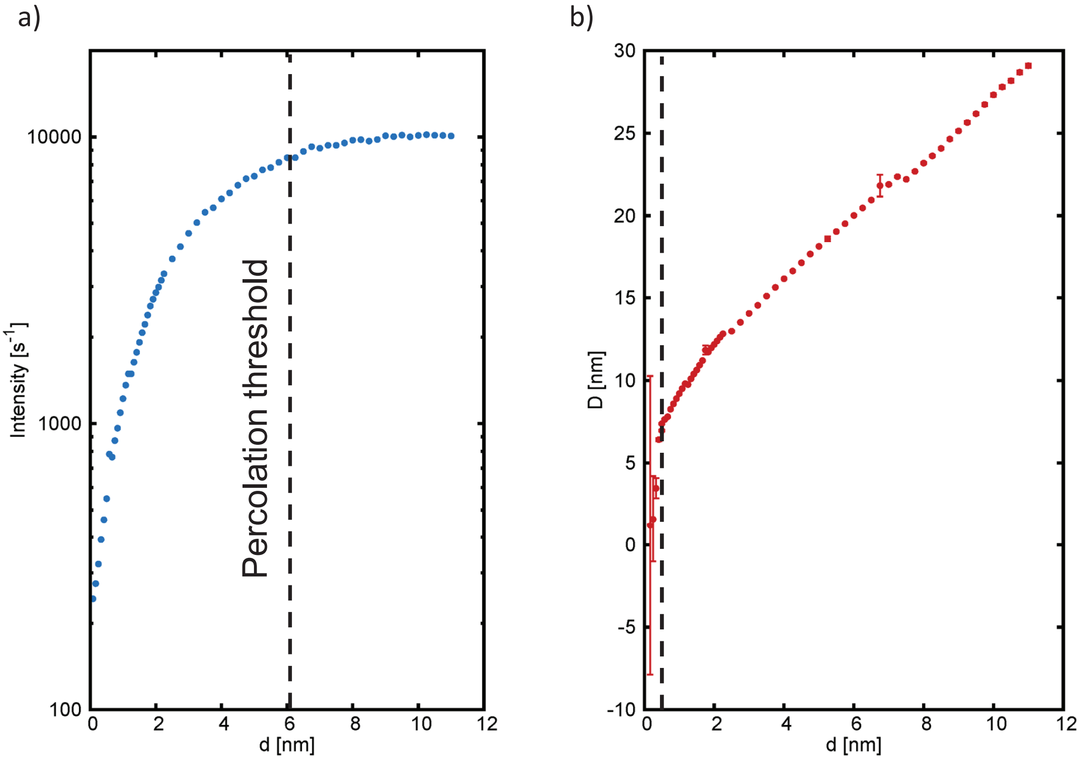

Figure 7.6:
a) Intensity evolution at α_f=0.41^o near the gold (Au)-Yoneda peak as a function of sputter deposited Au mass thickness d. The dashed lines marks the nominal percolation threshold.
b) Evolution of the most-prominent in-plane lenght D as a function of d. The dashed lines shows a first transition point at around d=0.6nm.

in detail the selective deposition of metals on polymers and to investigate the layer's nano-and mesostructure to obtain the relevant growth laws and correlations [5,6]. Here we report on novel stop-sputter-experiments at the Micro- and Nanofocus X-ray Scattering (MiNaXS) beamline P03 [4] of PETRA III, DESY. We combined in a novel way a high-flux, low divergence X-ray microfocus beam with a specially designed, automated RF sputter deposition chamber. We used an Au sputter rate of 0.5nm/min (RF power P=50W, Argon (Ar)-pressure $2x10^{-2}$mbar), comparable to [5,6], acidly cleaned silicon (Si) substrate, a beam size of $38x20\mu m^2$ and an incident angle of α_i=0.45^o. During the stop-sputter experiment, the Au deposition times were 10s (incremental Au mass deposit of Δd=0.083nm) up to a total Au layer thickness d<2.5nm and 30s afterwards. All acquisition times were fixed to t_{acq}=10s.

In summary, we have presented a first stop-sputter experiment using a model system (Au on Si), combining successfully RF sputter depositon and in-situ μGISAXS at MiNaXS. This type of experiment gives in future access to assess the metallic film nanostructure at low coverages. Due to the high flux in the microbeam, further investigations will focus on the influence of deposition parameters (rate, sample temperature, sputter pressure) on the structural build-up as well co-sputter deposition of hybrid materials.

[1] F. Faupel, V. Zaporojtchenko, T. Strunskus, M. Elbahri, *Adv. Eng. Mater.* **12**, 1177-1190 (2010)

[2] G. Kaune, M. A. Ruderer, E. Metwalli, W. Wang, S. Couet, K.Schlage, R. Röhlsberger, S. V. Roth, P. Müller-Buschbaum, *ACS Appl. Mater. Interfaces* **1**, 353-360 (2009)

[3] H. Greve, A. Biswas, U. Schürmann, V. Zaporojtchenko, F. Faupel, *Appl. Phys. Lett.* **88**, 123103 (2006)

[4] S. V. Roth, G. Herzog, V. Körstgens, A. Buffet, M. Schwartzkopf, J. Perlich, M. M. Abul Kashem, R. Döhrmann, R. Gehrke, A. Rothkirch, K. Stassig, W. Wurth, G. Benecke, C. Li, P. Fratzl, M. Rawolle and P. Müller-Buschbaum, *J. Phys. Cond. Matter* **23**, 254208 (2011)

[5] E. Metwalli, S. Couet, K. Schlage, R. Röhlsberger, V. Körstgens, M. Ruderer, W. Wang, G. Kaune, S. V. Roth, P. Müller-Buschbaum, *Langmuir* **24**, 4265-4272 (2008)

[6] A. Buffet, M. M. Abul Kashem, K. Schlage, S. Couet, R. Röhlsberger, A. Rothkirch, G. Herzog, E. Metwalli, R. Meier, G. Kaune, M. Rawolle, P. Müller-Buschbaum, R. Gehrke, S. V. Roth, *Langmuir* **27**, 343-346 (2011)

[7] http://www.desy.de/ beneckeg/dpdak

7.5 Spectral variations in thin film PV module performance under real conditions

Y. Boose, M. Lynass[1], P. Müller-Buschbaum

[1] GE Global Research, Garching, Germany

The total global photovoltaic (PV) installed Watt peak power increases rapidly every year and has reached approximately 24 GW in 2011. Due to this growth, the ability to predict the energy generated by PV becomes more and more crucial for solar plant and grid operators and the variability of the energy output plays a growing role. Apart from the effective solar module area and factors like defects or shading of the modules, the total energy output of a solar plant depends mostly on factors which effect the radiative conditions such as the air mass, the amount of sun hours and the degree of cloudiness. However, it is not well known yet how a varying solar spectrum influences the output for different PV technologies. Since variations in the solar spectrum are directly related to atmospheric processes they depend highly on the location of the solar plant. In this work we investigate for our campus location in Garching, Germany how changes in the spectrum influence the output of two thin film technologies, Cadmium Telluride (CdTe) and Copper Indium Gallium Diselenide (CIGS).

The efficiency of solar modules is defined under standard testing conditions (STC), meaning an irradiance of $1000Wm^{-2}$ under the AM1.5 Terrestrial Global Standard Spectrum and a module temperature of $25\,^{\circ}\mathrm{C}$. The spectral dependency of a material is described by its quantum efficiency (QE) or respectively its spectral response (SR).

In order to compare the energy output for STC with that under real conditions, meaning usually less then $1000Wm^{-2}$ and a different spectral distribution, the short circuit currents are useful. The spectral mismatch factor (sMMF) describes the ratio of the short circuit currents weighted with the respective irradiance and gives a measure to rate the use of a technology at a certain location from a spectral point of view. We investigate the sMMF theoretically by applying the SMARTS2 model for atmospheric radiative transfer of sunshine [1] as well as experimentally by setting up a system outdoors that measures continuously and synchronously the solar spectrum, the performance of two thin film technology modules as well as meteorological data. First experimental results give a spectral mismatch factor of up to 7.2% for CdTe and up to 5.7% for CIGS at our location.

Our experimental set up on the roof includes a spectrometer system measuring the plane of array global solar spectrum from 300-1680 nm with a temporal resolution of less than 10 seconds. Since the spectral response of the silicon based detector reaches only up to 1100 nm a second InGaAs based detector was installed to measure in the near infrared region. The current versus voltage characteristics of a CIGS and a CdTe module are recorded independently every second using an electronic load and a boost supply. Meteorological data such as humidity, ambient temperature and wind speed are logged by a weather station next to the set up. Global, direct and diffuse irradiance are measured by pyranometers and the module temperatures by PT100 sensors. Apart from that weather observations are carried out with the use of a fish eye camera.

Atmospheric processes such as scattering and absorption have an influence on the total but also on the spectral solar irradiance. The amount of water vapor, ozone and aerosols as well as the air pressure and the amount and type of clouds occurring at a specific location can lead to a shift of the spectrum towards the red or the blue. Depending on the used technology this shift can lead to a change in the performance of the modules. One approach to describe the spectral shift is the average wavelength (AWL) of the investigated spectrum. Looking at different weather situations in particular fast moving cumulus clouds lead to strong and fast variations in the solar spectrum especially at their edges. A number of effects can be detected. Due to reflections on the sharp edges of cumuli a momentary enhancement of the total irradiance even above the solar constant can occur. When a cloud shades the sun completely the total irradiance has decreased and the spectral irradiance has shifted towards the blue. Clouds can be seen in Fig.7.7 as blue vertical stripes in the afternoon because they decrease the irradiance over the whole spectrum. The AWL in Fig.7.8 drops down towards lower wavelengths. Yet, right before the cloud edge is about to move in front of the sun a small red-shift of the spectrum can be observed, as shown in Fig.7.8 around 16:00 pm. The reason for this shift has not yet been fully understood but a relation to humidity halos surrounding cumulus clouds under certain conditions is likely.

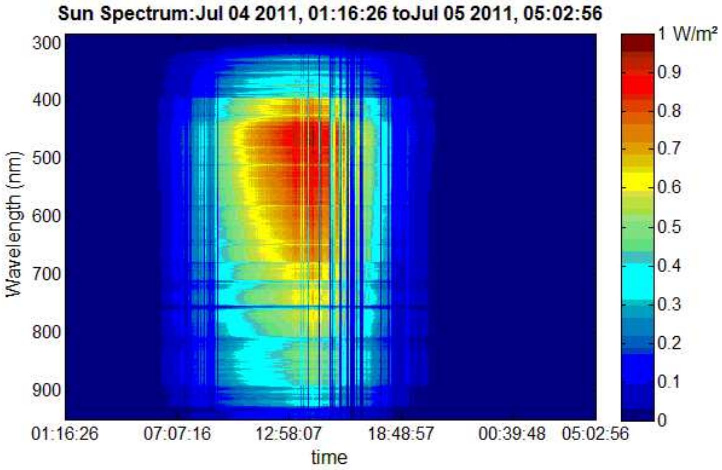

Figure 7.7: Solar Spectrum during the scope of a day

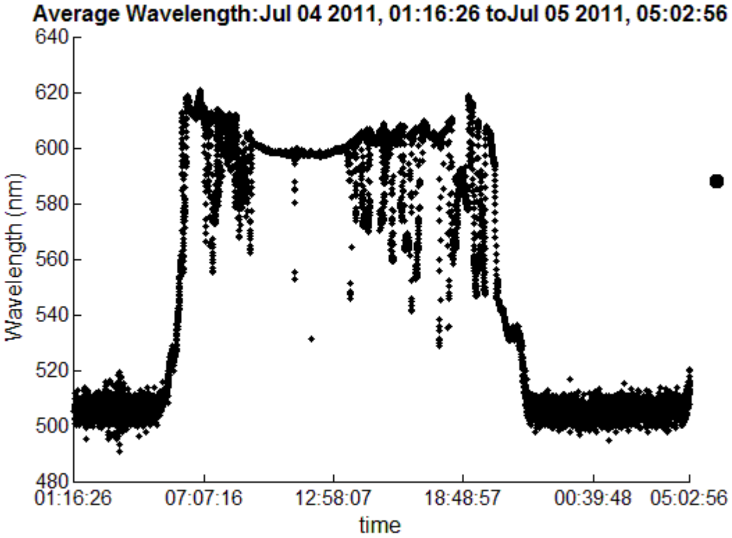

Figure 7.8: Average wavelength for the same sunny day with single clouds in the afternoon

We conclude that the effect of a from the AM1.5 Standard Spectrum deviating spectrum has a significant effect on the momentary energy output of the two examined modules. Further research will tackle the question how this effect changes with weather condition and season and on which temporal scales. Experimental results will be compared with annual energy prediction tools for solar plants such as the NREL SANDIA model [2]. Also, the origin and effect of the cloud edge shift will be further investigated.

[1] C. Gueymard, *Sol. Energy* **71**, 325-346 (2001)

[2] D. L. King, W. E. Boyson, J. A. Kratochvil, *Sandia NREL* **SAND2004-3535**, (2004)

7.6 Studying Fermi surfaces by positron annihilation

M. Leitner, J. Neuhaus, W. Petry

All properties of matter ultimately depend, either directly or indirectly, on the electronic structure. More precisely, in crystalline metals a wide range of phenomena can be understood in terms of only the Fermi surface, i.e., the boundary separating occupied from unoccupied states in reciprocal space. A specific example is the anomalous softening of phonons connected to a martensitic transformation into a long-range-modulated structure observed in certain alloys, which is thought to be due to a so-called nesting of the Fermi surface, that is the existence of a distinct vector that translates major parts of the Fermi surface onto itself, enabling low-energy electronic redistributions.

Resulting from ongoing investigations into the magnetic-shape-memory effect in Ni_2MnGa (a martensitic transformation triggered by an applied magnetic field) and its temperature-, composition-, and field-dependence [1], we plan to systematically study the Fermi surface under the corresponding conditions. The most suited method for this task is Angular Correlation of Positron Annihilation Radiation (ACPAR), as it allows measurements under arbitrary magnetic fields, ambient temperatures, and atomic disorder. An ACPAR-setup is currently being installed at the FRM II, to be upgraded to use the reactor positron beam NEPOMUC.

ACPAR consists in implanting positrons in the sample, which thermalize and in turn annihilate with the sample's electrons, and detecting the directions of the resulting two annihilation photons in coincidence mode. The essence of the method is that due to momentum conservation the sum of the photons' wavevectors gives the two-dimensional projection of the momentum of the annihilated electron, as the momentum of the thermalized positron can be neglected. Even though the information on the longitudinal component of the electron momentum is lost due to the photon detectors' insufficient energy resolution, the full three-dimensional information can be recovered by tomography. In contrast to most other fields such as medicine already a few independent projections constitute sufficient constraints for reconstructions to succeed because of the high symmetry of the crystalline state. How to choose the projection directions and how to implement the tomographical inversion in order to obtain an optimal result for a given number of coincident counts (i.e., measurement time) is the question we want to treat here.

The primary data in an ACPAR experiment are projections of the momentum density in an extended zone scheme with a resolution of $N \times N$ pixel, with N on the order of a few hundred given by the instrumental resolution. In order not to discard information, the three-dimensional reconstruction $\boldsymbol{\rho}$ therefore needs on the order of $N \times N \times N$ voxel. As the number of projections is much smaller than N, the unconstrained problem of finding the optimal reconstruction is severely underdetermined. Noise in the data would therefore drastically affect the reconstructed density. However, it is clear that the momentum distribution has to be smooth apart from the Fermi breaks in the valence contributions. In trials with simulated data it has proven successful to solve the regularized problem

$$\min_{\boldsymbol{\rho} \in \mathbb{R}_+^{N^3}} f(\boldsymbol{\rho}; p_i; \lambda) \quad \text{with} \quad f(\boldsymbol{\rho}; p_i; \lambda) = \sum_i \|p_i - P_i(\boldsymbol{\rho})\|_2^2 + \lambda \|\mathbf{D}^2(\boldsymbol{\rho})\|_2^2, \tag{7.1}$$

where p_i are the experimental projections, P_i the corresponding projectors, and $\mathbf{D}^2(\boldsymbol{\rho})$ is the discrete Laplacian applied to the density $\boldsymbol{\rho}$. The norm of the residuals is weighted according to Poisson statistics. The regularization parameter λ is iteratively refined in order to get a smooth density without introducing systematic residuals. Due to the dimensionality of the problem, Eq. (7.1) is solved iteratively by a limited-memory variant of the BFGS algorithm [2].

For a demonstration we treat here the case of stoichiometric Ni_2MnGa in the cubic high-temperature $L2_1$-phase above the Curie temperature. The electronic structure of the system has been computed by standard density-functional-theory codes, afterwards the positron wavefunction has been computed in the given electronic (and ionic) potential as is appropriate for vanishing positron densities and delocalized states. The resulting two-photon momentum density $\boldsymbol{\rho}$ is then essentially given by the squared Fourier coefficients of the product of the jth electronic and the positronic wavefunction, summed over all states j and weighted by the respective occupations at room temperature. The result is illustrated in Fig. 7.9 for a projection along $\langle 110 \rangle$. Correlation effects between the positron and the electrons (not included yet) would slightly affect the result.

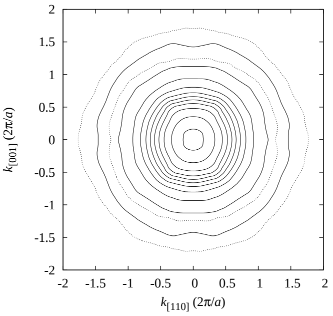

Figure 7.9:
Resulting two-photon momentum distribution for paramagnetic $L2_1$ Ni_2MnGa in the $\langle 110 \rangle$ projection. The solid contour lines are equidistant, the dotted lines are further bisections. The two-fold symmetry is clearly visible atop a broad isotropic contribution due to annihilation with core electrons.

Sets of projections subjected to Poisson noise corresponding to a certain number of total counts have been simulated. The three-dimensional momentum distribution $\boldsymbol{\rho}$ defined by Eq. (7.1) has been computed. The Fermi breaks can be most easily recognized by folding these momentum distributions back into the first Brillouin zone (i.e., transforming from the extended to the repeated zone scheme): the contributions from filled (core-)bands sum up to a slowly varying background, while the Fermi breaks in the outer Brillouin zones are translated back into the first zone and add coherently [3]. A cut through the resulting folded density is shown in Fig. 7.10.

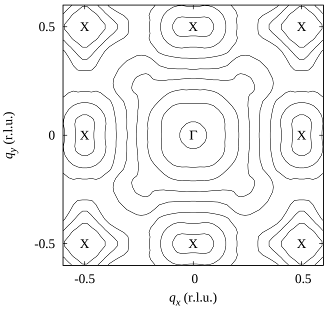

Figure 7.10:
Cut through the folded density on the reciprocal lattice of the fcc lattice for $q_z = 0$, contour lines are equidistant. Because of the finite temperature and the rather flat bands crossing the Fermi level, no sharp breaks are seen, but the hole around Γ and the filled pockets around X are clearly visible nevertheless.

This demonstration has used a signal of 10^8 total counts, which can be obtained within a few days with a standard ^{22}Na-source, and within a single day with NEPOMUC's flux. Concerning the number of projections it can be said that it is in principle better to distribute the measurement time between more projections than to take only one or two projections with exceedingly good statistics. Experimental inaccuracies in the sample orientation or detector alignment could potentially lead to an opposite effect, however. It is obviously desirable to cover a part of the irreducible wedge as large as possible, which includes for the cubic symmetry the $\langle 100 \rangle$, $\langle 110 \rangle$, and $\langle 111 \rangle$ directions, which was the choice used in this demonstration.

Funding of this project by the DFG via the Transregio 80 "From Electronic Correlations to Functionality" is gratefully acknowledged.

[1] S. Ener et al., this Report, 98-99

[2] J. Nocedal, *Math. Comput.* **35**, 773-782 (1980)

[3] D. G. Lock, V. H. C. Crisp, R. N. West, *J. Phys. F: Met. Phys.* **3**, 561-570 (1973)

7.7 Selective activities of the fuel development group at FRMII in 2011

H.-Y. Chiang, H. Breitkreutz, M. Däubler, R. Jungwirth, T. Zweifel, T. Huber, Ch. Steyer, R. Schenk, B. Baumeister, M. Kreß, M. Fuchs, W. Petry

Research for the developement of high density fuel of FRM II with lowered enrichment continued in 2011. Research focuses on theoretical as well as on the experimental side. In the following, an overview of the major activities of the group is given.

Simulations

Simulations of contact faults in fuel (H. Breitkreutz)

Contact faults between cladding and meat, so-called non-bonds, may have noticeable consequences on the thermal-hydraulic behaviour of fuel plates as they form a strong barrier for the heat flux from the fuel into the cladding and therefore deflect the heat to the opposite side (Fig 7.11). Furthermore, due to the resulting increased heat fluxes in some parts of the plate, the presence of such faults may lead to a drastic growth of the oxide layer, finally leading to oxide flaking. The time evolution of the oxide layer and the resulting impact on the thermal hydraulics of such a break-up were simulated for different fault sizes and meat materials using a CFD code. The effects have been calculated for small demonstration samples. It was shown that there is a notable dependence of the resulting (surface) temperatures and heat fluxes as well on the irradiation time as on the thermal conductivity of the fuel (Fig 7.12). Fuels with low thermal conductivities, e.g. monolithic UMo, generally perform worse than fuels with high thermal conductivity, especially regarding fuel temperatures. However, the oxide layer build-up and effects caused by this generally expose smaller differences between the different fuels than what is expected if no oxide layer is present.

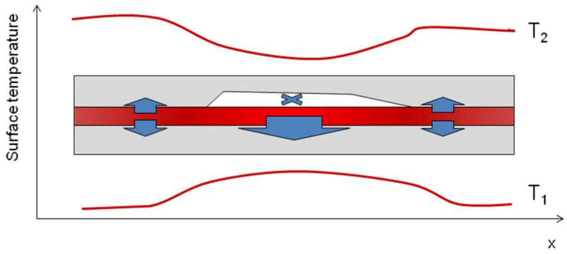

Figure 7.11:
Sketch of surface temperatures (red lines) and heat fluxes (blue arrows) due to a contact fault between cladding (grey) and fuel (red)

New reactor safety analysis of FRM II (M. Däubler)

Within the context of the possible conversion of FRM II, efforts to set up a new code system for reactor safety analysis have been made at FRM II. A methodology to analyse FRM II using the best-estimate coupled code technique has been developed and the US NRC coupled best-estimate code system TRACE/PARCS has been chosen to model FRM II. Employing TRACE/PARCS for FRM II safety analysis, the achievable accuracy of simulating FRM II with this system under BOL conditions is investigated. The accuracy is quantified by a code-to-code comparison of the calculation results obtained with the in-house X^2 program system for the current fuel assembly with its involute shaped fuel plates. The X^2 program system is used for high-detail 3D, steady-state coupled neutronics and thermal-hydraulics calculations of potential future fuel assembly designs. It couples the burn-up code sequence MONTEBURNS - coupling of MCNPX and ORIGEN - and the computational fluid dynamics code ANSYS CFX.

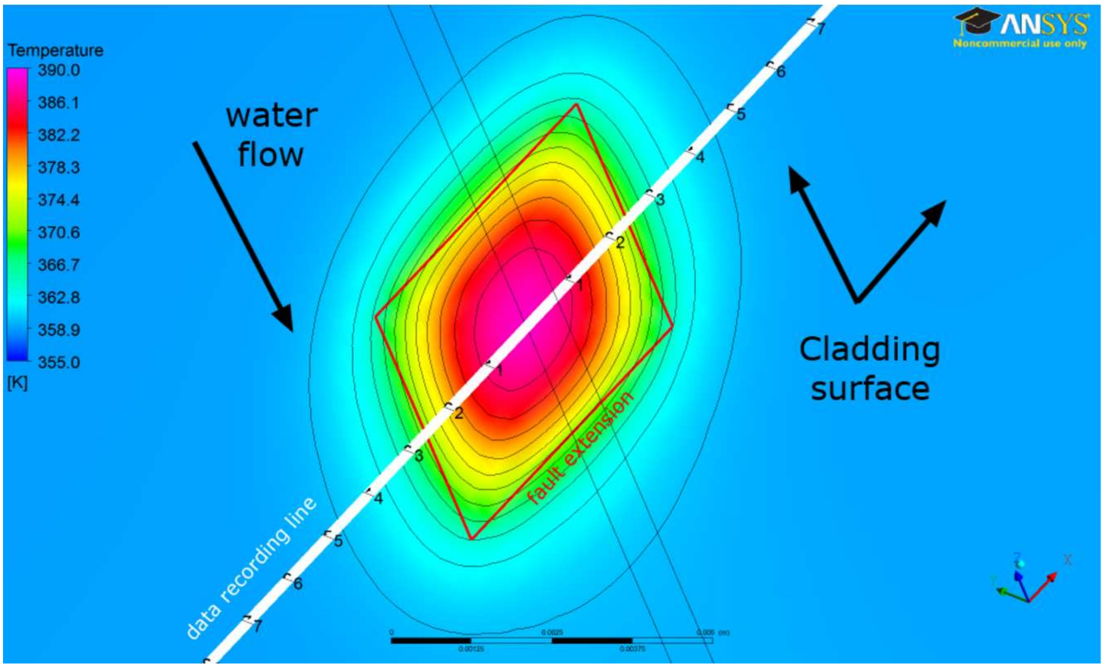

Figure 7.12:
Example solution: Cladding surface temperatures for a failure size of $5 \cdot 5\ mm^2$ and an expected heat flux of $350\ W/cm^2$ after 1 day. The red square shows the dimension of the failure. Water comes in from above. The white line indicates where data was taken for the following plots.

Experiments

Ion irradiation induced interactions of dispersed UMo fuel (R. Jungwirth)

The development of new UMo based disperse high-density fuels for research and test reactors worldwide has been retarded by unforeseeable high swelling of test fuel plates during in-pile irradiation. The main cause for the swelling is the build-up of an interaction layer at the interface between the UMo and the Al. It is known that the addition of some wt% Si to the Al matrix results in the formation of a silicon rich layer (SiRL) at the interface between the UMo and the Al. This SiRL forms during annealing in the course of fuel plate production. It retards the conventional UMo/Al interdiffusion during irradiation and therefore enhances the in-pile performance. However, a conventional UMo/Al interaction layer occurs as soon as the SiRL has been completely consumed. Since not all the Si added to the Al matrix is used to form the protective SiRL it has been suggested to apply the silicon directly where it is needed: at the interface between the UMo and the Al, thereby maximizing the availability of Si in the diffusion process. Another possibility to reduce the UMo/Al interaction is the application of a ZrN diffusion barrier. Both coatings were applied by sputter deposition. Samples from plates prepared with UMo powder coated with 300 nm Si, 600 nm Si and 1000 nm ZrN have been examined before and after irradiation with heavy ions (Iodine at 80MeV). In case of Si covered UMo, the Si layer has been transformed into a SiRL during plate processing. For ZrN, almost all UMo particles are covered by a ZrN layer. However, the layer usually reveals cracks that have been introduced during plate fabrication. A sufficiently thick SiRL – what is the case for 600 nm Si - or a dense ZrN layer around the UMo completely suppressed the formation of an IDL during irradiation. However, the presence of cracks inside the ZrN layer is still a clear drawback since at spots that reveal cracks a conventional UMo/Al diffusion occurs.

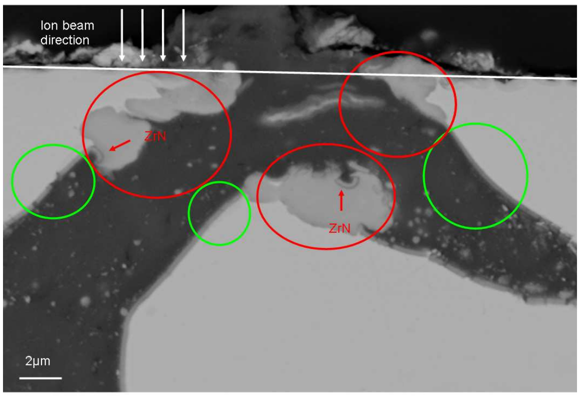

Figure 7.13:
UMo particles covered with 1000 nm ZrN after irradiation. In case of a dense ZrN layer (green circles) the UMo/Al diffusion has been completely suppressed. In case of a cracked ZrN layer a huge IDL has grown along the cracks.

Correlations between temperature and generations of IL under ion irradiation (T. Zweifel)
For the conversion of high performance research and test reactors worldwide from high enrichment towards lower enrichment a new high density fuel element is required in order to maintain the scientific quality of these facilities. One promising new fuel element is dispersed UMo powder inside an Al matrix. However, until now every in-pile test irradiation failed due to excessive swelling of the fuel during irradiation. Main reason for this abnormal swelling is the growth of an interaction layer (IL) at the UMo/Al interface which has an insufficient capability of retaining fission gas. It has been shown that the IL growth is significantly enhanced by temperature. In 2006 it has been demonstrated that the fission damage to the fuel in-pile can as well be simulated by heavy ion irradiation with 127 Iodine at 80 MeV which also leads to the growth of an interaction layer in UMo/Al systems (Fig 7.14). One big difference between ILs grown in-pile and those grown by heavy ion irradiation is that in-pile ones are amorphous while those out-of-pile are crystalline. This difference is not well understood yet. The aim of this thesis is the study of the IL growth in UMo/Al layer systems created by heavy ion irradiation at the MLL Tandem accelerator in Garching at different irradiation temperatures. Until now 15 samples have been irradiated at the MLL at different irradiation temperatures ranging from 120°C to 220°C. In these samples ILs have been created with thicknesses from 1 to $\sim$ 4 μm. The next steps of the IL investigation include TEM studies. The goal is to check whether there are small amorphous compounds inside the crystalline ILs obtained during heavy ion irradiation.

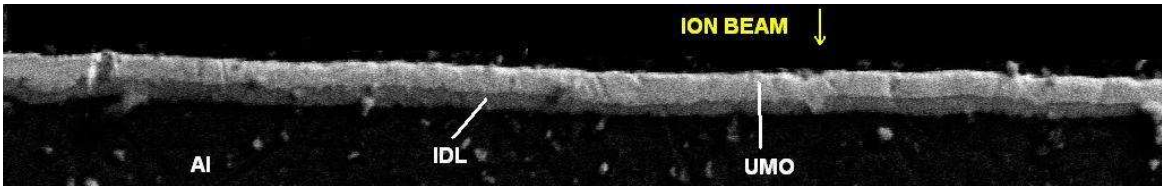

Figure 7.14:
Sample irradiated at T = 200°C. Growth of an interaction layer (dark gray area) with an average thickness of $\sim$ 1.3 μm.

Interactions between UMo/Al fuel and diffusion barriers under ion irradiation (H.-Y. Chiang)
The stability of the interaction layer between U-Mo fuel and Al matrix can be improved by adding alloying elements in the aluminum matrix or in the U-Mo alloy. It is also observed that the growth of the interaction layer during in-situ irradiation can be suppressed by adding a diffusion barrier element. To understand the interactions among UMo, diffusion barriers and

Al matrix, a sandwich structure has been fabricated. Diffusion barriers like transition metal niobium and ceramics titanium nitride have been tested. With the purpose to simulate typical in-pile irradiation conditions these two sandwich structures with Nb and TiN as diffusion barrier have been subjected to iodine ion irradiation with the purpose to simulate typical in-pile irradiation conditions: 80 MeV I^{6+} ions and a fluence of $1 \cdot 10^{17}/cm^2$. Scanning electron microscope (SEM) examinations show the complete suppression of the diffusion induced interaction layer (IDL) in both cases. However, atomic mixing in both sandwich structures is observed in energy-dispersive X-ray spectroscopy (EDX) (Fig 7.15).

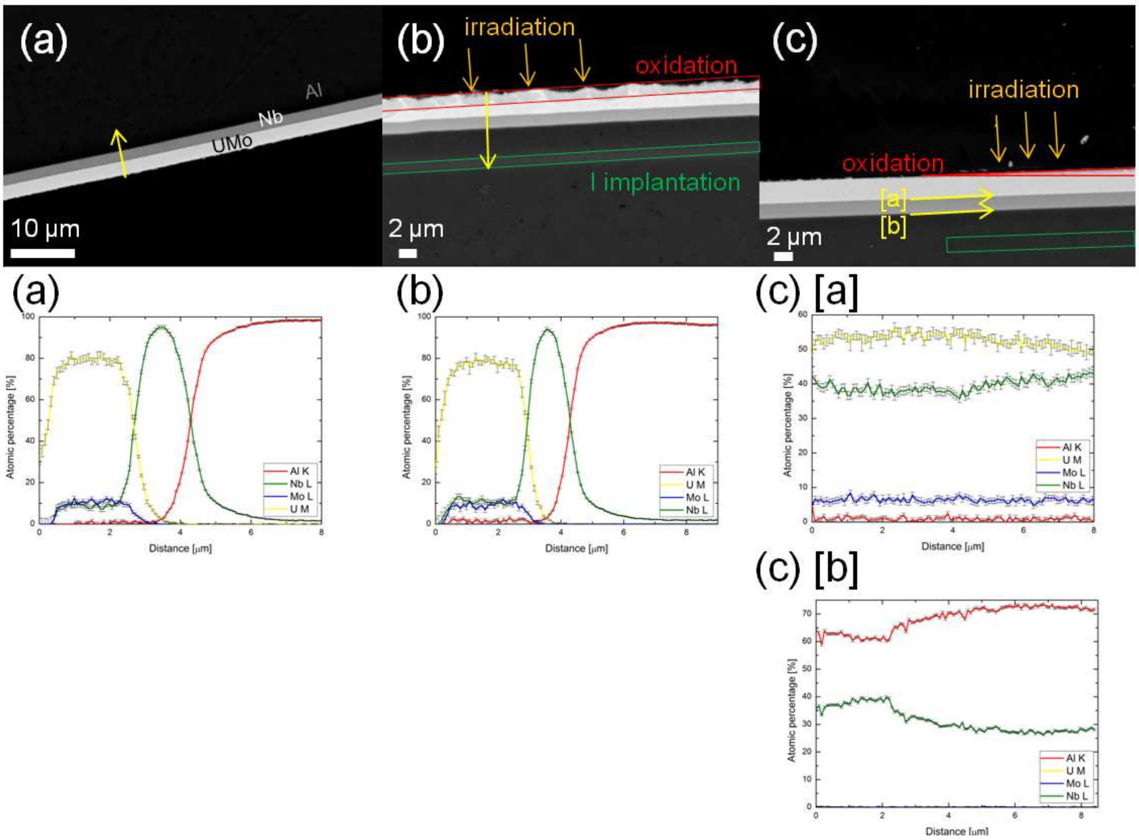

Figure 7.15:
Upper row: SEM images of UMo/Nb/Al are shown in (a) non-irradiated area, (b) irradiated area and (c) boundary between non-irradiated and irradiated area. Lower row: EDX line scans along the yellow arrows drawn in the corresponding SEM images.

Thermal Conductivity Measurements of Irradiated and non-irradiated U-Mo alloys
(T. Huber, M. Fuchs)

The thermal conductivity of nuclear fuel plays a significant role in the determination of the maximum operating power of a fuel element and also the available safety margins. The thermal conductivity is a composition of the density, heat capacity and thermal diffusivity of the material. There are different experimental methods to obtain the thermal diffusivity of a material: 2ω-Method, Scanning Thermal Diffusivity Microscope (STDM), LASER Flash Method and Thermography (Fig 7.16). The 2ω-Method, STDM and LASER Flash Method work on a microscopic scale of a few μm to mm, while the thermography apparatus can measure non-destructively on the macroscopic scale of several tens of cm. LASER Flash is a standard method, whereas the other methods have been developed for special purposes.

The STDM is adapted for measurements of disperse fuel due to its ability to measure on a very small scale using thermal expansion caused by LASER pulses. Single U-Mo grains and even interaction layers between the grains and the aluminium matrix can be studied.

The LASER Flash set-up is a well-known standard method to investigate the thermal diffusivity of materials by heating up the sample with a very short intense LASER pulse and is like the STDM set-up already installed in a hot cell, waiting for measurements on irradiated fuel.

Thermography allows, in contrast to STDM and LASER Flash Method, to measure the sample non-destructively, which is adapted for radioactive samples, i.e. the U-Mo alloy remains in its containing aluminium cladding and it is not necessary to handle open radioactive material. The principle of measurement is very similar to the LASER Flash Method, but on a larger scale. This method as well as the STDM was developed by the Idaho National Laboratory (INL). Recently different test measurements were performed in collaboration with Technische Universität München (TUM) with different materials (Mo, Zr, Nb, stainless steel and nonirradiated U-Mo) as inserts in Al-6061 plates with the Thermography apparatus before installation in a hot cell, where irradiated samples will be measured. The results from these measurements will be verified with measurements of the same plates with the LASER flash method.

The 2ω-Method was developed by TUM and measures the phase shift of a heat wave during transfer through a material at different frequencies. The method is already proofed for non-irradiated fuel and is currently used for measurements of fuel, which was irradiated by an ion-beam with a penetration depth of about $\sim 10\ \mu$m. The advantage of this type of measurement is to be able to measure samples with a thickness of $\sim 10\ \mu$m, while all other methods require a thickness of several hundredth of micron meter.

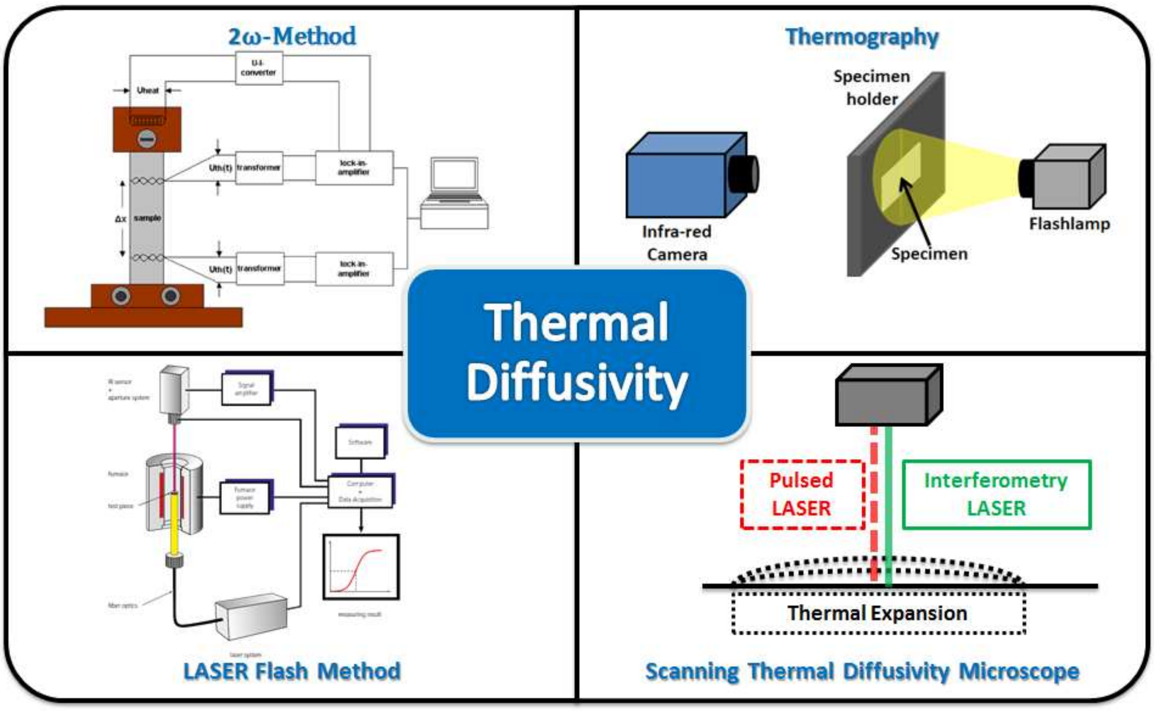

Figure 7.16: Schematic drawing of the different measurement set-ups.

Disperse fuel project (Ch. Steyer, R. Schenk)
There are two basic options for the meat of a new fuel element for the FRM II: a monolithic or a disperse fuel. A monolithic fuel element is composed of the aluminum cladding on both sides and only one solid, monolithic UMo plate inside. The meat of an element with a disperse fuel consists of small uranium particles embedded in an aluminum matrix. To investigate the producibility and properties of a disperse fuel as a meat for a future fuel element, we worked on several projects to be able to prepare samples of such a disperse UMo based fuel in the near future. These activities were divided into three main tasks:

- The design process for a device to produce the spherical UMo-Powder, which has a diameter distribution between 45 and $\sim$ 150 μm, was finished in 2011 and the machine is under construction now. This technique is based on an atomization process and is adjusted for usage in an inert gas glovebox system.
- To prevent the formation of interaction diffusion layers (IDL) it is necessary to coat the surface of each UMo particle with special materials (e.g. Si, ZrN, TiN) to build up an IDL barrier. We investigated the coating of spherical powder in a specially constructed sputter coating apparatus and examined the particle coating quality by SEM and EDX. An example of a spherical glass particle coated with aluminum can be seen in figure 7.17. We found, that sputter deposition allows application of homogenous coatings of various potential barrier materials in micrometer thickness onto spherical powder particles.
- Furthermore we adapted and improved our mounting, grinding, polishing und analyzing process from planar to powdery samples

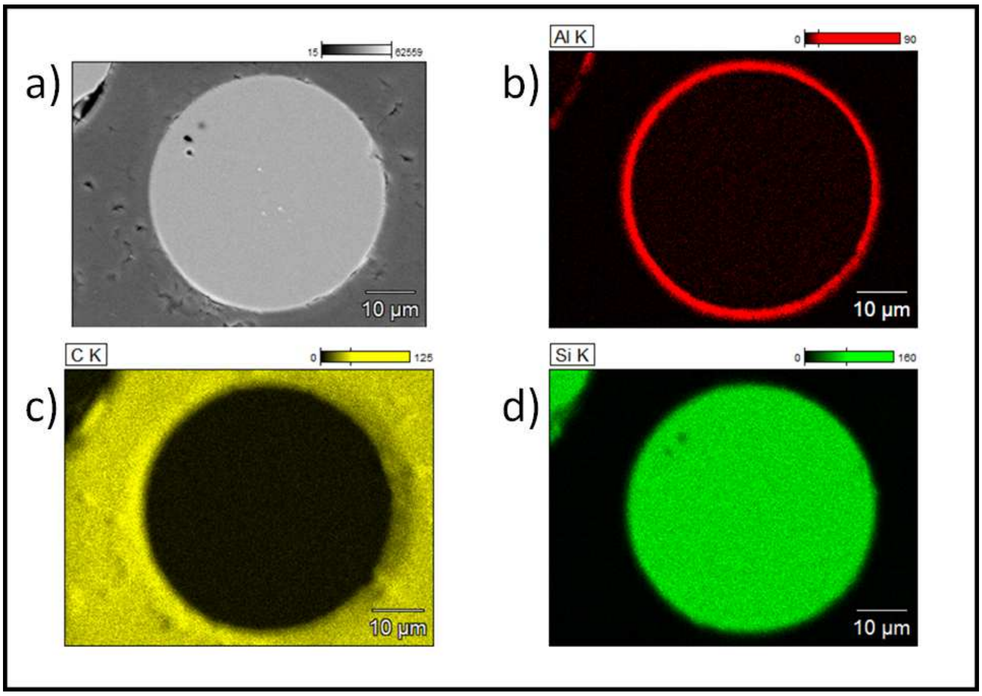

Figure 7.17:
BSE image of a coated glass particle (a), EDX image of the Al distribution (b), the C distribution (c) and Si distribution (d).

Evaluation of alternative chemical cleaning procedures for blank monolithic U-Mo foils

(B. Baumeister)

The cladding application to monolithic U-Mo fuel foils requires efficient in-depth surface cleaning procedures to remove uranium oxide aswell as other residues which are likely to come from precedent production steps. Besides the most commonly used method, etching with nitrc acid (HNO_3), some other chemical solutions like hydrochloric acid (HCl), sodium hydroxide solution ($NaOH$) and hydrogen peroxide (H_2O_2) were tested for their ability to remove those unwanted substances. The optical characterization by scanning electron microscopy aswell as an element-sensitive analysis by energy-dispersive X-ray microscopy showed that cleaning quality when using HNO_3 is comparable with a mixed $NaOH/H_2O_2$ solution when it comes to oxide removal, whereas a satisfying dissolution of other residues like silicon, carbon and aluminum can only be achieved by $NaOH/H_2O_2$ cleaning. Cleaning with HCl can not be recommended as it heavily damages the Uranium surface while leaving huge amounts of oxide on the surface (Fig 7.18).

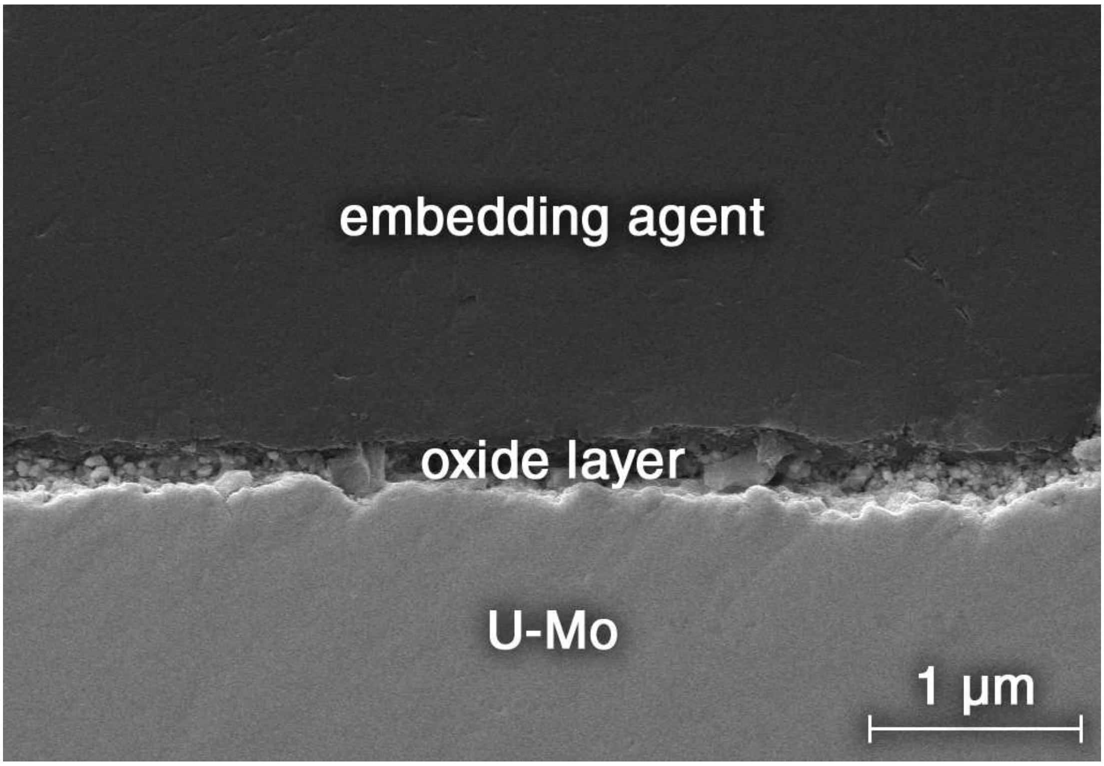

Figure 7.18:
Cross-section view of oxidized U-Mo foil. The porous oxide layer, which can not be found on cleaned surfaces, is clearly visible here.

Tensile tests on monolithic samples (M. Kreß)

To examine the adhesion strength between the layers of a two-component foil and to investigate a possible debonding among the layers (Fig 7.11), two tensile tests were prepared with U-Mo samples from Idaho National Laboratory. The samples have been produced by hot rolling, where a U-Mo foil was embedded between two layers of zirconium, and have been cut into squares with a side length of 20 mm. The preparation itself included several steps from rough cleaning till ultrasonic bath in acetone. The samples were mounted on the specimen holders with EP-15 from Masterbond Inc. as bonding agent (Fig 7.19) and were tensioned in a Zwick Roell Z100 tensile testing machine. In both tests the specimens failed due to a rupture in the bonding agent at forces of 15.76 kN respectively 11.54 kN, which corresponds to a maximum tension of 50.17 MPa respectively 36.4 MPa. Based on this result it is possible to state at least a minimum tension, the foils can withstand. Further tests and a more detailed evaluation of the results remain to be done in the near future.

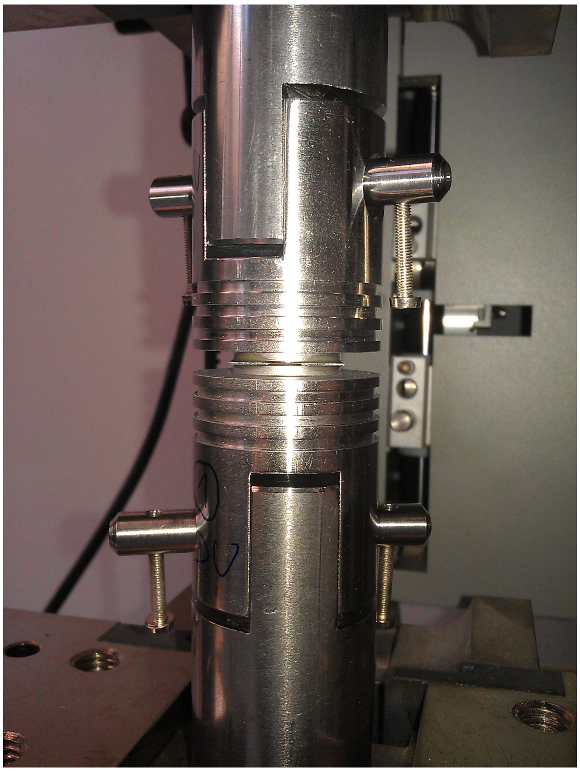

Figure 7.19:
View of the two specimen holders with mounted U-Mo-foil in between.

8 Teaching and outreach

8.1 Lectures, seminars and lab courses

Spring semester 2011

Prof. Dr. Peter Müller-Buschbaum, *Experimentalphysik 2 für Maschinenwesen*
Prof. Dr. Christine M. Papadakis, *Experimentalphysik 2 für Ingenieurwissenschaften*
Prof. Dr. Peter Müller-Buschbaum, Prof. Dr. Christine M. Papadakis, *Seminar über Struktur und Dynamik kondensierter Materie*
Prof. Dr. Peter Müller-Buschbaum, Prof. Dr. Christine M. Papadakis, *Studentenseminar: Grundlegende Phänomene der Physik der weichen Materie*
Prof. Dr. Peter Müller-Buschbaum, *Angewandte Physik: Polymerphysik 2*
Prof. Dr. Peter Müller-Buschbaum, Dr. Ezzeldin Metwalli Ali, *Nanostructured Soft Materials II*
Prof. Dr. Peter Müller-Buschbaum, Prof. Dr. Christine M. Papadakis, *Seminar: Polymere*
Prof. Dr. Peter Müller-Buschbaum, Prof. Dr. Christine M. Papadakis, *Bachelor-Seminar: Funktionelle weiche Materialien*
Prof. Dr. Peter Müller-Buschbaum, *Tutorenseminar zur Vorlesung Experimentalphysik 2 für Maschinenwesen*
Prof. Dr. Winfried Petry, Prof. Dr. Peter Böni, Prof. Dr. Wolfgang Häußler, Prof. Dr. Klaus Schreckenbach, *Seminar über Neutronen in Forschung und Industrie*
Prof. Dr. Winfried Petry, *Blockseminar Erasmus Mundus MaMaSELF Summerschool*

Fall semester 2011/2012

Prof. Dr. Peter Müller-Buschbaum, *Experimentalphysik 1 für Maschinenwesen*
Prof. Dr. Peter Müller-Buschbaum, *Angewandte Physik: Polymerphysik 1*
Prof. Dr. Peter Müller-Buschbaum, Prof. Dr. Christine M. Papadakis, *Seminar über Struktur und Dynamik kondensierter Materie*
Prof. Dr. Peter Müller-Buschbaum, Prof. Dr. Christine M. Papadakis, *Studentenseminar: Grundlegende Phänomene der Physik der weichen Materie*
Prof. Dr. Christine M. Papadakis, *Nanostructured Soft Materials I*
Prof. Dr. Christine M. Papadakis, *Grundlagen der Experimentalphysik 1 für das Lehramt an Berufsschulen (Technik)*
Prof. Dr. Peter Müller-Buschbaum, Prof. Dr. Christine M. Papadakis, *Seminar: Polymere*
Prof. Dr. Winfried Petry, Prof. Dr. Peter Böni, Prof. Dr. Wolfgang Häußler, Prof. Dr. Klaus Schreckenbach, *Seminar über Neutronen in Forschung und Industrie*

Lab courses 2011

Theoretische und praktische Einführung in AFM (Fortgeschrittenenpraktikum)
Thermische Analyse (Fortgeschrittenenpraktikum)
Neutronenstreuung am FRM II (Fortgeschrittenenpraktikum)
JCNS Laboratory Course - Neutron Scattering (Forschungspraktikum)

8.2 Conferences and public outreach

C. M. Papadakis
Tutorial 'Physics with Neutrons – From Proteins via Polymer Thin Films to Spin Waves'
in the framework of the spring meeting of the division Condensed Matter of Deutsche Physikalische Gesellschaft (DPG)
Dresden, 13 Mar 2011

Sunday

TUT 1: Physics with Neutrons – From Proteins via Polymer Thin Films to Spin Waves (CPP)

New neutron sources (FRM II, ESS, SNS) combined with advanced instrumentation enable the detailed characterization of structural as well as dynamic properties of hard and soft condensed matter. The tutorial covers a few of these methods: Small-angle neutron scattering allows one to investigate mesoscopic structures, e.g. in material and life science. Neutron reflectometry and grazing incidence small angle neutron scattering are used to reveal magnetic structures in thin films and lateral structures at interfaces, for instance. Neutron spectroscopy enables, among others, the investigation of magnetic excitations and is complementary to laboratory based spectroscopy methods.

Organization/Chair: Christine M. Papadakis (TU München)

Time: Sunday 16:00–18:30 Location: HSZ 403

Tutorial TUT 1.1 Sun 16:00 HSZ 403
Neutrons as a sensitive tool to investigate nano- and mesostructured materials — •STEPHAN FÖRSTER — University of Bayreuth, Fakultät für Chemie

Neutrons can be similarly used as x-rays to investigate the structure of nano- and mesoscale synthetic and biological materials. Since, compared to photons, neutrons posses a spin, penetrate deeper into materials, and because the neutron-scattering cross-sections can vary strongly for different isotopes of the same element, they are a much more sensitive and versatile tool.

In the tutorial the basic experiments that can be performed with neutrons, in particular neutron scattering, are described and a number of examples from material and life science are given for illustration. The tutorial also includes practical hints for the application of beam time at neutron facilities.

Tutorial TUT 1.2 Sun 16:45 HSZ 403
Reflectivity and GISAS — •ROLAND STEITZ — Helmholtz-Zentrum Berlin für Materialien und Energie, Berlin, Germany

Current problems in soft and hard matter science often require insight on the nanometer scale. In this contribution we show how surface sensitive scattering of neutrons, namely neutron reflectivity (NR) and grazing incidence small angle neutron scattering (GISANS) can be utilized to reveal details on thin films and stratified systems at solid-gas and solid-liquid interfaces. The first chapter provides a brief revision of the experimental techniques and underlying principles. Successive paragraphs deal with selected examples highlighting various aspects of experimental systems under study. Paragraph two examines polymer films at solid-gas interfaces, paragraph three addresses immobilisation of a protein at solid-liquid interfaces, paragraph four investigates the structure of the boundary of a hydrophobic polymer film and its adjacent water phase. The last two paragraphs concern laterally structured systems at interfaces and magnetic thin films, respectively.

It is noted that in particular neutrons penetrate deeply into matter, which makes them most suitable for studies of buried interfaces. In addition, investigations with neutrons benefit from the negligible impact of neutrons on the sample, i.e. there is no radiation damage, and as long as soft matter samples are considered neutrons can be used to highlight defined areas of interest by partial deuteration of the sample.

15 min. break

Tutorial TUT 1.3 Sun 17:45 HSZ 403
Neutron spectroscopy on solids — •ASTRID SCHNEIDEWIND — Helmholtz-Zentrum Berlin für Materialien und Energie

Neutron scattering is an outstanding and often a unique technique to study the dynamic properties of solids on an atomic scale. The tutorial will give an overview about the opportunities and the constraints of the method. Coming from the understanding of the properties of the neutron and the lattice, the nuclear and magnetic cross-sections for the interaction of the neutron with the lattice will be shown. Typical problems and the results of the required measurements will be presented and used to illustrate the aspects of the different techniques, with focus on three axis spectroscopy and time-of-flight methods. The specific role of neutron scattering in studies on magnetism will be accentuated. Finally, the complementarities to other methods as Raman and infrared spectroscopy, NMR and X-ray scattering will be pointed out.

D. Neher, V. Dyakonov, P. Müller-Buschbaum
SKM Symposium 'Elementary Processes in Organic Photovoltaics'
in the framework of the spring meeting of the division Condensed Matter of Deutsche Physikalische Gesellschaft (DPG)
Dresden, 14 Mar 2011

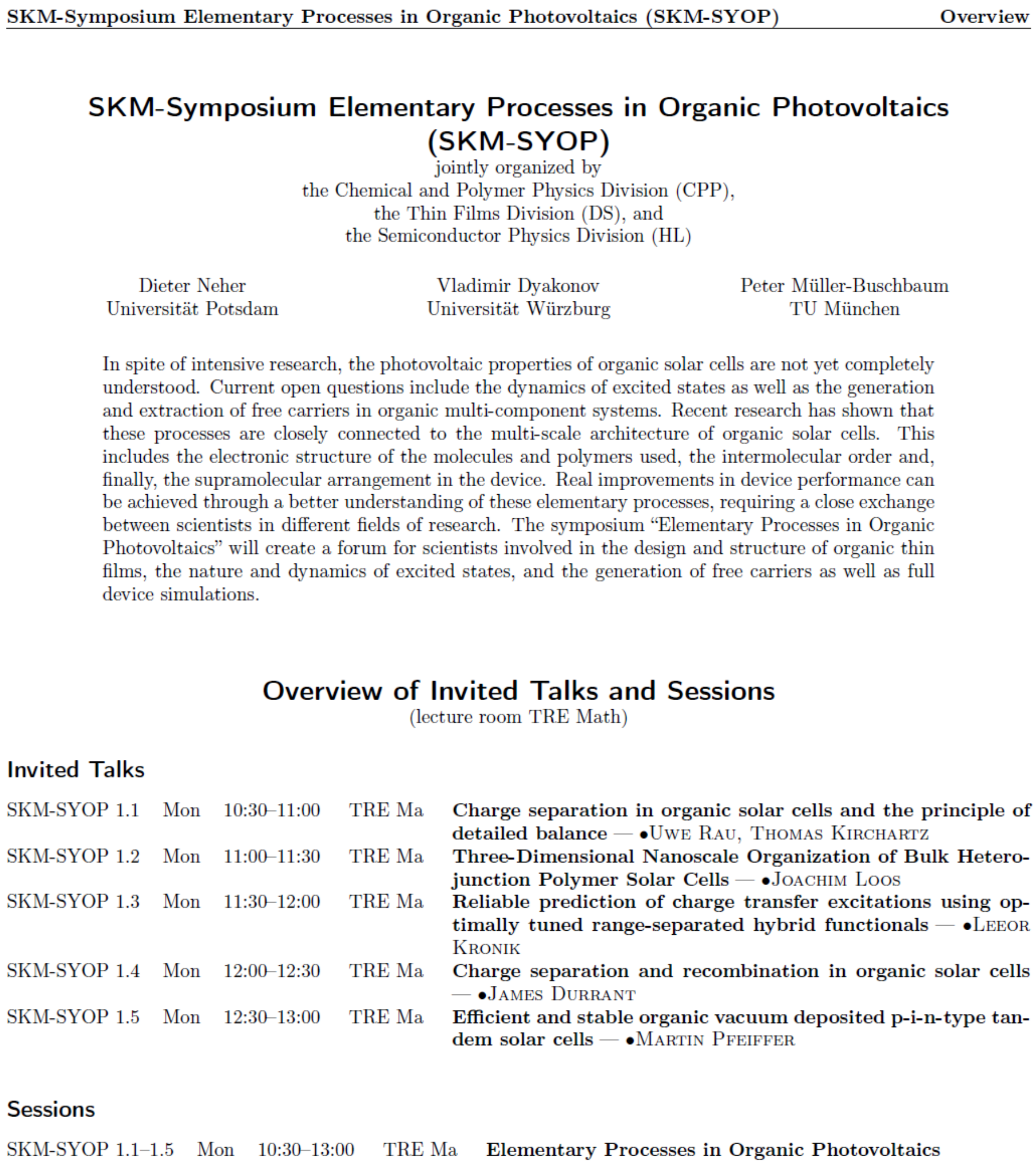

SKM-Symposium Elementary Processes in Organic Photovoltaics (SKM-SYOP)

jointly organized by
the Chemical and Polymer Physics Division (CPP),
the Thin Films Division (DS), and
the Semiconductor Physics Division (HL)

Dieter Neher Universität Potsdam	Vladimir Dyakonov Universität Würzburg	Peter Müller-Buschbaum TU München

In spite of intensive research, the photovoltaic properties of organic solar cells are not yet completely understood. Current open questions include the dynamics of excited states as well as the generation and extraction of free carriers in organic multi-component systems. Recent research has shown that these processes are closely connected to the multi-scale architecture of organic solar cells. This includes the electronic structure of the molecules and polymers used, the intermolecular order and, finally, the supramolecular arrangement in the device. Real improvements in device performance can be achieved through a better understanding of these elementary processes, requiring a close exchange between scientists in different fields of research. The symposium "Elementary Processes in Organic Photovoltaics" will create a forum for scientists involved in the design and structure of organic thin films, the nature and dynamics of excited states, and the generation of free carriers as well as full device simulations.

Overview of Invited Talks and Sessions

(lecture room TRE Math)

Invited Talks

SKM-SYOP 1.1	Mon	10:30–11:00	TRE Ma	**Charge separation in organic solar cells and the principle of detailed balance** — •Uwe Rau, Thomas Kirchartz
SKM-SYOP 1.2	Mon	11:00–11:30	TRE Ma	**Three-Dimensional Nanoscale Organization of Bulk Heterojunction Polymer Solar Cells** — •Joachim Loos
SKM-SYOP 1.3	Mon	11:30–12:00	TRE Ma	**Reliable prediction of charge transfer excitations using optimally tuned range-separated hybrid functionals** — •Leeor Kronik
SKM-SYOP 1.4	Mon	12:00–12:30	TRE Ma	**Charge separation and recombination in organic solar cells** — •James Durrant
SKM-SYOP 1.5	Mon	12:30–13:00	TRE Ma	**Efficient and stable organic vacuum deposited p-i-n-type tandem solar cells** — •Martin Pfeiffer

Sessions

SKM-SYOP 1.1–1.5	Mon	10:30–13:00	TRE Ma	**Elementary Processes in Organic Photovoltaics**

C. M. Papadakis, S. Jaksch, J. Adelsberger
Workshop 'Tanzender Matsch und volle Windeln – Nicht-Newton'sche Fluide und Polymergele'
in the framework of the program 'Innovative Naturwissenschaften TUM-WHG',
Werner-Heisenberg-Gymnasium Garching
05 Apr 2011

'Dancing mud and full diapers - physical and chemical gels' - this was the motto of the lesson held by Prof. Christine Papadakis and her coworkers in the compulsory optional subject Chemisty. First, the pupils prepared gels from superabsorbers as they are used in diapers or concrete. Then, they prepared mud from starch and water and made it dance on a loud speaker. The pupils were enthusiastic and discovered that physics is not necessarily dry and boring! Moreover, they were very interested in TUM and the soft matter research carried out at the Physics Department and the FRM II. This lesson was part of the cooperation program between TUM and the WHG in which pupils of the 8th grade learn about the different research directions present at TUM.

C. M. Papadakis

Girls' Day at the Physics Department

in the framework of the nationwide campaign 'Girls' Day – Future Prospects for Girls'
13 Apr 2011

Physics - what is that today? And what are physicists doing all day long? The Girls' Day gives girls from all over Germany the opportunity to discover professions in technology, information technology, handicraft and sciences. On that occasion, a pupil from Elsa-Brändström-Gymnasium in Pasing visited the Soft Matter Physics Group. First, she spent time in the lab to prepare gels from superabsorbers as they are used in diapers and in undersea cable coatings. During lunch in the canteen, she chatted with students and scientists and collected forces for the afternoon where she designed a 'television tower' and even made one herself on the lathe. A tour of the Department completed the day.

P. Müller-Buschbaum, W. Petry
Lehrerfortbildung 'Biologisch inspirierte Systeme'
35. Edgar-Lüscher-Seminar
Zwiesel, 06 – 08 May 2011

Programm

Freitag, 6. Mai 2011

13.00 - 14.30	Studienberatung der TUM
15.00 - 15.30	Begrüßung
15.30 - 16.45	**Einführung in die Welt der biologisch inspirierten Systeme** *Prof. Dr. Peter Fratzl, MPI Golm*
16.45 - 17.00	Diskussion

Samstag, 7. Mai 2011

09.00 - 10.15	**Biologisch inspirierte Sensorik** *Dr. Ulrich Rant, TUM*
10.15 - 11.00	Diskussion und Kaffeepause
11.00 - 12.15	**Biophysik der Mechanosensorik** *Prof. Dr. Leo van Hemmen, TUM*
12.15 -12.30	Diskussion
14.30 - 15.45	**Biomaterialien für einen Einsatz in der Biomedizin oder Nanotechnologie** *Prof. Dr. Thomas Scheibel, Uni Bayreuth*
15.45 - 16.30	Diskussion und Kaffeepause
16.30 - 17.45	**Bionanotechnologie** *Prof. Dr. Friedrich Simmel, TUM*
17.45 - 18.00	Diskussion
18.00 - 19.15	**Pflanzen und Tiere als Ideengeber für die Entwicklung neuer Materialien und Technologien** *Prof. Dr. Thomas Speck, Uni Freiburg*
19.15 - 19.30	Diskussion

Sonntag, 8. Mai 2011

09.00 - 10.15	**Molekulare Motoren** *PD Dr. Günther Woehlke, TUM*
10.15 - 11.00	Diskussion und Kaffeepause
11.00 - 12.15	**Biomimetik** *Dr. habil. Ingo Burgert, MPI Golm*
12.15 - 13.00	Diskussion, Themenfindung für das 36. Seminar

Organisation

Prof. Dr. Peter Müller-Buschbaum
TUM

Prof. Müller-Buschbaum befasst sich in seiner Forschungsarbeit mit der Entwicklung polymerbasierter Materialien mit neuartigen Struktur-Eigenschaftsbeziehungen. Strukturen aus leitfähigen Polymeren und deren Anwendungen für die Photovoltaik sind ein Schwerpunkt der Arbeiten.

Prof. Dr. Winfried Petry
TUM

Prof. Petry ist Ordinarius am Lehrstuhl E13 des Physik-Departments, Leiter des Prüflabors für Technische Physik, wissenschaftlicher Direktor der Forschungsneutronenquelle Heinz Maier-Leibnitz (FRM-II), Betreuungsprofessor des Physik Departments für die Bayerische Elite-Akademie und Vorsitzender der Arbeitsgemeinschaft Metall- und Materialphysik der Deutschen Physikalischen Gesellschaft.

Organisatorische Hinweise

Organisation vor Ort:

OStD Hans-Werner Janda,	*Gymnasium Zwiesel*
StD Wolfgang Achatz,	*Gymnasium Zwiesel*
StR Claus Starke,	*Gymnasium Zwiesel*
StR Christian Stoiber,	*Gymnasium Zwiesel*

Email:
sekretariat@gymnasium-zwiesel.de

Hinweise:

- Alle Veranstaltungen finden in der Aula des Gymnasiums Zwiesel statt. Die Teilnehmer erhalten am Ende des Seminars für 5,- € eine CD mit sämtlichen Vorträgen.
- Die Mensa des Gymnasiums ist während des Seminars geöffnet (Mittagessen, Kaffeepausen).
- Buch- und Lehrmittelausstellung in der Aula

Titelfoto: © Torsten Rempt / PIXELIO

35. Edgar-Lüscher-Seminar

am Gymnasium Zwiesel
Freitag, 6. Mai 2011, bis Sonntag, 8. Mai 2011

Biologisch inspirierte Systeme

Schirmherr:
Prof. Dr. Dr. h.c. mult. Wolfgang Herrmann,
Präsident der TUM

Veranstalter:
Ltd. OStD Klaus Drauschke,
Ministerialbeauftragter für die Gymnasien in Niederbayern

Wissenschaftliche Leitung:
Prof. Dr. Peter Müller-Buschbaum, *TUM*
Prof. Dr. Winfried Petry, *TUM*

W. A. Herrmann, W. Lang, M. Lienkamp, P. Müller-Buschbaum, H. Spliethoff, U. Stimming
Colloquium 'Sustainable Energy Supply of the Future'
1st Colloquium of the Munich School of Engineering
Garching, 18 Jul 2011

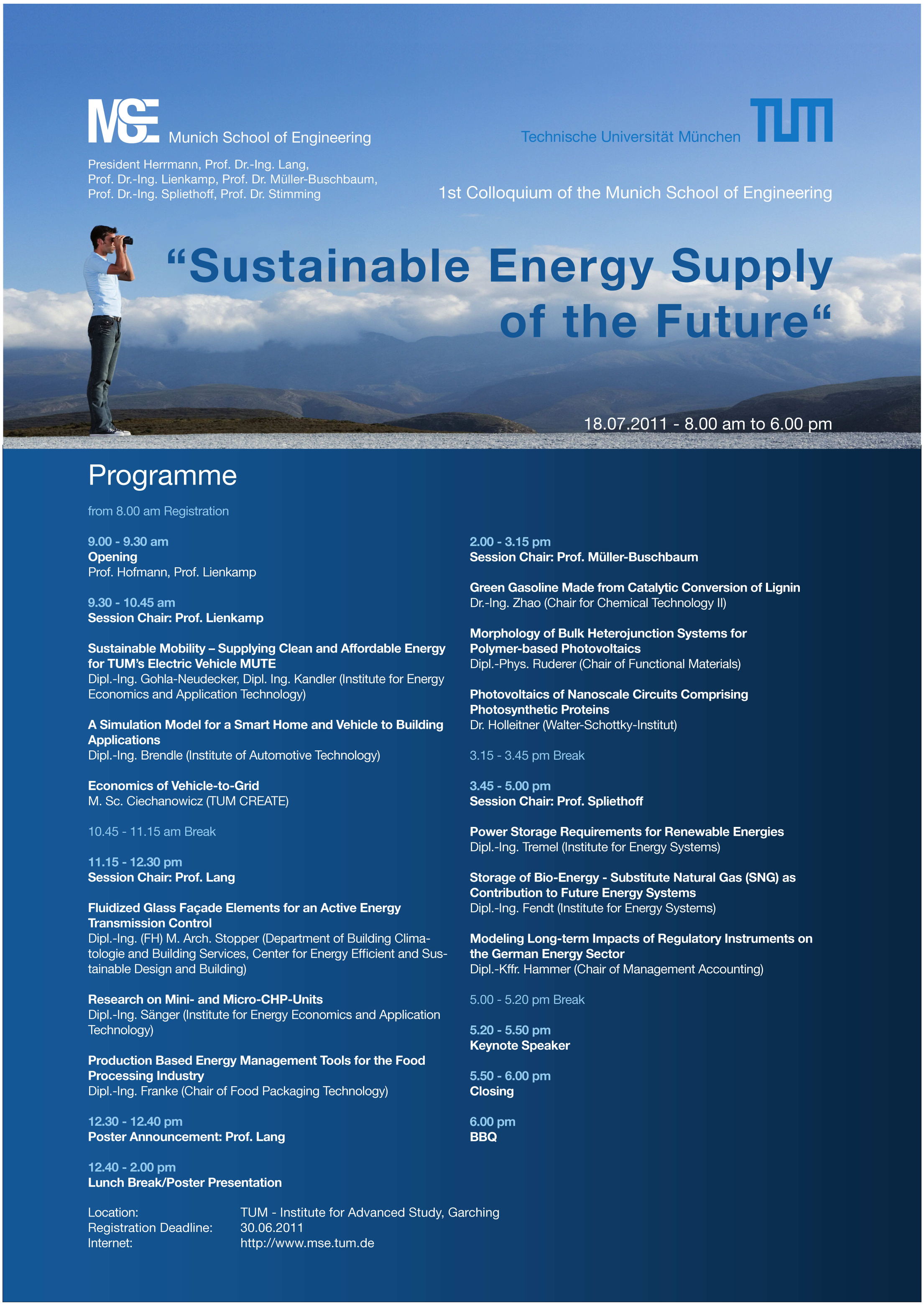

Munich School of Engineering

Technische Universität München

President Herrmann, Prof. Dr.-Ing. Lang,
Prof. Dr.-Ing. Lienkamp, Prof. Dr. Müller-Buschbaum,
Prof. Dr.-Ing. Spliethoff, Prof. Dr. Stimming

1st Colloquium of the Munich School of Engineering

“Sustainable Energy Supply of the Future“

18.07.2011 - 8.00 am to 6.00 pm

Programme

from 8.00 am Registration

9.00 - 9.30 am
Opening
Prof. Hofmann, Prof. Lienkamp

9.30 - 10.45 am
Session Chair: Prof. Lienkamp

Sustainable Mobility – Supplying Clean and Affordable Energy for TUM's Electric Vehicle MUTE
Dipl.-Ing. Gohla-Neudecker, Dipl. Ing. Kandler (Institute for Energy Economics and Application Technology)

A Simulation Model for a Smart Home and Vehicle to Building Applications
Dipl.-Ing. Brendle (Institute of Automotive Technology)

Economics of Vehicle-to-Grid
M. Sc. Ciechanowicz (TUM CREATE)

10.45 - 11.15 am Break

11.15 - 12.30 pm
Session Chair: Prof. Lang

Fluidized Glass Façade Elements for an Active Energy Transmission Control
Dipl.-Ing. (FH) M. Arch. Stopper (Department of Building Climatologie and Building Services, Center for Energy Efficient and Sustainable Design and Building)

Research on Mini- and Micro-CHP-Units
Dipl.-Ing. Sänger (Institute for Energy Economics and Application Technology)

Production Based Energy Management Tools for the Food Processing Industry
Dipl.-Ing. Franke (Chair of Food Packaging Technology)

12.30 - 12.40 pm
Poster Announcement: Prof. Lang

12.40 - 2.00 pm
Lunch Break/Poster Presentation

2.00 - 3.15 pm
Session Chair: Prof. Müller-Buschbaum

Green Gasoline Made from Catalytic Conversion of Lignin
Dr.-Ing. Zhao (Chair for Chemical Technology II)

Morphology of Bulk Heterojunction Systems for Polymer-based Photovoltaics
Dipl.-Phys. Ruderer (Chair of Functional Materials)

Photovoltaics of Nanoscale Circuits Comprising Photosynthetic Proteins
Dr. Holleitner (Walter-Schottky-Institut)

3.15 - 3.45 pm Break

3.45 - 5.00 pm
Session Chair: Prof. Spliethoff

Power Storage Requirements for Renewable Energies
Dipl.-Ing. Tremel (Institute for Energy Systems)

Storage of Bio-Energy - Substitute Natural Gas (SNG) as Contribution to Future Energy Systems
Dipl.-Ing. Fendt (Institute for Energy Systems)

Modeling Long-term Impacts of Regulatory Instruments on the German Energy Sector
Dipl.-Kffr. Hammer (Chair of Management Accounting)

5.00 - 5.20 pm Break

5.20 - 5.50 pm
Keynote Speaker

5.50 - 6.00 pm
Closing

6.00 pm
BBQ

Location:	TUM - Institute for Advanced Study, Garching
Registration Deadline:	30.06.2011
Internet:	http://www.mse.tum.de

P. Müller-Buschbaum
Lehrerfortbildung 'Nanophysik'
Edgar-Lüscher-Lectures
Dillingen, 14 – 16 Sep 2011

EDGAR–LÜSCHER–LECTURES DILLINGEN/DONAU 2011
Thema: Nanophysik
Datum: Mittwoch, 14. September bis Freitag, 16. September 2011
Tagungsort: Akademie für Lehrerfortbildung Dillingen
Veranstalter: Akademie für Lehrerfortbildung Dillingen und TU München
wissenschaftliche Leitung: Prof. Dr. Peter Müller-Buschbaum,
Technische Universität München.

Programm

Mittwoch, 14. 09. 2011
15:30 – 17:00 Dr Ulrich Rant
Nano-Sensorik

18:30 – 20:00 Prof. Dr. Othmar Marti
Rasterkraftmikroskopie zur Untersuchung von Nanostrukturen

Donnerstag, 15. 09. 2011
8:30 – 10:00 Prof. Dr. Dirk Grundler
Magnetische Nanostrukturen

10:00 – 10.30 Kaffeepause

10:30 – 12:00 Prof. Dr. Johannes Barth
Nanostrukturen an Grenzflächen

15:30 – 17:00 Dr. Stephan Roth
Synchrotronstrahlung für die Nanowelt

18:30 – 20:00 Prof. Dr. Winfried Petry
Neutronen für die Nanowelt

Freitag, 16. 09. 2011
8:30 – 10:00 Prof. Dr. Christine Papadakis
Polymere Nanostrukturen

10:00 – 10.30 Kaffeepause

10:30 – 12:00 Prof. Dr. Alexander Holleitner
Elektronische Eigenschaften von Nanostrukturen

S. V. Roth, R. Röhlsberger, R. Gehrke, P. Müller-Buschbaum
International workshop 'GISAXS 2011'
Hamburg, 10 – 12 Oct 2011

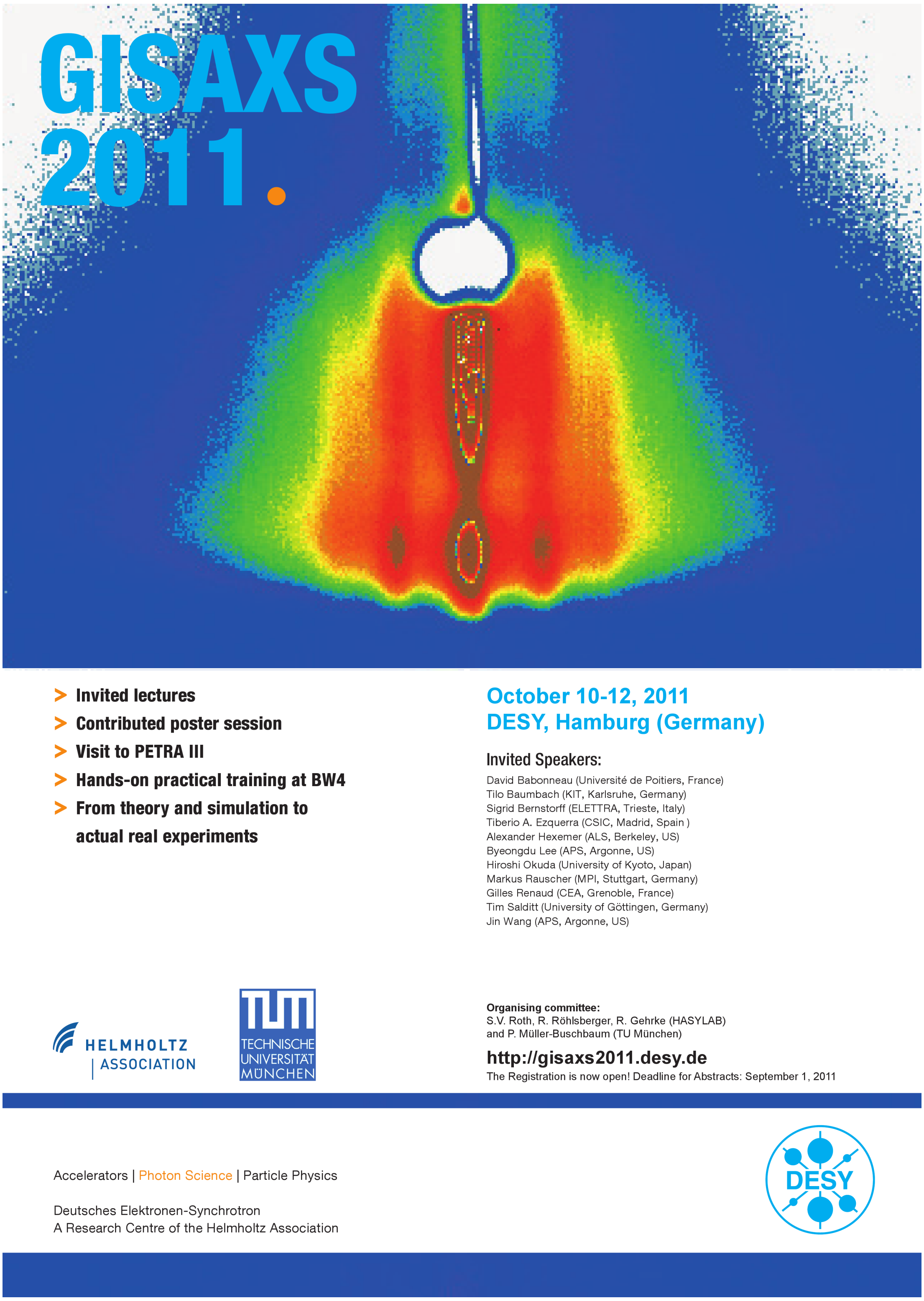

GISAXS 2011.

- **Invited lectures**
- **Contributed poster session**
- **Visit to PETRA III**
- **Hands-on practical training at BW4**
- **From theory and simulation to actual real experiments**

October 10-12, 2011
DESY, Hamburg (Germany)

Invited Speakers:
David Babonneau (Université de Poitiers, France)
Tilo Baumbach (KIT, Karlsruhe, Germany)
Sigrid Bernstorff (ELETTRA, Trieste, Italy)
Tiberio A. Ezquerra (CSIC, Madrid, Spain)
Alexander Hexemer (ALS, Berkeley, US)
Byeongdu Lee (APS, Argonne, US)
Hiroshi Okuda (University of Kyoto, Japan)
Markus Rauscher (MPI, Stuttgart, Germany)
Gilles Renaud (CEA, Grenoble, France)
Tim Salditt (University of Göttingen, Germany)
Jin Wang (APS, Argonne, US)

HELMHOLTZ | ASSOCIATION

TUM TECHNISCHE UNIVERSITÄT MÜNCHEN

Organising committee:
S.V. Roth, R. Röhlsberger, R. Gehrke (HASYLAB)
and P. Müller-Buschbaum (TU München)

http://gisaxs2011.desy.de
The Registration is now open! Deadline for Abstracts: September 1, 2011

Accelerators | Photon Science | Particle Physics

Deutsches Elektronen-Synchrotron
A Research Centre of the Helmholtz Association

DESY

P. Müller-Buschbaum, C. M. Papadakis
Workshop 'Hydrogel Analytics'
in the framework of the SPP 'Intelligente Hydrogele'
Garching, 25 – 26 Oct 2011

Workshop "Hydrogel Analytics"

TU München, October 25-26, 2011
SPP 1259 "Intelligente Hydrogele"

	Tuesday, October 25	Wednesday, October 26
09:00-10:00		**Olaf Holderer, JCNS, FZ Jülich** Slow dynamics in soft matter systems: neutron spin echo spectroscopy
10:00-10:30		**Martine Philipp, TU München** About hypersonic instabilities on different time scales in PNIPAM hydrogels
10:30-11:00		***Coffee break***
11:00-11:30		**Marcel Richter, TU Berlin** T.B.A.
11:30-12:00		**Fiete Dierkes, RWTH Aachen** Cavitation rheology
12:00-12:30		**David Magerl, TU München** Thermoresponsive swelling and deswelling of PNIPAM thin films
12:30-13:00	***Registration and Welcome***	***Lunch break 12:30-13:30h***
13:00-14:00	**Henrich Frielinghaus, JCNS, FZ Jülich** An introduction to small-angle neutron scattering	***Visit of FRM II 13:30-16:30 h***
14:00-14:30	**Margaritha Günther, TU Dresden** Hydrogels for biomedical sensors	
14:30-15:00	***Coffee break***	
15:00-15:30	**Joseph Adelsberger, TU München** Kinetics of collapse transition and cluster formation in a thermoresponsive micellar solution induced by a temperature jump	
15:30-16:00	**Qi Zhong, TU München** In-situ neutron reflectivity - a novel tool to probe switching kinetics of thermo-responsive PMDEGA hydrogel films	
16:00-16:30	**Apostolos Vagias, MPI-P Mainz** Tracer diffusion in confined media	
16:30-17:00	**Sebastian Jaksch, TU München** Switching behavior of thermoresponsive poly(2-oxazoline)s	
17:00-17:30	***Lab tour at the Chair of Functional Materials***	
20:00	***Workshop dinner***	

8.3 Service to the community

Peter Müller-Buschbaum

- since 2011 member of European Spallation Source (ESS) Scientific Advisory Panel (Reflectivity)

- since 2011 German representative of European Polymer Federation (EPF) for polymer physics

- since 2011 elected member of the 9th committee 'Forschung mit Synchrotronstrahlung' (KFS), section user matters

- since 2010 spokesman of the regenerative energies section (NRG) at the Munich School of Engineering (MSE) of TU Munich

- since 2010 member of TUMEnergie at TU München

- since 2010 spokesman of the Physics Department at TU München for the energy section

- since 2010 observer at the ESUO - European Synchrotron User Organization

- member of the scientific counsel of the Institut für Biophysik und Nanosystemforschung (Institute for Biophysics and Nanosystems research) of the Austrian Academy of Sciences IBN in Graz, Austria

- elected chairman of 'HASYLAB User Committee (HUC)' at the synchrotron radiation laboratory HASYLAB in Hamburg

Christine M. Papadakis

- member of the Project Review Panel 5: 'Soft Condensed Matter/Scattering' at HASYLAB, DESY, Hamburg
- vice women's representative of the Physics Department at TU München

Winfried Petry

- since 1999 liaison professor of Bayerische Eliteakademie (Bavarian Leadership Academy) and since May 2011 member of the curatorium
- since 2007 member of the Steering Committee of the Laue Langevin Institute and chairman of the instrumentation review panel of the CEA Léon Brillouin Laboratory
- since 2010 member of the proposal evaluation committee ′Experimental Physics of Condensed Matter′ of Deutsche Forschungsgemeinschaft

9 Publications, talks and funding

9.1 Publications

- M. M. Abul Kaschem, G. Kaune, A. Diethert, W. Wang, K. Schlage, S. Couet, R. Röhlsberger, S. V. Roth, P. Müller-Buschbaum
  Selective doping of block copolymer nanodomains by sputter deposition of iron
  Macromolecules **44**, 1621-1627 (2011)

- K. Achterhold, A. Ostermann, M. Moulin, M. Haertlein, T. Unruh, F. Parak
  Dynamical properties of the hydration shell of fully deuterated myoglobin
  Phys. Rev. E **84**, 041930 (2011)

- J. Adelsberger, A. Meier-Koll, A. M. Bivigou-Koumba, P. Busch, O. Holderer, T. Hellweg, A. Laschewsky, P. Müller-Buschbaum, C. M. Papadakis
  The collapse transition and the segmental dynamics in concentrated micellar solutions of P(S-b-NIPAM) diblock copolymers
  Colloid Polym. Sci. **289**, 711-720 (2011)

- M.-S. Appavou, S. Busch, W. Doster, A. Gaspar, T. Unruh
  The influence of 2 kbar pressure on the global and internal dynamics of human hemoglobin observed by quasielastic neutron scattering
  Eur. Biophys. J. Biophys. Lett. **40**, 705-714 (2011)

- H. Breitkreutz, W. Petry
  Thermal-hydraulic effects of cladding-meat contact faults
  Transactions RERTR 2011, Santiago, Chile (conference proceedings)

- A. Buffet, M. M. Abul Kashem, K. Schlage, S. Couet, R. Röhlsberger, A. Rothkirch, G. Herzog, E. Metwalli, R. Meier, G. Kaune, M. Rawolle, P. Müller-Buschbaum, R. Gehrke, S. V. Roth
  Cobalt nanoparticle growth on a multiple structured colloidal template
  Langmuir **27**, 343-346 (2011)

- P. Busch, M. Rauscher, J.-F. Moulin, P. Müller-Buschbaum
  Debye-Scherrer rings from block copolymer films with powder-like order
  J. Appl. Cryst. **44**, 370-379 (2011)

- S. Busch, T. Unruh
  The slow short-time motions of phospholipid molecules with a focus on the influence of multiple scattering and fitting artifacts
  J. Phys. Condens. Matter **23**, 254205 (2011)

- S. Busch, T. Unruh
  The Influence of Additives on the Nanoscopic Dynamics of the Phospholipid Dimyristoylphosphatidylcholine
  BBA-Biomembranes **1808**, 199-208 (2011)

- H.-Y. Chiang, R. Jungwirth, T. Zweifel, W. Schmid, W. Petry, F. Kraus
  Interactions between UMo/Al fuel and diffusion barriers Nb and TiN under heavy ion irradiation
  Transactions RERTR 2011, Santiago, Chile (conference proceedings)

- A. Diethert, K. Ecker, Y. Peykova, N. Willenbacher, P. Müller-Buschbaum
  Tailoring the near-surface composition profiles of pressure sensitive adhesive films and the resulting mechanical properties
  ACS Appl. Mater. Interfaces **3**, 2012-2021 (2011)

- A. Diethert, E. Metwalli, R. Meier, Q. Zhong, R. A. Campbell, R. Cubitt, P. Müller-Buschbaum
  In-situ neutron reflectometry study of the near-surface solvent concentration profile during solution casting
  Soft Matter **7**, 6648-6659 (2011)

- A. Diethert, P. Müller-Buschbaum
  Probing the near-surface composition profile of pressure sensitive adhesive films with x-ray reflectivity
  J. Adhes. **87**, 1067-1090 (2011)

- R. Gebhardt, W. Holzmüller, Q. Zhong, Müller-Buschbaum, U. Kulozik
  Structural ordering of casein micelles on silicon nitride micro-sieves during filtration
  J. Coll. Surf. B **88**, 240-245 (2011)

- A. A. Golosova, C. M. Papadakis, R. Jordan
  Chemical functionalization of carbon nanotubes with aryl diazonium salts
  MRS Proceedings **1362**, mrss11-1362-qq03-01 (2011)

- W. Häußler, O. Holderer, T. Unruh, J. Wuttke
  High-resolution neutron spectroscopy at the FRM II
  Neutron News **22**, 24-30 (2011)

- P. Heinz, K. Hindelang, A. Golosova, C. M. Papadakis, B. Rieger
  Self-assembly of linear and cyclic siloxane-containing mesogens: Investigation of layered structures in bulk and thin films
  ChemPhysChem **12**, 3591-3603 (2011)

- R. Jungwirth, W. Petry, H. Breitkreutz, W. Schmid, H. Palancher, A. Bonnin, M. Grasse, C. Jarousse and B. Stepnik
  Screening of different UMo/Al samples: protective oxide layers, Ti addition to the matrix and ternary U-Mo-X alloys
  Transactions RERTR 2011, Santiago, Chile (conference proceedings)

- R. Jungwirth, T. Zweifel, H. Chiang, W. Petry, S. van den Berghe, A. Leenaers
  Heavy ion irradiation of UMo/Al samples with protective Si and ZrN layers (SELENIUM)
  Transactions RERTR 2011, Santiago, Chile (conference proceedings)

- G. Kaune, E. Metwalli, R. Meier, V. Körstgens, K. Schlage, S. Couet, R. Röhlsberger, S. V. Roth, P. Müller-Buschbaum
  Growth and morphology of sputtered Aluminum thin films on P3HT surfaces
  ACS Appl. Mater. Interfaces **3**, 1055-1062 (2011)

- T. Kordel, D. Holland-Moritz, F. Yang, J. Peters, T. Unruh, T. Hansen, A. Meyer
  Neutron scattering experiments on liquid droplets using electrostatic levitation
  Phys. Rev. B **83**, 104205 (2011)

- V. Lauter, P. Müller-Buschbaum, H. Lauter, W. Petry
  Morphology of thin nanocomposite films of asymmetric diblock-copolymer and magnetite nanoparticles
  J. Phys. Condens. Matter **23**, 254215 (2011)

- A. Leenaers, S. van den Berghe, W. van Renterghem, F. Charollais, P. Lemoine, C. Larousse, A. Röhrmoser, W. Petry
  Irradiation behaviour of ground U(Mo) fuel with and without Si added to the matrix
  J. Nucl. Mater. **412**, 41-52 (2011)

- S. M. Maier, A. Jentys, E. Metwalli, P. Müller-Buschbaum, J. A. Lercher
  Determination of the redox processes in FeBEA catalysts in NH_3-SCR reaction by Mössbauer and X-ray absorption spectroscopy
  J. Phys. Chem. Lett. **2**, 950-955 (2011)

- M. A. Mangold, M. A. Niedermeier, M. Rawolle, J. Perlich, S. V. Roth, A. W. Holleitner, P. Müller-Buschbaum
  Correlation between structure and optoelectronic properties in a two-dimensional nanoparticle assembly
  phys.stat.sol.(RRL) **5**, 16-18 (2011)

- R. Meier, M. A. Ruderer, A. Diethert, G. Kaune, V. Körstgens, S. V. Roth, P. Müller-Buschbaum
  Influence of film thickness on the phase separation mechanism in ultrathin conducting polymer blend films
  J. Phys. Chem. B **115**, 2899-2909 (2011)

- R. Meier, M. Schindler, P. Müller-Buschbaum, B. Watts
  Residual solvent content in conducting polymer blend films mapped with scanning transmission x-ray microscopy
  Phys. Rev. B **84**, 174205 (2011)

- M. Memesa, S. Lenz, S. G. J. Emmerling, S. Nett, J. Perlich, P. Müller-Buschbaum, J. S. Gutmann
  Morphology and photoluminescence study of titania nanoparticles
  Colloid. Polym. Sci. **289**, 943-953 (2011)

- E. Metwalli, M. Nie, V. Körstgens, J. Perlich, S. V. Roth, P. Müller-Buschbaum
  Morphology of lithium-containing diblock copolymer thin films
  Macromol. Chem. Phys. **212**, 1742-1750 (2011)

- E. Metwalli, J.-F. Moulin, M. Rauscher, G. Kaune, M. A. Ruderer, U. van Bürck, M. Haese-Seiler, R. Kampmann, P. Müller-Buschbaum
  Structural investigation of diblock copolymer thin films using TOF-GISANS
  J. Appl. Cryst. **44**, 84-92 (2011)

- P. Müller-Buschbaum, V. Körstgens
  Scanning probe microscopy and grazing incidence small-angle scattering as complementary tools for the investigation of polymer films and surfaces
  Scanning Probe Microscopy in Nanoscience and Nanotechnology 2, B. Bhushan (editor), Springer-Verlag Berlin Heidelberg, 101-134 (2011)

- P. Müller-Buschbaum, D. Magerl, R. Hengstler, J.-F. Moulin, V. Körstgens, A. Diethert, J. Perlich, S. V. Roth, M. Burghammer, C. Riekel, M. Gross, F. Varnik, P. Uhlmann, M. Stamm, J. M. Feldkamp, C. G. Schroer
  Structure and flow of droplets on solid surfaces
  J. Phys. Condens. Matter **23**, 184111 (2011)
- H. Palancher, A. Bonnin, T. Zweifel, F. Charollais, M. Anselmet, P. Lemoine, V. Honkimski, T. Buslaps, W. Petry, R. Jungwirth, M. Grasse and B. Stepnik
  Quantitative crystallographic analysis of as-fabricated full size IRIS/E-FUTURE nuclear fuel plates
  Transactions RERTR 2011, Santiago, Chile (conference proceedings)
- C. M. Papadakis, C. Darko, Z. Di, K. Troll, E. Metwalli, A. Timmann, G. Reiter, S. Förster
  Surface-induced breakout crystallization in cylinder-forming P(I-b-EO) diblock copolymer thin films
  Eur. Phys. J. E **34**, 7 (2011)
- N. V. Pogodina, E. Metwalli, P. Müller-Buschbaum, K. Wendler, R. Lungwitz, S. Spange, J. L. Shamshina, R. D. Rogers , C. Friedrich
  Peculiar behavior of azolium azolate energetic ionic liquids
  J. Phys. Chem. Lett. **2**, 2571-2576 (2011)
- M. Philipp, U. Müller, R. Sanctuary, J. C. Gaukler, C. Wehlack, W. Possart, J. K. Krüger
  Heterogeneous transport processes and unexpected structure formation in layered epoxy and epoxy-alumina nanocomposite systems
  J. Adhesion **87**, 1073-1098 (2011)
- M. Rawolle, M. A. Ruderer, S. M. Prams, Q. Zhong, D. Magerl, J. Perlich, S. V. Roth, P. Lellig, J. S. Gutmann, P. Müller-Buschbaum
  Nanostructuring of titania thin films by a combination of microfluidics and block-copolymer-based sol-gel templating
  Small **7**, 884-891 (2011)
- S. V. Roth, G. Herzog, V. Körstgens, A. Buffet, M. Schwartzkopf, J. Perlich, M. M. Abul Kashem, R. Döhrmann, R. Gehrke, A. Rothkirch, K. Strassig, W. Wurth, G. Benecke, C. Li, P. Fratzl, M. Rawolle, P. Müller-Buschbaum
  In situ observation of cluster formation during nanoparticle solution casting on a colloidal film
  J. Phys. Condens. Matter **23**, 254208 (2011)
- M. A. Ruderer, P. Müller-Buschbaum
  Morphology of polymer-based bulk heterojunction films for organic photovoltaics
  Soft Matter **7**, 5482-5493 (2011)
- M. A. Ruderer, S. Guo, R. Meier, H.-Y. Chiang, V. Körstgens, J. Wiedersich, J. Perlich, S. V. Roth, P. Müller-Buschbaum
  Solvent induced morphology in polymer-based systems for organic photovoltaics
  Adv. Funct. Mater. **21**, 3382-3391 (2011)
- M. A. Ruderer, M. Hinterstocker, P. Müller-Buschbaum
  Structure in ternary blend systems for organic photovoltaics
  Synth. Met. **161**, 2001-2005 (2011)

- F. Schulz, V. Sumerin, S. Heikkinen, B. Pedersen, C. Wang, M. Atsumi, M. Leskel, T. Repo, P. Pyykk, W. Petry, B. Rieger
  Molecular Hydrogen Tweezers: Structure and Mechanisms by Neutron Diffraction, NMR, and Deuterium Labeling Studies in Solid and Solution
  JACS **133**, 20245-20257 (2011)

- W. Schmid, S. Dirndorfer, R. Jungwirth, H. Juranowitsch, W. Petry, T. Zweifel
  Tailored model systems for IDL investigation and diffusion barrier optimization
  Transactions RERTR 2011, Santiago, Chile (conference proceedings)

- A. Sepe, E. T. Hoppe, S. Jaksch, D. Magerl, Q. Zhong, J. Perlich, D. Posselt, D.-M. Smilgies, C. M. Papadakis
  The effect of heat treatment on the internal structure of nanostructured block copolymer films
  J. Phys. Condens. Matter **23**, 254213 (2011)

- R. Stoepler, A. Frei, S. Paul, H. Gerstenberg, W. Petry
  The ultracold laboratory at the FRM II
  Transactions RERTR 2011, Santiago, Chile (conference proceedings)

- S. Stuiber, G. Wu, J. Nehrkorn, J. Dreiser, Y. Lan, G. Novitchi, C. Anson, T. Unruh, A. Powell, O. Waldmann *Inelastic neutron scattering on an Mn10 supertetrahedron: Assessment of exchange coupling constants, ferromagnetic spin waves and an analogy to the Huckel method*
  Chem. Eur. J. **17**, 9094-9106 (2011)

- P. Uhlmann, P. Truman, F. Varnik, G. Zikos, J.-F. Moulin, P. Müller-Buschbaum, M. Stamm
  Microfluidic emulsion separation - simultaneous separation and sensing by multilayer nanofilm structures
  J. Phys. Condens. Matter **23**, 184123 (2011)

- F. Varnik, M. Gross, N. Moradi, G. Zikos, P. Uhlmann, P. Müller-Buschbaum, D. Magerl, D. Raabe, I. Steinbach, M. Stamm
  Stability and dynamics of droplets on patterned substrates: Insights from experiments and lattice Boltzmann simulations
  J. Phys. Condens. Matter **23**, 184112 (2011)

- A. Vorobiev, J. Major, H. Dosch, P. Müller-Buschbaum, P. Falus, G. P. Felcher, S. G. E. teVelthuis
  Phase and microphase separation of polymer thin films dewetted from silicon - a spin-echo resolved grazing incidence neutron scattering study
  J. Phys. Chem. B **115**, 5754-5765 (2011)

- X. Xia, E. Metwalli, M. A. Ruderer, V. Körstgens, P. Busch, P. Böni, P. Müller-Buschbaum
  Nanostructured diblock copolymer films with embedded magnetic nanoparticles
  J. Phys. Condens. Matter **23**, 254203 (2011)

- F. Yang, J. Kaplonski, T. Unruh, E. Mamontov, A. Meyer
  A high temperature high pressure cell for quasielastic neutron scattering
  Rev. Sci. Instr. **82**, 083903 (2011)

- F. Yang, T. Kordel, D. Holland-Moritz, T. Unruh, A. Meyer
  Structural relaxation as seen by quasielastic neutron scattering on viscous Zr-Ti-Cu-Ni-Be droplets
  J. Phys. Condens. Matter **23**, 254207 (2011)

- Q. Zhong, W. Wang, J. Adelsberger, A. Golosova, A. M. Bivigou-Koumba, A. Laschewsky, S. S. Funari, J. Perlich, S. V. Roth, C. M. Papadakis, P. Müller-Buschbaum,
  Collapse transition in thin films of poly(methoxydiethylenglycol acrylate)
  Colloid Polym. Sci. **289**, 569-581 (2011)

- T. Zweifel, H. Palancher, R. Jungwirth, A. Bonnin, W. Petry, M. Anselmet, F. Charollais, P. Lemoine, L. Beck
  Heavy ion irradiation on UMo/Al systems: temperature influence
  Transactions RERTR 2011, Santiago, Chile (conference proceedings)

9.2 Talks

- J. Adelsberger, E. Metwalli, A. Diethert, A. Bivigou-Koumba, A. Laschewsky, I. Grillo, P. Müller-Buschbaum, C. M. Papadakis
  Kinetics of structural changes in concentrated thermoresponsive blockcopolymer solutions
  DPG Frühjahrstagung, Dresden, 13 – 18 Mar 2011

- J. Adelsberger, A. Laschewsky, I. Grillo, P. Müller-Buschbaum, C. M. Papadakis
  Kinetics of structural changes in concentrated thermoresponsive blockcopolymer solutions
  Hydrogel Analytics - SPP 1259 Workshop, Garching, 25 – 26 Oct 2011

- S. Ener, J. Neuhaus, R. Mole, K. Hradil, W. Petry
  Effect of temperature and compositional changes on the vibrational properties of Ni-Mn-Ga alloys
  DPG Frühjahrstagung, Dresden, 13 – 18 Mar 2011

- S. Ener, J. Neuhaus, W. Petry
  Magnetic, magnetoelastic and dynamical properties of martensitic Heusler alloys: phonon spectra
  SPP 1239 Focus Meeting A, Düsseldorf, 13 – 12 Apr 2011

- S. Ener, J. Neuhaus, W. Petry
  Ni-Mn-Ga shape memory alloys: Phonon properties
  Invited seminar talk, Chemnitz, 24 May 2011

- S. Ener, J. Neuhaus, W. Petry
  Phonon properties of magnetic shape memory materials
  5th FRM II Science Meeting, Burg Rothenfels, 06 – 09 Jun 2011

- S. Ener, J. Neuhaus, W. Petry
  Vibrational properties of Ni-Mn-Ga ferromagnetic shape memory alloys
  DyProSo XXXIII, Aussois, France, 18 – 22 Sep 2011

- E.T. Hoppe, B. Wang, M. Haese-Seiller, J.-F. Moulin, I. Hopp, M. Port, B. Menges, C. M. Papadakis
  Density in polymer films and at the polymer-solid interface
  DPG Frühjahrstagung, Dresden, 13 – 18 Mar 2011

- S. Jaksch
  Switching behavior of thermoresponsive polyoxazolines – comparison between neutron and light scattering
  Hydrogel Analytics - SPP 1259 Workshop, Garching, 25 – 26 Oct 2011

- R. Jungwirth, T. Zweifel, H.-Y. Chiang, W. Petry, S. Van den Berghe, A. Leenaers
  Heavy ion irradiation of Umi/Al samples with protective Si and ZrN layers (SELENIUM)
  RERTR 2011, Santiago, Chile, 23 – 27 Oct 2011

- V. Körstgens
  Microfluidics and microGISAXS
  5th FRM II Science Meeting, Burg Rothenfels, 06 – 09 Jun 2011

- V. Körstgens, M. Rawolle, A. Buffet, G. Benecke, G. Herzog, J. Perlich, M. Schwartzkopf, M. Trebbin, J. Thiele, S. With, F. J. de Jong, M. Schlüter, S. V. Roth, S. Förster, P. Müller-Buschbaum
  Flow induced surface attachment of gold nanoparticles - an in situ x-ray investigation with microfluidic cell
  ICCE-19, International Conference on Composites or Nano Engineering, Shanghai, China, 24 – 30 Jul 2011

- V. Körstgens, M. Philipp, M. Rawolle, G. Benecke, G. Herzog, M. Schwartzkopf, S. V. Roth, P. Müller-Buschbaum
  In situ GISAXS investigation of flow induced surface attachment of gold nanoparticles in a microfluidic cell
  5th International Workshop on Polymer/Metal Nanocomposites, Bari, Italy, 20 – 22 Sep 2011

- D. Magerl
  Thermoresponsive swelling and deswelling of PNIPAM thin films
  Hydrogel Analytics - SPP 1259 Workshop, Garching, 25 – 26 Oct 2011

- R. Meier, H.-Y. Chiang, M. A. Ruderer, S. Guo, J. Wiedersich, V. Körstgens, J. Perlich, S. V. Roth, P. Müller-Buschbaum
  Thermal tuning of micro-structured conducting polymer thin films
  DPG Frühjahrstagung, Dresden, 13 – 18 Mar 2011

- R. Meier, P. Müller-Buschbaum
  Breaking the wall of organic photovoltaics
  Breaking the Walls Lab, Berlin, 08 – 09 Nov 2011

- E. Metwalli, V. Körstgens, K. Schlage, R. Meier, G. Kaune, S. Couet, S. V. Roth, R. Röhlsberger, P. Müller-Buschbaum
  Real time GISAXS study of magnetic nanoparticle assemblies on polymer templates
  Nanomagnetic-workshop, Munich, 28 Jan 2011

- E. Metwalli, A. Diethert, J. Adelsberger, R. Cubitt, U. Kulozik, P. Müller-Buschbaum
  Influence of temperature on the morphology of casein micellar films
  DPG Frühjahrstagung, Dresden, 13 – 18 Mar 2011

- E. Metwalli, V. Körstgens, K. Schlage, R. Meier, G. Kaune, S. Couet, S. V. Roth, R. Röhlsberger, P. Müller-Buschbaum
  Time resolved GISAXS study of magnetic nanoparticle growth on polymer templates
  EMRS 2011, Nice, 9 – 13 May 2011

- E. Metwalli
  Morphology of casein micellar films
  5th FRM II Science Meeting, Burg Rothenfels, 06 – 09 Jun 2011

- H. Morhenn, S. Busch, D. Richter, T. Unruh
  Short time dynamics of medium length molecules
  DPG Frühjahrstagung, Dresden, 13 – 18 Mar 2011

- H. Morhenn
  A summary on how to do molecular dynamics simulations
  Young Neutron Researchers Seminar, Garching, 13 Oct 2011

- P. Müller-Buschbaum
  Grazing incidence small neutron angle scattering - an advanced characterization technique for structured polymer films
  Workshop Max-Planck-Institutes at FRMII, Garching, 10 – 11 Jan 2011

- P. Müller-Buschbaum
  First GISAXS experiments at the new MiNaXS beamline: Hybrid-nanostructures for applications in organic photovoltaics
  HASYLAB User Meeting, SAXS-WAXS workshop, Hamburg, 27 – 28 Jan 2011

- P. Müller-Buschbaum
  Report of the HASYLAB User Committe (HUC) - report 2010
  HASYLAB User Meeting, Hamburg, 27 – 28 Jan 2011

- P. Müller-Buschbaum
  Conducting polymers with applications in organic photovoltaics;
  HASYLAB MiNaXS Diskussionstreffen, Hamburg, 08 Feb 2011

- P. Müller-Buschbaum
  2-3D structures – prospects for GISANS and off-specular scattering
  European Spallation Source (ESS) Scientific Advisory Panel meeting, Lund, Sweden, 05 May 2011

- P. Müller-Buschbaum, , S. V. Roth, A. Buffet, K. Schlage, M. M. Abul Kashem, G. Benecke, R. Gehrke, G. Herzog, V. Körstgens, J. Perlich, M. Rawolle, R. Röhlsberger, A. Rothkirch, M. Schwartzkopf
  In-situ observation of metal-polymer nano-composite thin film growth using microbeam GISAXS
  E-MRS Spring Meeting, Nice, France, 09 – 13 May 2011

- P. Müller-Buschbaum
  Introduction to organic photovoltaics;
  5th FRM II Science Meeting, Burg Rothenfels, 06 – 09 Jun 2011

- P. Müller-Buschbaum, M. A. Ruderer, S. Guo, R. Meier, H.-Y. Chiang, V. Körstgens, J. Perlich, S. V. Roth
  Solvent induced morphology in polymer-based systems for organic photovoltaics
  European Polymer Congress, Granada, 26 Jun – 01 Jul 2011

- P. Müller-Buschbaum, W. Wang, Q. Zhong, D. Magerl, J. Adelsberger, A. M. Bivigou Koumba, A. Miasnikova, A. Laschewsky, C. M. Papadakis
  Switching kinetics of thermo-responsive hydrogel films
  Hydrogele Tagung, Cologne, 13 – 15 Jul 2011

- P. Müller-Buschbaum, M. Rawolle, M. A. Niedermeier, K. Sarkar, P. Lellig, J. S. Gutmann
  Sol-gel templated titaniumdioxide films for solar cell applications
  ICCE-19, International Conference on Composites or Nano Engineering, Shanghai, China, 24 – 30 Jul 2011

- P. Müller-Buschbaum
  Nanophysik
  Edgar-Lüscher-Fortbildungskurs für Physiklehrer, 14 – 16 Sep 2011

- P. Müller-Buschbaum, G. Kaune, E. Metwalli, R. Meier, V. Körstgens, K. Schlage, S. Couet, S. V. Roth, R. Röhlsberger
  Growth and morphology of sputtered metal thin films on conducting polymer surfaces
  5th International Workshop on Polymer/Metal Nanocomposites, Bari, Italy, 20 – 22 Sep 2011

- P. Müller-Buschbaum, J. Perlich, G. Kaune, M. Rawolle, M. A. Niedermeier, M. Memesa, P. Lellig, J. S. Gutmann
  Inorganic-organic hybrid films with integrated function
  SPP 1181 Nanomat Abschlusskolloquium, Darmstadt, 27 – 28 Sep 2011

- P. Müller-Buschbaum
  Grazing incidence small angle x-ray scattering - an advanced characterization technique for structured polymer films
  Advances in Polymer Science and Technology (APST) 2, Linz, Austria, 29 – 30 Sep 2011

- P. Müller-Buschbaum
  Modeling grazing incidence small angle x-ray scattering data
  GISAXS 2011 Workshop, Hamburg, 10 – 12 Oct 2011

- P. Müller-Buschbaum
  Morphology in polymer-based systems for organic photovoltaics as probed with advanced scattering techniques
  2nd PETRA III SAXS extension Workshop, Hamburg, 13 – 14 Oct 2011

- P. Müller-Buschbaum
  Determination of local morphologies in polymer based devices using nanobeam scattering techniques
  Hard x-ray imaging at MAX IV Workshop, Stockholm, Sweden, 18 – 19 Oct 2011

- M. A. Niedermeier, F. Schaff, V. Körstgens, R. Meier, J. Perlich, S. V. Roth, P. Müller-Buschbaum
  Superstructuring of bicontinuous foam-like titania nanostructures in thin films
  DPG Frühjahrstagung, Dresden, 13 – 18 Mar 2011

- M. A. Niedermeier, E. Metwalli, V. Körstgens, J. Perlich, A. Buffet, M. Abul Kashem, K. Schlage, R. Röhlsberger, S. V. Roth, P. Müller-Buschbaum
  In-situ GISAXS study of metal electrode growth on semiconducting organic films
  E-MRS Spring Meeting, Nice, France, 09 – 13 May 2011

- C. M. Papadakis
  Dispersions of modified carbon nanotubes - a combined SAXS and SANS investigation
  Satellite Meeting of the HASYLAB Users' Meeting 'Status and Perspectives of Small Angle X-ray Scattering at DESY', Hamburg, 27 Jan 2011

- C. M. Papadakis
  Intelligente Hydrogele
  Tag der Physikerin, Garching, 10 Feb 2011

- C. M. Papadakis
  Thermoresponsive, self-assembled polymeric hydrogels
  Freiburger Makromolekulares Kolloquium, Freiburg, 24 – 26 Feb 2011

- C. M. Papadakis, C. Darko, G. Reiter
  Crystallization in block copolymer thin films
  DPG Frühjahrstagung, Dresden, 13 – 18 Mar 2011

- C. M. Papadakis
  Thermoresponsive polymeric hydrogels - what can neutrons tell us?
  Max-Planck-Institut für Extraterrestrische Physik, 11 Apr 2011

- C. M. Papadakis
  NSE on solutions and gels from thermoresponsive block copolymers – little surprises upon collapse
  ESS Design-Update Project Meeting WP-I2 Spin-Echo/Larmor Instruments, Jülich, 15 Apr 2011

- C. M. Papadakis
  Thermoresponsive polymeric hydrogels – what can neutrons tell us?
  5th FRM II Science Meeting, Burg Rothenfels, 06 – 09 Jun 2011

- C. M. Papadakis
  Kinetics of structural changes in concentrated thermoresponsive block copolymer solutions
  Meeting of the SPP 1259 'Intelligente Hydrogele', Cologne, 14 – 15 Jul 2011

- C. M. Papadakis
  Polymere Nanostrukturen
  Lüscher Lectures, Dillingen, 14 – 16 Sep 2011

- C. M. Papadakis
  In-situ, real-time GISAXS - structural changes in block copolymer thin films in solvent vapor
  BSS Theme Day, Cambridge, 01 Dec 2011

- W. Petry
  Neutron source Heinz Maier-Leibnitz (FRM II) – Status and prospects
  Workshop: MPIs at FRM II, Stuttgart, 10 – 11 Jan 2011

- W. Petry
  Light in the dark – neutrons for science, engineering and industry
  Physik-Kolloquium der Max-Planck-Institute, Stuttgart, 18 Jan 2011

- W. Petry
  Research reactor FRM II: contribution for future availability of Mo-99
  DGN-Kongress 2011, Dreiländertreffen, Bregenz, 14 Apr 2011

- W. Petry
  Das Risiko der Anderen
  Ethik nach Tschernobyl und Fukushima – Perspektiven für eine verantwortbare Energiestrategie, München, 24 May 2011

- W. Petry
  Teilnahme an der Podiumsdiskussion zum Thema: 'Nach Fukushima. Perspektiven einer fehlerfreundlichen Energiepolitik'
  Münchner Volkshochschule, Offene Akademie, 26 May 2011

- W. Petry
  User Facility FRM II - multiple purpose reactors for the 21st century
  Regional Workshop under IAEA TC project RER4032 (Enhancing the sustainability of research reactors and their safe operation through regional cooperation, networking and coalitions) Concerted actions in research and applications with neutron beams in europe, Budapest, Hungary, 01 – 03 Jun 2011

- W. Petry
  Nano with neutrons
  4th Joint Nanoworkshop of TU/e, DTU and TUM, Garching, 01 Jun 2011

- W. Petry
  The impossible: How to communicate that society may benefit from nuclear technology
  IGSEE (International School of Science and Engineering - TUM) Symposium, Burg Raitenhaslach, 10 Jun 2011

- W. Petry
  Neutronen - wozu, woher, wie sicher?
  Bündnis 90/Die Grünen, München, 11 Jul 2011

- W. Petry
  Light in the dark - neutrons for science, engineering and medicine
  W. Petry, ZS. Revay: User Facility FRM II, 13 Jul 2011

- W. Petry
  ESS issues - a thought provoking seminar
  ECNS 2011; ECNS-ESS side meeting: Science and Scientist at ESS. Get Involved! Prague, 17 – 21 Jul 2011

- W. Petry
  MaMaSELF Summerschool
  Erasmus Mundus MaMaSELF Summerschool, Rennes, France, 19 – 21 Sep 2011

- W. Petry
  Neutronen für die Nanowelt
  Lüscher Lectures, Dillingen, 14 – 16 Sep 2011

- W. Petry
  Neutronen - Wozu? Woher? Wie sicher?
  Besuch der Stadtratsfraktion München der 'Grünen' am FRM II, 08 Nov 2011

- W. Petry
  Licht im Dunkeln - Neuronen für Forschung, Industrie und Medizin
  UNI-TAG des Physik-Departments der TUM, 25 Nov 2011

- W. Petry, J. Knebel
  Research with neutrons in Germany in view of the phase out of nuclear power
  The 4th International Symposium on Material Testing Reactors (ISMTR-4), Oarai-town, Japan, 05 – 09 Dec, 2011

- M. Philipp, U. Müller, O. Astasheva, J. K. Krüger, P. Müller-Buschbaum
  About hypersonic instabilities on different time scales in PNIPAM hydrogels
  Hydrogel Analytics - SPP 1259 Workshop, Garching, 25 – 26 Oct 2011

- M. Rawolle, M. A. Ruderer, S. Guo, E. Metwalli, E. V. Braden, J. Perlich, S. V. Roth, T. Fröschl, N. Hüsing, P. Müller-Buschbaum
  New approach to low-temperature processed titania for application in inorganic-organic hybrid photovoltaics
  DPG Frühjahrstagung, Dresden, 13 – 18 Mar 2011

- M. Rawolle, M. A. Ruderer, S. M. Prams, Q. Zhong, D. Magerl, J. Perlich, S. V. Roth, P. Lellig, J. S. Gutmann, P. Müller-Buschbaum
  Combination of micro-fluidics and sol-gel templating for nanostructuring of titania thin films for photovoltaic application
  ICCE-19, International Conference on Composites or Nano Engineering, Shanghai, China, 24 – 30 Jul 2011

- M. Rawolle, D. Magerl
  Grazing incidence
  Young Neutron Researchers Seminar, Garching, 24 Nov 2011

- M. A. Ruderer, S. M. Prams, M. Rawolle, Q. Zhong, J. Perlich, S. V. Roth, P. Müller-Buschbaum
  Influence of annealing and blending of photoactive polymers on their crystalline structure
  APS March Meeting, Dallas, TX, USA, 21 – 25 Mar 2011

- M. A. Ruderer, S. M. Prams, M. Rawolle, G. Kaune, W. Wang, Q. Zhong, E. Metwalli, J. Perlich, S. V. Roth, P. Müller-Buschbaum
  Morphology of bulk heterojunction systems for polymer-based photovoltaics
  1st Colloquium of the Munich School of Engineering, Garching, 18 Jul 2011

- M. A. Ruderer
  Morphology of bulk heterojunction systems for polymer-based photovoltaics
  Complex Matter and Biophysics Seminar, Raleigh, NC, USA, 06 Dec 2011

- A. Sepe
  Block Copolymer Thin Films
  5th FRM II Science Meeting, Burg Rothenfels, 06 – 09 Jun 2011

- A. Sepe
  In situ studies of lamellar P(S-b-B) diblock copolymer thin films during heat and vapour treatment
  Cavendish Laboratory, University of Cambridge, United Kingdom, 20 Sep 2011

- Q. Zhong, G. Kaune, M. Rawolle, E. Metwalli, A. M. Bivigou-Koumba, A. Laschewsky, C. M. Papadakis, R. Cubitt, P. Müller-Buschbaum
  Switching kinetics of pMDEGA based thermo-responsive hydrogel films probed by in-situ neutron reflectivity
  DPG Frühjahrstagung, Dresden, 13 – 18 Mar 2011

9.3 Posters

- J. Adelsberger, A. Golosova, S. Jaksch, D. Magerl, M. A. Niedermeier, E. Metwalli, A. Diethert, S. Funari, I. Grillo, A. Bivigou Koumba, A. Laschewsky, P. Müller-Buschbaum, C. M. Papadakis
  Structure and kinetics of thermoresponsive blockcopolymer gels
  HASYLAB User Meeting 2011, Hamburg, 27 – 28 Jan 2011

- J. Adelsberger, A. Golosova, S. Jaksch, D. Magerl, M. A. Niedermeier, E. Metwalli, A. Diethert, S. Funari, I. Grillo, A. Bivigou Koumba, A. Laschewsky, P. Müller-Buschbaum, C. M. Papadakis
  Structure and kinetics of thermoresponsive blockcopolymer gels
  4th Joint Nanoworkshop of TU/e, DTU and TUM, Garching, 01 Jun 2011

- C. Birkenstock, R. Meier, P. Müller-Buschbaum
  Novel structuring routine of PEDOT:PSS applied to organic photovoltaics
  DPG Frühjahrstagung, Dresden, 13 – 18 Mar 2011

- G. De Paoli, S. Jaksch, A. Miasnikova, A. Laschewsky, P. Müller-Buschbaum, C. M. Papadakis
  Cononsolvency in thermoresponsive PNIPAM-based block copolymers
  DPG Frühjahrstagung, Dresden, 13 – 18 Mar 2011

- S. Ener, J. Neuhaus, R. Mole, K. Hradil, M. Siewert, I. Titov, M. E. Gruner, B. Pedersen, P. Entel, M. Acet, W. Petry
  Investigation of the phonon properties of Ni-Mn-Ga materials as a function of temperature
  ICFSMA'11, Dresden, 18 – 22 Jul 2011

- S. Guo, M. A. Ruderer, R. Meier, H-Y. Chiang, J. Perlich, S. V. Roth, P. Müller-Buschbaum
  Influence of different solvents on morphology in P3HT:PCBM bulk heterojunction systems for organic photovoltaics
  HASYLAB User Meeting, Hamburg, 27 – 28 Jan 2011

- S. Guo, M. A. Ruderer, R. Meier, H-Y. Chiang, J. Perlich, S. V. Roth, P. Müller-Buschbaum
  Influence of different solvents on morphology in P3HT:PCBM bulk heterojunction systems for organic photovoltaics
  Tag der Physikerin, Garching, 10 Feb 2011

- S. Guo, M. A. Ruderer, R. Meier, H-Y. Chiang, J. Perlich, S. V. Roth, P. Müller-Buschbaum
  Influence of different solvents on morphology in P3HT:PCBM bulk heterojunction systems for organic photovoltaics
  DPG Frühjahrstagung, Dresden, 13 – 18 Mar 2011

- S. Guo, M. A. Ruderer, M. Rawolle, V. Körstgens, J. Perlich, S. V. Roth, P. Müller-Buschbaum
  A systematic X-ray scattering study on highly efficient bulk heterojuntion P3HT:PCBM solar cell
  5th FRM II Science Meeting, Burg Rothenfels, 06 – 09 Jun 2011

- S. Guo, M. A. Ruderer, R. Meier, H-Y. Chiang, J. Perlich, S. V. Roth, P. Müller-Buschbaum
  Influence of different solvents on morphology in P3HT:PCBM bulk heterojunction systems for organic photovoltaics
  1st Colloquium of the Munich School of Engineering, Garching, 18 Jul 2011

- W. Hefter, E. Metwalli, V. Körstgens, A. Buffett, S.V. Roth, P. Müller-Buschbaum
  Lithium-containing diblock copolymer thin films for solid-state batteries
  DPG Frühjahrstagung, Dresden, 13 – 18 Mar 2011
- W. Hefter, E. Metwalli, P. Müller-Buschbaum
  Lithium-containing diblock copolymer thin films for solid-state batteries
  5th FRM II Science Meeting, Burg Rothenfels, 06 – 09 Jun 2011
- W. Hefter, E. Metwalli, V. Körstgens, A. Buffett, S.V. Roth, P. Müller-Buschbaum
  Lithium-containing diblock copolymer thin films for solid-state batteries
  1st Colloquium of the Munich School of Engineering, Garching, 18 Jul 2011
- E. M. Herzig, K. Wagenbauer, M. A. Ruderer, M. Rawolle, W. Wang, K. Sarkar, S. V. Roth, P. Müller-Buschbaum
  3-component systems in organic photovoltaics
  4th Joint Nanoworkshop of TU/e, DTU and TUM, Garching, 01 Jun 2011
- E. M. Herzig, K. Wagenbauer, M. A. Ruderer, M. Rawolle, W. Wang, K. Sarkar, S. V. Roth, P. Müller-Buschbaum
  The OPV - Hat Trick: 3 component systems
  5th FRM II Science Meeting, Burg Rothenfels, 06 – 09 Jun 2011
- E. M. Herzig, K. Wagenbauer, M. A. Ruderer, M. Rawolle, W. Wang, K. Sarkar, S. V. Roth, P. Müller-Buschbaum
  3-component systems in organic photovoltaics
  1st Colloquium of the Munich School of Engineering, Garching, 18 Jul 2011
- E. M. Herzig, K. Wagenbauer, M. A. Ruderer, M. Rawolle, W. Wang, K. Sarkar, S. V. Roth, P. Müller-Buschbaum
  Three component organic photovoltaics systems
  International Symposium on Advances in Photovoltaics and Photocatalysis, Garching, 21 – 22 Jul 2011
- E. T. Hoppe, B. Wang, I. Hopp, A. Sepe, M. Port, M. Haese-Seiller, J.-F. Moulin, B. Menges, C. M. Papadakis
  Polymer properties at the polymer solid interface
  4th Joint Nanoworkshop of TU/e, DTU and TUM, Garching, 01 Jun 2011
- S. Jaksch, J. Adelsberger, D. Magerl, G. de Paoli, S. Salzinger, S. Huber, R. Jordan, Z. Di, P. Busch, S. Funari, C.M. Papadakis
  Switching behavior of thermoresponsive poly(2-oxazoline) copolymers
  HASYLAB User Meeting 2011, Hamburg, 27 – 28 Jan 2011
- S. Jaksch, J. Adelsberger, D. Magerl, G. de Paoli, S. Salzinger, S. Huber, R. Jordan, Z. Di, P. Busch, S. Funari, C.M. Papadakis
  Switching behavior of thermoresponsive poly(2-oxazoline) copolymers
  DPG Frühjahrstagung, Dresden, 13 – 18 Mar 2011
- S. Jaksch, J. Adelsberger, D. Magerl, G. de Paoli, S. Salzinger, S. Huber, R. Jordan, Z. Di, P. Busch, S. Funari, C.M. Papadakis
  Switching behavior of thermoresponsive poly(2-oxazoline) copolymers
  4th Joint Nanoworkshop of TU/e, DTU and TUM, Garching, 01 Jun 2011

- S. Jaksch, J. Adelsberger, D. Magerl, G. de Paoli, S. Salzinger, S. Huber, R. Jordan, Z. Di, P. Busch, S. Funari, C.M. Papadakis
  Switching behavior of thermoresponsive poly(2-oxazoline) copolymers
  25th Conference of European Colloid and Interface Society, 4 – 9 Sep 2011

- G. Kaune, M. Haese-Seiller, R. Kampmann, J.-F. Moulin, Q. Zhong, P. Müller-Buschbaum
  Quantitative determination of network porosity and degree of pore filling for inorganic-organic hybrid structures
  DPG Frühjahrstagung, Dresden, 13 – 18 Mar 2011

- V. Körstgens, M. Rawolle, A. Buffet, M. Abul Kashem, M. Schwartzkopf, S. V. Roth, P. Müller-Buschbaum
  Gold nanoparticle deposition onto doped polyaniline thin films - an in situ investigation with a combination of μGISAXS and imaging ellipsometry
  DPG Frühjahrstagung, Dresden, 13 – 18 Mar 2011

- V. Körstgens, M. Rawolle, A. Buffet, M. Abul Kashem, M. Schwartzkopf, S. V. Roth, P. Müller-Buschbaum
  Microfluidics and microGISAXS
  4th Joint Nanoworkshop of TU/e, DTU and TUM, Garching, 01 Jun 2011

- V. Körstgens, K. Sarkar, M. Philipp, M. Rawolle, F. J. de Jong, A. Buffet, G. Benecke, G. Herzog, M. Schwartzkopf, S. V. Roth, P. Müller-Buschbaum
  Flow incuced surface attachment of gold nanoparticles in a micro-fluidic cell – in situ GISAXS investigations
  GISAXS 2011 Workshop, Hamburg, 10 – 12 Oct 2011

- D. Magerl, X.-P. Qiu, F. M. Winnik, M. Rawolle, G. Herzog, S. V. Roth, P. Müller-Buschbaum
  Interface correlation in cyclic poly(N-isopropylacrylamide)
  HASYLAB User Meeting, Hamburg, 27 – 28 Jan 2011

- D. Magerl, X.-P. Qiu, F. M. Winnik, P. Müller-Buschbaum
  A comparison of the thermoresponsive switching behavior in thin films of cyclic and linear PNIPAM
  DPG Frühjahrstagung, Dresden, 13 – 18 Mar 2011

- D. Magerl, X.-P. Qiu, F. M. Winnik, M. Rawolle, G. Herzog, S. V. Roth, P. Müller-Buschbaum
  A comparison of the morphology and thermoresponsive switching behavior in thin films of cyclic and linear poly(N-isopropylacrylamide)
  5th FRM II Science Meeting, Burg Rothenfels, 06 – 09 Jun 2011

- D. Magerl, X.-P. Qiu, F. M. Winnik, M. Rawolle, G. Herzog, S. V. Roth, P. Müller-Buschbaum
  A comparison of the morphology and thermoresponsive switching behavior in thin films of cyclic and linear poly(N-isopropylacrylamide)
  European Polymer Congress, Granada, 26 Jun – 01 Jul 2011

- D. Magerl, X.-P. Qiu, F.M. Winnik, M. Rawolle, G. Herzog, S.V. Roth, P. Müller-Buschbaum
  A comparison of the morphology and thermoresponsive switching behavior in thin films of cyclic and linear poly(N-isopropylacrylamide
  GISAXS 2011 Workshop, Hamburg, 10 – 12 Oct 2011

- R. Meier, M. A. Ruderer, M. Haese-Seiller, R. Kampmann, P. Müller-Buschbaum
  GISANS Study on Complex Protonated Polymer Blend Films Probing the Solvent Content
  5th FRM II Science Meeting, Burg Rothenfels, 06 – 09 Jun 2011

- R. Meier, C. Birkenstock, P. Müller-Buschbaum
  Structured polymer films and their application for organic photovoltaics
  1st Colloquium of the Munich School of Engineering, Garching, 18 Jul 2011

- E. Metwalli, J.-F. Moulin, J. Perlich, W. Wang, A. Diethert, S. V. Roth, P. Müller-Buschbaum
  Progressive selective gold deposition from a flowing stream of solution onto a polymer template
  4th Joint Nanoworkshop of TU/e, DTU and TUM, Garching, 01 Jun 2011

- H. Morhenn, S. Busch, T. Unruh
  Short time dynamics of a medium length polythylene melt
  International Workshop on Dynamics in Viscous Liquids III, Rome, Italy, 30 Mar – 02 Apr 2011

- H. Morhenn, S. Busch, T. Unruh
  Short time dynamics of alkanes as seen by neutron scattering and MD simulations
  First Annual NBIA Meeting on ESS Science, Copenhagen, Denmark, 27 Jun – 01 Jul 2011

- H. Morhenn, S. Busch, T. Unruh
  What happens before long-range diffusion? Dynamics in an alkane melt.
  3rd EAM Symposium, Oberhof, 07 – 10 Nov 2011

- H. Morhenn, S. Busch, T. Unruh
  Chain dynamics in an alkane melt: Which motions are seen by quasielastic neutron scattering?
  Perspectives in Terahertz Spectroscopy with Neutrons - Workshop, Berlin, 29 – 30 Nov 2011

- M. A. Niedermeier, D. Magerl, Q. Zhong, A. Nathan, V. Körstgens, J. Perlich, S. V. Roth, P. Müller-Buschbaum
  Hierarchically structured titania thin films by iterative block copolymer based sol-gel templating
  HASYLAB User Meeting, Hamburg, 27 – 28 Jan 2011

- M. A. Niedermeier, V. Körstgens, J. Perlich, P. Müller-Buschbaum
  Custom tailoring of titania thin films for application in organic photovoltaics
  5th FRM II Science Meeting, Burg Rothenfels, 06 – 09 Jun 2011

- M. A. Niedermeier, V. Körstgens, J. Perlich, P. Müller-Buschbaum
  Custom tailoring of titania thin films for application in organic photovoltaics
  1st Colloquium of the Munich School of Engineering, Garching, 18 Jul 2011

- M. A. Niedermeier, V. Körstgens, J. Perlich, P. Müller-Buschbaum
  Custom tailoring of titania thin films for application in organic photovoltaics
  International Workshop on Advances in Photovoltaics and Photocatalysis, Garching, 21 – 22 Jul 2011

- C. M. Papadakis, J. Adelsberger, P. Müller-Buschbaum, T. Hellweg, A. M. Bivigou-Koumba, A. Laschewsky
  Time-resolved SANS and NSE on solutions from thermo-responsive block copolymers - little surprises upon collapse
  Jülich Soft Matter Days 2011, Bonn, 15 – 18 Nov 2011

- M. Philipp, D. Magerl, R. Aleksandrova, U. Müller, O. Astasheva, M. König, C. Dawson, J. K. Krüger, P. Müller-Buschbaum
  Structural properties of poly(N-isopropyl acrylamide)-based systems
  4th Joint Nanoworkshop of TU/e, DTU and TUM, Garching, 01 Jun 2011

- M. Philipp, D. Magerl, R. Aleksandrova, U. Müller, O. Astasheva, M. König, C. Dawson, J. K. Krüger, P. Müller-Buschbaum
  Structural properties of poly(N-isopropyl acrylamide)-based systems
  5th FRM II Science Meeting, Burg Rothenfels, 06 – 09 Jun 2011

- M. Philipp, D. Magerl, R. Aleksandrova, U. Müller, O. Astasheva, M. König, C. Dawson, J. K. Krüger, P. Müller-Buschbaum
  Structural properties of poly(N-isopropyl acrylamide)-based systems
  GISAXS 2011 Workshop, Hamburg, 10 – 12 Oct 2011

- S. Raith, B. Miller, M. Schmiele, E. Metwalli, C. M. Papadakis
  Crystallization and mesoscopic structures in polymer nanocomposites for batteries
  1st Colloquium of the Munich School of Engineering, Garching, 18 Jul 2011

- M. Rawolle, M. A. Ruderer, S. M. Prams, Q. Zhong, D. Magerl, P. Lellig, J. S. Gutmann, J. Perlich, S. V. Roth, P. Müller-Buschbaum
  Nanostructuring of titania thin films by combination of micro-fluidics and block copolymer based sol-gel templating
  HASYLAB User Meeting, Hamburg, 27 – 28 Jan 2011

- M. Rawolle, M. A. Ruderer, S. M. Prams, Q. Zhong, D. Magerl, P. Lellig, J. S. Gutmann, J. Perlich, S. V. Roth, P. Müller-Buschbaum
  Nanostructuring of titania thin films by combination of micro-fluidics and block copolymer based sol-gel templating
  Tag der Physikerin, Garching, 10 Feb 2011

- M. Rawolle, D. Magerl, J. Perlich, S. V. Roth, A. Opitz, M. Gruber, J. Wagner, W. Brütting, P. Müller-Buschbaum
  Structure and morphology of organic donor-acceptor photovoltaic cells based on DIP and C_{60}
  DPG Frühjahrstagung, Dresden, 13 – 18 Mar 2011

- M. Rawolle, K. Sarkar, M. A. Niedermeier, P. Lellig, J. S. Gutmann, P. Busch, J.-F. Moulin, M. Haese-Seiller, P. Müller-Buschbaum
  Infiltration of the network structure of nanoporous titania films for applications in photovoltaics
  5th FRM II Science Meeting, Burg Rothenfels, 06 – 09 Jun 2011

- M. Rawolle, M. A. Ruderer, S. M. Prams, Q. Zhong, D. Magerl, P. Lellig, J. S. Gutmann, J. Perlich, S. V. Roth, P. Müller-Buschbaum
  Nanostructuring of titania thin films by combination of micro-fluidics and block copolymer based sol-gel templating
  1st Colloquium of the Munich School of Engineering, Garching, 18 Jul 2011

- M. Rawolle, P. Lellig, M. A. Niedermeier, M. C. Lechmann-Dorn, J. Perlich, S. V. Roth, T. Fröschl, N. Hüsing, J. S. Gutmann, P. Müller-Buschbaum
  Inorganic-organic hybrid films with integrated function
  Final Meeting DFG Priority Programme SPP 1181 NANOMAT, Darmstadt, 27 – 28 Sep 2011

- M. A. Ruderer, S. M. Prams, M. Rawolle, S. Guo, J. Perlich, S. V. Roth, P. Müller-Buschbaum
Internal morphology of BHJ solar cells probed in-situ with GISAXS during operation
HASYLAB User Meeting, Hamburg, 27 – 28 Jan 2011

- M. A. Ruderer, S. Guo, R. Meier, H.-Y. Chiang, J. Wiedersich, V. Körstgens, J. Perlich, S. V. Roth, P. Müller-Buschbaum
Solvent induced morphology in polymer-based systems for organic photovoltaics
E-MRS Spring Meeting, Nice, France 09 – 13 May 2011

- M. A. Ruderer, C. Wang, A. Hexemer, P. Müller-Buschbaum
Resonant soft X-ray scattering on conducting polymer systems
5th FRM II Science Meeting, Burg Rothenfels, 06 – 09 Jun 2011

- M. A. Ruderer, C. Wang, A. Hexemer, P. Müller-Buschbaum
Resonant soft X-ray scattering on conducting polymer systems
International Workshop of Advances in Photovoltaics and Photocatalysis, Garching, 21 – 22 Jul 2011

- K. Sarkar, M. Rawolle, M. A. Niedermeier, P. Müller-Buschbaum
ZnO nanostructures templated by a PS-b-PEO diblock copolymer via sol-gel route
Tag der Physikerin, Garching, 10 Feb 2011

- K. Sarkar, M. Rawolle, M. A. Niedermeier, P. Müller-Buschbaum
ZnO nanostructures templated by a PS-b-PEO diblock copolymer via sol-gel route
DPG Frühjahrstagung, Dresden, 13 – 18 Mar 2011

- K. Sarkar, M. Rawolle, E. M. Herzig, W. Wang, P. Müller-Buschbaum
ZnO nanostructures templated by a PS-b-PEO diblock copolymer via sol-gel route
4th Joint Nanoworkshop of TU/e, DTU and TUM, Garching, 01 Jun 2011

- K. Sarkar, M. Rawolle, E. M. Herzig, W. Wang, P. Müller-Buschbaum
ZnO nanostructures templated by a PS-b-PEO diblock copolymer via sol-gel route
5th FRM II Science Meeting, Burg Rothenfels, 06 – 09 Jun 2011

- K. Sarkar, M. Rawolle, E. M. Herzig, W. Wang, P. Müller-Buschbaum
ZnO nanostructures templated by a PS-b-PEO diblock copolymer via sol-gel route
1st Colloquium of the Munich School of Engineering, Garching, 18 Jul 2011

- K. Sarkar, M. Rawolle, E. M. Herzig, W. Wang, P. Müller-Buschbaum
ZnO nanostructures templated by a PS-b-PEO diblock copolymer via sol-gel route
GISAXS 2011 Workshop, Hamburg, 10 – 12 Oct 2011

- M. Schindler, R. Meier, B. Watts, P. Müller-Buschbaum
Solvent mapping in conducting polymer films using scanning transmission x-ray microscopy
DPG Frühjahrstagung, Dresden, 13 – 18 Mar 2011

- M. Schindler, R. Meier, B. Watts, P. Müller-Buschbaum
Solvent mapping in conducting polymer films using scanning transmission x-ray microscopy
5th FRM II Science Meeting, Burg Rothenfels, 06 – 09 Jun 2011

- M. Schindler, M. Al Hussein, A. Buffet, S. V. Roth, P. Müller-Buschbaum
Spray deposition of pressure sensitive adhesives followed in-situ with GISAXS
GISAXS 2011 Workshop, Hamburg, 10 – 12 Oct 2011

- A. Sepe, D. Posselt, E. T. Hoppe, S. Jaksch, D. Magerl, Q. Zhong, J. Perlich, D.-M. Smilgies, C. M. Papadakis
  *In-situ study of lamellar poly(styrene-*b*-butadiene) diblock copolymer thin films during heat treatment*
  HASYLAB User Meeting 2011, Hamburg, 27 – 28 Jan 2011

- A. Sepe, D. Posselt, E. T. Hoppe, S. Jaksch, D. Magerl, Q. Zhong, J. Perlich, D.-M. Smilgies, C. M. Papadakis
  *In-situ study of lamellar poly(styrene-*b*-butadiene) diblock copolymer thin films during heat treatment*
  NIM / CompInt Joint Winter School, St. Christoph, Arlberg, Austria, 27 Mar – 02 Apr 2011

- A. Sepe, D. Posselt, S. Jaksch, E. T. Hoppe, D. Magerl, Q. Zhong, J. Perlich, D.-M. Smilgies, C. M. Papadakis
  Kinetics of structural changes in lamellar poly(styrene-b-butadiene) diblock copolymer thin films during thermal treatment
  DPG-Frühjahrstagung, Dresden, 13 – 18 Mar 2011

- A. Sepe, D. Posselt, S. Jaksch, E. T. Hoppe, D. Magerl, Q. Zhong, J. Perlich, D.-M. Smilgies, C. M. Papadakis
  Kinetics of structural changes in lamellar poly(styrene-b-butadiene) diblock copolymer thin films during heat treatment
  4th Joint Nanoworkshop of TU/e, DTU and TUM, Garching, 01 Jun 2011

- W. Wang, M. A. Ruderer, S. Guo, Q. Zhong, C. Birkenstock, P. Müller-Buschbaum
  Organic solar cells with carbon nanotube electrodes
  Tag der Physikerin, Garching, 10 Feb 2011

- W. Wang, M. A. Ruderer, S. Guo, Q. Zhong, C. Birkenstock, P. Müller-Buschbaum
  Effect of annealing processes on morphology of photoactive polymer layers for solar cell applications
  DPG Frühjahrstagung, Dresden, 13 – 18 Mar 2011

- W. Wang, M. A. Ruderer, S. Guo, E. Metwalli, K. Scherer, P. Müller-Buschbaum
  Morphology of bulk heterojunction systems for polymer-based photovoltaics
  5th FRM II Science Meeting, Burg Rothenfels, 06 – 09 Jun 2011

- W. Wang, M. A. Ruderer, S. Guo, E. Metwalli, K. Scherer, P. Müller-Buschbaum
  Morphology of bulk heterojunction systems for polymer-based photovoltaics
  1st Colloquium of the Munich School of Engineering, Garching, 18 Jul 2011

- W. Wang, M. A. Ruderer, S. Guo, E. Metwalli, K. Scherer, P. Müller-Buschbaum
  Morphology of bulk heterojunction systems for polymer-based photovoltaics
  GISAXS 2011 Workshop, Hamburg, 10 – 12 Oct 2011

- Y. Yao, E. Metwalli, H. Choe, P. Busch, P. Müller-Buschbaum
  Alignment of Magnetic Nanoparticles in Diblock Copolymer Films under External Magnetic Fields
  Tag der Physikerin, Garching, 10 Feb 2011

- Y. Yao, E. Metwalli, H. Choe, P. Busch, P. Müller-Buschbaum
  Alignment of magnetic nanoparticles in diblock copolymer films under external magnetic fields
  DPG Frühjahrstagung, Dresden, 13 – 18 Mar 2011

- Y. Yao, E. Metwalli, H. Choe, M. Opel, P. Müller-Buschbaum
  Alignment of magnetic nanoparticles in diblock copolymer films under external magnetic fields
  5th FRM II Science Meeting, Burg Rothenfels, 06 – 09 Jun 2011

- Y. Yao, E. Metwalli, H. Choe, M. Opel, P. Müller-Buschbaum
  Alignment of magnetic nanoparticles in diblock copolymer films under external magnetic fields
  GISAXS 2011 Workshop, Hamburg, 10 – 12 Oct 2011

- J. Zhang, A. Sepe, R. Steinacher, J. Perlich, D. Posselt, C.M. Papadakis
  Structural evolution in diblock copolymer thin films with perpendicular lamellar structure during solvent vapor treatment
  GISAXS 2011 Workshop, Hamburg, 10 – 12 Oct 2011

9.4 Invited talks at LS Funktionelle Materialien

- Dr. Dietmar Schwahn, Institut für Festkörperforschung, Forschungszentrum Jülich
  Polymere Mischungen als Modellsystem zur Untersuchung kritischer Phänomene
  18 Jan 2011

- Dr. Heide Götz, Dr. Markus Seitz, Deutsches Patent- und Markenamt
  Das deutsche Patentsystem und Online-Recherchedienste 03 May 2011

- Prof. Yongfeng Men, Changchun Institute of Applied Chemistry, Changchun, China
  Deformation mechanism of semi-crystalline polymers
  04 May 2011

- Dr. Yannis Georgalis, Lehrstuhl für Biotechnologie TUM
  Scattering studies on the major eye-lens protein alpha-crystallin
  17 May 2011

- Prof. Sabine Hild, Johannes-Kepler-Universität Linz, Austria
  Characterization of material properties of polymers on the sub-μm scale
  20 May 2011

- Dr. Henrich Frielinghaus, Forschungszentrum Jülich
  Microemulsions adjacent to planar hydrophilic walls 24 May 2011

- Konstantinos Kyriakos, National Technical University of Athens, Greece
  Dielectric and thermal studies of the interfacial and confined segmental dynamics in PDMS/ZrO2/SiO2 nanocomposites
  25 May 2011

- Benjamin März, Ludwig-Maximilians-Universiät München
  Ratched effects in two dimensions
  Jul 20, 2011

- Amelie Koch, Ludwig-Maximilians-Universiät München
  Polymer brushes on graphene and functionalization of GaN
  Aug 2, 2011

- Claudia Palumbiny, Hybrid Nanostructures, Ludwig-Maximilians-Universiät München
  Nanostructured Solar Cells
  10 Aug 2011

- Dr. Ulrich Müller, Université du Luxembourg, Luxembourg
  Temperature modulated refractometry: a novel access to structural changes in isotropic media coupling to the optical refractive index
  23 Nov 2011

- Christoph Schaffer, Soft Condensed Matter Group, Ludwig-Maximilians-Universiät München
  Electronic and structural properties of HBCs
  30 Nov 2011

- Prof. Satoshi Koizumi, Ibaraki University, Japan
  In-situ observation of operating polymer electrolyte fuel cell (PEFC) by neutron small-angle scattering – contrast variation by using deuterium gas
  12 Dec 2011

- Ahmed Mourran, Rheinisch-Westfälische Technische Hochschule Aachen
  Mono- and multilayers in hierarchically organized thin films – from polymersomes to functional oligothiopene
  19 Dec 2011

9.5 Funding

Deutsche Forschungsgemeinschaft:

- Within DFG priority program SPP 1164:
  Non-equilibrium flow at gradient surfaces: Fluid kinetics of droplets and particle motion
  Grant Number: MU 1487/2-3
  Project Leader: Prof. Dr. Peter Müller-Buschbaum

- Within DFG priority program SPP 1181:
  Nanoskalige anorganische Materialien durch molekulares Design: Neue Werkstoffe für zukunftsweisende Technologien, Anorganisch-organische Hybridfilme mit integrierter Funktion
  Grant Number: MU 1487/5-3
  Project Leader: Prof. Dr. Peter Müller-Buschbaum

- Within DFG priority program SPP 1259:
  Struktur und Kinetik stimuli-responsiver, dünner Hydrogelfilme aus amphiphilen Blockcopolymeren
  Grant Number: MU 1487/8-2
  Project Leader: Prof. Dr. Peter Müller-Buschbaum

- Within DFG priority program SPP 1259:
  Struktur und Kinetik stimuli-responsiver, dünner Hydrogelfilme aus amphiphilen Blockcopolymeren
  Grant Number: MU 1487/8-3
  Project Leader: Prof. Dr. Peter Müller-Buschbaum

- *Beschaffung einer Anlage für die Röntgenklein- und -weitwinkelstreuung für den Lehrstuhl für Experimentalphysik IV, Physik-Department E13*
  Grant Number: INST 95/1112-1
  Project Leader: Prof. Dr. Peter Müller-Buschbaum

- Within DFG priority programm SPP 1239
  Änderung von Mikrostruktur und Form fester Werkstoffe durch äußere Magnetfelder
  Grant Number: NE 1405/1-2
  Project Leader: Dr. Jürgen Neuhaus

- *Rolle der Mikrospannungen bei der Eigenspannungsanalyse mittels Neutronenbeugung in mehrphasigen Hochleistungslegierungen*
  Grant Number: PE 580/7-1
  Project Leader: Prof. Dr. Winfried Petry

- *Kinetik der Phasenumwandlung in Ausferritischem Gusseisen (ADI)*
  Grant Number: PE 580/11-1
  Project Leader: Prof. Dr. Winfried Petry

- *In-suit Eigenspannungsanalyse an Verbundgusskörpern mittels Neutronendiffraktometrie*
  Grant Number: PE 580/12-1
  Project Leader: Prof. Dr. Winfried Petry

- Within DFG priority program SPP 1259:
  Struktur und Kinetik stimuli-responsiver, dünner Hydrogelfilme aus amphiphilen Blockcopolymeren
  Grant Number: PA 771/4-3
  Project Leader: Prof. Dr. Christine M. Papadakis

- *Multicompartment systems based on poly (2-oxazoline)s*
  Grant Number: PA 771/6-2
  Project Leader: Prof. Dr. Christine M. Papadakis

- *Lokale Viskosität und Dichte in der Grenzphase von Polymeren an einer festen Grenzfläche - Fluoreszenz-Korrelationsspektroskopie und Neutronenreflektrometrie*
  Grant Number: PA 771/7-1
  Project Leader: Prof. Dr. Christine M. Papadakis

Bundesministerium für Bildung und Forschung:

- *MiNaXS-Mikrofluidik: Entwicklung und Aufbau des Mikrofluidik Messplatzes am Instrument NiNaXS am Synchrotron PETRA III*
  Grant Number: 05K10WOA
  Project Leader: Prof. Dr. Peter Müller-Buschbaum

Others:

- Forschungskooperation Johannes Gutenberg-Universität Mainz
  Feldtheoretische Beschreibung von Eigenschaften weicher kondensierter Materie
  Project Leader: Prof. Dr. Winfried Petry

- Im Rahmen des Internationalen Graduiertenkollegs: Material Science of Complex Interfaces (CompInt)
  Thin films of photoactive semiconducting polymers with incorporated nanoparticles
  Project Leader: Prof. Dr. Peter Müller-Buschbaum

- Im Rahmen des Internationalen Graduiertenkollegs: Material Science of Complex Interfaces (CompInt)
  Strukturelle Änderungen in nanostrukturierten Blockcopolymerfilmen - Zeitaufgelöste in-situ-Untersuchungen mit Röntgenkleinwinkelstreuung unter streifendem Einfall
  Project Leader: Prof. Dr. Christine M. Papadakis

- Im Rahmen der International Graduate School of Science and Engineering (IGSSE)
  Preparation and characterization of functional nanocomposites by directed assembly of modified carbon nanotubes in block copolymer matrices
  Project Leader: Prof. Dr. Christine M. Papadakis, PD Dr. Rainer Jordan (Department Chemie, Technische Universität München)

- Im Rahmen des Fonds National de la Recherche Luxembourg: Forschungskooperation mit der Universiät Luxemburg
  Marie Curie Cofunded, Aides à la formation recherche (AFR) Postdoc project: Volume phase transitions of PNIPAM-based aqueous bulk and thin film systems
  Project Leader: Prof. Dr. Peter Müller-Buschbaum; Co-Advisor: Prof. Dr. Dr. hc Jan Kristian Krüger

Outreach:

- Im Rahmen der Munich School of Engeneering (MSE): Netzwerk Regenerative Energien
  Aufbau eines interdisziplinären Netzwerks aus Lehrstühlen der Technischen Universität München und anderen Forschungseinrichtungen zur Förderung der Forschungsaktivitäten im Bereich der regenerativen Energien
  Project Leader: Prof. Dr. Peter Müller-Buschbaum

10 The chair

10.1 Graduations

- **Accomplished PhD theses**

Harald Breitkreutz
Coupled neutronics and thermal hydraulics of high density cores for FRM II

Alexander Diethert
Near-surface composition of pressure-sensitive adhesive films and its impact on adhesion

Anastasia Golosova
Chemical modification of carbon nanotubes for nanocomposite applications

Rainer Jungwirth
Irradiation behavior of modified high-performance nuclear fuels

Katharina Rolfs
Influence of the alloying element cobalt on the key properties of ferromagnetic shape memory Ni-Mn-Ga single crystals

Wolfgang Schmid
Construction of a sputtering reactor for the coating and processing of monolithic U-Mo nuclear fuel

- **Accomplished diploma theses**

Christian Brandt
Der Einfluss von Elektronenbestrahlung auf Kaskadensolarzellen für Hochtemperatur-Solargeneratoren

Marta González Martí
Assessment and further development of programs for medical therapy using fission neutrons

Stephan Roßbauer
Organic-metal oxide hybrid phototransistors

Jürgen Sarvas
Optimisation of high density fuel elements for FRM II

Christian Steyer
Sputterdeposition zur Beschichtung von sphärischem UMo Kernbrennstoffpulver

- **Accomplished master theses**

Christopher Birkenstock
Structuring polymer films for applications in organic photovoltaics

Stefan Raith
Structures of Lithium-containing block copolymers for lithium batteries

- **Accomplished bachelor theses**

Bruno Baumeister
Reinigungsverfahren für metallische Uran-Molybdän-Kernbrennstoffe / Cleaning procedures for metallic Uranium-Molybdenum nuclear fuel

Erik Braden
Hybride Strukturen zur Anwendung in der Photovoltaik

Philipp Braun
Development and analysis of a momentum spectrometer for charged particles emitted after the photo double ionization of ethyne and ethylene

Sarah Catharina Brüningk
Neue Systeme für den Transport medizinischer Wirkstoffe

Isabell Groß
Überstrukturierung von Titandioxidfilmen für die Anwendung in der Fotovoltaik

Patrick Kirchschlager
Herstellung von Titandioxid-Nanostrukturen zur Anwendung in der organischen Photovoltaik

Bastian Miller
Thermische Eigenschaften von Blockcopolymeren für Lithiumbatterien

Sebastian Reinl
Entwicklung und Konstruktion eines RF-Sputterkopfes für Zirkonnitrid und Borcarbid

Jochen Schönweiß
Smart thin films made by hydrogels – Intelligente, dünne Filme aus Hydrogel

Xuhu Shen
Characterization of amphiphilic thermoresponsive triblock copolymers

Klaus Wagenbauer
Polymer blends in application for organic photovoltaics

Marcus Wießner
Aufbau eines Demonstrationsversuchs: Compton-Streuung von Röntgenstrahlung an Plexiglas

10.2 Staff

Chair: Prof. Dr. Winfried Petry

Head: Prof. Dr. Peter Müller-Buschbaum

Professors

Prof. Dr. Christine Papadakis
Prof. Dr. Walter Schirmacher

Fellows

Dr. Gabriele De Paoli
Dr. Eva Maria Herzig
Dr. Joana Rebelo Kornmeier
Dr. Volker Körstgens
Dr. Michael Leitner
Dr. Peter Link
Dr. Wiebke Lohstroh
Dr. Ezzeldin Metwalli Ali
Dr. Jürgen Neuhaus
Dr. Martine Philipp
Dr. Giovanna Giulia Simeoni
Dr. Tobias Unruh
Dr. Johannes Wiedersich
Dr. Jianqi Zhang

PhD students

Josef Adelsberger
Harald Breitkreutz
Sebastian Busch
Hsin-Yin Chiang
Alexander Diethert
Semih Ener
Anastasia Golosova
Shuai Guo
Christian Hesse
Tobias Hollmer
Tilo Hoppe
Tanja Huber
Sebastian Jaksch
Rainer Jungwirth
Konstantinos Kyriakos
David Magerl
Robert Meier
Andreas Meier-Koll
Humphrey Morhenn
Martin Niedermeier
Claudia Palumbiny
Monika Rawolle
Katharina Rolfs
Matthias Ruderer
Kuhu Sarkar
Robert Schenk
Markus Schindler
Wolfgang Schmid
Martin Schmiele
Alessandro Sepe
Luca Silvi
Weijia Wang
Yuan Yao
Qi Zhong
Tobias Zweifel

Diploma students

- Yvonne Boose
- Christian Brandt
- Miriam Däubler
- Matthias Fuchs
- Alexandra Fuxman
- William Hefter
- Tim Hülsheger
- Anna Naumann
- Stephan Roßbauer
- Jürgen Sarvas
- Kai-Hermann Scherer
- Christian Steyer

Master students

- Ammara Akhtar
- Christopher Birkenstock
- Sarah Lindner
- Wei Liu
- Stefan Raith
- Greg Tainter

Bachelor students

- Bruno Baumeister
- Erik Braden
- Philipp Braun
- Sebastian Reinl
- Sarah Catharina Brüningk
- Christian Gebbe
- Isabell Groß
- Patrick Kirchschlager
- Bastian Miller
- Sofia Ramirez
- Jochen Schönweiß
- Xuhu Shen
- Klaus Wagenbauer
- Marcus Wießner

Students assistants

- Carola Alonso de Celada Casero
- Minglong He
- Christoph Heller
- Tobias Hollmer
- Enzo Kopperger
- Bastian Miller
- Thomas Pöschl
- Florian Schaff
- Tarunjot Singh
- Michael Hinterstocker
- Klaus Wagenbauer

Technical/administrative staff

- Philipp Bork
- Petra Douglas
- Erik Faber
- Susanna Fink
- Reinhold Funer
- Lukas Hein
- Raffael Jahrstorfer
- Josef Kaplonski
- Dieter Müller
- Jandal Ringe
- Marion Waletzki

10.3 Guests

- Prof. Yongfeng Men, Changchun University of Technology, Changchun, China
  04 May 2011
- Prof. Sabine Hild, Johannes-Kepler-Universität Linz, Austria
  20 May 2011
- Konstantinos Kyriakos, National Technical University of Athens, Greece
  25 May 2011
- Dr. Mahmoud Omar Mustafa Al-Hussein, University of Jordan, Amman, Jordan
  01 Jun – 15 Aug 2011
- Prof. Dr. Françoise Winnik, Faculty of Pharmacy and Department of Chemistry Université de Montréal, Canada
  19 – 21 Jul 2011
- Dr. Neelima Paul, Helmholtz-Zentrum Berlin für Materialien und Energie
  since 01 Oct 2011